

Ben Thomas Pepper

**Effects of the  $^{12}\text{C}(\alpha, \gamma)^{16}\text{O}$  Reaction Rates on  
Single Stellar Evolution Computations**

---

**Efeitos das Taxas de Reação  $^{12}\text{C}(\alpha, \gamma)^{16}\text{O}$  em  
Computações de Evolução Estelar Simples**

Porto Alegre, Brazil

2022



Ben Thomas Pepper

**Effects of the  $^{12}\text{C}(\alpha, \gamma)^{16}\text{O}$  Reaction Rates on Single  
Stellar Evolution Computations**

---

**Efeitos das Taxas de Reação  $^{12}\text{C}(\alpha, \gamma)^{16}\text{O}$  em  
Computações de Evolução Estelar Simples**

Thesis proposal which is submitted to the Programa de Pós-Graduação em Física at the Federal University of Rio Grande do Sul. This submission is one of the requirements to the completion of the degree of Doctor in Sciences.

Universidade Federal do Rio Grande do Sul – UFRGS

Instituto de Física

Programa de Pós-Graduação em Física

Supervisor: Professor Alejandra Daniela Romero

Co-supervisor: Professor Kepler de Souza Oliveira Filho

Porto Alegre, Brazil

2022

Ben Thomas Pepper

Effects of the  $^{12}\text{C}(\alpha, \gamma)^{16}\text{O}$  Reaction Rates on Single Stellar Evolution Computations / Ben Thomas Pepper. – Porto Alegre, Brazil, 2022-150p. : il. (algumas color.) ; 30 cm.

Supervisor: Professor Alejandra Daniela Romero

Tese (Doutorado) – Universidade Federal do Rio Grande do Sul – UFRGS  
Instituto de Física  
Programa de Pós-Graduação em Física, 2022.

1. Nuclear Reactions. 2. Stars: Abundances. 3. Stars: Evolution. I. Profa. Alejandra Daniela Romero. II. Universidade Federal do Rio Grande do Sul. III. Faculdade de Astrofísica. IV. Effects of the  $^{12}\text{C}(\alpha, \gamma)^{16}\text{O}$  Reaction Rates on Single Stellar Evolution Computations

Ben Thomas Pepper

# **Effects of the $^{12}\text{C}(\alpha, \gamma)^{16}\text{O}$ Reaction Rates on Single Stellar Evolution Computations**

## **Efeitos das Taxas de Reação $^{12}\text{C}(\alpha, \gamma)^{16}\text{O}$ em Computações de Evolução Estelar Simples**

Thesis proposal which is submitted to the Programa de Pós-Graduação em Física at the Federal University of Rio Grande do Sul. This submission is one of the requirements to the completion of the degree of Doctor in Sciences.

Trabalho aprovado. Porto Alegre, Brazil, 10 de maio de 2022:

---

**Professor Alejandra Daniela Romero**  
Supervisor

---

**Professor Kepler de Souza Oliveira Filho**  
Co-Supervisor

---

**Professor Alan Alves Brito**  
Convidado 1

---

**Professor Charles Bonato**  
Convidado 2

---

**Francis Timmes**  
Convidado 3

---

**Walter Maciel**  
Convidado 4

Porto Alegre, Brazil

2022

*This work is dedicated to those who have helped and guided me to become who I am today,  
thank you to all who have shared in this journey with me.*





# Acknowledgements

I would first like to acknowledge my family. To Mam and Dad, thank you for instilling into me the dedication, independence and charisma I needed to get here. Also for giving me all the chances that were possible in the world for me to be my best self, your hardwork has paid off and it won't ever be forgotten. To Katie, my sister, thank you for growing up with me. Your love and support was always appreciated, without growing up with you I wouldn't be who I am today. To all of my grandparents, thank you for helping a young boy to fulfil their highest potential, as well as raising a son/daughter of your own that knew how to bring out the best in their children.

To Prof. Alejandra Daniela Romero and Prof. Kepler de Souza Oliveira. Thank you for being magnificent supervisors and being there to answer any doubts that I have had, no matter how complex or trivial. You have both made a complex program to be straightforward, I have had clarity on what I need to do every step of the way. I strive to make the best use of the advice, mentoring and knowledge you have passed to me and will continue to pass to me as I go on.

To Dr Alina Istrate. Your help in producing stellar sequences was invaluable. Without it, the sequences that we calculated would not have been as detailed as they are. Also your attention to detail in the referee reports was second-to-none, making for a much smoother submission process. For this, I thank you.

To all of my friends, thank you for your guidance, the good times and your support when I needed it. I hope we can keep in contact in the future. I give specific thanks to Space School UK (SSUK) and my friends which I made there. SSUK is a summer school for students aimed at inspiring and educating students with regards to everything space-related. This is where I decided that I wanted to study astrophysics beyond secondary school.

I give thanks to the Instituto de Física (IF) and the Programa de Pós-Graduação em Física (PPGFís) at the Universidade Federal do Rio Grande do Sul (UFRGS) for opening your program to international students and for the infrastructure necessary for this work to be completed.

I give thanks to the Conselho Nacional de Desenvolvimento Científico e Tecnológico (CNPq) and Coordenação de Aperfeiçoamento de Pessoal de Nível Superior (CAPES) for the bursary which provided me with financial support.

I give thanks to all the MESA code developers for providing the world with an open source tool for which was used extensively in this work.



*“I’ve never done something for the common consensus. I do things to please me. If you are happy with something yourself, you become bulletproof.*

*- Ricky Gervais*



# Abstract

One of the largest uncertainties in stellar evolutionary computations is the accuracy of the considered reaction rates. The  $^{12}\text{C}(\alpha, \gamma)^{16}\text{O}$  reaction is important in stars of all masses, but is of particular importance for the study of low to intermediate-mass stars. Particularly, the  $^{12}\text{C}(\alpha, \gamma)^{16}\text{O}$  will determine the C/O ratio of the core at the final white dwarf cooling curve. Thus, there is a need for a study of how the computations of white dwarfs and their progenitors that are made to date may be affected by the uncertainties of the  $^{12}\text{C}(\alpha, \gamma)^{16}\text{O}$  reaction rates. In this work we compute fully evolutionary sequences using the MESA code with initial masses in the range of  $0.90 \leq M_i/M_\odot \leq 3.05$ . We consider different adopted reaction rates, obtained from the literature, as well as the extreme limits within their uncertainties for the  $^{12}\text{C}(\alpha, \gamma)^{16}\text{O}$  reaction. As expected, we find that previous to the core helium burning stage there are no changes to the evolution of the stars. However, the subsequent stages are all affected by the uncertainties of the considered reaction rates. In particular, we find differences to the convective core mass during the core helium burning stage which may affect pulsation properties of subdwarfs, the number of thermal pulses during the asymptotic giant branch and trends between final oxygen abundance and the progenitor masses of the remnant white dwarfs. Furthermore, as a result of the modifications in the chemical profiles, specially to the central C/O ratio, we hypothesise that the axion emission due to the Bremsstrahlung and Compton scattering effects will be altered.

**Keywords:** nuclear reactions – stars: abundances – stars: evolution



# Resumo

Uma das maiores incertezas em computações evolutivas estelares é a precisão das taxas de reação consideradas. A reação  $^{12}\text{C}(\alpha, \gamma)^{16}\text{O}$  é importante em estrelas de todas as massas, mas é de particular importância para o estudo de estrelas de massa baixa a intermediária. Particularmente, a taxa  $^{12}\text{C}(\alpha, \gamma)^{16}\text{O}$  determinará a razão C/O do núcleo na curva final de resfriamento da anã branca. Assim, há a necessidade de um estudo de como os cálculos de anãs brancas e seus progenitores que são feitos até hoje podem ser afetados pelas incertezas dos  $^{12}\text{C}(\alpha, \gamma)^{16}\text{O}$  taxas de reação. Neste trabalho computamos sequências totalmente evolutivas usando o código MESA com massas iniciais na faixa de  $0,90 \leq M_i/M_\odot \leq 3,05$ . Consideramos diferentes taxas de reação adotadas, obtidas da literatura, bem como os limites extremos dentro de suas incertezas para a reação  $^{12}\text{C}(\alpha, \gamma)^{16}\text{O}$ . Como esperado, descobrimos que antes do estágio de queima de hélio do núcleo não há mudanças na evolução das estrelas. No entanto, os estágios subsequentes são todos afetados pelas incertezas das taxas de reação consideradas. Em particular, encontramos diferenças na massa do núcleo convectivo durante o estágio de queima de hélio do núcleo que podem afetar as propriedades de pulsação das subanãs, o número de pulsos térmicos durante o ramo gigante assintótico e as tendências entre a abundância final de oxigênio e as massas progenitoras das anãs brancas remanescentes. Além disso, como resultado das modificações nos perfis químicos, especialmente na relação C/O central, hipotetizamos que a emissão de áxions devido aos efeitos de espalhamento de Bremsstrahlung e Compton será alterada.

**Keywords:** reações nucleares – estrelas: abundâncias – estrelas: evolução





# List of Figures

Figure 1 – Diagram of Stellar Evolution . . . . .	26
Figure 2 – Schematic Hertzsprung–Russell Diagram . . . . .	30
Figure 3 – Cross–section as a function of energy . . . . .	36
Figure 4 – The astrophysical S-Factor as a function of energy . . . . .	37
Figure 5 – Basic energy level diagram . . . . .	39
Figure 6 – Energy level diagram with considerations to the intrinsic spins . . . . .	40
Figure 7 – Effects of different resonant energies . . . . .	41
Figure 8 – Effects of resonance on the S-Factor . . . . .	44
Figure 9 – Energy level diagram of an excited $^{16}\text{O}$ nucleus . . . . .	48
Figure 10 – Ratio of the Selected Reaction Rates as a Function of Temperature . . . . .	50
Figure 11 – Schematic of the radial mesh in MESA . . . . .	58
Figure 12 – Flowchart that represents the order of process in MESA . . . . .	59
Figure 13 – Chemical profiles for a DA with C/O core . . . . .	66
Figure 14 – Kippenhahn diagram for original models . . . . .	70
Figure 15 – Kippenhahn diagram for new Asymptotic Giant Branch models . . . . .	71
Figure 16 – Central C/O ratio at the end of the CHB as a function of initial mass . . . . .	74
Figure 17 – A comparison of the CHB duration between reaction rate uncertainties . . . . .	75
Figure 18 – History of the convective mass and luminosity during the CHB (NACRE) . . . . .	77
Figure 19 – History of the convective mass and luminosity during the CHB (An et al. (2016)) . . . . .	78
Figure 20 – Energy production during the CHB . . . . .	80
Figure 21 – Helium core mass at the start of the TP-AGB as a function of initial mass . . . . .	82
Figure 22 – Helium core growth from TP-AGB until it enters the WD stage . . . . .	83
Figure 23 – Number of TPs as a function of initial mass . . . . .	86
Figure 24 – Initial-to-final mass relation . . . . .	88
Figure 25 – Final ages and cooling ages for the WDs formed . . . . .	90
Figure 26 – Final oxygen mass fraction in the core as a function of initial mass . . . . .	91
Figure 27 – Chemical profiles for $M_i = 1.30 M_{\odot}$ . . . . .	93



# List of Tables

Table 1 – Tables of values for the helium core mass growth and hydrogen fuel mass	85
Table 2 – General Table of Values . . . . .	148



# List of abbreviations and acronyms

ZAMS	Zero Age Main Sequence
MS	Main Sequence
RGB	Red Giant Branch
CHB	Horizontal Branch
AGB	Asymptotic Giant Branch
TP	Thermal Pulse
TP-AGB	Thermally Pulsing Asymptotic Giant Branch
WD	White Dwarf
H-R	Hertzsprung-Russell
KE	Kinetic Energy
PE	Gravitational Potential Energy
$V_C$	Potential Energy of the Coulomb Barrier
MLT	Mixing Length Theory
HFC	Hydrogen Free Core
TDU	Third Dredge-Up
C/O	Carbon-Oxygen
IFMR	Initial-to-Final Mass Relation
$C\alpha$	Luminosity of $^{12}\text{C}(\alpha, \gamma)^{16}\text{O}$
CSPN	Central Stars of Planetary Nebula



# List of symbols

$\gamma$	Photon
$\Gamma$	Energy Width of an energy level within the nucleus
$\tau$	Timescale for a particle to decay from an energy level
$h$	Planck's Constant
$\hbar$	$h/2\pi$
$\alpha$	Alpha particle/mixing length parameter
$\mu$	Reduced Mass
$\epsilon$	Rate of Energy Generation
$\eta$	Scale Factor for mass-loss/electron degeneracy parameter
$\sigma$	Cross-Section
$\langle\sigma v\rangle$	Thermal average of the product of the particle velocity and cross-section
$\lambda$	De Broglie Wavelength
${}^A_ZX$	Standard notation for elements ( $X$ = element, $A$ = nucleon number and $Z$ = atomic number)
$M_i$	Initial Mass
$M_\odot$	Solar Mass
$Z_i$	Initial Metallicity
$\dot{M}$	mass-loss Rate
$N_{TP}$	Number of Thermal Pulses
$l$	Angular Momentum quantum number
$J$	Total Quantum Angular Momentum
$k$	Boltzmann Constant
$S(E)$	S-Factor as a function of energy
$n$	Neutron

$\nabla_T$	True temperature gradient
$\nabla_a$	Adiabatic temperature gradient
$\nabla_\mu$	Composition gradient
$\nabla_L$	Ledoux gradient ( $\nabla_a + \nabla_\mu$ )



# Contents

<b>1</b>	<b>INTRODUCTION</b>	<b>25</b>
<b>1.1</b>	<b>Stellar Evolutionary Theory</b>	<b>25</b>
<b>1.2</b>	<b>Stellar Nuclear Reactions</b>	<b>30</b>
1.2.1	Kinematics of Reactions	31
1.2.2	Reaction Rates	32
1.2.3	The Cross-Section	33
1.2.4	The Astrophysical S-Factor	34
1.2.5	Non-Resonant Reactions	36
1.2.6	Resonant Reactions	38
<b>1.3</b>	<b>History of Stellar Reaction Rates</b>	<b>43</b>
1.3.1	$^{12}\text{C}(\alpha, \gamma)^{16}\text{O}$	45
<b>1.4</b>	<b>Motivation and Aims</b>	<b>50</b>
<b>2</b>	<b>NUMERICAL TOOLS</b>	<b>55</b>
<b>2.1</b>	<b>The stellar structure equations</b>	<b>55</b>
<b>2.2</b>	<b>The MESA Code</b>	<b>56</b>
2.2.1	Microphysics	60
2.2.2	Macrophysics	61
<b>2.3</b>	<b>Building the Code</b>	<b>63</b>
2.3.1	Input Physics	63
2.3.2	Implementation of Alternate Reaction Rates	67
2.3.3	Added subroutines	67
<b>2.4</b>	<b>Additional Models</b>	<b>68</b>
<b>3</b>	<b>THE IMPACT OF THE <math>^{12}\text{C}(\alpha, \gamma)^{16}\text{O}</math> REACTION RATE ON STELLAR EVOLUTION</b>	<b>73</b>
<b>3.1</b>	<b>The Core Helium Burning Phase</b>	<b>73</b>
3.1.1	Central C/O Ratio	73
3.1.2	CHB Lifetime	74
3.1.3	Convective Mixing Episodes during the CHB	75
3.1.4	The Effect of the $C\alpha$ Luminosity	76
<b>3.2</b>	<b>The Asymptotic Giant Branch Phase</b>	<b>79</b>
3.2.1	Helium Core Mass Growth	81
3.2.2	Thermal Pulses	83
3.2.3	Third Dredge-Up Episodes	84
<b>3.3</b>	<b>The White Dwarf Final Cooling Track</b>	<b>87</b>

3.3.1	Initial-to-Final Mass Relation . . . . .	87
3.3.2	Final Age and Cooling Time . . . . .	87
3.3.3	Final Oxygen Abundance . . . . .	89
3.3.4	Inner Chemical Profile . . . . .	91
<b>4</b>	<b>CONCLUSION . . . . .</b>	<b>95</b>
	<b>BIBLIOGRAPHY . . . . .</b>	<b>99</b>
	<b>APPENDIX . . . . .</b>	<b>113</b>
	<b>APPENDIX A – PUBLISHED WORKS . . . . .</b>	<b>115</b>
	<b>APPENDIX B – INLISTS USED IN THIS WORK . . . . .</b>	<b>131</b>
	<b>APPENDIX C – TABLES OF KEY RESULTS . . . . .</b>	<b>147</b>
	<b>APPENDIX D – PERSPECTIVES FOR FUTURE WORK . . . . .</b>	<b>149</b>
<b>D.1</b>	<b>Emission of particles during stellar evolution: Axions . . . . .</b>	<b>149</b>
<b>D.2</b>	<b>Differing Wind Schemes during the AGB . . . . .</b>	<b>150</b>

# 1 Introduction

## 1.1 Stellar Evolutionary Theory

Since the Big Bang<sup>1</sup>, the Universe has been littered with giant clouds of gas containing hydrogen, helium and small amounts of heavier elements that are hereafter referred to as metals. From these gas clouds stars are formed, the building blocks of the visible Universe that we know today. The gas clouds initially have radii up to the order of 10 parsecs and they contract under their own gravity. As a cloud contracts, it fragments into clouds of smaller masses. This fragmentation is actually related to many factors such as: the total mass, particle density and the metallicity of the cloud. [Jeans \(1902\)](#) showed this to be the case and developed the concepts that we know today as the Jeans mass and the Jeans length. The Jeans mass is the limit to the mass that can occupy a spherical volume with a radius characterised by the Jeans length. If the mass of a region characterised by this volume exceeds the Jeans mass, then it will collapse under its own gravity. This is a repetitive process that occurs until the fragment has the suitable conditions to form a stable star.

For a stable star to form from a fragmented gas cloud it must have a mass larger than  $0.08M_{\odot}$ , for solar metallicity ([Burrows; Liebert, 1993](#)). Above this mass, the temperature in the central regions of a protostar reaches  $10^6$  K, allowing the fusion of hydrogen into helium. The energy released from this fusion halts further collapse by providing an outward thermal pressure. The maximum mass for a star of solar metallicity is of the order of  $100M_{\odot}$  ([Eddington, 1926; Öpik, 1938](#)) and it is related to the Eddington luminosity<sup>2</sup>, which describes the maximum luminosity that achieves a balance between radiative pressure and gravitational collapse. If the luminosity is larger than the Eddington luminosity the stellar wind caused by radiative pressure overcomes the gravitational collapse, and the protostar cannot reach the conditions to ignite hydrogen burning.

The ignition of hydrogen burning marks the birth of the star at the Zero-Age Main Sequence (ZAMS) stage. The star evolves on the main sequence (MS) continuing with the fusion of hydrogen within its core. It is on the MS that the star will spend the majority of its existence. The timescale of the MS can be approximated by the equation 1.1 ([Hansen; Kawaler, 1994](#)),

$$t_{MS} \approx 10^{10} \left( \frac{M}{M_{\odot}} \right)^{-2} \text{ yr} \quad (1.1)$$

<sup>1</sup> The Big Bang Theory was theorised by the original version of [Hubble \(1929\)](#). This was later supported by [Lemaître \(1931\)](#) and still continues to be tested.

<sup>2</sup>  $L_{Edd} = \frac{4\pi GMm_p c}{\sigma_T}$

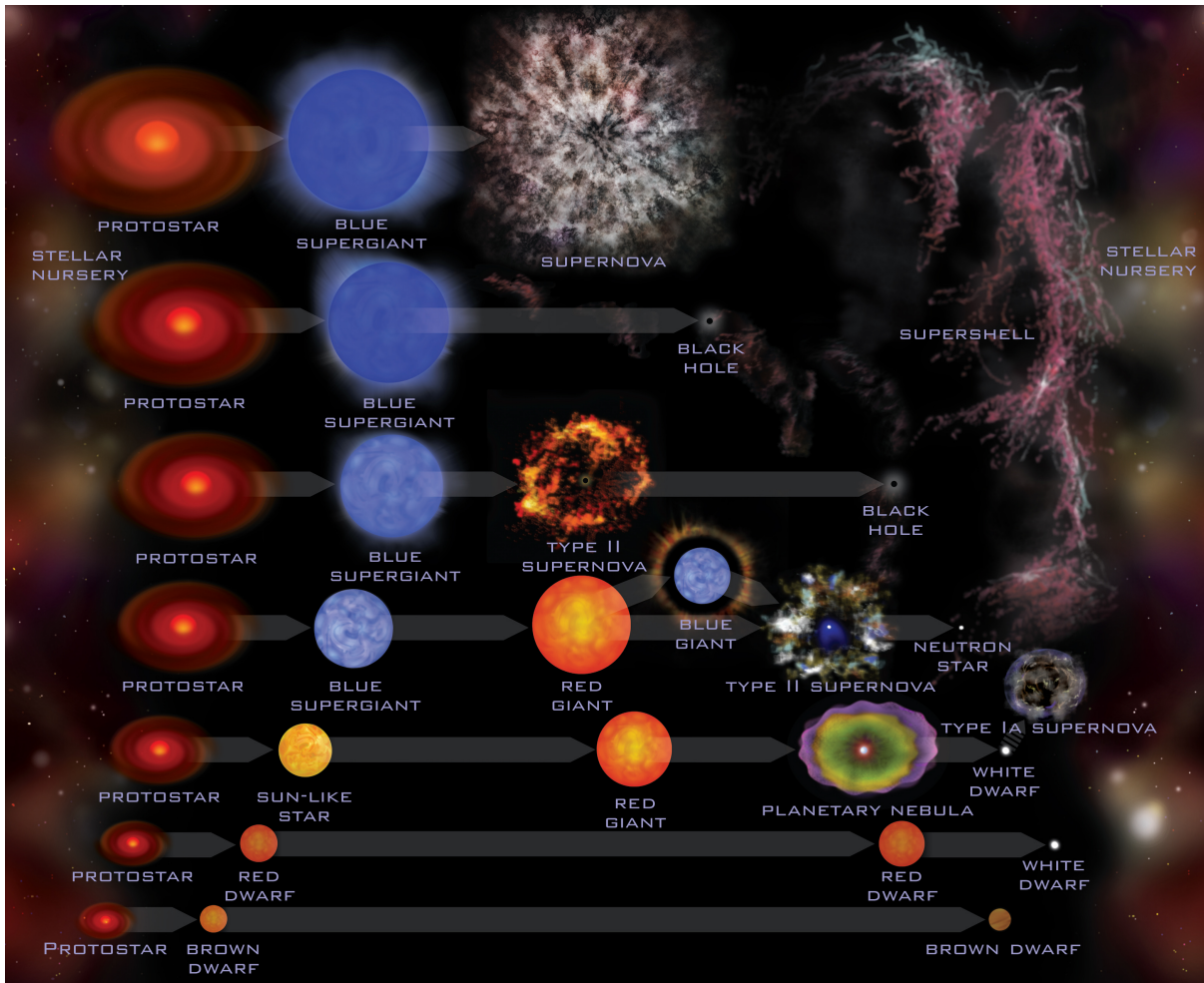


Figure 1 – Illustration of stellar evolution for different initial masses. The lower masses appear at the bottom of the figure and increase vertically. Credit to [JPLPublic \(2019\)](#).

Once  $\sim 10\%$  of the hydrogen is consumed, the star has reached the Schönberg-Chandrasekhar limit and thus cannot support itself further from its gravitational collapse ([Schönberg; Chandrasekhar, 1942](#)). The core (which is now made up of helium) of the star begins to contract. Half of the gravitational potential energy heats up the core, and the other half is radiated away. The energy which is radiated away expands the hydrogen layer of the star considerably<sup>3</sup>.

The hydrogen layer cools significantly from the expansion, reaching effective temperatures around 3000 K, turning the star into a Red Giant. At this stage the temperature gradient within the star is very large, particularly within the hydrogen layer. This produces unsatisfied Schwarzschild and Ledoux criteria<sup>4</sup>, as seen in Equation 1.2 and 1.3, respectively:

<sup>3</sup> This layer surrounds the helium core.

<sup>4</sup> These are criteria that determine whether a region is stable against convection.

$$\nabla_T < \nabla_a, \quad (1.2)$$

$$\nabla_T < \nabla_a + \frac{\phi}{\delta} \nabla_\mu, \quad (1.3)$$

where  $\nabla_T$  is the true temperature gradient,  $\nabla_a$  is the adiabatic temperature gradient,  $\nabla_\mu$  is the composition gradient with  $\psi$  and  $\delta$  derivatives from the 1st law of thermodynamics<sup>5</sup>. The sum on the right hand side of equation 1.3 of the adiabatic temperature gradient and the composition gradient gives the Ledoux gradient,  $\nabla_L$ . The Schwarzschild criterion determines such a value for homogeneous gases (Schwarzschild, 1906) and the Ledoux criterion determines the same for non-homogeneous gases since the stability against convection is dependent on the composition gradient (Ledoux, 1947). Such conditions during the Red Giant phase forces the hydrogen envelope of the star to become convective. This convection brings metals from the interior of the star, which by this time contains carbon and nitrogen in it's composition, to the surface. This is known as the first dredge-up. Due to the first dredge-up, the ratios of  $^{12}\text{C}/^{13}\text{C}$  and C/N begin to decrease as the hydrogen in the atmosphere can fuse with the carbon that is dredged up (Snedden, 1991). At the base of the hydrogen envelope, the increase in temperature of the core eventually allows hydrogen to fuse into helium in a shell burning process via the CNO-cycle.

For stars with an initial mass up to  $2.00 M_\odot$  [depending on the star's initial metallicity: an increased initial metallicity produces a lower upper limit to the initial mass (Romero; Campos; Kepler, 2015)], the core during the RGB is degenerate (Bertelli et al., 1986; Bressan et al., 2012; Kalirai; Marigo; Tremblay, 2014; Marigo et al., 2020). The pressure provided by a degenerate region is a function of density only; there is no dependence on temperature. When the helium core reaches a mass of  $0.45M_\odot - 0.46M_\odot$  [e.g. Renedo et al. (2010), Romero, Campos & Kepler (2015)], the temperature is sufficiently large ( $\sim 2 \cdot 10^8\text{K}$ ) to allow the helium in the core to fuse through the triple- $\alpha$  ( $3\alpha$ ) process. The ignition of helium burning marks the beginning of a new stage - the Core Helium Burning phase (CHB). The  $3\alpha$  process combines three  $\alpha$  particles to form a carbon nucleus through the following reaction chain (Salpeter, 1952a; Kippenhahn; Weigert, 1990; Prialnik, 2009):



5

$$\phi = \left(\frac{\partial \ln \rho}{\partial \ln \mu}\right)_{P,T}, \quad \delta = -\left(\frac{\partial \ln \rho}{\partial \ln n}\right)_{P,\mu}$$

Nuclear reactions in degenerate conditions are unstable, and a large amount of energy is released in a short timescale in the form of a “Helium Flash”. Part of the energy released is used to lift the core degeneracy and the central helium burning continues in normal non-degenerate conditions. For stars with initial masses larger than  $2.00M_{\odot}$ , the core temperature at the end of the MS is large enough to begin core helium burning under non-degenerate conditions. Although helium fusion begins, there is no explosive event like the helium flash as in the case for the lower masses.

During the CHB it is possible to produce oxygen through the reaction between an  $\alpha$  particle and a carbon nucleus. Towards the end of the CHB, the oxygen production rate is greater than the carbon production rate. This can cause a higher abundance of oxygen than carbon within the core. It is because the probability of combining two particles to form oxygen is higher than that of combining three particles to form carbon, once the carbon abundance is high enough (Kippenhahn; Weigert, 1990; Prialnik, 2009). Once the helium in the core is depleted, the star must stop producing energy in the core through the  $3\alpha$  process and the oxygen production.

The exhaustion of helium within the core of the star on the CHB forces the carbon/oxygen core to contract again as it cannot support itself against the gravitational collapse. For core masses below the Chandrasekhar limit<sup>6</sup>, a similar process as the one at the end of the MS causes an expansion of the surrounding envelopes and an increase to the core temperature in accordance with the virial theorem. This core collapse continues until degeneracy pressure is sufficient to halt any further collapse. The carbon/oxygen core is surrounded by a helium envelope which is further surrounded by a hydrogen envelope. With the expansion of the envelope post-helium burning, the star ascends to the Asymptotic Giant Branch (AGB). The star becomes vigorously convective bringing metals to the surface, which is known as the second dredge-up (Kippenhahn; Weigert, 1990). The helium and hydrogen layers are still actively burning to form carbon and helium respectively. Above the hydrogen burning region, there is an additional hydrogen-rich envelope that is inactive due to the lower temperatures.

In stars with initial masses in the range  $6.0 \leq M_i/M_{\odot} \leq 12.0$  the core temperature reaches  $\sim 5 \cdot 10^8$  K where carbon burning can occur, leading to compositions of O/Ne/Mg (Bertelli; Bressan; Chiosi, 1985; Bressan et al., 1993; García-Berro; Ritossa; Iben ICKO, 1997; Umeda et al., 1999; Bono et al., 2000; Siess, 2007; Lauffer; Romero; Kepler, 2018). Post-CHB, stars within this mass range will form core masses greater than the Chandrasekhar mass ( $M_{Ch}$ ). If the core mass does not reduce, the star will experience all stages of core burning (Doherty et al., 2017). This mass is reduced through the second dredge-up and in an event known as dredge-out (see Ritossa, García-Berro & Iben Icko (1999), Siess (2007),

---

<sup>6</sup> This limit refers to the maximum mass that can be supported by relativistic electron degeneracy pressure. See Chandrasekhar (1931), for details.

Poelarends et al. (2008), Doherty et al. (2015), for more details). Above this mass range the fusion can produce even heavier metals up to iron.

Once the helium burning shell is severely depleted of its fuel, the abundance of helium in this layer is sustained by the helium produced from the hydrogen shell burning that lies above. The build up of helium within this thin layer below the hydrogen burning shell eventually ignites an unstable helium burning. This process is known as a helium shell flash, or a thermal pulse (TP), which are very luminous as at these temperatures the energy generation rate is dependent on temperature as<sup>7</sup>,

$$\epsilon_{3\alpha} \propto T^{40}, \quad (1.6)$$

causing rapid, extremely energetic helium shell flashes. The energy produced from TPs causes ejection of material through strong winds and expansion of the stellar envelope which subsequently cool as a result. The expansion halts the hydrogen burning which resumes during the subsequent contraction of the star. Additionally, the TPs induce convection that brings material from the interior to the surface, which is also dependent on the metallicity, and this is referred to as the third dredge-up (TDU). This is a cyclic process that occurs because of instabilities in the helium-burning shell causing the star to expand and contract. This recurrent process stops when the hydrogen envelope becomes thin enough (because of mass-loss) that it cannot form enough helium and subsequent TPs cannot occur. This occurs when the envelope mass is less than  $M_H \leq 10^{-3} M_\odot$ . The number of TPs that the star experiences changes from star to star, although as a general relation, the number of thermal pulses increases with mass and metallicity (Herwig et al., 1997; Karakas; Lattanzio; Pols, 2002; Weiss; Ferguson, 2009; Romero; Campos; Kepler, 2015; De Gerónimo et al., 2017).

Once the star leaves the AGB, depending on the mass and metallicity, one of three different stellar remnants can form. For initial stellar masses up to  $M_i = 10.5 - 11.8 M_\odot$  (Smartt, 2009; Lauffer; Romero; Kepler, 2018), depending on the metallicity, a white dwarf forms. For white dwarfs up to  $1.06 M_\odot$ , the core has a C/O composition (Bertelli; Bressan; Chiosi, 1985; Bressan et al., 1993; Siess, 2007), whilst more massive white dwarfs form a O/Ne/Mg core (García-Berro; Ritossa; Iben ICKO, 1997; Lauffer; Romero; Kepler, 2018). The maximum mass that a white dwarf can have is known as the Chandrasekhar limit, and it has a value of  $M_{Ch} = 1.44 M_\odot$ , for O/Ne/Mg WDs. A Hertzsprung–Russell diagram for a star that will form a white dwarf can be found in Figure 2. Above the initial mass limit  $M_i = 11.8 M_\odot$ , the core will actually reach carbon burning temperatures ( $\sim 10^9$  K), and will synthesise heavier metals until a core of iron has formed. Iron has the highest binding energy per nucleon and so will not fuse with itself naturally, unless a large amount of external energy is applied. Instead, the star will collapse and the outer layers ricochet

<sup>7</sup> Kippenhahn & Weigert (1990), Prialnik (2009).

off of the iron core in a highly energetic event known as a supernova. This occurs for stars that will have final masses larger than the Chandrasekhar limit and so electron degeneracy pressure alone cannot support this collapse. The collapse past the electron degeneracy stage causes protons in the nuclei to absorb the electrons forming a sea of neutrons (inverse beta decay). The neutrons become degenerate and have a stronger degeneracy pressure than that of electrons, allowing the mass limit for neutron stars to be  $2.16 M_{\odot}$  (Özel et al., 2012; Chamel et al., 2013; Rezzolla; Most; Weih, 2018). Above this mass, the neutron star cannot support itself and will collapse to a singularity to become a black hole. Figure 1 gives a simple illustration of the evolution of a single star. The lowest initial masses are found at the bottom of Figure 1 and the initial mass increases vertically.

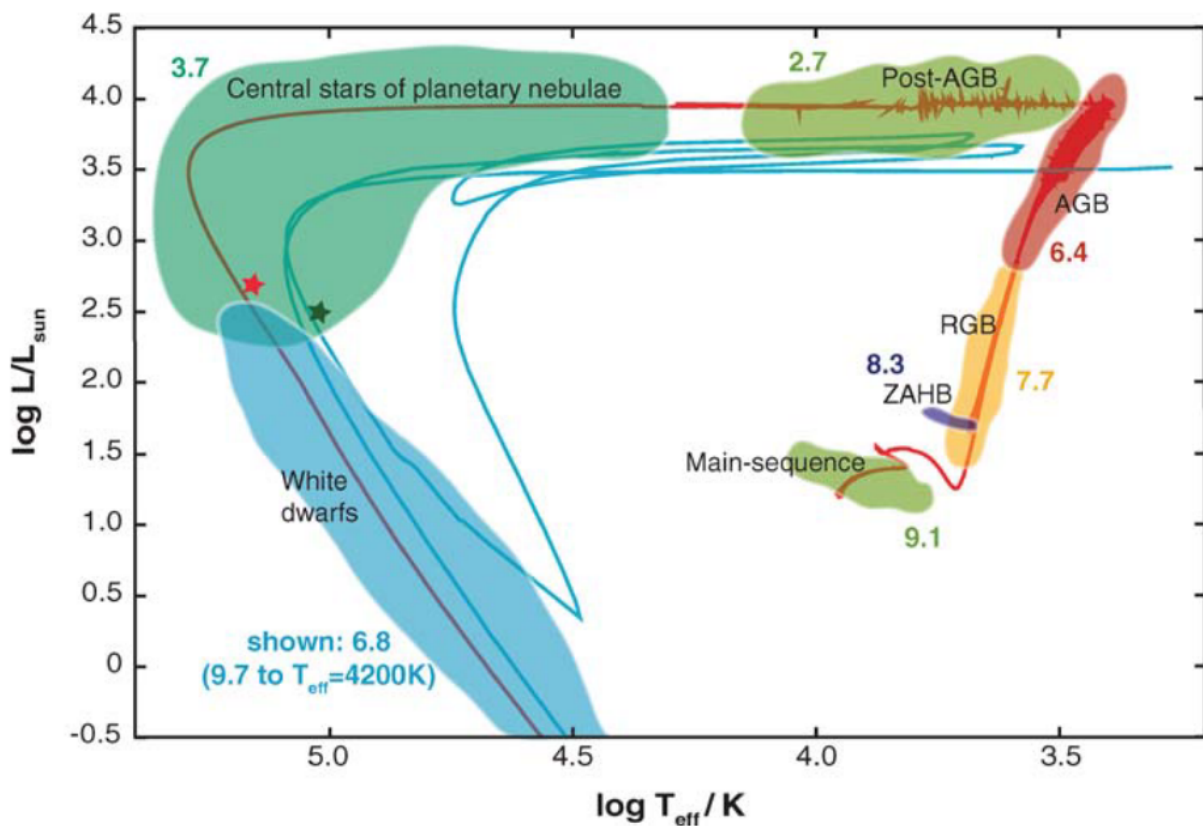


Figure 2 – Hertzsprung–Russell diagram showing the evolutionary path of a star with an initial mass of  $2.00 M_{\odot}$ . The Hertzsprung–Russell shows the evolutionary path by plotting the stellar luminosity against the effective temperature. Each stage is represented clearly by the different colours and labels, which show the log of the approximate duration of each stage. Figure adapted from Herwig (2005).

## 1.2 Stellar Nuclear Reactions

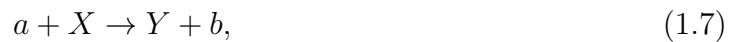
The thermonuclear reactions that occur within stars are what gives them life. Without them, the star would simply collapse to a singularity in less than one million years, according to the Kelvin–Helmholtz timescale (Bradt, 2008) and the Universe would be a cold, dark wasteland. The thermal energy that supports the star against this otherwise



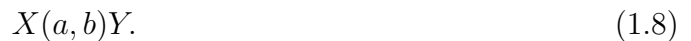
inevitable collapse is produced from the liberation of binding energy in the atomic nuclei. The binding energy is the amount of energy required to break up a nucleus of an atom into its constituent protons and neutrons, which are collectively referred to as nucleons.

### 1.2.1 Kinematics of Reactions

Consider a reaction between a particle,  $a$ , and a nucleus,  $X$ . This reaction will form a nucleus  $Y$  and an outgoing particle  $b$ . This reaction is shown below,



which can also be represented as,



Such a reaction must obey the conservation laws of linear and angular momentum, energy, charge, baryon and lepton numbers. The binding energy per nucleon varies for different nuclei, so as one nucleus forms a new nucleus through thermonuclear reactions, energy is released/absorbed from changes to this quantity. Up to a nucleus of iron, the binding energy per nucleon increases with atomic number, so fusion of nuclei up to iron will release energy equal to the mass difference between the formed nucleus,  $Y$ , the reacted nucleus,  $X$ , and the reactants,  $a$  and  $b$ .

In this scenario the two considered particles travel with velocities of  $v_a$  and  $v_X$ , having masses of  $m_a$  and  $m_X$ , respectively. The two particles coalesce, forming a particle of mass  $m_a + m_X$  and has a centre of mass velocity  $V$ , such that when we consider the conservation of momentum, it is found that,

$$m_a v_a + m_X v_X = (m_a + m_X)V, \quad (1.9)$$

which allows us to find a relation for  $V$ ,

$$V = \frac{m_a v_a + m_X v_X}{m_a + m_X}. \quad (1.10)$$

It is important to note that only the non-relativistic velocities are considered, as is the case within stellar interiors due to low kinetic energies.

We will find in Section 1.2.3, that it is useful to instead show the conservation of momentum in the frame of either particle ( $X$  or  $a$ ) such that it considers itself to be at rest. If we consider such a frame the relative velocity of particle  $X$  as seen by the coalesced

particle is  $v_{rel} = v_X - V$ . Additionally, we can consider the momentum of the coalesced product to be 0 as it considers itself to be at rest. The relative momentum is then,

$$m_X(v_X - V) = \frac{m_a m_X}{m_a + m_X}(v_X - v_a) = \mu v, \quad (1.11)$$

where  $\mu = \frac{m_a m_X}{m_a + m_X}$  and is called the reduced mass, and relative velocity between particles  $a$  and  $X$  is shown below:

$$v = v_X - v_a. \quad (1.12)$$

This returns the non-relativistic interaction energy with the form:

$$E = \frac{1}{2}\mu v^2. \quad (1.13)$$

where  $\mu$  is the reduced mass and  $v$  is the relative velocity, which are both defined above.

## 1.2.2 Reaction Rates

Thermonuclear reactions are not instantaneous events, because certain criteria must be met for a reaction to occur. The quantum tunnelling effect plays an important role in thermonuclear fusion. The number of reactions per unit volume per unit time is known as the reaction rate. To calculate this quantity, the cross-section for a reaction must first be considered. The cross-section is a measure of the probability for a pair of particles to undergo a reaction and has units of area. It is important to note that the cross-section is not simply the physical cross-sectional area of both/either of the reactants, but a product of many factors such as energy and incident particle velocity (Clayton, 1968). The cross-section for a reaction is given as

$$\sigma = \frac{\text{number of reactions/particle X/unit time}}{\text{number of incident particles/unit area/unit time}}. \quad (1.14)$$

Now imagine the case of particles,  $a$ , colliding with particles  $X$ . Although not physically correct, it is helpful to imagine that a reaction occurs every time a particle,  $a$ , strikes a particle,  $X$ , within an area of the cross-section,  $\sigma$ . The consideration of relative velocity further defines the cross-section as the flux of the incident particles per unit area per unit time as function of velocity, and so  $\sigma \rightarrow \sigma(v)$ . We can assume this as relative of one particle, the other particle is stationary. In this picture we have a gas that is of uniform density of nuclei  $X$ , which we refer to as  $N_X$ . The particles,  $a$ , are of uniform density  $N_a$ , and move toward the  $X$  particles at a velocity,  $v$ . The reaction rate between particles  $a$  and  $X$ ,  $r_{aX}$ , is therefore given as:

$$r_{aX} = \sigma(v)vN_aN_X. \quad (1.15)$$

The velocity distribution of the particles is given by a function  $\phi(v)$ , such that  $\int_0^\infty \phi(v)dv = 1$ . With this, we can generalise equation 1.15 to account for collisions of all relative velocities given by  $\phi(v)$  to form equation 1.16,

$$r_{aX} = N_a N_X \int_0^\infty v \sigma(v) \phi(v) dv = N_a N_X \langle \sigma v \rangle, \quad (1.16)$$

where  $N_a$  and  $N_X$  are the number densities of particles a and X respectively, and  $\langle \sigma v \rangle$  is the thermally averaged product of the relative velocity and the cross-section.

We can make a final, small but still significant, correction to equation 1.16. If we consider the case of  $a = X$ , that is to say they are the same particle, we must not make the mistake of double counting the pairs of available particles. In this case, the total number density of the particles is not given as  $N^2$ , but  $\frac{1}{2}N^2$ . To generalise this effect, the Kronecker delta function  $\delta_{aX}$  is used, which takes the value of 1 for identical particles and 0 for non-identical particles. Thus, equation 1.16 becomes

$$r_{aX} = (1 + \delta_{aX})^{-1} N_a N_X \langle \sigma v \rangle. \quad (1.17)$$

### 1.2.3 The Cross-Section

The number densities of reactants are specific to the environment of the star, real, computed or otherwise. The troubles in the evaluations of a reaction rate are the values for  $\langle \sigma v \rangle$  which are evaluated from for cross-sections measured within laboratories. Assuming the star to be in local thermodynamic equilibrium, we can consider the particle velocity distribution,  $\phi(v)$ , to follow a Maxwell-Boltzmann distribution. For a specific particle of species 'a', the number density of particles with velocities within a range of  $d^3v$  is given as,

$$N_a(v_a) d^3v_a = N_a \left( \frac{m_a}{2\pi kT} \right)^{\frac{3}{2}} \exp \left( -\frac{m_a v_a^2}{2kT} \right) dv_{ax} dv_{ay} dv_{az}, \quad (1.18)$$

where  $m_a$  is the mass of species  $a$ ,  $v_a^2 = v_{ax}^2 + v_{ay}^2 + v_{az}^2$  is the total velocity of this particle,  $N_a$  is the total number density of particles,  $k$  is the Boltzmann constant and  $T$  is the temperature. If we consider the relative velocity and the velocity of the centre of mass, rather than the individual velocities of both species, the product of the distributions of both species then becomes

$$N_a(v_a) d^3v_a N_X(v_X) d^3v_X = N_a N_X \frac{(m_a m_X)^{\frac{3}{2}}}{(2\pi kT)^3} \exp \left[ -\frac{m_a V^2}{2kT} - \frac{m_X V^2}{2kT} - \frac{\mu v^2}{2kT} \right] d^3v_a d^3v_X, \quad (1.19)$$

where  $V$  is the centre of mass velocity and  $v$  is the relative velocity. Through a Jacobian manipulation, it can be shown that  $d^3v_a d^3v_X = A d^3V d^3v$ , where  $A$  is a scaling constant, dependent on the particle masses ( $A = \frac{\mu}{1amu}$ ). This can be achieved by considering equations 1.10 and 1.12 to produce an expression that relates the particle masses to the relative velocity, centre of mass velocity and the particle masses. A further in-depth

analysis of the derivation of equation 1.19 and the Jacobian analysis can be found in Clayton (1968). The integration across all of the centre of mass velocities,  $V$ , is normalised and so produces unity. Integrating equation 1.19 with the product of relative velocity and the cross-section over all relative velocities recovers a familiar parameter - the reaction rate:

$$r_{aX} = N_a N_X \int 4\pi v^3 \sigma(v) \left( \frac{\mu}{2\pi kT} \right)^{\frac{3}{2}} \exp\left(-\frac{\mu v^2}{2kT}\right) dv. \quad (1.20)$$

Where the substitution,  $d^3v = 4\pi v^2 dv$ , was used. The distributions are normalised so integrating over  $d^3V$  leads to unity and the reduced mass formula given in equation 1.11. Comparing equation 1.20 to equation 1.17 finds an equation for  $\langle \sigma v \rangle$ , for unlike reactants:

$$\langle \sigma v \rangle = 4\pi \left( \frac{\mu}{2\pi kT} \right)^{\frac{3}{2}} \int_0^\infty v^3 \sigma(v) \exp\left(-\frac{\mu v^2}{2kT}\right) dv. \quad (1.21)$$

#### 1.2.4 The Astrophysical S-Factor

For nuclear fusion to occur, the particles must overcome the mutual repulsion between them due to the Coulomb barrier. This is a well known quantity and has the value:

$$V_C = \frac{1.44 Z_a Z_X}{R(\text{fm})} \text{MeV}, \quad (1.22)$$

where  $V_C$  is the energy of the Coulomb barrier,  $Z$  is the atomic number of each respective particle and  $R$  is the distance in fm ( $10^{-15}$  m) between the centre of mass of each nucleus. In stars, the kinetic energy of the particles is lower than this value and nuclear reactions cannot occur according to classical mechanics. Of course the tail-end of the velocity distribution for the particles extends to very high energies, but there are exponentially very few of them.

Gamow (1928) found that two particles can actually ‘tunnel’ through the Coulomb barrier that prevents them from reacting. The probability for this to occur is proportional to

$$P \propto \exp\left(-\frac{2\pi Z_a Z_X}{\hbar v}\right). \quad (1.23)$$

The cross-section of a particle is proportional to the square of the de Broglie wavelength of the particle, and so is also proportional to the inverse of the particle energy.

$$\sigma \propto \pi \lambda^2 \propto p^{-2} \propto E^{-1}, \quad (1.24)$$

where  $\sigma$  is the cross-section,  $\lambda$  is the de Broglie wavelength,  $p$  is the particle momentum and  $E$  is the particle energy. With this relation, the cross-section can be redefined in terms of energy instead of velocity to introduce a new parameter,  $S(E)$ , which is the

astrophysical S-Factor<sup>8</sup>:

$$S(E) = \sigma(E)E \exp\left(-\frac{2\pi Z_a Z_X e^2}{\hbar v}\right). \quad (1.25)$$

Essentially, the  $S(E)$  gives a re-scaled cross-section that accounts for Coulomb interactions between the reactant particles. For high incident particle energies, the S-Factor varies rapidly, whilst for low temperatures such as those within stellar interiors, it is almost constant varying only slightly with increasing energy. Utilising equation 1.25 in equation 1.21, in addition to changing the integration variable from relative velocity,  $v$ , to the energy of the interaction,  $E$ , we find that the thermally averaged product of the cross-section and the relative velocity is<sup>8</sup>:

$$\langle \sigma v \rangle = \int_0^\infty S(E)E^{-1} \exp\left(-\frac{2\pi Z_a Z_X e^2}{\hbar v}\right) v(E)\psi(E)dE \quad (1.26)$$

where  $E$  is the energy,  $v(E)$  is the relative velocity in terms of the interaction energy and  $\psi(E)$  is the distribution of particle energies. Note that  $\psi(E)$  is already known, a comparison between equations 1.16 and 1.20 retrieves a relation for the normalised distribution for  $\phi(v)$ .  $\psi(E)$  from  $\phi(v)$  are obtained from changing the density of states

$$\psi(E)dE = \phi(v)\frac{dv}{dE}dE. \quad (1.27)$$

such that  $\psi(E)dE$  has the following form:

$$\psi(E)dE = -\frac{2}{\sqrt{\pi}} \frac{E}{kT} \exp\left(-\frac{E}{kT}\right) \frac{dE}{\sqrt{kTE}}. \quad (1.28)$$

The values of cross-sections are measured in laboratories, through scattering or absorption experiments. It is impossible to recreate these experiments in laboratories at the very low energies associated with stellar temperatures (typical values are between the magnitudes of  $10^7 \leq T/\text{K} \leq 5 \cdot 10^8$ , which has the resulting energy range  $12 \leq E/\text{keV} \leq 60$ ). Thus, extrapolation down to these temperatures cannot be avoided. This is depicted in Figure 3, which shows the observed cross-sections for higher energies and the extrapolation to lower energies for the reaction  $^{12}\text{C}(p, \gamma)^{13}\text{N}$ . Once this extrapolated function has been reproduced, equation 1.26 can be evaluated to produce an estimate value for  $\langle \sigma v \rangle$ .

Now an equation for the average product of the cross-section and particle velocity as a function of energy has been derived. The last step in finding this value is to understand how  $S(E)$  varies with this energy. This is not always trivial as there are key characteristics that must be considered. This is explored in the Sections 1.2.5 and 1.2.6 that follow.

<sup>8</sup> Expression adapted from Clayton (1968)

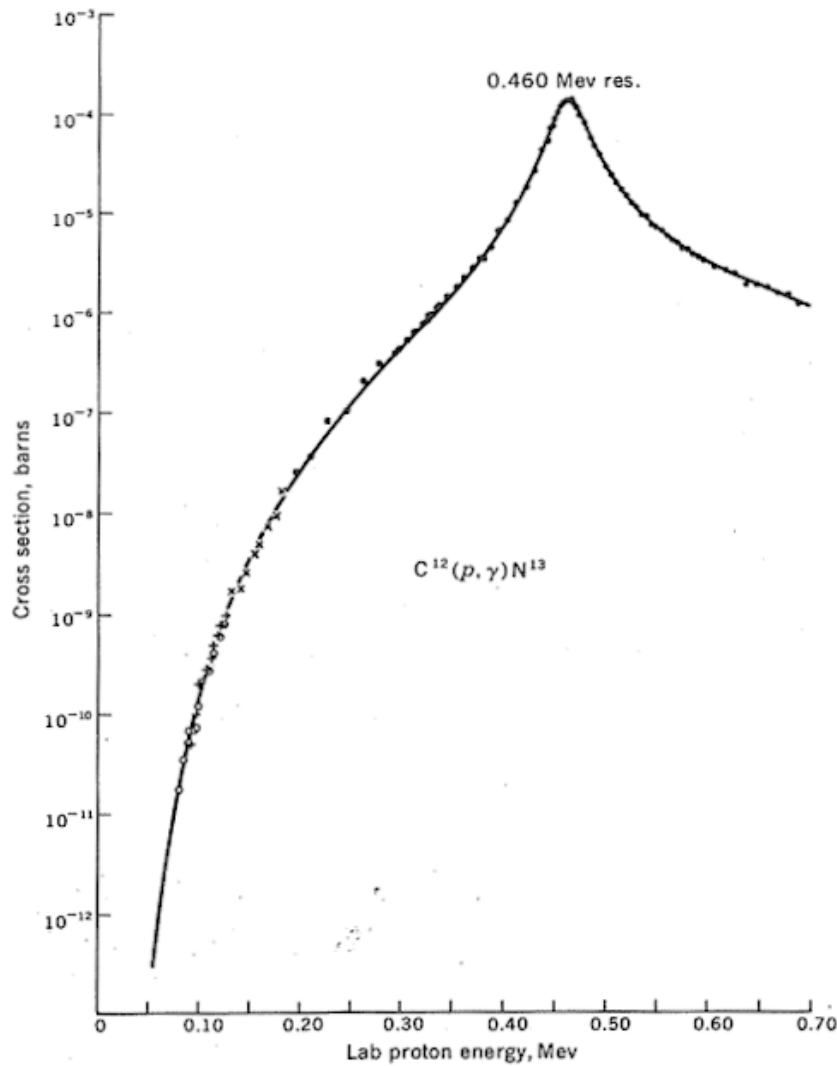


Figure 3 – Measured cross-sections for the  $^{12}\text{C}(p, \gamma)^{13}\text{N}$  reaction as a function of incident proton energy. The minimum energy for a measurement is larger than the range of possible stellar energies. An extrapolation of the curve is made for these energies. The peak near  $E = 0.46 \text{ MeV}$  is due to a resonance and will be expanded upon in Section 1.2.6. Credit to [Fowler, Caughlan & Zimmerman \(1967\)](#).

### 1.2.5 Non-Resonant Reactions

The extrapolation of the actual cross-section has a lower precision than an extrapolation of  $S(E)$ . It is uncertain how the cross-section will behave at different energies which cannot be directly measured.  $S(E)$  behaves as an exponential function which allows a semi-theoretical fit that yields a larger accuracy than an extrapolation of  $\sigma(E)$ . Figure 4 shows the extrapolation of the S-factor rather than the cross-section for the same case found in Figure 3, for an example of these extrapolations.

For non-resonant reactions the function  $S(E)$  does not vary significantly over the energy range of stellar interiors ([Clayton, 1968](#); [Thompson; Nunes, 2009](#)). Or at least, it varies linearly with energy with a small gradient. This is important as at low energies,

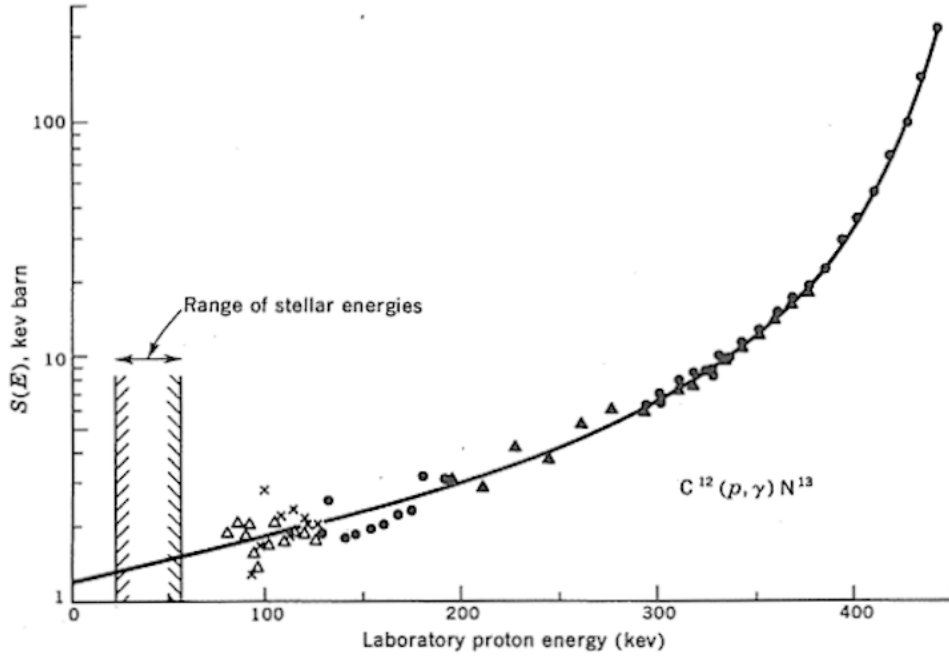


Figure 4 – Plot depicting the extrapolation of the S-Factor as a function of incident proton energy for the  $^{12}\text{C}(p, \gamma)^{13}\text{N}$  reaction. The extrapolation is from higher energies down to the region of stellar energies. Credit to [Hebbard & Vogl \(1960\)](#).

the cross-section decreases rapidly with decreasing energy. This is due to the exponential factor as found in equation 1.25, such that the low energies reduce the probability of a particle tunnelling through the Coulomb barrier as found earlier.

The evaluation for  $\langle\sigma v\rangle$  for the non-resonant reaction case is relatively straightforward as  $S(E)$  can be considered to be constant. Still considering the case to be non-relativistic, we consider the energy of interaction to be that which is defined in equation 1.13. Using this relation for energy and considering equation 1.26 whilst following the derivation of [Clayton \(1968\)](#), equation 1.29 is found,

$$\langle\sigma v\rangle = \left(\frac{8}{\mu\pi}\right) \frac{S_0}{(kT)^{\frac{3}{2}}} \int_0^\infty \exp\left(-\frac{E}{kT} - \frac{2\pi Z_a Z_X e^2 A^{\frac{1}{2}}}{\sqrt{E}}\right) dE, \quad (1.29)$$

where  $S_0$  is the constant value for  $S(E)$  at low energies,  $A = \frac{\mu}{1\text{amu}}$ , where amu is an atomic mass unit. The quantity  $S_0$  is also the value of  $S(E)$  where the particles have the highest chance of penetrating the Coulomb barrier. This can be calculated by considering the maximum value of  $-\frac{E}{kT} - \frac{2\pi Z_a Z_X e^2 A^{\frac{1}{2}}}{\sqrt{E}}$ . This point is found by calculating where its gradient is equal to zero. The energies from these two components are depicted in Figure 3. The most likely energy is the maximum value, this quantity is called  $E_0$ , hence  $S_0 = S(E_0)$ .  $E_0$  is given as

$$E_0 = \left(2\pi Z_a Z_X e^2 A^{\frac{1}{2}} kT\right)^{\frac{2}{3}}.$$

The energy ranges related to stellar interiors are much lower than  $E_0$ . It can therefore be assumed that  $S(E)$  is constant.

Introducing the quantity  $b$ , where  $b = 2\pi Z_a Z_X e^2 A^{\frac{1}{2}}$  as well as  $C$ , such that  $C = \exp\left(-\frac{E_0}{kT} - \frac{b}{\sqrt{E_0}}\right)$ , equation 1.29 becomes

$$\langle \sigma v \rangle = \left(\frac{8}{\mu\pi}\right) \frac{C}{(kT)^{\frac{3}{2}}} \int_0^\infty S(E) \exp\left[\frac{\sqrt{3}(E - E_0)}{2E_0 kT}\right] dE, \quad (1.30)$$

where the variables are the same as in equation 1.29. This can be completed by considering the function  $S(E)$  to be constant as before, or a Taylor series expansion can be made for improved accuracy. For most non-resonant cases, this can be negligible. Clayton (1968) goes through this correction factor in detail and determines that a correction to the first order is linear with temperature and higher orders can be neglected.

### 1.2.6 Resonant Reactions

It is not always the case that  $S(E)$  remains constant through all stellar energies. In fact, sometimes the cross-sections can be many orders of magnitude higher at stellar energies than one would expect from a simple extrapolation from higher energies. This is the cause of resonant reactions. Reactions which the particle transitions between energy levels within the nucleus are more likely due to certain resonant energies that causes particles in a particular state to oscillate. To understand the cause of these resonances, the structure of the nucleus must first be understood.

Consider Figure 5 which depicts a simple model of nuclear structure. The energy-levels in this figure are approximated by

$$E_{n,l} = -V_0 + \frac{\hbar^2}{2MR} \left[ \pi^2 \left( n + \frac{l}{2} \right)^2 - l(l+1) \right] \quad (1.31)$$

where  $n$  is the quantum number,  $l$  is the quantum angular momentum number,  $M$  is the mass of a nucleon and  $R$  is the radius of the nucleon. Further consideration to the spin component of the nucleons,  $s = \pm\frac{1}{2}$ , is also required. This provides the further splitting as seen in Figure 6, which illustrates the splitting of energy levels due to the intrinsic spins of nucleons. These energy levels are characterised by the eigenvalues  $j$ , where  $j = l \pm \frac{1}{2}$ . The final form for each energy is then  $nB(l)_j$ . Where  $n$  represents the quantum number,  $j$  is the half-integer as defined above and  $B(l)$  is a representation of the quantum angular momentum number through an assigned lower case character (for example,  $l = 0, 1, 2, 3$  is represented as  $B(l) = s, p, d, f$ ) (Clayton, 1968; Thompson; Nunes, 2009).

Resonances occur if the kinetic energy of the particles at infinity is equal to the energy of a quasistationary state of the nucleus. Otherwise, the reaction is non-resonant. As hinted earlier, the reaction between  $a$  and  $X$  first forms a coalesced particle before forming the final products. The coalesced/compound particle is hereafter referred to as  $W$ , such that the nuclear reaction process is now



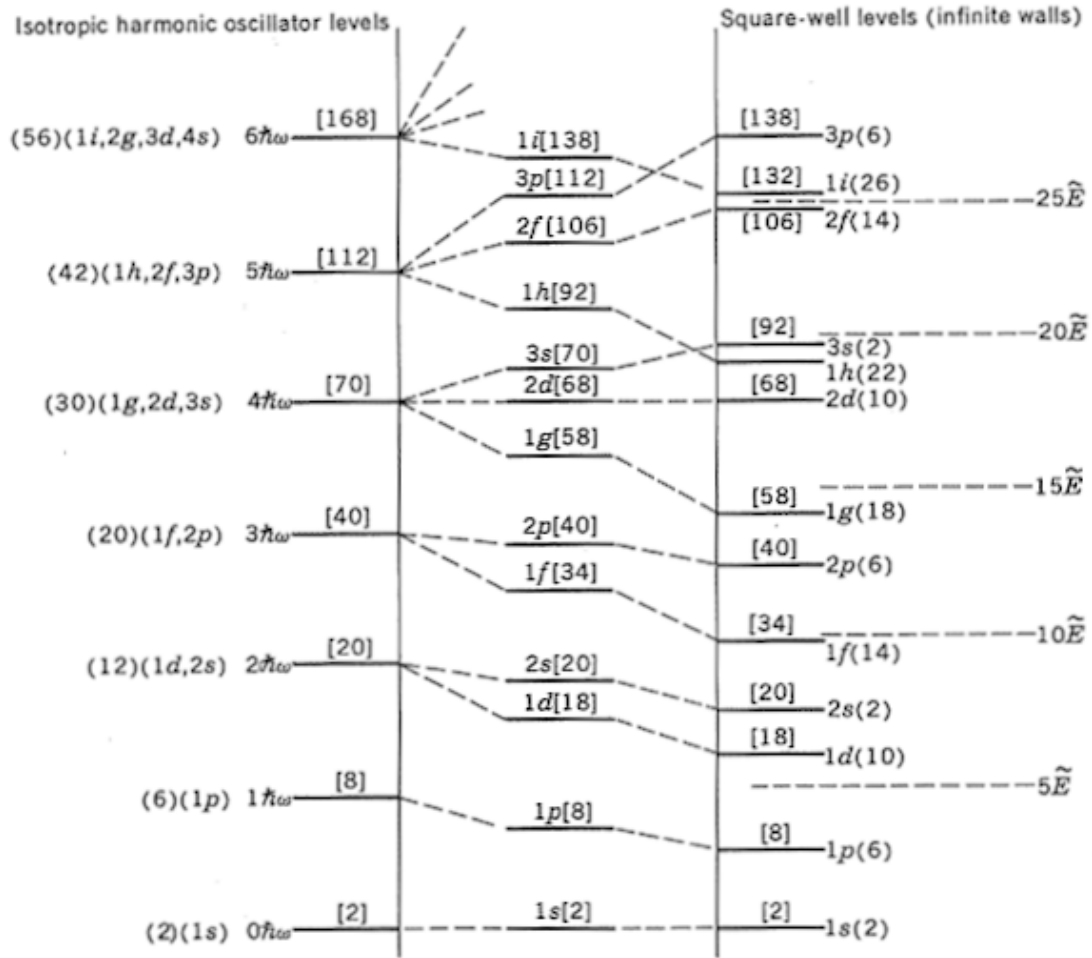


Figure 5 – Diagram illustrating the basic energy levels with energies calculated by equation 1.31. This is a general case which does not consider a particular element. Credit to [Preston & Whaling \(1963\)](#)



Additionally, for a resonant reaction to occur, the parity quantity must also be conserved. Such that

$$\pi(W) = \pi(a)\pi(X)(-1)^l \quad (1.32)$$

where  $\pi$  represents the parity of the particle and  $l$  is the relative angular momentum between  $a$  and  $X$ . The result of this is that not all energy-levels coincide with being able to resonate.

The affect of such resonance as discussed at the start of this subsection is that the cross-section at these resonant interaction energies is much larger than one would expect. But it not only has an affect at this energy, but at lower energies as well. In Figure 7, which shows the cross-sections of resonant nuclear interactions, we can see that as we move away from a resonant interaction energy the cross-section reduces exponentially ([Preston;](#)

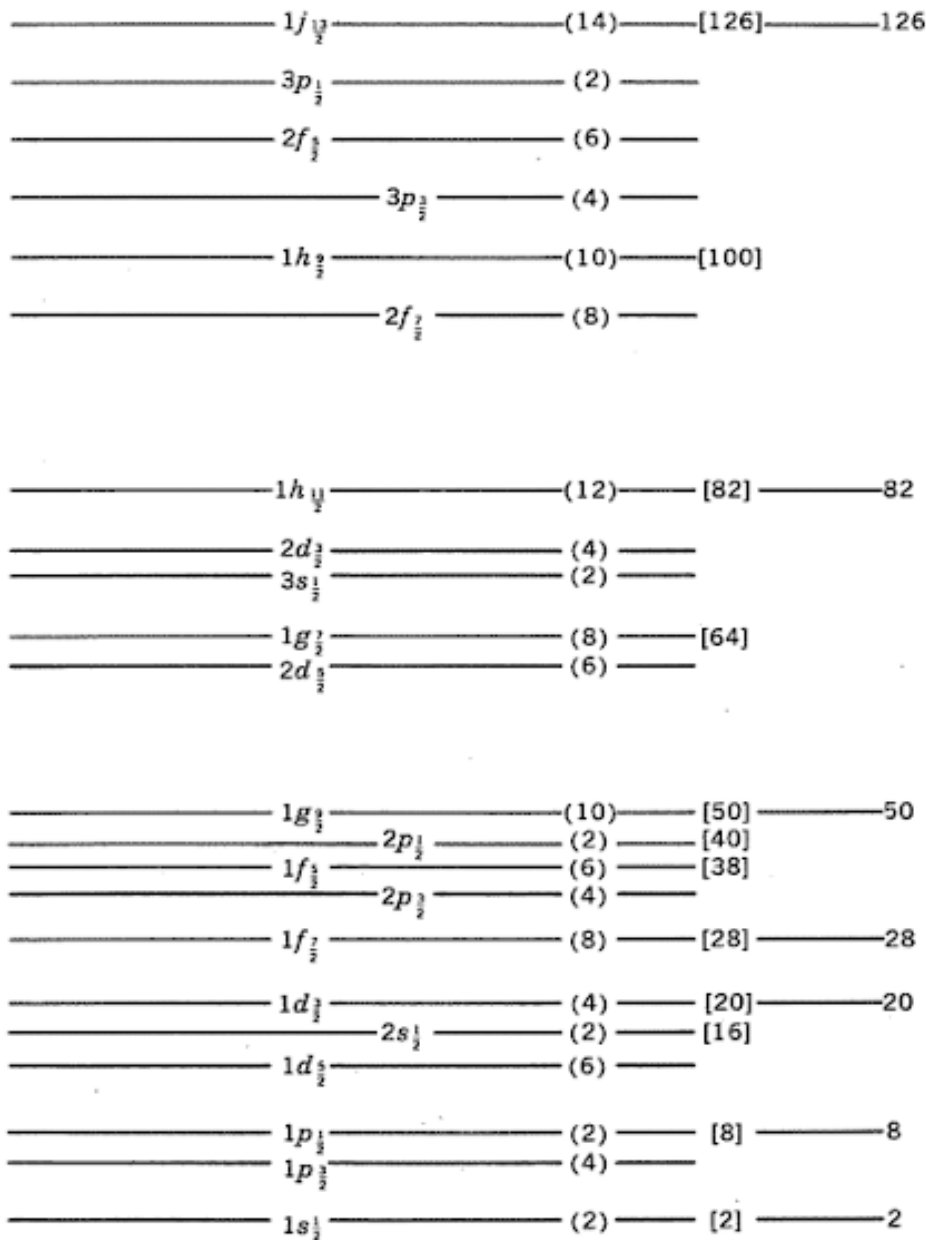


Figure 6 – Diagram illustrating the energy level splitting due to the intrinsic spins of the nucleons. Credit to [Preston & Whaling \(1963\)](#)

[Whaling, 1963; Clayton, 1968](#)). As such, the resonant cross-section will have an affect at lower energies and must be considered when evaluating the overall cross-section.

However, in fact, the energy of interaction and the energy of the state between the incident particle and the compound particle,  $W$ , does not need to be equal for resonance to occur. Nuclear energy levels have a natural width that is related to the lifetime of the energy level,  $\tau$ , by the Heisenburg uncertainty principle ([Heisenberg, 1927](#)). It is found that the energy-levels have energy widths at which resonant reactions can occur as

$$\Gamma = \frac{\hbar}{\tau} \quad (1.33)$$

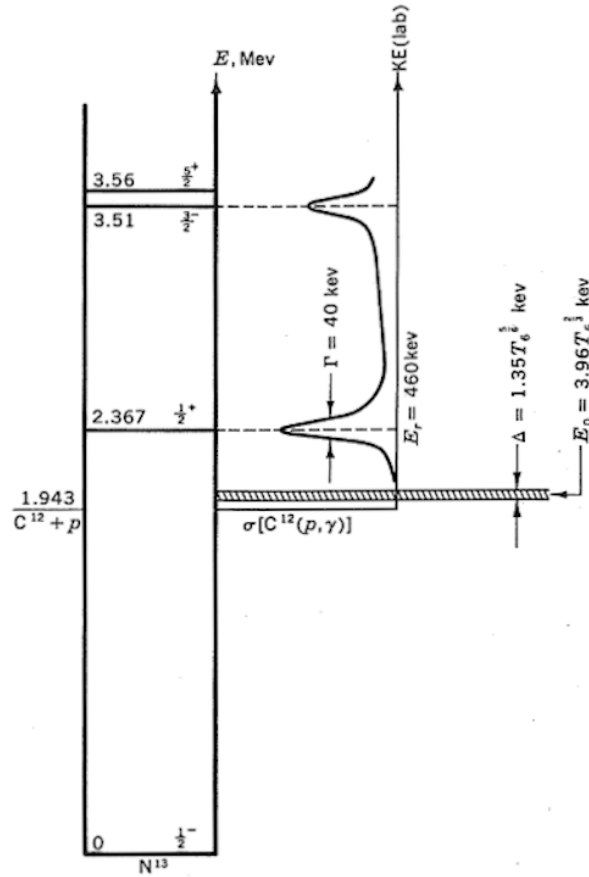


Figure 7 – Diagram illustrating effects on the cross-sections at different resonant energies for the  $^{12}\text{C}(p, \gamma)^{13}\text{N}$  reaction. Energy increases vertically upwards and the cross-section increases horizontally to the left. The hatched band shows the region of stellar energies. One can see that  $E = 0.46 \text{ MeV}$ , there lies an energy level where parity is conserved increasing the cross-section for the interaction. It is also apparent that there are other nearby energy levels, one of which is resonant and the other is not due to parity not being conserved. Credit to [Preston & Whaling \(1963\)](#)

where  $\Gamma$  is the energy width and  $\tau$  is the timescale a particle can occupy the energy level before decaying to a lower state. It is important to note that  $\Gamma$  is a summation of all possible decay mechanisms. The existence of the lifetimes and widths of different energy states allows us to produce a probability of finding a particle within a resonant energy state,  $E_r$ , for an arbitrary energy,  $E$ .

$$P(E) = \frac{\hbar/2\pi\tau}{(E - E_r)^2 + (\hbar/2\tau)^2} \quad (1.34)$$

where  $E$  is the system energy,  $E_r$  is the energy of the resonant state and  $\tau$  is the lifetime of the state. Now a distinction has been made of how resonant reactions are different to the non-resonant case, it is now possible to quantify how the cross-section evaluations are affected by this phenomena.

Considering a semi-classical scenario, it is possible to explain how the cross-section for a reaction occurs through resonance. If the reader is interested, a full quantum analysis is shown in Clayton (1968). Consider that the energy levels for each value of  $l$ , are equally spaced by the de Broglie wavelength,  $\bar{\lambda}$ , in concentric circles. Thus, the  $l$ th zone would have an angular momentum of  $l\hbar$ , which corresponds to an impact parameter of  $l\bar{\lambda}$ . It is then true that the next energy level has an impact parameter of  $(l + 1)\bar{\lambda}$ . The maximum resonant cross-section,  $\sigma_r$ , is then the difference between the 2 zones as it gives the area of the “actively” interacting zone,

$$\sigma_{r,l}(\text{max}) = \pi[(l + 1)\bar{\lambda}]^2 - \pi[l\bar{\lambda}]^2,$$

where  $\bar{\lambda}$  is the de Broglie wavelength. This maximum resonant cross-section can only occur if the energy of the reactants and the products occur at the exact energy of the resonant state,  $E_r$ , of the compound nucleus (Clayton, 1968).

The rate of forming such a state within the compound nucleus for particles of energy,  $E$ , is proportional to the probability of the state having an energy,  $E$  (equation 1.34). In addition, the cross-section must be proportional to the energy width,  $\Gamma_a$ , if the reaction is to be initiated by the particle,  $a$ . Finally, it must also be proportional to the energy width of the exit channel which, for an incident particle  $a$ , is  $\Gamma - \Gamma_a$ , otherwise there is a probability of the exit channel decaying into particle  $a$ , as if no reaction had occurred. It is clear from equation 1.34 that the largest probability occurs for  $E = E_r$ .

Furthermore, it is found that if the probability function (equation 1.34) is used, the cross-section is proportional to the energy width of the energy state. Such as

$$\sigma_r \propto \frac{\Gamma_a(\Gamma - \Gamma_a)}{(E - E_r) + \frac{\Gamma}{2}},$$

where  $\Gamma_a$  is the energy width for the state for a reaction with a particle  $a$ ,  $E$  is the energy of the state and  $E_r$  is the resonant energy. With some analysis, one can determine that the maximum value of this relation is unity. And so this unity yields the maximum value for  $\sigma_r$ . Additionally, the factor of  $\Gamma - \Gamma_a$  is the sum of all the partial energy widths for the breakup of the compound state formed from the excitation of the  $a$  particle. The required exit channel must release a particle  $b$ , and so the change,  $(\Gamma - \Gamma_a) \rightarrow \Gamma_b$ , is adopted instead. Since this maximum value is unity, it can be multiplied by the maximum cross-section for the  $l$ th partial wave to produce a general expression which is given in equation 1.35, below:

$$\sigma_{r,l}(a, b) = (2l + 1)\pi\bar{\lambda}^2 \frac{\Gamma_a\Gamma_b}{(E - E_r)^2 + \left(\frac{\Gamma}{2}\right)^2}. \quad (1.35)$$

As the approach to this derivation has been in a semi-classical description, the quantum effects of particle spin have been neglected. To make up for this approximation, the total angular momentum,  $J$ , must be considered to correctly account the number of

nucleons in each state that has been split by rotation. In this case, the factor  $(2l + 1)$ , can be modified to reflect the cross-section in each sub-state. It is found that to correctly account for this, the following change must be made

$$(2l + 1) \rightarrow \frac{(2J + 1)}{(2J_a + 1)(2J_X + 1)} = \omega, \quad (1.36)$$

where  $l$  is the relative angular momentum,  $J$  is the total angular momentum such that  $J = J_a + J_X + L$ ,  $J_a$  is the eigenvalue for the total angular momentum of particle  $a$  and  $J_X$  is the same as  $J_a$  for particle  $X$ . Substituting equation 1.36 into equation 1.35, we retrieve the full Breit-Wigner single-level formula,

$$\sigma_{r,l} = \pi \bar{\lambda}^2 \omega \frac{\Gamma_a \Gamma_b}{(E - E_r)^2 + \left(\frac{\Gamma}{2}\right)^2}. \quad (1.37)$$

The evaluation for the values of  $\langle \sigma v \rangle$  is now relatively trivial. An example can be followed in Clayton (1968). A substitution of equation 1.37 can be made into the function  $S(E)$  found in equation 1.25. From there it is possible to follow the same steps in resolving the integral, substituting our new S-factor into equation 1.26. Finding

$$\langle \sigma v \rangle = \left( \frac{2\pi \hbar^2}{\mu kT} \right) \sum_r \left( \frac{\omega \Gamma_a \Gamma_b}{\hbar \Gamma} \right)_r \exp\left(-\frac{E_r}{kT}\right). \quad (1.38)$$

The result for these enhanced cross-sections increase the S-Factor, even at energies far from  $E_0$ , remembering that this is the energy at which reactions are most likely to occur. Extrapolation from resonant energies can be made using the Breit-Wigner formula derived in equation 1.37. The wing of the resonance at which  $E_0$  lies increases the value of  $S(E)$ , making the reaction more likely to occur. This effect is illustrated in Figure 8. The closer the resonant energies are to  $E_0$ , the more likely the reaction will take place. One final point to note is that if the resonant energies lie close to or within stellar energies, it can occur that the product of the resonant cross-section and the Maxwell-Boltzmann probability at  $E_r$  is larger than the cross-section and the same probability integrated over  $E_0$ . If this occurs, the reaction will take place through the resonant energy channel instead of  $E_0$ . This is because the cross-sections for resonant reactions at resonant energies are much larger than if only the non-resonant case is considered.

### 1.3 History of Stellar Reaction Rates

Single stellar evolution is fuelled by nuclear reactions that occur within the interior of stars Bethe (1939), Hoyle (1946), Hoyle (1954), Burbidge et al. (1957). The study of these reactions is where nuclear physics and astronomy come together; a developed understanding of what happens at the fundamental level provides a better knowledge of how stars evolve

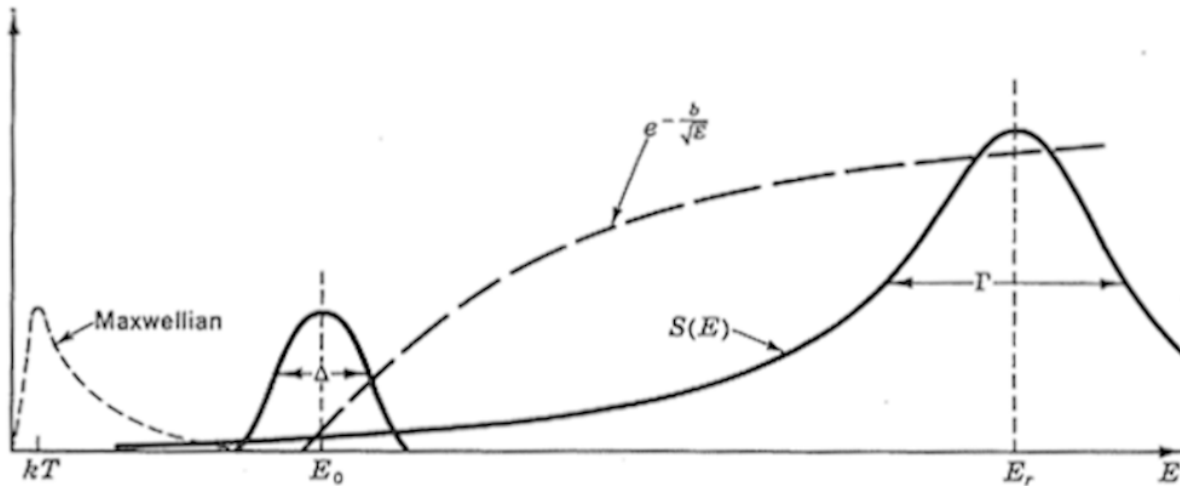


Figure 8 – S-Factor values as a function of energy. An example of the superposition of  $S(E)$  is shown from the non-resonant cases and an arbitrary resonance at higher energies. Credit to Clayton (1968).

and influence their environment. The first work dedicated to calculations of a stellar reaction rate for different reactions was that from Bethe (1939), which calculated the reaction rates for the p-p chain and the CNO cycle. Bethe (1939) assumed a temperature of  $T = 2 \cdot 10^7 K$  and used the formula provided by Gamow & Teller (1938) with cross-sections from Ladenburg & Kanner (1937), Doolittle (1936), Williams, Haxby & Shepherd (1937), Williams, Shepherd & Haxby (1937), Williams et al. (1937). However, as shown in Section 1.2.2, the reaction rate is a function of energy and most reactions at stellar energies cannot be reproduced on Earth due to the potential barrier of Coulomb repulsion being much larger than the kinetic energy of particles at stellar temperatures, classically inhibiting the fusion of two nuclei (Salpeter, 1952b; Clayton, 1968; Caughlan; Fowler, 1988; Angulo et al., 1999). Such an evaluation of a reaction rate was produced in the work of Salpeter (1952b), who estimated the reaction rate for the complete p-p chain, improving the understanding of stellar evolution and the accuracy of stellar evolution codes (Caughlan; Fowler, 1988; Angulo et al., 1999; Xu et al., 2013).

Since then, many works dedicated to the calculation of reaction rate cross-sections have emerged. Early works such as Fowler, Caughlan & Zimmerman (1967) created a bank of reaction rates for a series of different reactions. As higher energies and different methods of determination were available, a better understanding of nuclear structure was managed. This allows a better understanding of how nuclei and particles interact at different energies allowing a reduction in the uncertainty of the cross-sections. Highly cited works which built upon Fowler, Caughlan & Zimmerman (1967) are Caughlan & Fowler (1988), Angulo et al. (1999), Xu et al. (2013). Lately, works dedicated to a single reaction have been produced. This allows a deeper understanding of the nuclear structure of the compound nucleus and the experiment can be customised for the intricacies of each reaction, rather performing a general process over a lot of reactions (Heil et al., 2008; Kunz et al., 2002;

An et al., 2016).

Several other methods of reaction rate evaluations are currently being studied. By comparing the pulsation properties of certain variable stars and models which behave with similar modes, by changing the internal structure using reaction rates as independent variables, allows for a constraint on the considered reaction rate. This method removes the need for the uncertain extrapolation to stellar-like energies. However, matching chemical profiles is not uniquely dependent on the desired reaction rate but a summation of the effects from other reactions, convection and other mixing modes.

Another method to determine the energy states with the compound nucleus is by considering the photo-disintegration of the reverse reaction (Gai et al., 2010; Aliotta et al., 2021). This information is added to the R-Matrix when determining the reaction rate. This method is not as dependent on the energy used as in the actual rate determination, thus can occur within laboratories (Aliotta et al., 2021; Gai, 2012).

Some individual reactions are found to be more important than others as the products they form can influence the subsequent evolution. Such a reaction is that of the  $^{12}\text{C}(\alpha, \gamma)^{16}\text{O}$  reaction (Caughlan; Fowler, 1988; D’Antona; Mazzitelli, 1990; Angulo et al., 1999; Kunz et al., 2002; Xu et al., 2013; deBoer et al., 2017). The following subsection is dedicated to describing the structure of this reaction and the energy levels found in the compound nucleus, a history of it’s evaluation by different authors and it’s importance in stellar evolution.

### 1.3.1 $^{12}\text{C}(\alpha, \gamma)^{16}\text{O}$

The  $^{12}\text{C}(\alpha, \gamma)^{16}\text{O}$  reaction is of great importance in theoretical stellar evolution computations for low and intermediate mass stars, since it is vital to model their carbon-oxygen (C/O) abundance profiles (Woosley; Weaver, 1995; Weaver; Woosley, 1993; Rauscher; Thielemann, 2001; Wallerstein et al., 1997). As discussed above, after a star leaves the RGB it ascends to the horizontal branch where it begins central helium burning. The carbon formed from the triple- $\alpha$  process can combine with another  $\alpha$  particle to form  $^{16}\text{O}$  through the  $^{12}\text{C}(\alpha, \gamma)^{16}\text{O}$  reaction (deBoer et al., 2017).

Differences in the C/O abundance affects the evolution of higher mass stars as the core abundance of O/Ne/Mg in white dwarfs may differ as a result. Uncertainties in the rate of the  $^{12}\text{C}(\alpha, \gamma)^{16}\text{O}$  reaction will directly modify how much carbon is converted to oxygen, leading to central compositions that are different. Additionally, the C/O profile affects the evolution along the white dwarf cooling branch as a result of differences in the thermal energy content of the stars and the details of the core crystallization process (D’Antona; Mazzitelli, 1989a; D’Antona; Mazzitelli, 1989b; D’Antona; Mazzitelli, 1990; Mazzitelli; Dantona, 1986).

The  $^{12}\text{C}(\alpha, \gamma)^{16}\text{O}$  reaction rate is one of the most uncertain (Kunz et al., 2002; deBoer et al., 2017). Furthermore, there is an urgent need for a more precise  $^{12}\text{C}(\alpha, \gamma)^{16}\text{O}$  reaction rate, as claimed by Kunz et al. (2002), Tur, Heger & Austin (2010). Some works further claim that the uncertainty must be less than 10% to be on par with non-nuclear physical uncertainties (see Woosley et al. (2003), deBoer et al. (2017), for details). Currently, the uncertainty is  $\sim 20\%$  from the adopted rate at helium burning temperatures where this reaction is specially important, although earlier works find uncertainties up to 40% (Angulo et al., 1999; Kunz et al., 2002; Xu et al., 2013; An et al., 2016). The combination of this large uncertainty and of its importance in the literature has caused much controversy.

A large part of the uncertainty in the evaluation of the  $^{12}\text{C}(\alpha, \gamma)^{16}\text{O}$  reaction rate lies within the energy states around the principle entrance channel where the reaction occurs. That is, the most likely energy in which the reaction occurs (Clayton, 1968; Thompson; Nunes, 2009). The principle entrance channel for the  $^{12}\text{C} + \alpha$  mechanism ( $E_{\alpha_0} = 7.16$  MeV) does not have a resonance channel close to this threshold, the closest occurring at  $E_x = 9.59$  MeV. Instead, the low energy cross-section is largely influenced by the  $1^{-1}$  ( $E_x = 7.12$  MeV) and  $2^{+}$  ( $E_x = 6.92$  MeV) subthreshold states (see Figure 9, for details). The primary influence of these two nearby subthreshold states and the addition of possible resonant transitions in the wings of the broad channel at  $E_x = 9.59$  MeV makes the nuclear cross-section extremely difficult to estimate (Fowler; Caughlan; Zimmerman, 1967; Caughlan; Fowler, 1988; Kunz et al., 2002; An et al., 2016; deBoer et al., 2017; Deboer; Brune; Wiescher, 2019; Aliotta et al., 2021).

Fowler, Caughlan & Zimmerman (1967) organised the first symposium of reaction rate cross-sections that included the  $^{12}\text{C}(\alpha, \gamma)^{16}\text{O}$  reaction. At the time, many resonant factors were neglected due to the complex nature of the  $^{16}\text{O}$  nucleus. See Figure 9 for a detailed diagram that shows the energy levels within the excited  $^{16}\text{O}$  nucleus and the most common energies at which different reactions occur. This work was updated by Caughlan & Fowler (1988) in an attempt to rectify the neglected resonant factors, but it is believed that some resonances were still neglected and the treatment of the S-factor in this work produced values that are too small and require a scale factor of  $\sim 2$  to produce a realistic S-Factor (Angulo et al., 1999; Kunz et al., 2002; Heil et al., 2008; An et al., 2016; Deboer; Brune; Wiescher, 2019).

Built upon the works of Fowler, Caughlan & Zimmerman (1967), Caughlan & Fowler (1988) and those associated works in between, Angulo et al. (1999) provided a strong basis for the  $^{12}\text{C}(\alpha, \gamma)^{16}\text{O}$  reaction rate with the NACRE (Nuclear Astrophysics Compilation of REactions) survey. Xu et al. (2013) later updated this survey with the publication of NACREII. Currently, the reaction rate for the  $^{12}\text{C}(\alpha, \gamma)^{16}\text{O}$  reaction is often taken from NACRE or from Kunz et al. (2002) (De Gerónimo et al., 2015; De Gerónimo



et al., 2017). More recently, An et al. (2016) produced a work which aimed to evaluate the reaction rate for  $^{12}\text{C}(\alpha, \gamma)^{16}\text{O}$ , only. The mentioned works previous to Kunz et al. (2002) employed an analytical analysis, known as an R-matrix, for S-factor calculations rather than a Breit-Wigner fit (see equation 1.37, for details). An analytical approach is important for applications where the temperatures cause reactions to occur at energies close to resonant energies. The  $^{16}\text{O}$  nucleus is very complex and at energies associated with stellar temperatures the effects of many different resonances are apparent, see Figure 9 (Fowler; Caughlan; Zimmerman, 1967; Caughlan; Fowler, 1988; Angulo et al., 1999; Kunz et al., 2002; Xu et al., 2013; An et al., 2016).

For S-factor evaluations, Angulo et al. (1999) sum the values for the non-resonant energies. For narrow resonances, however, they fit the resulting cross-section using a Breit-Wigner model. When the effects of different resonant energies overlap, they use a multi-resonance fit, shown in equation 29 of Angulo et al. (1999). The analysis of cross-sections in the work of Angulo et al. (1999) is numerical. However, they do provide an analytical approach for each reaction for completeness, although they make it clear that they find their numerical results to be more realistic and that the analytical values are to be used for comparisons to determinations which use a similar analytical approach. NACRE find that their numerical approach yields a higher accuracy for their evaluated reaction rate. The quoted S-Factor value from NACRE for a stellar energy of 300 keV is  $S(300 \text{ keV}) = 199 \pm 64 \text{ keV b}$  (where b is the barn, a unit of cross-sectional area,  $1 \text{ b} = 10^{-24} \text{ cm}^2$ ), resulting in a reaction rate ( $RR$ ) of  $RR(300 \text{ keV}) = (9.11^{+3.69}_{-3.67}) \cdot 10^{-15} \text{ cm}^3 \text{ mole}^{-1} \text{ s}^{-1}$ .  $E = 300 \text{ keV}$  is often chosen as the energy at which to compare the S-factors across different works as it is associated with the ignition of core helium burning.

Kunz et al. (2002) provides an evaluation of the reaction rate for the  $^{12}\text{C}(\alpha, \gamma)^{16}\text{O}$  reaction. They use an R-matrix analysis which can simultaneously determine cross-sections of narrow resonances and the interference effects from overlapping resonances. Kunz et al. (2002) also developed a further analysis of cascading transitions where photons are released. However, Kunz et al. (2002) also point out that the resonance parameters that they used from Tilley, Weller & Cheves (1993) are missing  $\alpha$ -capture measurement for the higher energy range,  $E_{cm} > 2.8 \text{ MeV}$ , and that the fitting procedures they used to cover this region are somewhat speculative. Differences between Angulo et al. (1999) and Kunz et al. (2002) arise due to differences in the handling of S-factor calculations and the addition of interference at larger energies in Kunz et al. (2002). For instance, Kunz et al. (2002) found that  $S(300 \text{ keV}) = 165 \pm 50 \text{ keV b}$ , instead of the higher value of NACRE [ $S(300 \text{ keV}) = 199 \pm 64 \text{ keV b}$ ]. The corresponding reaction rate is  $RR(300 \text{ keV}) = (7.58^{+2.62}_{-2.33}) \cdot 10^{-15} \text{ cm}^3 \text{ mole}^{-1} \text{ s}^{-1}$ .

Metcalfe (2003) presented constraints on the values for the  $^{12}\text{C}(\alpha, \gamma)^{16}\text{O}$  reaction rates at stellar energies from observations of white dwarfs. This was achieved by finding

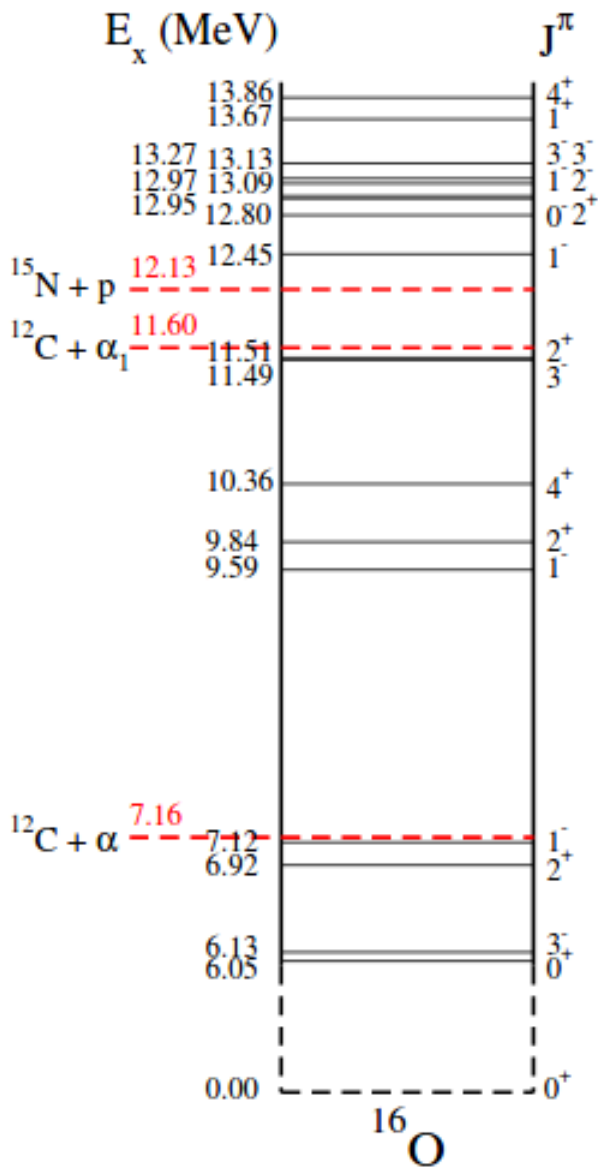


Figure 9 – Energy level diagram of an excited  $^{16}\text{O}$  nucleus. The interaction energies for the different entrance channels are shown in red, as can be seen they are close to the energy levels residing in the nucleus, causing resonance and a larger uncertainty in determining the resulting cross-section. Only the relevant energy levels for resonant reactions are shown, the parity states which do not lead to resonance are omitted. Taken from (deBoer et al., 2017).

an optimal model that allowed the mass of a helium atmosphere WD star to vary between  $0.45 M_\odot$  and  $0.95 M_\odot$  to match the periods of well-known DBV pulsators GD358 and CBS114 (Winget et al., 1994; Metcalfe; Winget; Charbonneau, 2001; Handler; Metcalfe; Wood, 2002). The central C/O abundance was then modified by adjusting the  $^{12}\text{C}(\alpha, \gamma)^{16}\text{O}$  reaction rate to match the central C/O ratio and the total mass in agreement with the optimal model found for each case. As mentioned in above, this method is fraught with uncertainties contained within the stellar models. In particular, convection during the CHB is particularly problematic, where the  $^{12}\text{C}(\alpha, \gamma)^{16}\text{O}$  reaction is most active (Straniero

et al., 2003; Straniero, 2007; Salaris et al., 2010). The prescription of convection used can affect the C/O ratios of the core during this stage (Romero; Campos; Kepler, 2015; De Gerónimo et al., 2017). This will certainly lead to a large uncertainty within the evaluated reaction rate. The values for both DBV pulsators were found to be within the uncertainties quoted by NACRE for extrapolations to a stellar energy of 300 keV.

An et al. (2016) point out that the resonance parameters used by Kunz et al. (2002), which were taken from Tilley, Weller & Cheves (1993), neglect the ground state transitions from the works of Brochard, F. et al. (1975), Ophel et al. (1976), resulting in a higher value for the expected reaction rate. Instead, An et al. (2016) use the reduced R-matrix and S-factor derived by An et al. (2015) to produce the reaction rate found in their work, which accounted for all transitions. In their computations, An et al. (2015) and An et al. (2016) found a significant reduction to the uncertainty of their S-factors  $S(300 \text{ keV}) = 162.7 \pm 7.3 \text{ keV b}$ , similar to that of Kunz et al. (2001), Kunz et al. (2002). The reaction rate for the same energy resulted  $RR(300 \text{ keV}) = (7.83 \pm 0.35) \cdot 10^{-15} \text{ cm}^3 \text{ mole}^{-1} \text{ s}^{-1}$ . Figure 10 shows a comparison between reaction rates considerations for those from An et al. (2016) and the uncertainties from NACRE as a ratio of adopted rate from NACRE (NACRE\_A, see Section 1.4 for a discussion of related abbreviations). These relations are represented as a function of temperature. For an analysis including other works, see Figure 4 of An et al. (2016). As can be seen from this figure, for energies characteristic of stellar energies, particularly for the region of helium burning temperatures (shaded region), the reaction rate from An et al. (2016) is lower than that extracted from NACRE\_A. We expect, therefore, to have a higher C/O ratio in the core of the final white dwarf that is formed. At much higher energies the reaction rate from An et al. (2016) is larger than that from NACRE\_A, although these temperatures are not reached in the sequences computed within this work.

The method of photo-disintegration currently is focused on characterising the resonant  $J_\pi = 2^+$  state around an incident energy of  $E_X \sim 10.0 \text{ MeV}$ . Such a state was first theorised by Morinaga (1956) which began a five decade long search for the desired state (Fynbo; Freer, 2011). Most photo-disintegration experiments agree that the second  $J_\pi = 2^+$  lies in the range  $9.8 \leq E_X/\text{MeV} \leq 10.03$  (see Figure 9, for details) with the differences between the determinations being due to the fits used in each work (deBoer et al., 2017; Aliotta et al., 2021; Zimmerman et al., 2013; Gai, 2012).

At the time when this work started, the reaction rate evaluated by An et al. (2016) was the most recent determination, whilst also being extremely thorough. From the inclusion of previously neglected resonances, new analysis into the S-factor using a derived R-matrix which was produced by the same group (An et al., 2015), I find that their determination of their adopted rate to be well determined and should produce more realistic stellar evolution computations. Additionally, evaluated values of the reaction

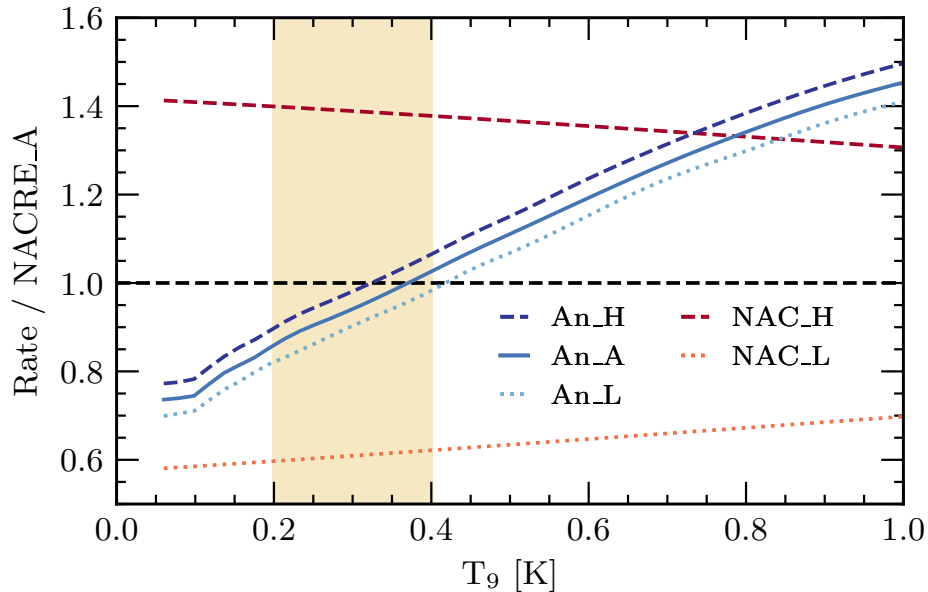


Figure 10 – Evaluated reaction rates for each prescription considered as a ratio of NACRE\_A for the  $^{12}\text{C}(\alpha, \gamma)^{16}\text{O}$  reaction. This value is represented as a function of temperature where  $T_9 = T/10^9$ . The shaded region defines the temperatures where helium burning occurs. During the core helium burning stage is also where the  $^{12}\text{C}(\alpha, \gamma)^{16}\text{O}$  reaction is most prominent. The light-orange dotted and red dashed lines represent the NACRE\_L and NACRE\_H considerations, respectively. The solid blue line defines An\_A (the adopted rate from An et al. (2016)) with the An\_L and An\_H rates being depicted as light-blue dotted and dark-blue dashed lines, respectively.

rate from An et al. (2016) are within the uncertainties which are quoted by Angulo et al. (1999), meanwhile the uncertainties of the reaction rate values from An et al. (2016) are much smaller than those from the NACRE survey, although critiqued by deBoer et al. (2017) which will be discussed in Section 1.4. I find that the widespread use of those reaction rates from the NACRE database is due to their accessibility, reputation and ease of comparisons to other works studying similar problems.

## 1.4 Motivation and Aims

Nuclear reaction rates can have large intrinsic uncertainties, specially if the compound nucleus contains resonances close to energies that are characteristic of stellar interiors or widths of other energy levels overlap (Angulo et al., 1999; deBoer et al., 2017; Aliotta et al., 2021). With more detailed studies of the compound nucleus and the mechanisms of such reactions, it has been possible to reduce these uncertainties slightly (Zimmerman et al., 2013; An et al., 2016; deBoer et al., 2017). No detailed study to date in the literature has shown how these uncertainties affect all stages of the complete evolution of a star (both single-isolated stars and binaries).

It has been shown that individual stages and properties of fully evolutionary

sequences are affected if a different reaction rate is considered for certain reactions. The  $^{12}\text{C}(\alpha, \gamma)^{16}\text{O}$  reaction is of great importance in theoretical stellar evolution computations. Such as, influencing the pulsation properties of ZZ Ceti stars (De Gerónimo et al., 2015; De Gerónimo et al., 2017). Differences between the considered  $^{12}\text{C}(\alpha, \gamma)^{16}\text{O}$  reaction rate will also affect the duration of the core helium burning stage (deBoer et al., 2017). In addition, the  $^{12}\text{C}(\alpha, \gamma)^{16}\text{O}$  reaction impacts supernova explosions as the outcome is related to the composition of the final WD (e.g. Iben I. & Tutukov (1984), Wu et al. (2020)) and third dredge-up episodes (TDUs) during the asymptotic giant branch (AGB) stage (Frost; Lattanzio, 1996; Karakas; Lattanzio; Pols, 2002; Marigo, 2002; Karakas; Lattanzio, 2003; Marigo, 2007; Cristallo et al., 2009; Weiss; Ferguson, 2009; Ventura; Marigo, 2009; Kalirai; Marigo; Tremblay, 2014; Matteucci, 2021). Furthermore, the variation of the C/O impacts the ignition of Type 1a supernovae, an important event in constraining cosmological parameters (Perlmutter; Turner; White, 1999; Riess et al., 1998). The enrichment of the outer layer of the AGB stars from dredge-up and the mass-loss affects the chemical evolution of galaxies (Matteucci, 2012; Boothroyd; Sackmann, 1988; Kobayashi; Karakas; Lugaro, 2020; Ventura et al., 2020; Cristallo et al., 2015; Matteucci, 2021). Additionally, the  $^{12}\text{C}(\alpha, \gamma)^{16}\text{O}$  reaction governs whether a star will form a neutron star or black hole (Brown et al., 2001; Heger et al., 2002; Woosley; Heger; Weaver, 2002; Tur; Heger; Austin, 2007; West; Heger; Austin, 2013; Sukhbold; Adams, 2020). Gravitational wave detections from black hole mergers can also be used to constrain the  $^{12}\text{C}(\alpha, \gamma)^{16}\text{O}$  reaction rate by determining the mass of the black hole and the fraction of carbon and oxygen that remains (see Farmer et al. (2020), for details).

In this work, we perform stellar evolutionary computations to study the impact of the  $^{12}\text{C}(\alpha, \gamma)^{16}\text{O}$  reaction rate on the stellar structure and evolution of low and intermediate-mass stars. We compute fully evolutionary sequences using the open source stellar evolution code MESA version-r15140 (Paxton et al., 2011; Paxton et al., 2013; Paxton et al., 2015; Paxton et al., 2018), with initial masses in the range  $M_i = 0.90\text{--}3.05 M_\odot$  and an initial metallicity of  $Z_i = 0.01$ . This mass range is selected such that all sequences evolve into a carbon–oxygen WD (examples of works which consider/include a similar mass range are (Renedo et al., 2010; Romero; Campos; Kepler, 2015; De Gerónimo et al., 2017; Marigo et al., 2020)). Furthermore, for larger initial masses there could be a contamination of neon, sodium or magnesium which are products from carbon burning. The final masses for the calculated sequences range between  $0.513 M_\odot$  and  $0.691 M_\odot$ . The considered reaction rates for all reactions are taken from the work of NACRE. However, a special consideration to the  $^{12}\text{C}(\alpha, \gamma)^{16}\text{O}$  reaction, where we also produce sequences which consider the rate from An et al. (2016). We analyse the impact of these reaction rates and their uncertainties across all stages of evolution from the ZAMS until the WD cooling track when the star reaches a luminosity of  $\log(L/L_\odot) = -3$ . Each considered initial mass is computed six times with a different considered  $^{12}\text{C}(\alpha, \gamma)^{16}\text{O}$  reaction rate. The different  $^{12}\text{C}(\alpha, \gamma)^{16}\text{O}$

reaction rates used in this are named, described and listed below:

- NACRE\_A, which relates to the adopted rate from the NACRE data base (Angulo et al., 1999);
- NACRE\_H, which relates to the upper limit due to the uncertainty for the reaction rate evaluated by the NACRE data base Angulo et al. (1999);
- NACRE\_L, which relates to the lower limit due to the uncertainty for the reaction rate evaluated by the NACRE data base Angulo et al. (1999);
- An\_A, which relates to the adopted rate evaluated by An et al. (2016);
- An\_H, which relates to the upper limit due to the uncertainty for the reaction rate evaluated by An et al. (2016);
- An\_L, which relates to the lower limit due to the uncertainty for the reaction rate evaluated by An et al. (2016).

By analysing the adopted rate in addition to the High/Low limits for each source of  $^{12}\text{C}(\alpha, \gamma)^{16}\text{O}$  reaction rate, we can achieve an insight into how different properties of different stellar evolutionary stages are affected by the  $^{12}\text{C}(\alpha, \gamma)^{16}\text{O}$  reaction. Furthermore, by considering NACRE\_A we can compare with other works that consider similar initial conditions from different stellar evolutionary codes, such as the La Plata evolutionary code (LPCODE). It is important to note, however, the S-factor calculation of An et al. (2015), seems to neglect external contributions for ground state energy levels, making this approximation not valid for high precision analysis (deBoer et al., 2017). Therefore, we treat the uncertainties of the  $^{12}\text{C}(\alpha, \gamma)^{16}\text{O}$  reaction rate from An et al. (2016) as arbitrary differences to determine the effect of the urgent need for more precise  $^{12}\text{C}(\alpha, \gamma)^{16}\text{O}$  reaction rate uncertainties, as claimed by Kunz et al. (2002), Tur, Heger & Austin (2010). Some works further claim that the uncertainty must be less than 10% to be on par with non-nuclear physical uncertainties (see Woosley et al. (2003), deBoer et al. (2017), for details).

The output of the evolution code describes the following phases of evolution: the main sequence (MS), the red giant branch (RGB), the core helium burning stage (CHB), the asymptotic giant branch (AGB) and the white dwarf (WD). However, we do not report results from the MS or RGB as the  $^{12}\text{C}(\alpha, \gamma)^{16}\text{O}$  reaction only becomes significant during late times of the CHB. The reader can refer to Figure 2 to help identify the location of these stages. We consider a star to be evolving on the MS as long as the central hydrogen abundance is larger than  $10^{-6}$  by mass. It then evolves along the RGB so long as the central helium luminosity is less  $10^3 L_{He,\odot}$  (where  $L_{He,\odot}$  is the helium luminosity of the

Sun), where it then evolves on the CHB until the central helium abundance is smaller than  $10^{-6}$  by mass. It then evolves along the AGB and TP-AGB until the mass of the outer hydrogen layer is less than  $0.001M_{\odot}$ . The final WD stage is followed until it reaches a luminosity of  $\log(L/L_{\odot}) = -3$ , where our calculation is terminated.

The aims of this study are to find where the following points are affected by the  $^{12}\text{C}(\alpha, \gamma)^{16}\text{O}$  reaction rate:

- Identify the stages most affected by the uncertainties associated with the  $^{12}\text{C}(\alpha, \gamma)^{16}\text{O}$  reaction rate.
- Research if the properties of key events, such as thermal pulses, are affected by the uncertainties in the  $^{12}\text{C}(\alpha, \gamma)^{16}\text{O}$  reaction rate.
- Identify the possibility of the  $^{12}\text{C}(\alpha, \gamma)^{16}\text{O}$  reaction rate uncertainties affecting pulsations within regions of instability across all stages of the evolutionary sequence - particularly for sdB stars where the  $^{12}\text{C}(\alpha, \gamma)^{16}\text{O}$  reaction is active in the core during the CHB.
- Discover if crystallisation temperature may be affected as a result of differences in the C/O core composition from the uncertainties in the reaction rates used.

Chapter 2 provides the reader with a deeper understanding of the MESA codes (particularly for version-r15140 which is utilised in this work), as well as including changes I have made to the code itself, in addition to the input lists (“inlists”), to complete the current work. Here I also include details of the initial conditions for all computed sequences. Chapter 3 reports the results found thus far for each stage (apart from the MS and RGB, as discussed above) and is accompanied by a discussion of the results. In this chapter, I also include what their implications may be. Chapter 4 summarises and concludes the results of this work, in addition to discussing the validity of the reaction rates considered in this work. An example of the inlists used in this work is provided in the appendix.





## 2 Numerical Tools

This chapter provides a description of the computational tools used in this work. Additionally, details on the input micro-physical and macro-physical properties of stellar matter are also provided. It is also shown how the tools were implemented and adapted for the purposes of this study. I include new subroutines that are not present within MESA which are useful not only within the scope of the current work, but also in future works that will be discussed later.

### 2.1 The stellar structure equations

The structure and composition of computed stars are calculated by combining structural and equilibrium equations 2.1 - 2.4 using state-of-the-art adaptive mesh refinement.  $m_r$  represents the stellar mass within a radius  $r$ . Assuming spherical symmetry, hydrostatic equilibrium and neglecting the effects of rotation and magnetic fields we can build a spherical stellar model with concentric shells that have a mass  $m_r$ . It follows that if we consider the luminosity ( $L_r$ ), pressure ( $P_r$ ) and temperature ( $T_r$ ), we can build relations for hydrostatic equilibrium (Eq. 2.1), mass continuity (Eq. 2.2), energy transport (Eq. 2.3) and energy generation (Eq. 2.4)<sup>1</sup>:

$$\frac{dP_r}{dm_r} = -\frac{Gm_r}{4\pi r^4}, \quad (2.1)$$

$$\frac{dr}{dm_r} = -\frac{1}{4\pi r^2 \rho}, \quad (2.2)$$

$$\frac{dT_r}{dm_r} = -\frac{Gm_r T}{4\pi r^4 P} \nabla_T, \quad (2.3)$$

$$\frac{dL_r}{dm_r} = \epsilon_{nuc} + \epsilon_{grav} - \epsilon_q - \epsilon_{\nu,th}, \quad (2.4)$$

where  $G$  is the gravitational constant,  $\nabla_T$  is the temperature gradient which defines whether a region is unstable against convection or not,  $\epsilon_{nuc}$  is the total nuclear reaction energy generation (not including the energy of neutrinos produced in nuclear reactions),  $\epsilon_{grav}$  is the rate of change of gravitational energy from expansion/contraction,  $\epsilon_q$  is the rate of energy lost through thermal radiation, and finally,  $\epsilon_{\nu,th}$  is the thermal neutrino-loss rate. This set of equations is not yet finished. Equations of state, opacities and reaction rates

<sup>1</sup> Equations 2.1 - 2.4 are well documented and can be found in Clayton (1968), Kippenhahn & Weigert (1990).

are required to provide relations between each parameter - this will be further explored in Section 2.2.1.

## 2.2 The MESA Code

The Modules for Experiments in Stellar Astrophysics (MESA) are a set of code modules written in Fortran 95 that call on each other to simulate how a star evolves by solving Equations 2.1 - 2.4 (Paxton et al., 2011; Paxton et al., 2013; Paxton et al., 2015; Paxton et al., 2018; Paxton et al., 2019). The code is one-dimensional and so assumes that the star is spherically symmetric. The one-dimensional array is built up of a series of cells which represent different regions of the star. The first cell represents the surface, whilst the base of the final cell represents the centre of the star. Within each cell of the one-dimensional array, MESA considers the nuclear processes that occur within the star as well as the hydrodynamics of the star itself. This is possible by considering and solving the structure equations (Equations 2.1 - 2.4) using the composition in each cell for each model of the sequence. The code advances to the next model by implementing an appropriate timestep, which may seem confusing as Equations 2.1 - 2.4 have no dependency on time. The first timestep is an initial input. The chemical structure of the star is calculated for the next model using an appropriate timestep and Equation 2.5:

$$\delta X_{i,k}(\delta t) = \frac{dX_{i,k}}{dt} \delta t + (F_{i,k+1} - F_{i,k}) \frac{\delta t}{dm_k}, \quad (2.5)$$

where  $\delta X_{i,k}(\delta t)$  is the change of mass fraction for an element  $i$  in cell  $k$  across a timestep  $\delta t$ . The first term in Equation 2.5 represents the change of species due to nuclear reactions and the second term relates to the change of species due to mixing between regions, across a timestep  $\delta t$  (see Paxton et al. (2011), for more details). From the new chemical structure which is calculated by Equation 2.5, the structure equations are recalculated to form the next model. After the first timestep, which is supplied by the user, the values of subsequent timesteps are controlled by MESA.

The timestep for the next model ( $\delta t_{i+1}$ , where  $i$  is the current model number) is adjusted by considering Equation 2.6:

$$\delta t_{i+1} = \delta t_i f \left[ \frac{f(v_t/v_{c,i}) f(v_t/v_{c,i-1})}{f(dt_i/dt_{i-1})} \right]^{\frac{1}{4}}, \quad (2.6)$$

where  $f(x) = 1 + 2 \tan^{-1}[0.5(x - 1)]$ ,  $v_{c,i}$  and  $v_{c,i-1}$  are the current and previous control variables which are the unweighted averages over all cells of the relative changes of  $\ln \rho$ ,  $\ln T$  and  $\ln R$ .  $v_t$  is the target value for the control variable and has the default value of  $10^{-4}$ , and finally,  $\delta t_{i-1}$ ,  $\delta t_i$  and  $\delta t_{i+1}$  are the previous, current and next timestep. This setup

allows for a timestep such that rapid changes can be made without causing undesirable fluctuations in the computations (Paxton et al., 2011). This is desired as the MS, for example, is relatively simple to calculate and so a large timestep is implemented between each model, but a rapid reduction occurs at the end of the MS where a much smaller timestep is required. Here, a large timestep would lead to large errors in the sequence as important processes that occur within short timescales can be neglected. Once the new timestep is calculated, the next model can be calculated and is then quality checked again by comparing the relative changes of each parameter. If a parameter changes more than the desired limit between models, the step is retried with timestep equal to half of the original value. This continues until the next model passes the quality check for the minimum timestep is reached and the computation terminates for this model.

The structure of the star is calculated on a series of concentric radial cells (where we assume spherical symmetry of a 1D array). Each cell is characterised by a value of pressure, temperature and density. The first cell represents the surface of the star, and the base of the final cell is the centre of the star. Figure 11 illustrates the individual properties of each cell and how they differ to the next cell in the array (Paxton et al., 2011; Paxton et al., 2013; Paxton et al., 2015; Paxton et al., 2018; Paxton et al., 2019). Some variables are mass-averages of the cell, other variable values are defined at the outer face of the cell. Each cell  $k$  has a mass of  $dm_k$ , such that the sum of cell mass over all  $k$  integers provides the total mass of the star. In MESA these cells are also referred to as zones. Additionally, the number of zones can increase/decrease from model to model, which is controlled by the adaptive radial mesh. If the difference between two zones is negligible, the code can reduce the number of zones to increase the computational efficiency. Likewise, if a zone can be split, the code will resolve a finer structure in the star and preserve the numerical fidelity of the model. A fine-balance between computational efficiency and spatial resolution is maintained automatically by MESA.

Figure 12 depicts the order of processes and routines by MESA. Each computation begins by reading the inlist files, which contain the physical inputs the user desires and are further separated into two sections: `star_job` and `controls`. `Star_job` provides the code with the physics included in the computations, such as the reaction networks and reaction rate values. The controls within the inlist allow the user to input the properties and processes that the code requires to run and their related options, such as the initial mass and metallicities, convection, the efficiency of overshooting and gravitational settling. The input variables that we use will be discussed in Section 2.3.1.

'Extras' can also be included in the controls section of the inlist. These are additional subroutines that the user can create and execute within the computation. These are essential for computing variables that may not be contained in the modules provided by MESA or alternate equations that are not formally a part of the MESA code.

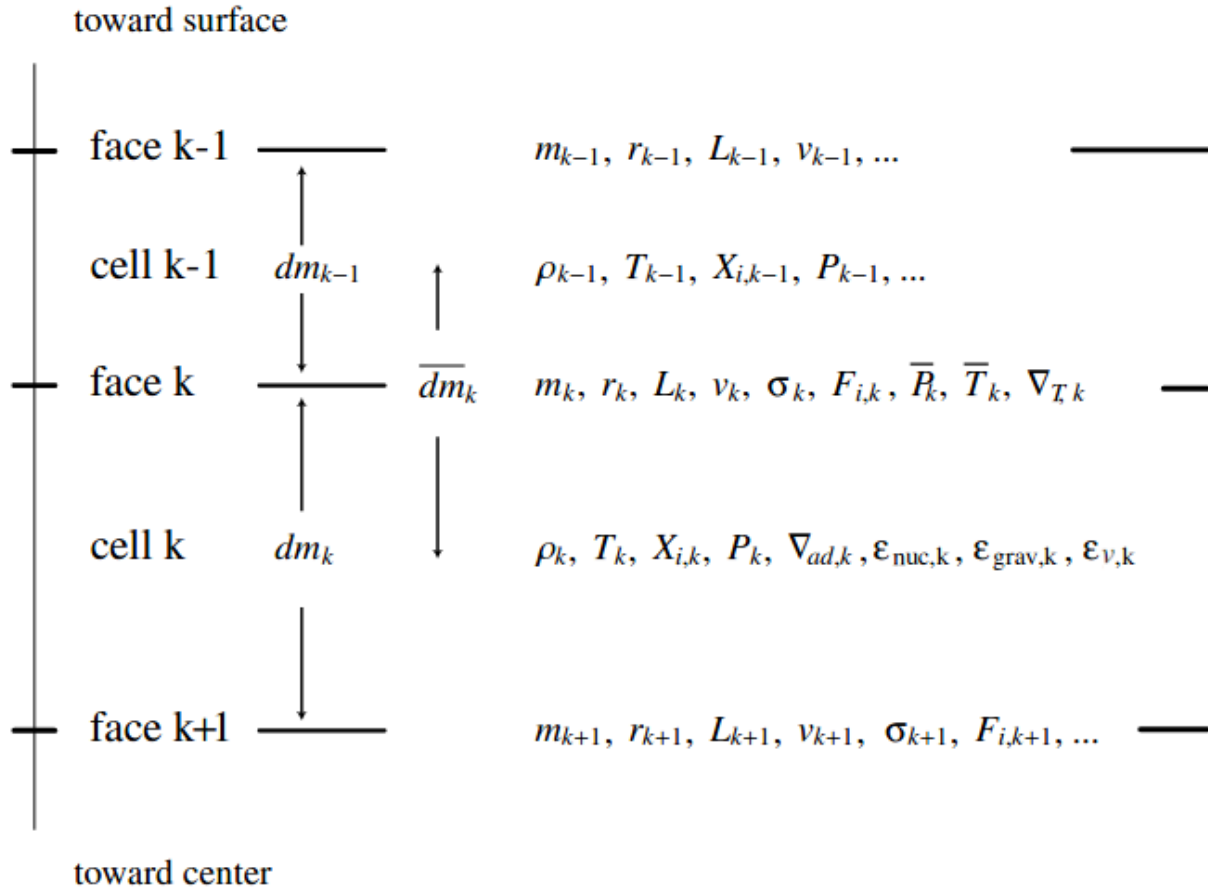


Figure 11 – Schematic of the radial mesh in the MESA code. Some variables are averaged over the cell and some are defined at its outer boundary. Adapted from (Paxton et al., 2011).

After considering these extras, the code reads in the previous model or creates a 'start-up' if no model is provided. The code begins to calculate all properties throughout the model at the 'take\_step' stage of the flowchart found in Figure 12. This model can be successful if the convergence conditions are satisfied, or it can be retried with a smaller timestep if the conditions are not satisfied. The conditions for a successful model are dependent on the residuals of the variable differentials and to the corrections of variables that are derived from those residuals. If the residuals and corrections satisfy a comprehensive convergence criteria, then the model is accepted. Further details on the convergence of models can be found in the works of Paxton et al. (2011), Paxton et al. (2013), Paxton et al. (2015), Paxton et al. (2018), Paxton et al. (2019).

The versatility of MESA is very apparent. Not only can it simulate all masses related to stellar objects with a wide range of initial metallicities, it has also been applied to simulations of binary systems, brown dwarfs and even planetary systems. Other advantages of MESA include being a user-friendly open-source code that is highly optimised and it can accept code modules written by the user, allowing an expanding range of potential applications.

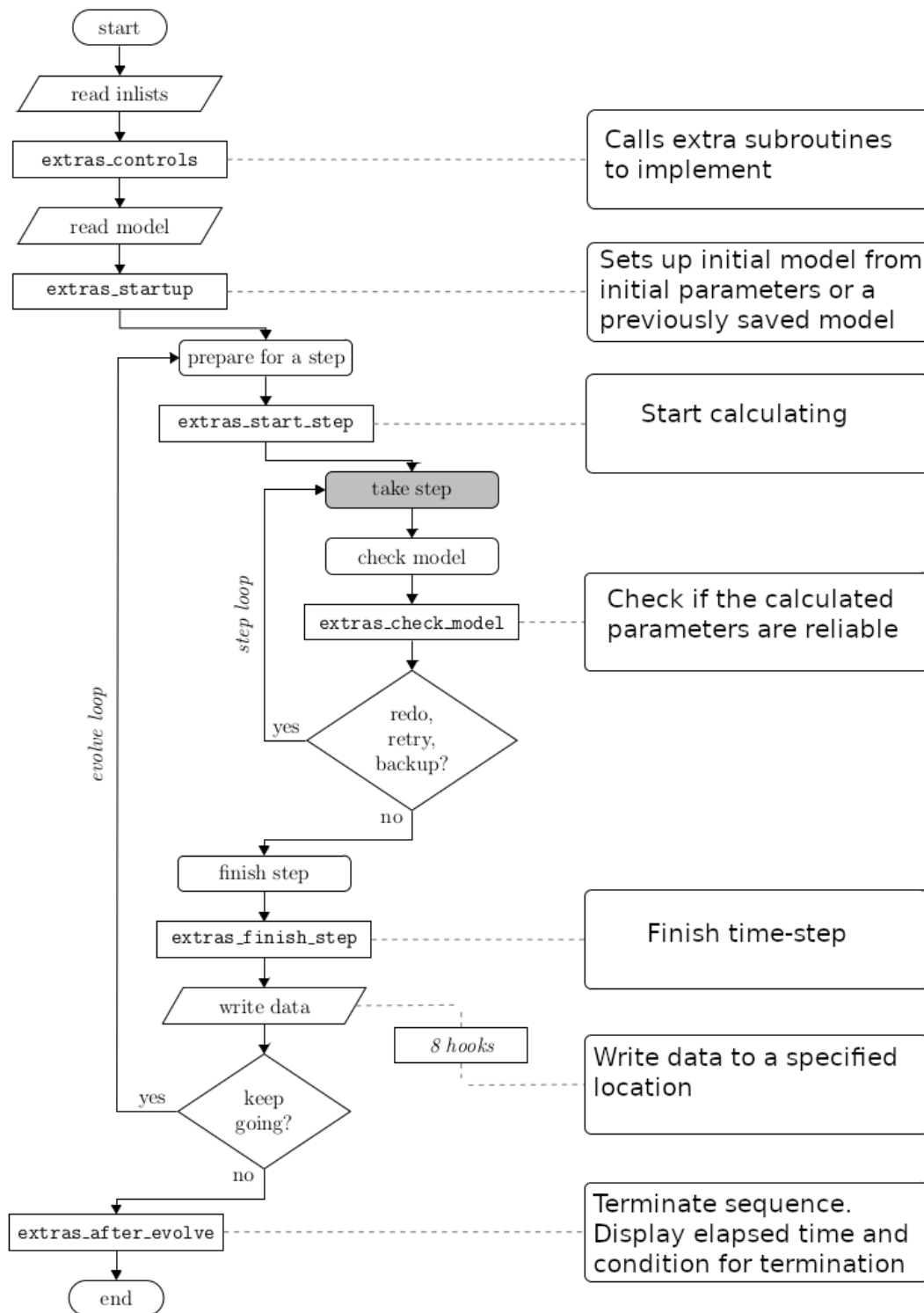


Figure 12 – Flowchart illustrating the order of processes MESA uses to evolve stellar computations. First the inlists are read, then the extra subroutines are called in 'extras\_controls'. Then the steps are calculated using timesteps evaluated by MESA as well as considerations within the subroutine 'extras\_check\_model'. Once MESA has completed a step, it will continue or redo a step if it has a large uncertainty. MESA displays information before saving and then decides if the stopping criteria have been satisfied.

Examples of the vast range of applications by MESA include: studies of the impact of different nuclear reaction networks (Suda; Hirschi; Fujimoto, 2011; Guzik et al., 2020); evolutionary computations of massive white dwarfs (Laufer; Romero; Kepler, 2018); testing stellar opacities (Daszynska-Daszkiwicz et al., 2019); pulsation mode identification using asteroseismological techniques (Lenz, 2012; Beck, 2013; Takayama; Saio; Ita, 2013; Sahoo et al., 2020); AGB envelope evolution (Chamandy et al., 2020); formation and properties of supernova (Augustine et al., 2019; Wu et al., 2020); planetary evolution (Kunitomo et al., 2011); studies of helium flashes (Gautschi, 2012); analysis of convection (Augustson et al., 2012; Montalbán et al., 2013), as well studying how axion emission affects the evolution of the sequences (Aoyama; Suzuki, 2015).

### 2.2.1 Microphysics

MESA provides a vast choice of equation of state (EoS) tables. Here is only a description of those that are used within this work. For a wider description of all EoS tables, see Paxton et al. (2011), Paxton et al. (2013), Paxton et al. (2015), Paxton et al. (2018), Paxton et al. (2019). This work considers the equation of state (EoS) tables from OPAL2 (Rogers; Nayfonov, 2002) and from SCVH tables (Saumon; Chabrier; van Horn, 1995) for low temperatures (Paxton et al., 2011) ( $2.1 \leq \log T \leq 8.2$ ). For temperatures outside of this range (up to  $\log T = 13$  and densities up to  $\log \rho = 15$ ), the HELM EOS tables (Timmer; Swesty, 2000) are used. The tables that are actually used in the code are the DT2 and ELM tables, which are subsets derived from the OPAL/SCVH EOS and HELM EOS, respectively. They consider smaller increments within variables for improved accuracy (Paxton et al., 2018; Paxton et al., 2019).

The radiative opacities are merged with the electron conduction opacities and are considered from opacity tables by Cassisi et al. (2007) (Paxton et al., 2011). Although, outside the density and temperature ranges ( $-6 \leq \log \rho \leq 9.75$  and  $3 \leq \log T \leq 9$ ), the opacity tables are those from Hubbard & Lampe (1969) and Yakovlev & Urpin (1980) for the non-degenerate and degenerate cases, respectively. The radiative opacity tables are taken from Ferguson et al. (2005) ( $2.7 \leq \log T \leq 4.5$ ) and Iglesias & Rogers (1993), Iglesias & Rogers (1996) ( $3.75 \leq \log T \leq 8.7$ ). Those low temperature opacities from Ferguson et al. (2005) include the effects that molecules and grains have on the opacity. Described above are merely the opacity tables that we have considered within this work. For further descriptions of other opacity table options see Paxton et al. (2011), Paxton et al. (2013), Paxton et al. (2015), Paxton et al. (2018), Paxton et al. (2019).

Nuclear reaction rates are taken from Angulo et al. (1999) (NACRE), Caughlan & Fowler (1988) (CF88) and Cyburt et al. (2010) (JINA REACLIB). Alternate nuclear reaction rates are also available for:  $^{14}\text{N}(p, \gamma)^{15}\text{O}$  (Imbriani et al., 2004); triple- $\alpha$  from Fynbo et al. (2005);  $^{14}\text{N}(\alpha, \gamma)^{18}\text{F}$  (Görres et al., 2000) and  $^{12}\text{C}(\alpha, \gamma)^{16}\text{O}$  (Kunz et al.,

2002). Weak interactions are also included as they contribute to hydrogen burning (Paxton et al., 2011; Paxton et al., 2013; Paxton et al., 2015; Paxton et al., 2018; Paxton et al., 2019).

### 2.2.2 Macrophysics

Convection is characterised by the mixing length theory by Böhm-Vitense (1958) as presented by Henyey, Vardya & Bodenheimer (1965). This is characterised by the mixing length parameter  $\alpha_{MLT}$ . MESA also allows for additional mixing episodes during the giant stages; an important factor in determining the final composition of the WD core in addition to mixing episodes during the CHB (Prada Moroni; Straniero, 2002; Straniero et al., 2003; Renedo et al., 2010). Such additional mixing episodes that are similar to convection (such as semiconvection) are treated as effective diffusion processes within MESA. A constant value for  $\alpha_{MLT}$  is not strictly appropriate for all stages and regions within a star. Works dedicated to finding consistent formulas for  $\alpha_{MLT}$  are Tremblay et al. (2013), Tremblay et al. (2013), Tayar et al. (2017) and Cukanovaite et al. (2019), which consider dependencies on metallicities, radius and mass. The first released version of the MESA code (Paxton et al., 2011) considered convective instabilities within stellar interiors due to temperature gradients (Schwarzschild criterion (Schwarzschild, 1906)), but they neglected the effect of composition gradients (Ledoux criterion (Ledoux, 1947; Kippenhahn; Weigert, 1994)). This is rectified in Paxton et al. (2013) and their subsequent works (Paxton et al., 2015; Paxton et al., 2018; Paxton et al., 2019) which now consider both, but have the option to only consider either the Schwarzschild criterion or the Ledoux criterion if desired. The reader can refer back to Section 1.1 for details on the Schwarzschild and Ledoux criterion.

As of Paxton et al. (2013), a region is considered convective when both the Ledoux and the Schwarzschild criteria are not fulfilled, meaning that the region is dynamically unstable. Semiconvection is considered when the Ledoux criterion is fulfilled, but the Schwarzschild criterion is not. This can occur due the composition gradient between regions. A result of this is a less efficient heat transport mechanism which behaves similarly to convection - that can be described as a time-dependent diffusion process characterised by the diffusion coefficient,  $D_{sc}$ , Equation 2.7,

$$D_{sc} = \alpha_{sc} \left( \frac{K}{6C_P\rho} \right) \frac{\nabla_T - \nabla_{ad}}{\nabla_L - \nabla_T}, \quad (2.7)$$

where  $K = 4acT^3/(3\kappa\rho)$  is the radiative conductivity,  $C_P$  is the specific heat at a constant pressure,  $\alpha_{sc}$  is a dimensionless efficiency parameter (Langer, 1991; Yoon; Langer; Norman, 2006),  $\nabla_T$  is the true temperature gradient,  $\nabla_L$  is the Ledoux gradient which is the sum of the adiabatic temperature gradient and the composition gradient, and  $\nabla_{ad}$  is the adiabatic temperature gradient.

Another mixing process that MESA implements is thermohaline mixing. This process occurs when the difference between the temperature gradient and the adiabatic gradient is less than the composition gradient. This causes an inversion of the mean molecular weight of a formally stable region according to the Ledoux criterion (Paxton et al., 2013). The diffusion coefficient for this process follows an analysis of Ulrich (1972) and Kippenhahn, Ruschenplatt & Thomas (1980) and is shown in equation 2.8.

$$D_{th} = \alpha_{th} \frac{3K}{2\rho C_P} \frac{B}{\nabla_T - \nabla_{ad}}, \quad (2.8)$$

where  $\alpha_{th}$  is an efficiency parameter,  $K$  is the radiative conductivity,  $C_P$  is the specific heat capacity at a constant pressure,  $B$  is the Brunt composition gradient,  $\nabla_T$  is the true temperature gradient and  $\nabla_{ad}$  is the adiabatic gradient. See Equation 1.2 and Equation 1.3 for more details.

Overshooting from convection is also considered within MESA, that is, how far a convective element rises above the edge of a convective boundary. Such a process is characterised by an exponential decay of a convective diffusion coefficient. MESA utilises that from Herwig (2000).

$$D_{EM} = D_0 \exp(-2z/fH_P) \quad (2.9)$$

where  $H_P$  is the pressure scale-height at the convective boundary,  $D_0$  is the diffusion coefficient of unstable regions that are near the convective boundary.  $z$  is the geometric distance from the convective boundary.  $f$  is an adjustable free parameter that controls the efficiency of mixing by setting the scale height of the overshooting region (Herwig, 2000).

Towards the end of the core helium burning stage, small increases in the helium abundance can vastly enhance the energy production and increase the luminosity. This extends the core convective boundary and leads to a convective runaway (Straniero et al., 2003). This is known as a 'breathing pulse' and it is not believed to be a physical attribute to stellar evolution, rather a unfortunate by-product of numerical stellar evolution. For more information on this phenomena the reader can refer to Straniero et al. (2003). These breathing pulses can be neglected within MESA, however, we find it better to use our own prescription (see Section 2.3.3 and Section 2.3.1).

It is well known that denser materials displace those beneath that are less dense. Within stellar physics, these processes is known as Rayleigh-Taylor instabilities (RTIs) (Rayleigh, 1883; Taylor, 1950; Cook; Youngs, 2009). This movement of materials from RTIs is possible due to gravitational settling within the star. This process is important as it makes the denser elements within the star sink to the centre. This produces smoother abundance profiles as the denser metals are brought to the core and the less dense elements such as hydrogen and helium float towards the surface. Such movements are controlled by element diffusion.



Element diffusion in MESA is described as the physical mechanism for mixing chemicals that includes gravitational settling, thermal diffusion and chemical diffusion. Gravitational settling leads to denser element diffusing towards the core while lighter elements float towards the surface. Gravitational settling within MESA is part of the 'diffusion' module and is characterised by solving the Burger's equations (Burgers, 1969) using coefficients from Iben & MacDonald (1985) (Paxton et al., 2011; Paxton et al., 2013; Paxton et al., 2015; Paxton et al., 2018; Paxton et al., 2019). Thermal diffusion acts in the same direction as gravitational settling, although to a lesser extent, bringing highly charged and more massive species to the central regions of the star. Chemical diffusion, however, works against this general direction (see Iben & MacDonald (1985), Thoul, Bahcall & Loeb (1994), for details). In addition to the aforementioned processes, MESA includes radiative accelerations (Hu et al., 2011) into their element diffusion prescription. These radiative forces are negligible in hot regions as well as being computationally demanding. Hence, we do not consider the effects of radiative levitation. Our element diffusion process is applied to the following isotopes:  $^1\text{H}$ ,  $^3\text{He}$ ,  $^4\text{He}$ ,  $^{12}\text{C}$ ,  $^{14}\text{N}$ ,  $^{16}\text{O}$ ,  $^{20}\text{Ne}$ ,  $^{24}\text{Mg}$ .

Mass-loss can be considered in MESA by applying a fixed mass-loss rate or a mass-loss rate related to the "stellar wind". The latter is a rate that is usually related to the stellar luminosity, radius and occasionally the rotation period (Reimers, 1975; Bloeker, 1995; Vassiliadis; Wood, 1993). The strength of the selected mass-loss due to wind scheme can be controlled by a scale factor that multiplies the mass lost per year by the factor set. Furthermore, the selected wind scheme may change throughout the evolution of the sequence due to physical changes within the star. Such examples are new layers forming within the star, radius and rotation velocity (Reimers, 1975; Bloeker, 1995; Vassiliadis; Wood, 1993).

For more considerations to mass-loss on each stage of the evolutions, see Paxton et al. (2011), Paxton et al. (2013), Paxton et al. (2015), Paxton et al. (2018), Paxton et al. (2019).

## 2.3 Building the Code

This section describes the main input physics that we include within our inlist. We then discuss in further detail the implementation of reaction rates not included within MESA. Finally, we conclude this section by explaining the subroutines that we have added to our works as part of this programme.

### 2.3.1 Input Physics

We have adapted the template '1M\_pre\_ms\_to\_wd' found in the MESA test\_suite to the purposes of this work. Different versions of MESA have slight differences between the

inlists due the inclusion of new controls or the exclusions of old controls. As most of this work is performed with MESA-r15140, the reader should assume that this is the version that we consider, unless otherwise stated. This adapted template is specially useful as the evolution sequences that are considered within this work have initial masses in the range  $0.90 \leq M_i/M_\odot \leq 3.05$  and as such end with an object of similar structure. Each initial mass is computed six times with six different considerations for the  $^{12}\text{C}(\alpha, \gamma)^{16}\text{O}$  reaction rate (NACRE\_H, NACRE\_A, NACRE\_L, An\_H, An\_A and An\_L), defined in Section 1.4. Other reactions consider the respective adopted reaction rates from NACRE (Angulo et al., 1999). In total we compute 246 sequences with final WD masses in the range  $0.513M_\odot \leq M_f/M_\odot \leq 0.691M_\odot$ . The initial mass range considered in this work is selected such that all sequences evolve into a carbon–oxygen WD (examples of works which consider a similar mass range are Renedo et al. (2010), Romero, Campos & Kepler (2015), De Gerónimo et al. (2017), Marigo et al. (2020)).

We use the MESA nuclear reaction network ‘basic.net’, that includes the full p-p chain, the CNO cycle and the  $3\alpha$  reactions up until  $^{24}\text{Mg}$ , which contains the  $^{12}\text{C}(\alpha, \gamma)^{16}\text{O}$  reaction. This network also includes 8 individual isotopes:  $^1\text{H}$ ,  $^3\text{He}$ ,  $^4\text{He}$ ,  $^{12}\text{C}$ ,  $^{14}\text{N}$ ,  $^{16}\text{O}$ ,  $^{20}\text{Ne}$ ,  $^{24}\text{Mg}$  in addition to elementary and  $\alpha$  particles.

In our computations, we consider the default radiative opacity tables within MESA. These are from Ferguson et al. (2005) (for  $2.7 \leq \log T \leq 4.5$ ) and from the OPAL project (for  $3.75 \leq \log T \leq 8.7$ ) (Iglesias; Rogers, 1993; Iglesias; Rogers, 1996). Furthermore, we consider OPAL Type 2 tables as they allow for varying amounts of C and O, which are needed for helium burning and beyond (Iglesias; Rogers, 1996; Paxton et al., 2011).

We adopt the standard mixing length free parameter as  $\alpha = 2.0118$ . This value is adopted from the work of Guzik et al. (2016) who found this value to be a good approximation for sequences that consider the solar metallicity when using the opacity tables from the OPAL project. To derive this value, Guzik et al. (2016) compared calculated non-adiabatic solar oscillation frequencies and solar interior sound speeds to observed frequencies and helioseismic inferences. However, it should be noted that Guzik et al. (2016) consider an initial metallicity of  $Z_i = 0.015$ , rather than the value we consider in this work ( $Z_i = 0.01$ ). Such a difference would alter the value of the  $\alpha$  parameter if a similar analysis was performed with this initial metallicity consideration. Convective mixing is treated as a time-dependent diffusion process, with the diffusion coefficient given in Equation 2.9. We take the value of  $f = 0.016$  for all regions of the model for this work, following the same consideration of overshooting as Herwig (2000), Weiss & Ferguson (2009), De Gerónimo et al. (2017). This treatment of the convective boundaries was also adopted by other authors for single stellar evolution computations (Frost; Lattanzio, 1996; Karakas; Lattanzio; Pols, 2002; Weiss; Ferguson, 2009; Ventura; Marigo, 2009; Cristallo et al., 2009; Romero; Campos; Kepler, 2015; De Gerónimo et al., 2017).

The presence of dredge-up episodes during the core helium burning stage is relevant for the final composition of WDs (Prada Moroni; Straniero, 2002; Herwig, 2000; Straniero et al., 2003; Renedo et al., 2010). During the thermally pulsing AGB phase, although overshooting was considered at the boundary of the convective H-rich envelope during the TP-AGB, the third dredge-up episodes did not occur. Therefore, the evolution of the hydrogen-exhausted core (which is hereafter simply referred to as “the helium core mass”) and the final mass of the sequences for those which should experience some third dredge-up episodes will be affected (see Section 2.4). We define the “helium core mass” as the region from the centre until the cell in the 1D array that has a mass fraction of hydrogen that is greater than  $10^{-6}$ . Additional models were computed to assess the impact of the third dredge-up on the core mass growth during the thermal pulses (see Section 2.4, for details).

For regions stable against convection according to the Ledoux criterion, but there is an inversion of mean molecular weight, we employ thermohaline mixing. In MESA this is treated as a diffusion process, as above, with a diffusion coefficient produced by the stability analysis of Ulrich (1972) and Kippenhahn, Ruschenplatt & Thomas (1980). For the efficiency parameter of thermohaline mixing, we consider  $\alpha_{th} = 1.0$  (see Equation 14 of Paxton et al. (2013), for details). Thermohaline mixing was considered in order to smooth a discontinuity in the carbon and oxygen chemical profiles at the edge of the C/O core, during the early-AGB.

Towards the end of the core helium burning stage, when the central He abundance is lower than  $\sim 10\%$ , breathing pulse-like instabilities may appear. However, these events are attributed to adopted algorithms rather than to the physics of convection (see Straniero et al. (2003), Romero, Campos & Kepler (2015), Constantino et al. (2016), Constantino, Campbell & Lattanzio (2017), for details). To suppress the breathing pulses, when the central abundance of He drops below 0.13, we neglect convection until the central abundance of helium decreases below  $10^{-6}$ , similar to the prescription used by Renedo et al. (2010) and Romero, Campos & Kepler (2015). Without this prescription, the final carbon-to-oxygen (C/O) ratios can vary rapidly (up to  $\pm 0.1$ ) with small increments of initial mass ( $0.05 M_{\odot}$ ).

During the main sequence (MS), red-giant branch (RGB) and core helium burning stages, the mass-loss due to stellar winds follows the rate based on the Reimers formula (see Reimers (1975)). The asymptotic giant branch and subsequent evolution follow a rate based on the Bloeker formula instead (see Bloeker (1995)). We set our scale factors to be  $\eta_R = 0.5$  and  $\eta_B = 0.2$  for the Reimers and Bloeker formulae, respectively. These values are chosen as they reproduce a WD with a similar final mass to that found by Renedo et al. (2010) for  $M_i = 1.00 M_{\odot}$  with  $Z_i = 0.01$ . It was made certain that these sequences would reproduce a DA in the final model, such that the outer layer is not removed due to the strength of the stellar winds. A DA is a hydrogen atmosphere WD: a C/O core (in our case) surrounded by a helium envelope which is itself surrounded by a thinner hydrogen

envelope, see Figure 13.

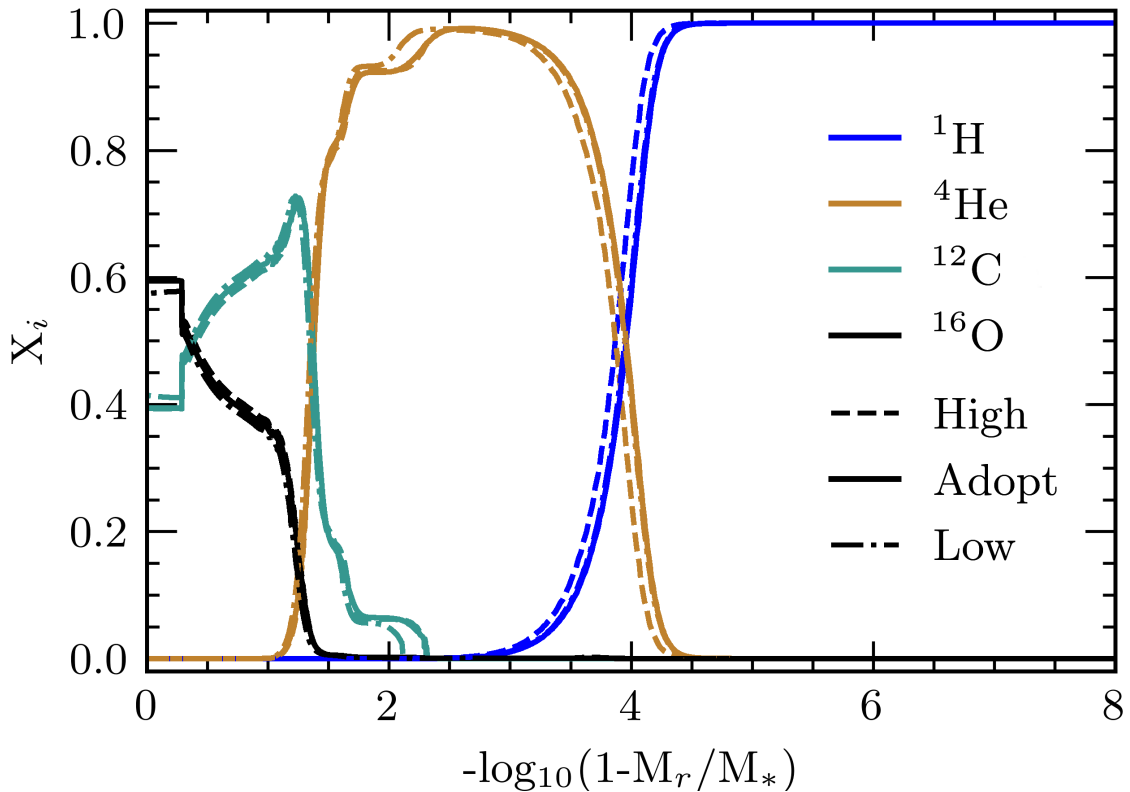


Figure 13 – Chemical profiles for DAs with C/O core. This case shows a hydrogen atmosphere WD with an effective temperature of 20 000K whilst on the final cooling track. The initial conditions of this sequence were  $M_i = 1.30 M_\odot$  and  $Z_i = 0.01$  with the reaction rate prescriptions of An\_H, An\_A and An\_L.

A grey atmosphere is employed for the entire evolution of all sequences, which utilises the grey Eddington  $\tau$  relation. We consider the equations of state ELM EOS and DT2 EOS, which are derived from the HELM EOS [Timmes & Swesty \(2000\)](#) and the SCVH tables [Saumon, Chabrier & van Horn \(1995\)](#), respectively.

Once the star leaves the AGB, we employ an element diffusion process from the work of [Burgers \(1969\)](#). We refer to element diffusion as the physical mechanism for mixing chemicals that includes gravitational settling, thermal diffusion and chemical diffusion. Gravitational settling leads to denser element diffusing towards the core, while lighter elements float towards the surface. Thermal diffusion acts in the same direction as gravitational settling, although to a lesser extent, bringing highly charged and more massive species to the central regions of the star. Chemical diffusion, however, works against this general direction (see [Iben & MacDonald \(1985\)](#), [Thoul, Bahcall & Loeb \(1994\)](#), for details). In addition to the aforementioned processes, MESA includes radiative accelerations ([Hu et al., 2011](#)) into their element diffusion prescription. These radiative forces are negligible in hot regions, as well as being computationally demanding. Hence, we do not consider the effects of radiative levitation. Our element diffusion process is applied to the following elements:  $^1\text{H}$ ,  $^3\text{He}$ ,  $^4\text{He}$ ,  $^{12}\text{C}$ ,  $^{14}\text{N}$ ,  $^{16}\text{O}$ ,  $^{20}\text{Ne}$ ,  $^{24}\text{Mg}$ .

In this work, we have added to the MESA code as well as new parameters that MESA does not contain as a default. The `NACRE_H`, `NACRE_L`, `An_H`, `An_A` and `An_L` reaction rates are not included in MESA thus have to be added within the code (see Sections 2.3.2 and 2.3.3, for details).

### 2.3.2 Implementation of Alternate Reaction Rates

Some estimations for the reaction rate for the  $^{12}\text{C}(\alpha, \gamma)^{16}\text{O}$  reaction are not part of MESA and so must be applied by the user. Firstly, the user must create a separate file which contains the total number of values to be supplied, followed by two columns. The first column contains the values for the desired reaction rate and the second contains corresponding values of temperature,  $T$ . The temperature values must be of the form  $T_8$ , where  $T_8 = T/10^8$ . The user can use this new rate by using the `'rate_tables_dir'` command where its value is the location of the created file.

### 2.3.3 Added subroutines

As discussed in Section 2.2.2, breathing pulses are considered to be a numerical problem rather than a physical one. We therefore suppress them. To do this, we follow the same prescription as [Romero, Campos & Kepler \(2015\)](#). In order to do this, we turn off overshooting during the CHB whilst the central helium abundance lies within the range of  $10^{-6} \leq X_{\text{He}} \leq 0.13$ . This inhibits the mixing of fresh hydrogen into the core at late-times during the CHB which can lead to a convective runaway. Without this prescription we find large rapid changes within the final core C/O ratio ( $\pm 0.1$ ) within small changes of initial mass ( $0.05 M_{\odot}$ ).

We force the rehomogenisation of the C/O core during the WD cooling sequence. This allows us to find a constant, mass-averaged value, for the elements within in this region. This is important for the asteroseismology which may be performed in the future. To do this, we first find the cell where the C/O core starts from iterating through each cell from the surface. As the mass fraction of oxygen increases as we move to the edge of the C/O core from the centre, we find the edge of the C/O by finding the first cell in which the oxygen abundance is greater than the central oxygen abundance. We then apply the cell mass-average for the cells that represent the C/O core of each element in the net that we use. This returns the weighted average values of each element while keeping the sum of all element mass-fractions the same, before and after applying the rehomogenisation.

During this programme, a different formulation for  $\alpha_{\text{MLT}}$  was experimented upon some sequences. This was implemented by creating a subroutine called `'other_alpha_MLT'`. This formula was used in an attempt to fix a problem of convection within the envelopes of a star on the RGB where in some cases a constant value of  $\alpha_{\text{MLT}}$  was not sufficient. The

formula used was taken from [Tayar et al. \(2017\)](#) and is given as,

$$\alpha_{\text{MLT}} = 0.162[\text{Fe}/\text{H}] + 1.90, \quad (2.10)$$

where  $[\text{Fe}/\text{H}]$  is the metallicity and is equal to  $\log_{10} \left( \frac{Z/X}{Z_{\odot}/X_{\odot}} \right)$ . Equation 2.10 is applicable within the range  $-2.2 \leq [\text{Fe}/\text{H}] \leq +0.6$ . This is because the derivation was produced by observational data. The objects within the data only consisted of metallicities of this range. The subroutine must be called within the main code and also by a command in the controls section of the inlist. This was produced within an older release of MESA, version-r12115. However, no detailed results have been reported as the analysis here is in the preliminary stages. Other works have also highlighted the need for a more general  $\alpha_{\text{MLT}}$  parameter, such as [Spruit \(2015\)](#), [Constantino et al. \(2015\)](#), [Constantino et al. \(2016\)](#), [Constantino, Campbell & Lattanzio \(2017\)](#).

The formula for mass-loss by [Vassiliadis & Wood \(1993\)](#) was implemented in a similar way to that of the alternative  $\alpha_{\text{MLT}}$ . The subroutine was called 'other\_wind\_scheme' and the command to use in the inlist is 'use\_other\_wind\_scheme = .true.'. The mass-loss formula from [Vassiliadis & Wood \(1993\)](#) is a function of pulsation period for AGB-type pulsators (such as Mira variables and OH/IR stars, see [Goldreich & Scoville \(1976\)](#), [Goldman et al. \(2018\)](#), [Ireland et al. \(2004\)](#), [Battinelli & Demers \(2014\)](#), [Glass & Evans \(1981\)](#) for discussions on these topics), which is itself a function of mass and radius. [Vassiliadis & Wood \(1993\)](#) provide two separate formulas for different mass ranges  $M \leq 2.5M_{\odot}$  and  $M > 2.5M_{\odot}$ . Thus far we have only tested this for initial masses up to  $M_i = 2.00M_{\odot}$ . Therefore only the first formula is considered. This mass-loss prescription is as follows,

$$\log \dot{M}(M_{\odot}\text{yr}^{-1}) = -11.4 + 0.0123 P(\text{days}), \quad (2.11)$$

with,

$$\log P(\text{days}) = -2.07 + 1.94 \log R/R_{\odot} - 0.9 \log M/M_{\odot}, \quad (2.12)$$

where  $P$  is the pulsation period,  $R$  is the radius and  $M$  is the stellar mass. Although the analysis is in the early stages, it is found that the helium core and final mass at the end of the AGB and the WD, respectively, is larger if the mass-loss formula provided by [Vassiliadis & Wood \(1993\)](#) is considered, rather than [Bloeker \(1995\)](#). This implementation was made in version-r12115 of MESA.

## 2.4 Additional Models

The original models with the physics described in Section 2.3.1 are valid for stellar interiors, particularly the core. However, we found no M-star to C-star transitions during the TP-AGB for progenitor masses that are expected to make this transition ([Herwig et al., 1997](#); [Karakas; Lattanzio; Pols, 2002](#); [Weiss; Ferguson, 2009](#); [Romero; Campos; Kepler, 2015](#);

Marigo et al., 2020). Upon inspection it was found that the third dredge-up was not occurring, preventing carbon from being dredged-up from the interior to the surface. Once we revisited the inlist, we found that overshooting only occurred at the helium core mass convective boundary and not the at the semi-convective boundary of the He-exhausted core.

Figure 14 shows the Kippenhahn diagram for the case of  $M_i = 3.05 M_\odot$  during the TP-AGB in the original NACRE\_A models. We represent the mass co-ordinate on the first y-axis and the surface C/O ratio on the second y-axis. Both values are plotted against the age of the sequence. As stated, these original models did not consider convective overshooting around the border of the He-exhausted core. Green slashed areas show convective regions, red back slashed areas represent semi-convective regions and the purple regions are where overshooting occurs. The purple dotted line shows the history of the He-exhausted core mass and the blue dotted line represents the history of the helium core mass. The colour bar measures the energy generation rate from nuclear reactions. The solid orange line represents the C/O ratio at the surface. It can be seen that the overshooting occurs close to the envelope boundary and there is no overshooting about the semi-convective region of the He-exhausted core. As a result of this, we do not observe TDU episodes in the original models. We can be sure that there are no TDU episodes because of the lack of change in helium core mass and that the surface C/O ratio remains constant, which would change if TDUs were experienced (Frost; Lattanzio, 1996; Herwig et al., 1999; Karakas; Lattanzio; Pols, 2002; Weiss; Ferguson, 2009; Romero; Campos; Kepler, 2015; De Gerónimo et al., 2017; Marigo et al., 2020).

In these additional models, we changed the inlist such that convective overshooting was allowed to occur across all convective boundaries. Figure 15 shows the same as Figure 14 but allows for convective overshooting at each convective boundary. We find that, with the new prescription, convection and overshooting extends throughout the helium buffer. For this reason material can be “dredged-up” from the core to the surface. This results in the helium core mass and He-exhausted core masses changing with each convective episode - an outcome of TDU episodes (Frost; Lattanzio, 1996; Herwig et al., 1999; Karakas; Lattanzio; Pols, 2002; Weiss; Ferguson, 2009; Romero; Campos; Kepler, 2015; De Gerónimo et al., 2017; Marigo et al., 2020). Furthermore, we find an increase in the surface C/O ratio with each TDU as material travels from the stellar interior to the surface. The surface C/O ratio, however, remains less than 1. This indicates a larger overshooting parameter is required for M-star to C-star transitions.

A further discussion of these results will be made in Section 3.2.

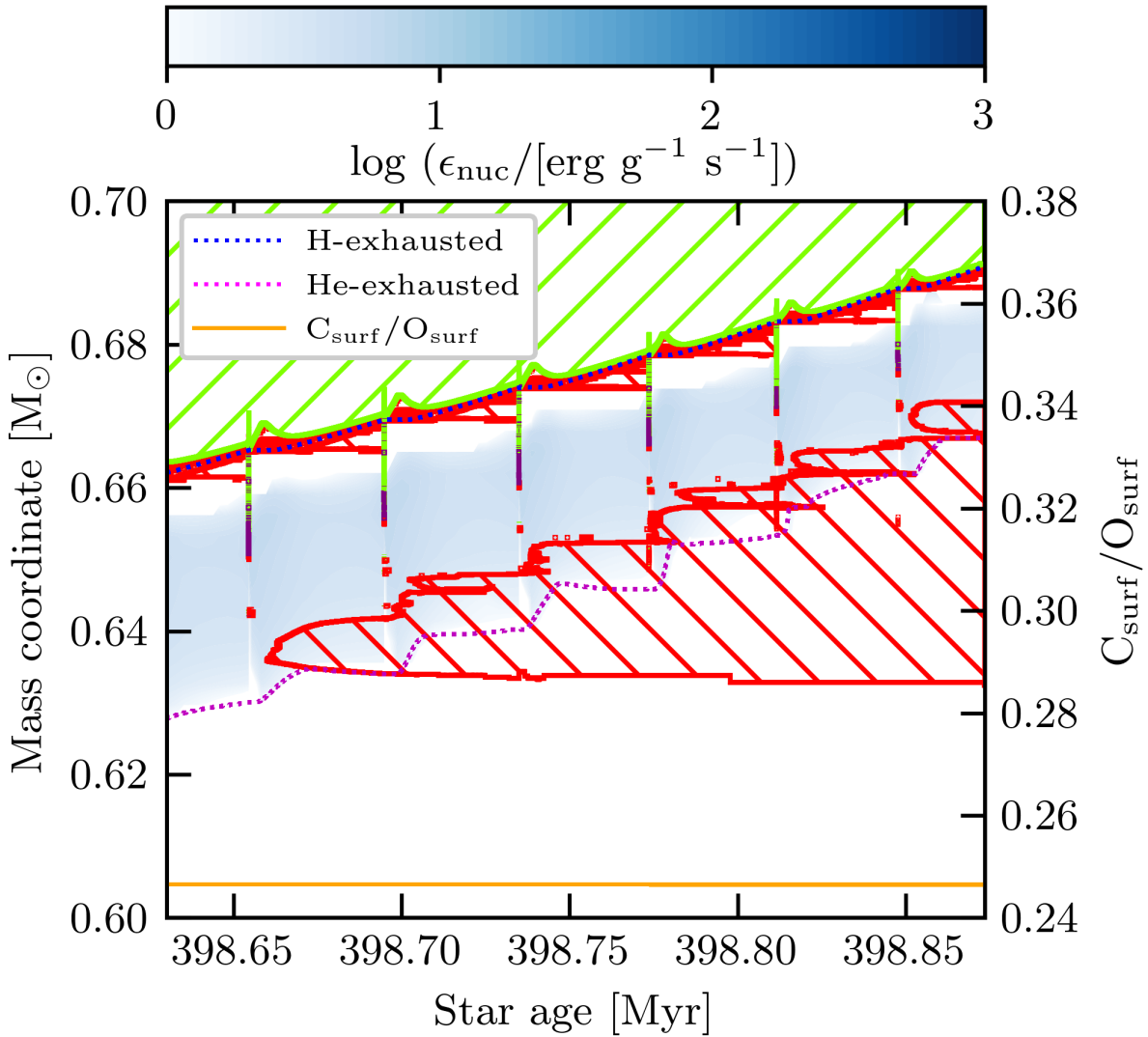


Figure 14 – Kippenhahn diagram for during the Thermally Pulsing-Asymptotic Giant Branch for the case of  $M_i = 3.05 M_{\odot}$  of the original models. We represent the mass co-ordinate on the first y-axis and the surface C/O ratio on the second y-axis. Both values are plotted against the age of the sequence. This model did not consider convective overshooting at boundary of the He-exhausted core which inhibited the Third Dredge-Up episodes. The colour bar measures the energy generation rate from nuclear reactions. The blue dotted line represents the helium core mass while the purple dotted line represents the He-exhausted core. Green slashed regions show convection and the red back slashed regions represent where regions of the star are semi-convective. Finally, purple areas are where overshooting occurs.



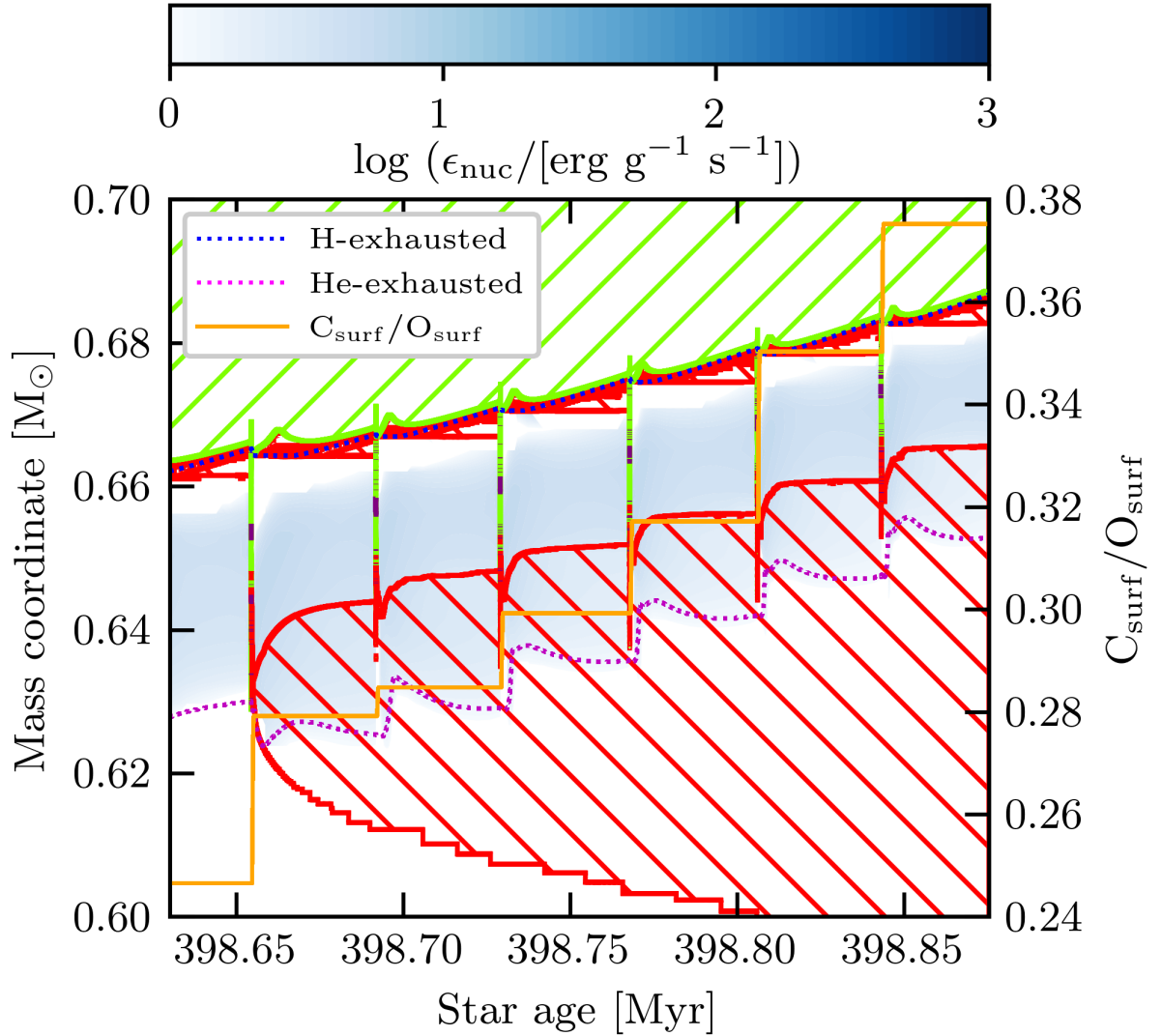


Figure 15 – Kippenhahn diagram for during the Thermally Pulsing-Asymptotic Giant Branch for the case of  $M_i = 3.05 M_{\odot}$  of the new models. We represent the mass co-ordinate on the first y-axis and the surface C/O ratio on the second y-axis. Both values are plotted against the age of the sequence. The colour bar measures the energy generation rate from nuclear reactions. This model considered convective overshooting at all convective boundaries, allowing for Third Dredge-Up episodes to occur. The blue dotted line represents the helium core mass while the purple dotted line represents the He-exhausted core. Green slashed regions show convection and the red back slashed regions represent where regions of the star are semi-convective. Finally, purple areas are where overshooting occurs.



## 3 The Impact of the $^{12}\text{C}(\alpha, \gamma)^{16}\text{O}$ Reaction Rate on Stellar Evolution

Below are the reported results from the outcome of this course. The effects of  $^{12}\text{C}(\alpha, \gamma)^{16}\text{O}$  reaction rate uncertainties across all stages of single stellar evolution for initial masses in the range  $0.90 \leq M_i/M_\odot \leq 3.05$  are presented. The results for each stage are presented in separate stages, chronologically. As expected, during the pre-main sequence, main sequence (MS) and red-giant branch (RGB), we find no differences to the evolution since the  $^{12}\text{C}(\alpha, \gamma)^{16}\text{O}$  reaction only becomes important, and increasingly more dominant, during the CHB as the central helium abundance decreases (Salaris; Cassisi, 2005; Spruit, 2015; Deboer; Brune; Wiescher, 2019). Thus, we report no difference between the different  $^{12}\text{C}(\alpha, \gamma)^{16}\text{O}$  reaction rates at the time of, or shortly after, the helium-flash or a non-degenerate helium ignition. We show the results from the CHB, AGB and WD stages where we expect some differences to occur due to the uncertainties and separate literature sources of the  $^{12}\text{C}(\alpha, \gamma)^{16}\text{O}$  reaction rate.

### 3.1 The Core Helium Burning Phase

During the core helium burning stage, the luminosity is provided by two nuclear sources, the central helium burning and the hydrogen shell-burning. In the core, helium is burnt into carbon via the  $3\alpha$  process, where three  $\alpha$  particles combine to form a carbon nucleus (Salpeter, 1952a; Kippenhahn; Weigert, 1990; Prialnik, 2009). Once the abundance of carbon is sufficiently large, the  $^{12}\text{C}(\alpha, \gamma)^{16}\text{O}$  reaction starts to consume carbon, increasing the oxygen abundance. Thus, the efficiency of the  $^{12}\text{C}(\alpha, \gamma)^{16}\text{O}$  reaction is crucial to determine the final core composition.

#### 3.1.1 Central C/O Ratio

Figure 16 shows the carbon-to-oxygen (C/O) ratio for each star at the end of CHB, as a function of initial mass. As expected due to the large uncertainties of the reaction rate from NACRE, the smallest and largest C/O ratios come from the NACRE\_H and NACRE\_L rates, respectively. Note that when all reaction rates from An et al. (2016) are considered, the values for the C/O ratios are between the values corresponding to NACRE\_A and NACRE\_L.

We find that the C/O ratio at the end of the CHB decreases for all considered reaction rates around an initial mass of  $M_i = 1.90 M_\odot$ . This mass corresponds to the

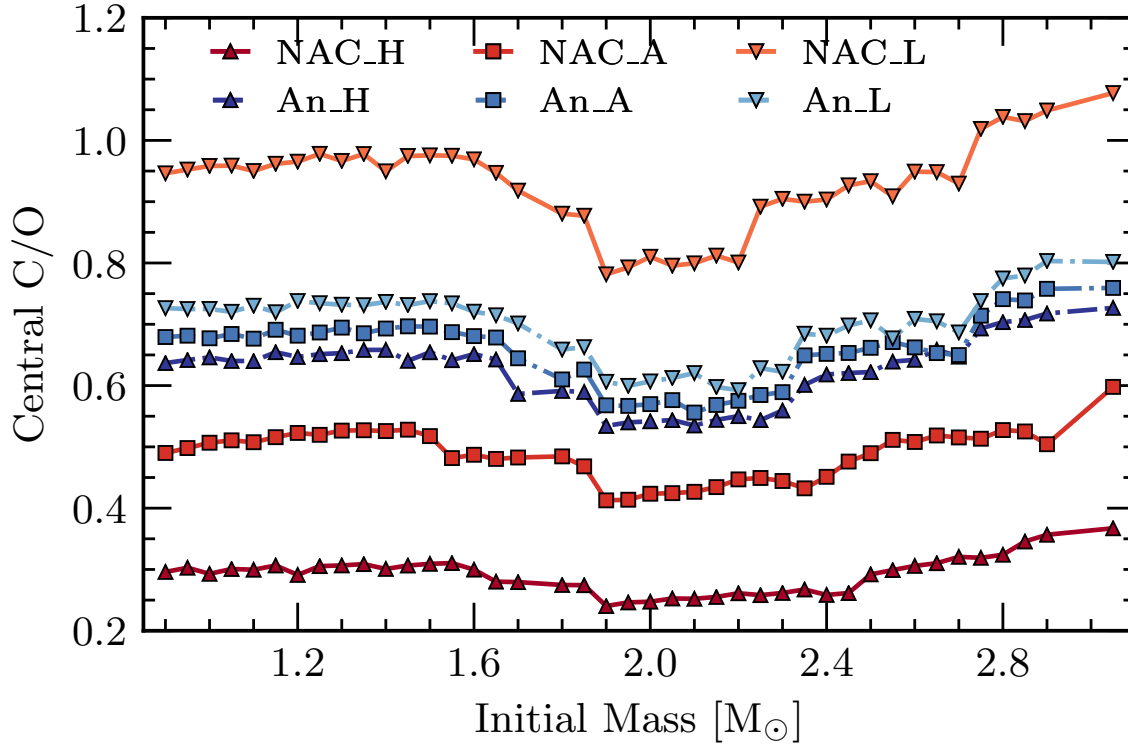


Figure 16 – Central C/O ratio at the end of the CHB as a function of initial mass. The red points represent the reaction rates considered by NACRE and the blue points are those considered by [An et al. \(2016\)](#). Additionally, squares represent the respective adopted rates while darker-coloured triangles and lighter-coloured upside-down triangles represent the high and low limit uncertainties, respectively.

minimum mass for which helium burning starts in non-degenerate conditions, and will be referred to as the transition mass. The C/O ratio increases again for higher initial masses (between  $2.20 \leq M_i/M_\odot \leq 2.45$ ). This phenomenon is also found in other works such as [Salaris et al. \(1997\)](#), [Romero, Campos & Kepler \(2015\)](#). We find that the initial mass where the increase of the C/O ratio occurs is dependent on the considered  $^{12}\text{C}(\alpha, \gamma)^{16}\text{O}$  reaction rate, such that higher reaction rates have a wider initial mass range for the decreased C/O ratio and lower reaction rates have a narrower initial mass range. For example, the NACRE\_H has the widest range ( $1.90 \leq M_i/M_\odot \leq 2.45$ ) whereas the NACRE\_L has the narrowest range ( $1.90 \leq M_i/M_\odot \leq 2.20$ ). Furthermore, we find no difference to the initial mass range between the adopted rate from [An et al. \(2016\)](#) and the An\_H and An\_L rates. We also add that the decrease in the C/O ratio is more pronounced for less efficient reaction rates, see [Figure 16](#), for details.

### 3.1.2 CHB Lifetime

[Figure 17](#) shows the time spent in the CHB as a function of initial mass for the High and Low reaction rate formulas for NACRE (left panel) and [An et al. \(2016\)](#) (right panel). We consider the difference in the CHB age from the values obtained using the

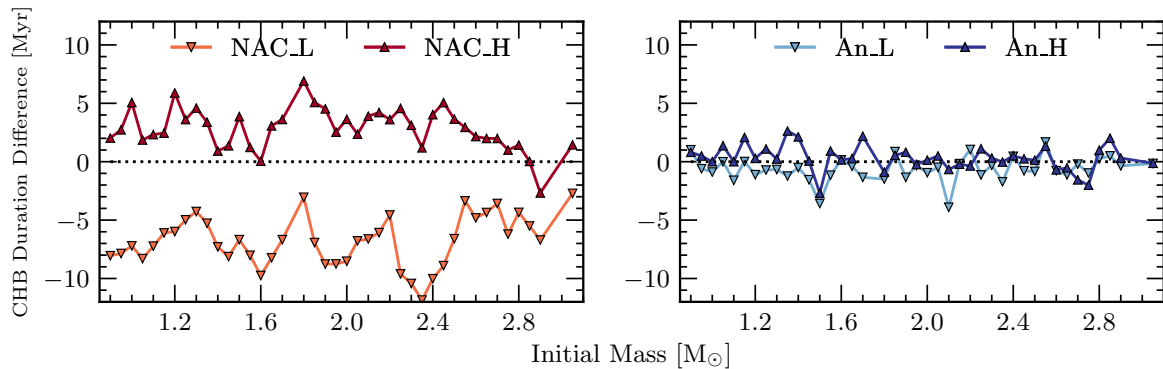


Figure 17 – Differences to the duration of the CHB stage due to associated reaction rate uncertainties as a function of initial mass. The differences are calculated between each limit of the reaction rate due to their uncertainties and the adopted rate of each case. The left panel shows the differences of the uncertainties of the rate calculated by NACRE and the right panel shows the same from the rate of An et al. (2016). Darker-coloured triangles and lighter-coloured upside-down triangles represent the high and low limit uncertainties, respectively.

respective adopted reaction rate for each panel. Considering the NACRE rates (left panel of Figure 17), we find that the CHB lifetime can be up to 12 Myr shorter (longer) from the adopted rate if we consider the NACRE\_L (NACRE\_H) reaction rate, which is roughly a 7% difference. On the other hand the differences between the An et al. (2016) rates are much lower (right panel of Figure 17), up to 4 Myr translating to a difference of 4%. In particular, Constantino et al. (2016) found that the difference in the ratio of HB-to-AGB stars in a sample of 48 globular clusters could be explained by the differences in the CHB duration due to the uncertainties in the  $^{12}\text{C}(\alpha, \gamma)^{16}\text{O}$  reaction rate.

### 3.1.3 Convective Mixing Episodes during the CHB

The top panel of Figure 18 shows the CHB history of the convective mass. The convective mass is defined as the mass-coordinate of the core convective boundary, such that convection occurs between this mass-coordinate and the centre. Additionally, the bottom panel of Figure 18 shows the luminosities of the  $3\alpha$  process and the  $^{12}\text{C}(\alpha, \gamma)^{16}\text{O}$  reaction (the latter will be referred to as  $\text{C}\alpha$  luminosity), for the NACRE reaction rates. As expected, the  $\text{C}\alpha$  luminosity increases when the more efficient reaction rates are considered. Furthermore, the contribution from the  $3\alpha$  process decreases for higher reaction rates due to the helium reservoir being depleted faster by the more efficient  $^{12}\text{C}(\alpha, \gamma)^{16}\text{O}$  reaction.

Mixing episodes due to the convective core during the CHB extends from the C/O core to the He-rich layers above, so we define the convective mass as the mass of the convective core. Figure 18 also shows that higher reaction rates produce more mixing episodes which are characterised by sudden increases of the convective mass. These enhanced convective episodes bring fresh helium from the helium region above the C/O

core which not only increases the duration of the CHB but also increases the abundance of oxygen in the core (Ghasemi et al., 2017; Guo; Li, 2018).

Convective mixing episodes induce a chemical discontinuity between the fully mixed core and the radiative layer, increasing the opacity beyond the convective boundary. In a class of CHB pulsating stars, sdB stars (see Heber (2009), for an in depth discussion), g-modes propagate from the surface all the way until the boundary of the convective core (Ghasemi et al., 2017). Since we find significant differences to the size of the convective core and number of mixing episodes between the NACRE adopted reaction rate and its uncertainties for the  $^{12}\text{C}(\alpha, \gamma)^{16}\text{O}$  reaction rate, the precision of asteroseismology for these objects is limited and must be considered in the calculations of the pulsation period spectrum. However for the adopted rate taken from An et al. (2016), the high and low limits (An\_H and An\_L, respectively) do not produce a significant change to the convective core mass and the total number of mixing episodes and would therefore produce a more precise study of the g-mode pulsations, see Figure 19 for an example of the convective mixing episodes which consider the reaction rates from An et al. (2016). The implications for asteroseismology from the treatment to mixing during the CHB has been studied by Constantino et al. (2015) who found that changes to the composition and He-burning reaction rates do not significantly change the period spacing of pulsations for pulsators during the CHB stage. However, the period values could be more sensitive to the changes in the chemical profile.

### 3.1.4 The Effect of the $\text{C}\alpha$ Luminosity

The total energy produced by the  $^{12}\text{C}(\alpha, \gamma)^{16}\text{O}$  reaction during the CHB is presented in Figure 20. The values shown in Figure 20 are moving averages. We compute the total energy by integrating the  $\text{C}\alpha$  luminosity with respect to time for the CHB duration. Figure 20 shows the ratio between the different reaction rates and the NACRE\_A (top panel) and An\_A (bottom panel) reaction rates, as a function of initial mass. If we consider the reaction rates from An et al. (2016), the differences are generally smaller than 10%, the largest difference occurs for the sequence with an initial mass of  $2.85 M_{\odot}$  that considers An\_H. In most cases, the differences are no larger than 5% (70.7% of the sequences for An\_H and 82.9% of the sequences for An\_L).

We find larger differences between the limits of  $^{12}\text{C}(\alpha, \gamma)^{16}\text{O}$  NACRE rates when compared to the NACRE\_A formula, as shown in the top panel of Figure 20. In this case we also compare the adopted reaction rate from An et al. (2016). If we consider how NACRE\_H differs from NACRE\_A, we find that the energy production for the majority of the sequences are greater than 10% than that of the NACRE\_A case, with a few exceeding a difference of 20%. For NACRE\_L, the carbon energy produced differs more than 30% from the NACRE\_A rate. The extra energy produced from the high rates when compared

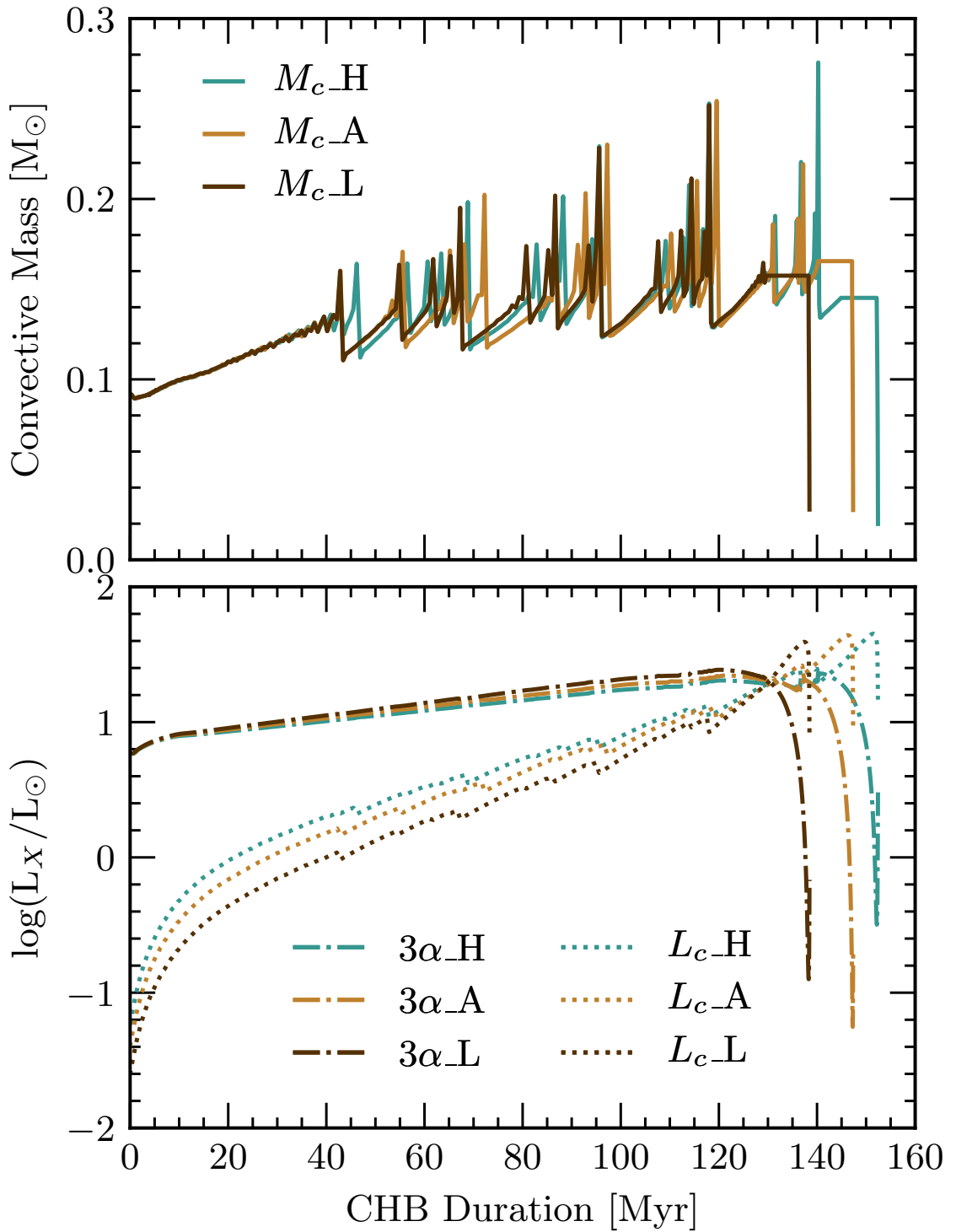


Figure 18 – History of the convective mass (top panel),  $3\alpha$  luminosity and the luminosity of the  $^{12}\text{C}(\alpha, \gamma)^{16}\text{O}$  reaction during the CHB (bottom panel). The history is given in terms of the CHB duration. This plot in particular considers all NACRE prescriptions for the  $^{12}\text{C}(\alpha, \gamma)^{16}\text{O}$  reaction rate for an initial mass of  $M_i = 2.45 M_{\odot}$ . Blue lines represent NACRE\_H, orange-brown depicts NACRE\_A and dark-brown shows NACRE\_L. Furthermore, the solid line represents the convective mass, dotted lines show the luminosity of the  $^{12}\text{C}(\alpha, \gamma)^{16}\text{O}$  reaction and dot-dash lines portray the  $3\alpha$  luminosity.

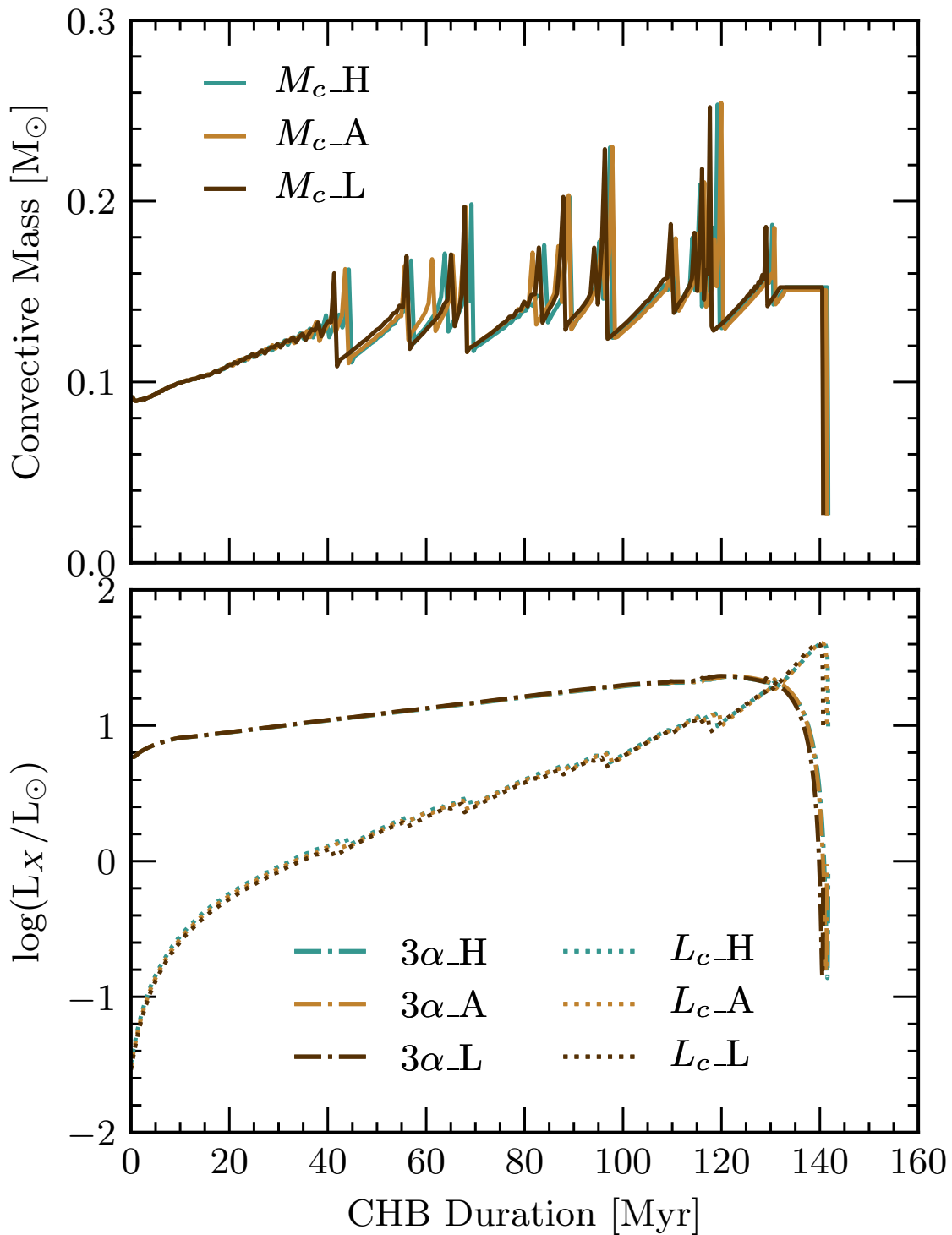


Figure 19 – History of the convective mass (top panel),  $3\alpha$  luminosity and the luminosity of the  $^{12}\text{C}(\alpha, \gamma)^{16}\text{O}$  reaction during the CHB (bottom panel). The history is given in terms of the CHB duration. This plot in particular considers all [An et al. \(2016\)](#) prescriptions for the  $^{12}\text{C}(\alpha, \gamma)^{16}\text{O}$  reaction rate for an initial mass of  $M_i = 2.45 M_{\odot}$ . Blue lines represent An\_H, orange-brown depicts An\_A and dark-brown shows An\_L. Furthermore, the solid line represents the convective mass, dotted lines show the luminosity of the  $^{12}\text{C}(\alpha, \gamma)^{16}\text{O}$  reaction and dot-dash lines portray the  $3\alpha$  luminosity.



to the adopted rates increases the temperature gradient further allowing convection to continue, causing the extra mixing episodes shown in Figure 18 (Kippenhahn; Weigert, 1990; Prialnik, 2009).

Considering the adopted rate from An et al. (2016), the absolute value of the differences in carbon energy produced due to An\_H and An\_L appears to be independent of either selection. This is not the case for the NACRE rates. A limiting factor for the amount of energy produced is the abundance of available helium. This is more of a limit for the NACRE\_H case due to lack of available helium inhibiting further reactions to occur. The NACRE\_L will always produce less carbon energy and so is not limited by the helium abundance or lack thereof. The smaller uncertainties of the rates taken from An et al. (2016) are not large enough to produce such an effect.

The CHB stage is where the  $^{12}\text{C}(\alpha, \gamma)^{16}\text{O}$  reaction is the most active. In particular, we find that the largest differences due to the considered  $^{12}\text{C}(\alpha, \gamma)^{16}\text{O}$  reaction rate appear in the final C/O ratio, CHB duration, energy generation rate and the number of experienced mixing episodes. The primary reason that we find such changes to these properties is due to the changes in energy generation that affect the convection efficiency in this phase. Furthermore, we find that the differences between the An\_H and An\_L rates from the An\_A rate are generally insignificant, unlike those of the NACRE uncertainties which are intrinsically larger. A final point to add is that, in future works, the use of overshooting parameters specifically designed for the CHB would be interesting. Works such as Spruit (2015) claim to keep the convective boundaries stable inhibiting the need for manual breathing pulse suppression, as performed in this work, whilst keeping “stable” convection active throughout the evolution (Spruit, 2015; Constantino; Campbell; Lattanzio, 2017).

## 3.2 The Asymptotic Giant Branch Phase

During the AGB the energy production is given by two shell sources, the hydrogen-shell at the base of the hydrogen-rich envelope and the He-shell on top of the C/O core. Hydrogen burning occurs through the CNO cycle, while He-burning is through the  $3\alpha$  process. Towards the end of the AGB, the He-burning shell will become thin enough to trigger unstable burning, and the thermal pulses (TPs) begin (e.g. Kippenhahn & Weigert (1990)). During the interpulse period between the TPs, the outer convection zone may be deep enough to bring the products of He-shell burning to the surface, this is known as the third dredge-up (TDU) (Wallerstein et al., 1997; Busso; Gallino; Wasserburg, 1999; Herwig, 2005; Karakas; Lattanzio, 2014).

Well known consequences of TDUs are a reduction of the helium core mass and changes to the surface composition, leading to the formation of C-stars (Frost; Lattanzio, 1996; Busso; Gallino; Wasserburg, 1999; Karakas; Lattanzio; Pols, 2002; Cristallo et al.,

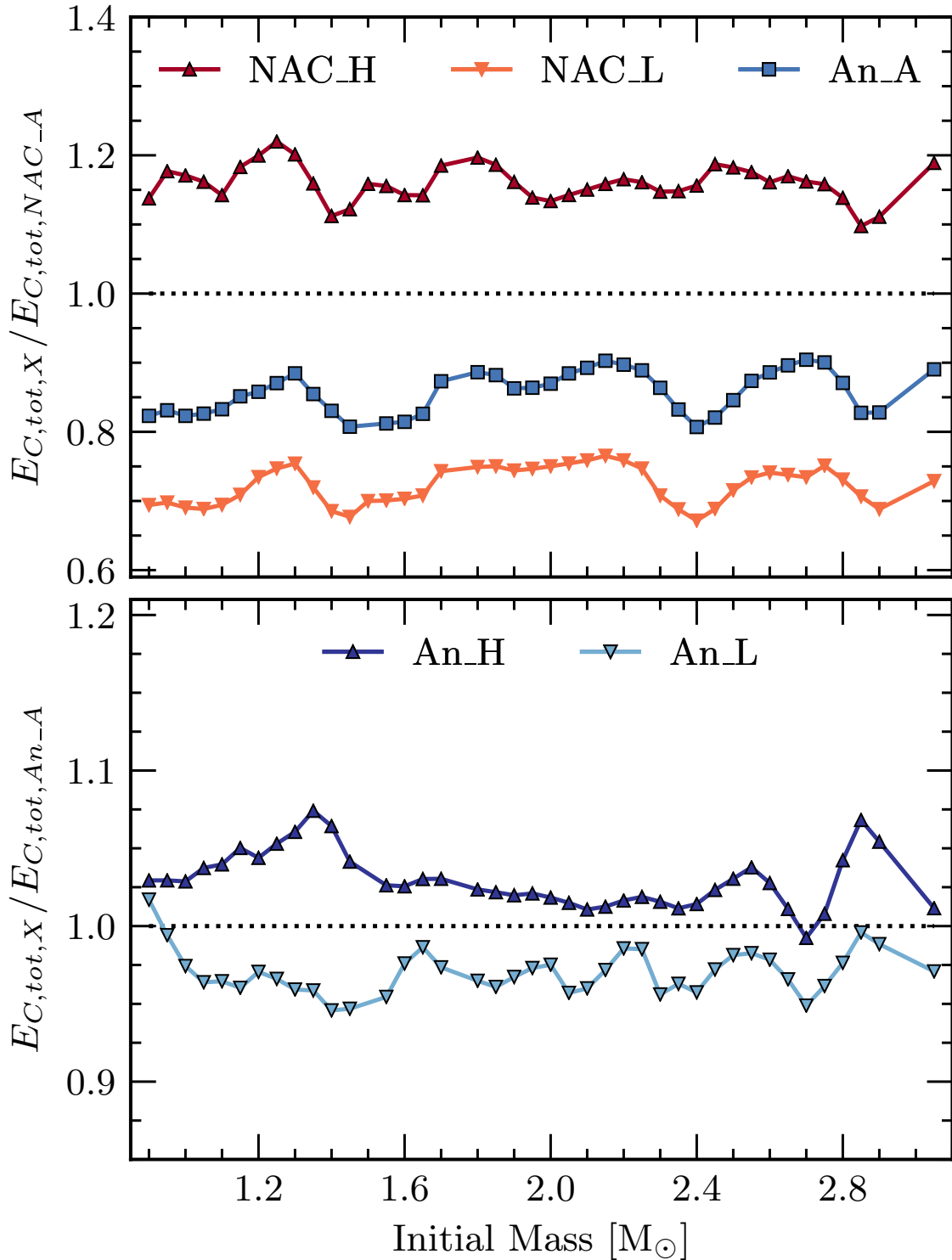


Figure 20 – Ratios of the total energy produced by the  $^{12}\text{C}(\alpha, \gamma)^{16}\text{O}$  reaction as a function of initial mass. Values are presented in the form of moving averages. The energy produced is calculated by integrating the  $\text{C}\alpha$  luminosity shown in Figure 18 and is integrated with respect to time. The ratios in the top panel are in terms of the NACRE\_A rate and the ratios in the bottom panel are made in terms of An\_A. The red points represent the reaction rates considered by NACRE and the blue points are those considered by An et al. (2016). Additionally, squares represent the respective adopted rates while darker-coloured triangles and lighter-coloured upside-down triangles represent the high and low limit uncertainties, respectively.

2009; Weiss; Ferguson, 2009; Ventura; Marigo, 2009; Romero; Campos; Kepler, 2015; Marigo et al., 2020). The extent of the reduction of the helium core mass from TDU episodes is parameterised by the dredge-up efficiency parameter,  $\lambda_d^1$  (see Karakas, Lattanzio & Pols (2002), Marigo et al. (2013), for details). The  $^{12}\text{C}(\alpha, \gamma)^{16}\text{O}$  reaction during this stage is essentially inactive. There may be some fusion reactions between  $^{12}\text{C}$  and alpha particles at the edge of the C/O core but they are, however, insignificant (Wallerstein et al., 1997; Busso; Gallino; Wasserburg, 1999; Herwig, 2005). Thus, any difference between the sequences during the AGB is due to the effect that the  $^{12}\text{C}(\alpha, \gamma)^{16}\text{O}$  reaction rate has during the CHB.

### 3.2.1 Helium Core Mass Growth

Figure 21 shows the helium core mass at the first TP of each sequence as a function of initial mass. A minimum value occurs for an initial mass  $M_i = 1.90 M_\odot$ , which is the transition point as described in Section 3.1. The same result was found in the work of Kalirai, Marigo & Tremblay (2014), whose initial models come from those produced in Bressan et al. (2012). However, their transition point occurs for  $M_i = 2.00 M_\odot$  due to the larger initial metallicity affecting the mass for which core helium burning ignites in degenerate conditions (Bertelli et al., 1986; Romero; Campos; Kepler, 2015). We find that there is no significant difference to the helium core mass at the first TP as a result of different  $^{12}\text{C}(\alpha, \gamma)^{16}\text{O}$  reaction rates for masses lower than the transition point. Above this mass, the maximum difference between the NACRE rates is  $\sim 0.01 M_\odot$ , with NACRE\_L producing lower helium core masses and NACRE\_H producing larger helium core masses. This is due to the difference in energy outputs between the adopted rate, NACRE\_A, and the NACRE\_H/NACRE\_L rates. Higher reaction rates during the CHB increase the temperature throughout the star which favours the CNO-cycle (Boeltzig et al., 2016), allowing the helium core mass to develop further than sequences which consider lower reaction rates. There are no significant differences in the helium core mass at the first TP between the adopted rate from An et al. (2016) and An\_H/An\_L for any of the considered initial masses.

Figure 22 shows the growth of the helium core mass during the TP-AGB as a function of initial mass for each considered reaction rate. We find that the dramatic increase of core growth (for helium core mass growth  $\geq 10\%$  (Kalirai; Marigo; Tremblay, 2014)) occurs in the range  $1.70 \leq M_i/M_\odot \leq 2.60$ , with a maximum increase of 19% occurring at  $M_i \approx 2.00 M_\odot$ . This result is in agreement with that of Bird & Pinsonneault (2011) and is similar to that of Kalirai, Marigo & Tremblay (2014), who find a helium core growth up to 30%. This discrepancy between their work and ours is due to not only a different initial metallicity, but also their consideration of a less efficient mass-loss scheme for stages

<sup>1</sup> The dredge-up efficiency parameter is defined as the fraction of helium core mass lost during the TDU episode over the helium core mass growth since the last TDU

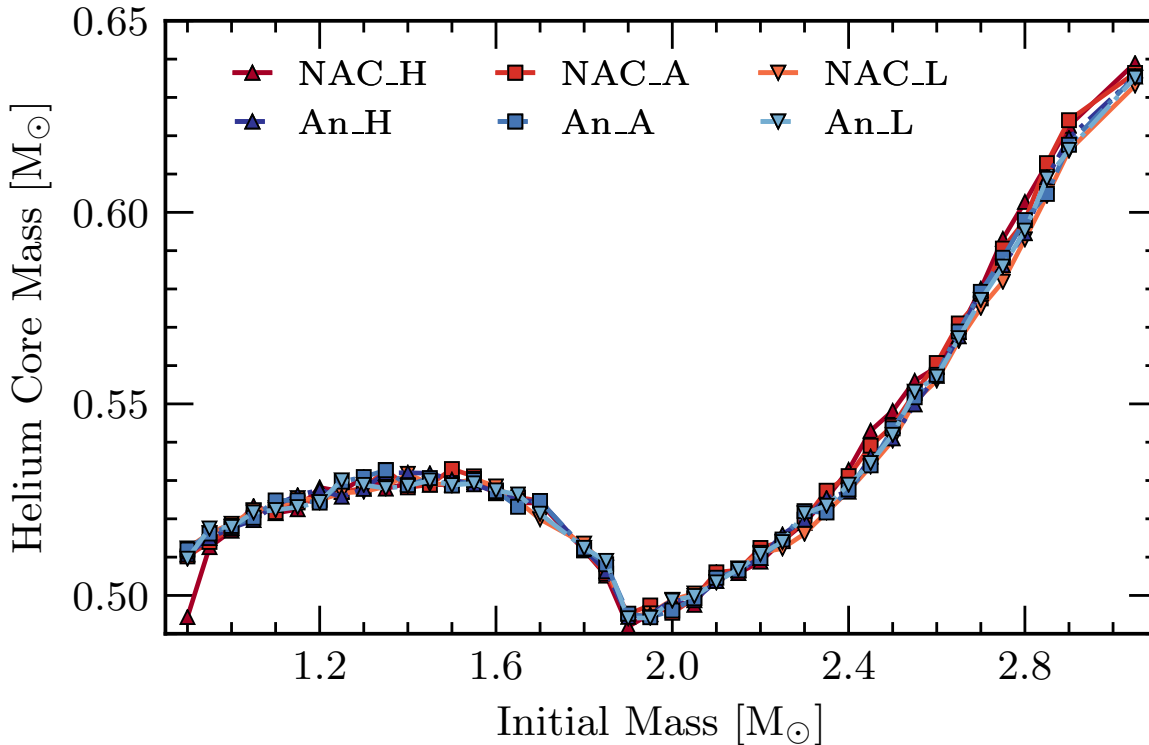


Figure 21 – Helium core mass at the start of the first TP as a function of initial mass. All of the considered reaction rates and their uncertainties are shown within this figure. We find a minimum to the helium core mass for the same initial mass which corresponds to the transition mass where core helium burning begins on a non-degenerate core rather an electron degenerate core ( $M_i = 1.90 M_\odot$ ). Within the uncertainties, we find differences up to  $0.01 M_\odot$  for masses larger than  $M_i = 1.90 M_\odot$ . The red points represent the reaction rates considered by NACRE and the blue points are those from An et al. (2016). Additionally, squares represent the respective adopted rates while darker-coloured triangles and lighter-coloured upside-down triangles represent the high and low limit uncertainties, respectively.

previous to the AGB (Reimers law with  $\eta_R = 0.2$  (Bressan et al., 2012)). Thus, the models used by Kalirai, Marigo & Tremblay (2014) have a larger mass of hydrogen fuel to produce a larger final mass (see Table 1 for our values of this variable and Bird & Pinsonneault (2011) for an in-depth discussion of the hydrogen fuel variable). In addition, Kalirai, Marigo & Tremblay (2014) considered a different mass-loss due to wind scheme that allowed more time spent on the TP-AGB stage, which they show leads to larger core growths. Furthermore, possible differences to the energy produced in the H-rich envelope during the TP-AGB may affect the rate of the helium core growth (see Forestini & Charbonnel (1997), Marigo et al. (2013), Kalirai, Marigo & Tremblay (2014), for details).

Considering only the difference in helium core mass growth for NACRE\_A rate and it's NACRE\_H/NACRE\_L limits, we find that NACRE\_L has a larger core growth and NACRE\_H has smaller core growth. The increased core growth during the AGB for the NACRE\_L sequences is due to the smaller helium core mass at the first TP (see

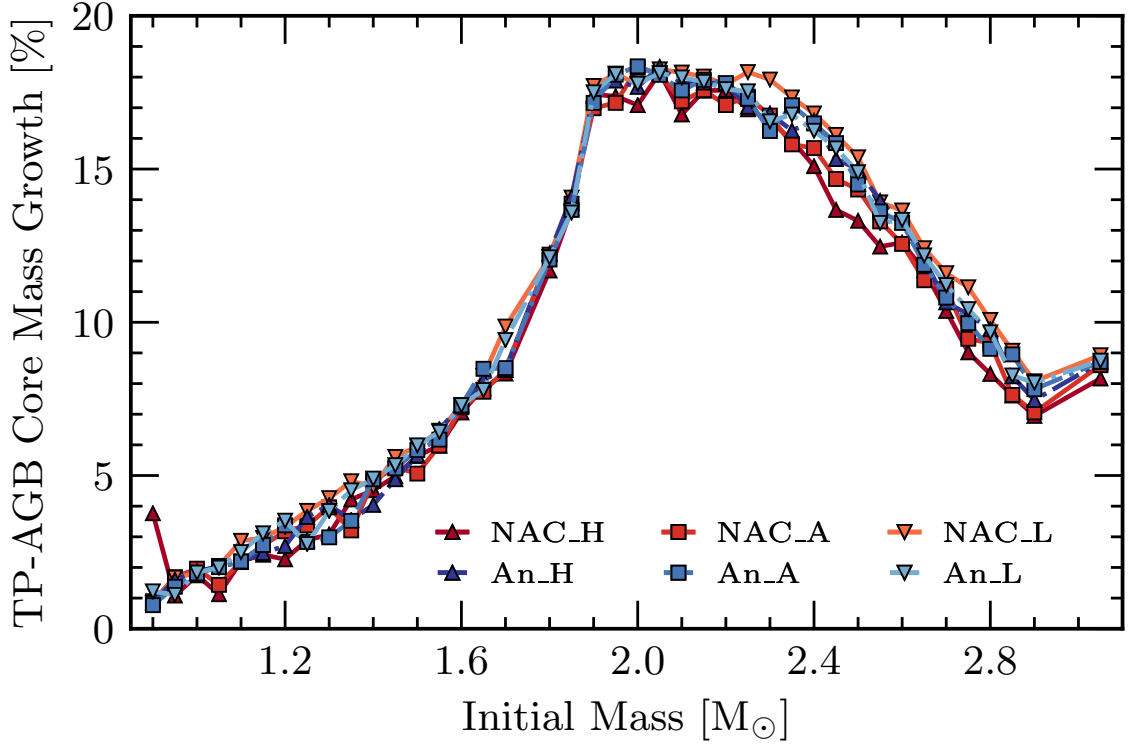


Figure 22 – Percentage growth of the helium core mass during the AGB as a function of initial mass. Growth is calculated as the difference between the final mass of the core and the helium core mass described in Figure 21. We find that the largest growth occurs for initial masses  $\approx 2.0 M_{\odot}$ , peaking at 19%. Above initial masses of  $M_i = 2.90 M_{\odot}$ , it appears that the growth begins to plateau around 8-9%. The red points represent the reaction rates considered by NACRE and the blue points are those from An et al. (2016). Additionally, squares represent the respective adopted rates while darker-coloured triangles and lighter-coloured upside-down triangles represent the high and low limit uncertainties, respectively.

Figure 21) and as such more fuel to keep He-shell burning sustained, particularly for initial masses above the transition point where the core growth differences are greater (see Table 1). Additionally, during the TP-AGB, we find differences in the energy generation from the CNO cycle between the NACRE\_H/NACRE\_L limits in comparison with the NACRE\_A. The energy generation can be up to 25% lower (higher) when the NACRE\_H (NACRE\_L) reaction rate is considered.

### 3.2.2 Thermal Pulses

Figure 23 shows the number of thermal pulses as a function of initial mass for each considered reaction rate. Moreover, it shows that lower reaction rates experience more TPs than higher reaction rates. This is related to the larger amount of available hydrogen to aid the outward growth of the helium core through a greater number of unstable He-shell burning episodes - TPs. We do not find any M-star to C-star transitions (see Marigo et al.

(2020), for example) as convective overshooting about the boundary between the helium core and the He-exhausted core was disregarded during the TP-AGB, inhibiting the TDU (Romero; Campos; Kepler, 2015). However, overshooting still occurred at the boundary of the H-rich core. We define the “He-exhausted core” as the region from the centre until the local abundance of helium is greater than  $10^{-6}$ .

Thermal pulses are strongly dependent on the mass-loss rate, helium core mass and initial metallicity (Gallino et al., 1998; Karakas; Lattanzio; Pols, 2002; Karakas; Lattanzio, 2003; Cristallo et al., 2009; Weiss; Ferguson, 2009; Renedo et al., 2010; Romero; Campos; Kepler, 2015; De Gerónimo et al., 2017). We find that the number of thermal pulses in our computations is lower than that from the works of Weiss & Ferguson (2009), Renedo et al. (2010) and Romero, Campos & Kepler (2015) for a given initial mass, a similar treatment of convection and a similar helium core mass at the beginning of the TP-AGB phase. Difference in the number of TPs could be related to the different mass-loss schemes during the RGB stage. In this work we consider the mass-loss prescription from Bloeker (1995) while the works of Weiss & Ferguson (2009), Renedo et al. (2010) and Romero, Campos & Kepler (2015) the mass-loss scheme considers a “super wind” stage towards the last TPs, making it more efficient (see Vassiliadis & Wood (1993), van Loon et al. (2005), for details). However, the trend in the number of experienced TPs as a function of initial mass obtained in our work agrees with other works (see Weiss & Ferguson (2009), Renedo et al. (2010), Romero, Campos & Kepler (2015)).

### 3.2.3 Third Dredge-Up Episodes

To assess the effect of the TDU during the TP-AGB, we computed additional sequences, allowing convective overshooting to occur at all fully- or semi-convective boundaries, with  $f = 0.016$  (see Section 2.4, for details on its effect). For sequences that consider the NACRE\_A prescription, TDU episodes occur for initial masses larger than  $M_i \geq 2.40 M_{\odot}$ , with the dredge-up efficiency parameter ( $\lambda_d$ ) showing values of  $\lambda_d = 0.033 - 0.124$  that increase with increasing initial mass. The abundance of carbon and oxygen at the surface does increase during each TDU in these additional models, but the C/O is still lower than 1 meaning that our models show an oxygen dominated surface. A higher value of the overshooting parameter may be necessary to produce C-stars (Herwig et al., 1997; Karakas; Lattanzio; Pols, 2002; Weiss; Ferguson, 2009; Romero; Campos; Kepler, 2015; Marigo et al., 2020). On the other hand, the use of thermohaline mixing may have affected our dredge-up efficiency due to the inversions in mean molecular weights that occur (see Stancliffe et al. (2007), Stancliffe & Glebbeek (2008), Stancliffe (2010), for details). For sequences where convective overshooting was considered across all boundaries during the AGB we find a decrease in the final helium core mass up to 0.63%. This value is much lower than the 15% decrease found by Karakas, Lattanzio & Pols (2002), Romero, Campos

$M_i/M_\odot$	$\Delta M_{\text{growth}}/M_\odot$				$M_{\text{fuel}}/M_\odot$			
	NACRE_H	NACRE_A	NACRE_L	An_A	NACRE_H	NACRE_A	NACRE_L	An_A
1.00	0.009	0.010	0.009	0.009	0.007	0.008	0.007	0.008
1.50	0.030	0.027	0.031	0.031	0.024	0.022	0.026	0.025
1.60	0.037	0.038	0.039	0.038	0.030	0.031	0.031	0.031
2.00	0.085	0.091	0.089	0.091	0.069	0.073	0.072	0.073
2.90	0.043	0.044	0.050	0.048	0.035	0.035	0.040	0.039

Table 1 – Values showing the TP-AGB helium core mass growth and fuel mass. We report the values from the following reaction rate considerations: NACRE\_H, NACRE\_A, NACRE\_L and An\_A. We do not report the values from the uncertainties of the rate taken from [An et al. \(2016\)](#) since they are negligible when compared to their adopted rate.

& [Kepler \(2015\)](#).

The sequences that have initial masses  $M_i < 2.40 M_\odot$  do not show any third dredge-up episodes, as such we do not expect any difference to the growth of the helium core or the final mass. For those sequences with initial masses  $M_i \geq 2.40 M_\odot$ , a more detailed study of the convective boundaries during the TP-AGB is required for more thorough analysis of why we find such weak dredge-up efficiency parameters.

In the case of NACRE\_H and NACRE\_L, we find that TDU episodes occur for the same initial mass range as that of the NACRE\_A sequences ( $2.40 \leq M_i/M_\odot \leq 3.05$ ). Additionally, the dredge-up efficiency parameters are also similar to those of the NACRE\_A sequences, with  $\lambda_d = 0.040 - 0.123$ . From the results gathered in this work, we find that the uncertainties of current  $^{12}\text{C}(\alpha, \gamma)^{16}\text{O}$  reaction rates are not significant in modelling the TDU.

The  $^{12}\text{C}(\alpha, \gamma)^{16}\text{O}$  reaction during the AGB is negligible during the TP-AGB. Instead, the main energy source occurs through the  $3\alpha$  reaction series ([Herwig, 2005](#); [Karakas; Lattanzio, 2014](#)). Thus, we do not find any significant change to the peak TP luminosity nor the depth of each TDU, since the changes in core mass at the beginning of the TP-AGB are negligible as a result of the uncertainties of the  $^{12}\text{C}(\alpha, \gamma)^{16}\text{O}$  reaction rate, as shown in Figure 21 (see [Frost & Lattanzio \(1996\)](#), [Wallerstein et al. \(1997\)](#), [Wagenhuber & Groenewegen \(1998\)](#), [Busso, Gallino & Wasserburg \(1999\)](#), [Herwig \(2005\)](#), [Karakas & Lattanzio \(2014\)](#), for details). However, the uncertainties of the overshooting efficiency raises a greater uncertainty in the surface composition during the AGB, as such we leave a detailed discussion for a future work that considers the overshooting efficiency in more detail ([Abia et al., 2002](#); [Herwig, 2005](#); [Cristallo et al., 2009](#); [Ventura; Marigo, 2009](#); [Karakas; Lattanzio, 2014](#)).

The relation of the effects that the  $^{12}\text{C}(\alpha, \gamma)^{16}\text{O}$  reaction rate uncertainties have on the TP-AGB have been discussed. What may be an interesting additional constraint is the study of the composition gradients surrounding central stars of planetary nebulae (CSPN). As discussed, no differences to the TDU episodes regarding the uncertainties

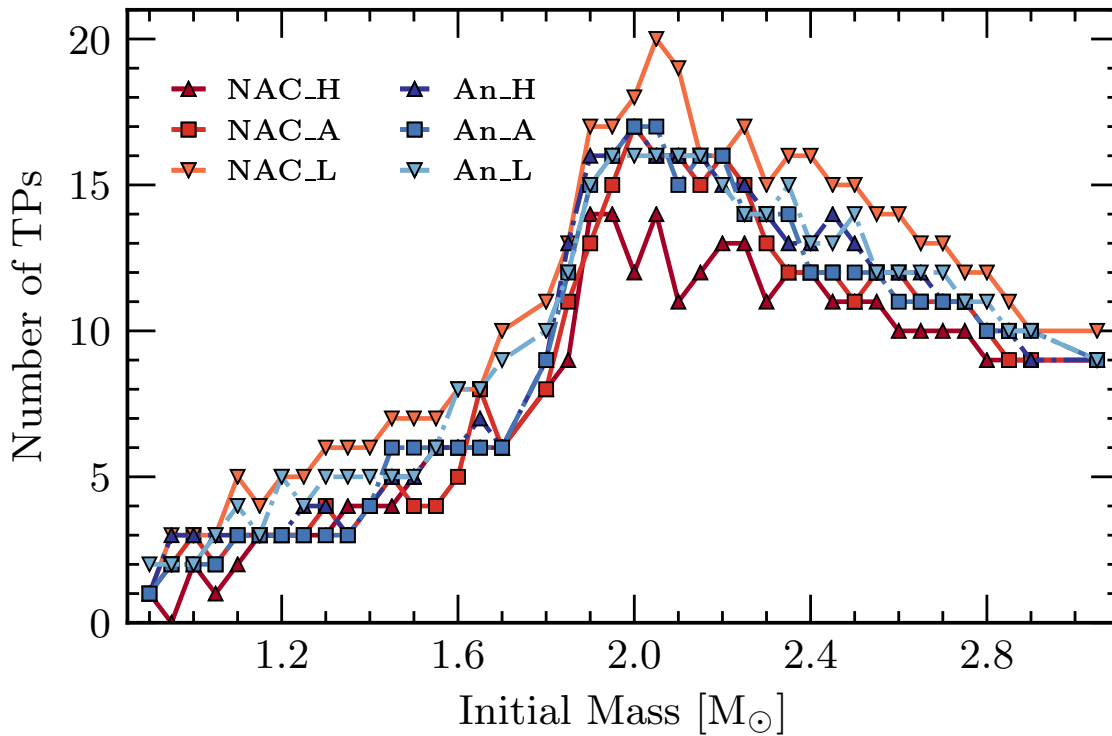


Figure 23 – Number of TPs experienced as a function of initial mass. Each reaction rate consideration and their uncertainties are shown. We find that the number of TPs peaks at initial masses  $\approx 2.00 M_{\odot}$ , in-line with the largest core growth, as in Figure 22. We also show that lower reaction rates for the  $^{12}\text{C}(\alpha, \gamma)^{16}\text{O}$  reaction produce more TPs. The red points represent the reaction rates considered by NACRE and the blue points are those from An et al. (2016). Additionally, squares represent the respective adopted rates while darker-coloured triangles and lighter-coloured upside-down triangles represent the high and low limit uncertainties, respectively.

of the  $^{12}\text{C}(\alpha, \gamma)^{16}\text{O}$  reaction rate were found, nor any transitions from M-star to C-star. This was perhaps due to the AGB mass-loss due to wind scheme considered in this work (Romero; Campos; Kepler, 2015; Marigo et al., 2020). Considering a different mass-loss scheme may allow more time on the TP-AGB allowing differences in the TDU as a result of the  $^{12}\text{C}(\alpha, \gamma)^{16}\text{O}$  reaction rate uncertainties to be observed. Here is where constraining the reaction rate using CSPN may be possible - as comparisons between the evolution of the surface compositions and the composition gradients of the planetary nebula can be made to determine the significance of the uncertainties in addition to their ages (Maciel; Rodrigues; Costa, 2011; Keller; Bianchi; Maciel, 2014).



## 3.3 The White Dwarf Final Cooling Track

### 3.3.1 Initial-to-Final Mass Relation

Figure 24 shows the initial-to-final mass relation (IFMR) for all sequences produced in this work. We find that there is no significant difference in the final mass of any given initial mass due to the  $^{12}\text{C}(\alpha, \gamma)^{16}\text{O}$  reaction rate. Considering the largest difference in the reaction rates, between NACRE\_H and NACRE\_L, the largest difference in the final mass for a given initial mass is less than  $0.01 M_{\odot}$  ( $< 2\%$ ).

In the interest of the pursuit for a global IFMR, we compare our IFMR to those of other works of a similar metallicity. We consider the IFMRs from the works of Weidemann (2000), Salaris et al. (2009) and Renedo et al. (2010). We find a similar trend with the work of Weidemann (2000), both of which consider the same mass-loss scheme from Bloeker (1995) for the AGB phase. The IFMRs from the works of Salaris et al. (2009) and Renedo et al. (2010) consider the mass-loss scheme from Vassiliadis & Wood (1993) for the AGB and show a much steeper gradient in their IFMRs. However, the core masses between this work and the works of Weidemann (2000), Salaris et al. (2009) and Renedo et al. (2010) are similar at the first TP. Thus, it is reasonable to assume that the difference is due to their considered mass-loss scheme for the IFMR determination.

By considering the third-order polynomial nature of the IFMR computed in this work, we fit a function to the NACRE\_A final masses to produce a general relation from the results of this work. This allows for a comparison to other IFMRs as well as other masses to be easily estimated, if desired. The following IFMR reproduces the IFMR of NACRE\_A well, such that the R-square value is  $R^2 = 0.9995$ :

$$M_f = 0.02047M_i^3 - 0.1051M_i^2 + 0.2323M_i + 0.3783M_{\odot} \quad (3.1)$$

where  $M_f$  is the final mass and  $M_i$  is the initial mass. The non-linear relation is due to the non-linear relations of mass-loss, specially those with large dependencies on luminosity such as the scheme from Bloeker (1995) used in the AGB part of the evolution. It would be interesting to see how this holds for observational data as well as its dependency on metallicity - an important dependence as discussed in Romero, Campos & Kepler (2015).

### 3.3.2 Final Age and Cooling Time

In Figure 25 we show, in panel a), the final ages of a WD that has cooled to an effective temperature of  $T_{\text{eff}} = 10\,000\text{K}$  (log scale) as a function of initial mass for all the sequences computed in this work. The differences in the final ages due to the High/Low limits of each considered  $^{12}\text{C}(\alpha, \gamma)^{16}\text{O}$  reaction rate are in general negligible, with variations of the order  $\sim 0.01$  Gyr for both the NACRE and An et al. (2016)  $^{12}\text{C}(\alpha, \gamma)^{16}\text{O}$  reaction

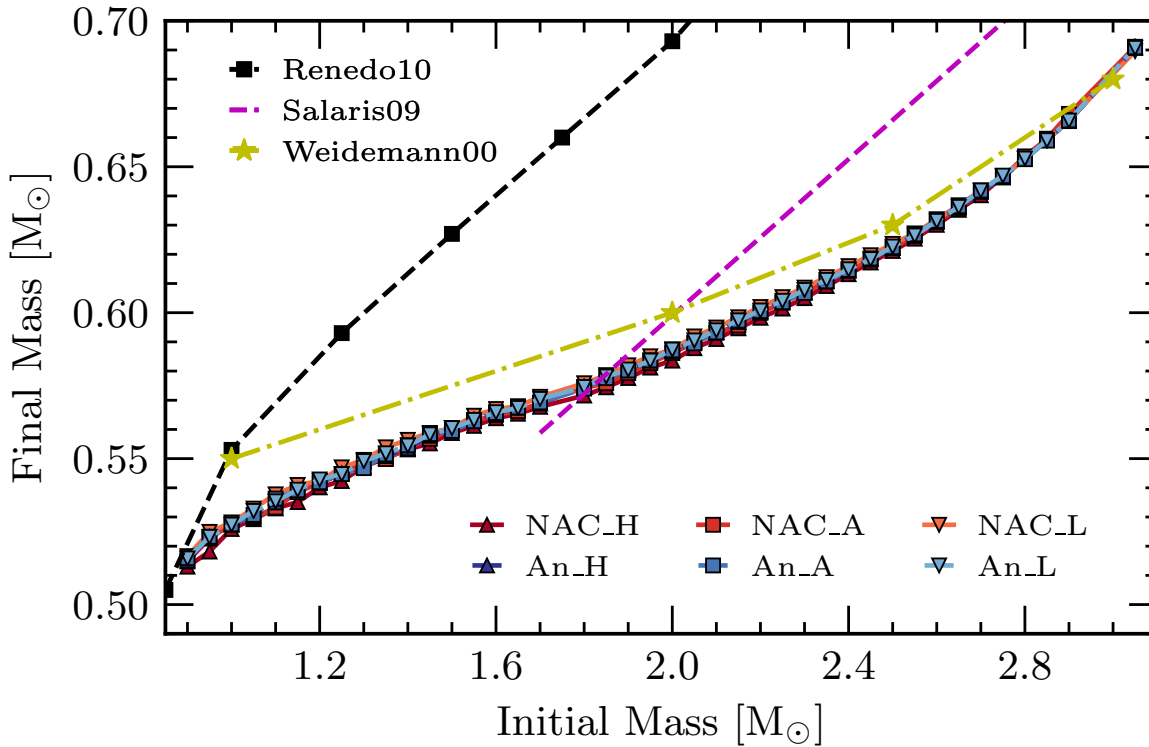


Figure 24 – Initial-to-final mass relation of all sequences calculated as part of this work. Also shown are other IFMRs from the works of Weidemann (2000), Salaris et al. (2009), Renedo et al. (2010) (yellow stars, purple dashed line and black squares, respectively) for a comparison of their trends. The red points represent the reaction rates considered by NACRE, and the blue points are those from An et al. (2016). Additionally, squares represent the respective adopted rates while darker-coloured triangles and lighter-coloured upside-down triangles represent the high and low limit uncertainties, respectively. We find that the slope of the IFMR has a strong dependency on the considered mass-loss scheme considered during the AGB, with the scheme from Vassiliadis & Wood (1993) producing a steeper gradient and that from Bloeker (1995) showing a shallower gradient.

rate. The variations in the reported final ages due to the uncertainties of the  $^{12}\text{C}(\alpha, \gamma)^{16}\text{O}$  reaction rate are a magnitude lower than the populations studied in the works of Hansen et al. (2013), Forbes et al. (2015), Campos et al. (2016). As such, the impact that the  $^{12}\text{C}(\alpha, \gamma)^{16}\text{O}$  reaction rate has on final ages of WD models is currently negligible as compared to the greater uncertainty of ageing stellar populations.

Panels c) and d) of Figure 25 show the moving average for the time spent on the cooling track for the NACRE and An et al. (2016)  $^{12}\text{C}(\alpha, \gamma)^{16}\text{O}$  reaction rates, respectively. We define this quantity as the time taken for a star on the final cooling track to cool from its maximum effective temperature until an effective temperature of  $T_{\text{eff}} = 10\,000\text{K}$ . During the final cooling track, the differences in the duration due to the reaction rates between the Adopted and High/Low limits generally differ up to 0.030 Gyr for those of NACRE and up to 0.015 Gyr for An et al. (2016). The general trend is in agreement with

past discussions of the effect of the  $^{12}\text{C}(\alpha, \gamma)^{16}\text{O}$  reaction rate and cooling time during this stage of evolution, such that more oxygen-rich cores will produce a lower cooling time. This is due to the gravitational energy release during stratification occurring at earlier times for more oxygen-rich cores. As a consequence, the WD is left with a lower thermal content to feed the surface luminosity at later times. The larger the luminosity at which the stratification occurs, the shorter the resulting cooling times will be (D’Antona; Mazzitelli, 1990; Prada Moroni; Straniero, 2002; Salaris et al., 2010). Furthermore, for the High/Low limits of the NACRE rate, we find that NACRE\_L produces a greater absolute difference than that of NACRE\_H. This is due to the availability of helium during the CHB as discussed in Section 3.1.

### 3.3.3 Final Oxygen Abundance

After the settling and diffusion processes described in Section 2.2.2, the final oxygen abundances within the core of the sequences are presented in Figure 26, as a function of initial mass. We find similar trends to the oxygen mass fraction in this stage to those found at the end of the CHB. Although there are slight increases to the oxygen mass fraction due to the aforementioned diffusion processes (Unglaub; Bues, 2000). Additionally, diffusion affects the C/O ratio throughout the star up to the surface and not just in the core (see Herwig (2000), Straniero et al. (2003), for details).

The onset of crystallisation starts when the core cools to a certain temperature,  $T_c$  (Segretain et al., 1994; Horowitz; Schneider; Berry, 2010). This temperature is dependent on the internal composition of the star. Through observations of the globular cluster NGC 6397, Winget et al. (2009) report that the crystallisation of the WD core is similar to that of a pure carbon core. According to the phase diagram produced in Horowitz, Schneider & Berry (2010) and their limits for the maximum crystallisation temperature, this would require a limit to the oxygen mass fraction of  $X_{\text{O}} \leq 0.64$ . This requires that the maximum S-factor at 300 keV has an upper limit of  $S(300 \text{ keV}) \leq 170 \text{ keV b}$ . Considering the relationship between oxygen mass fraction and initial mass presented in Figure 26, we find that NACRE\_H and NACRE\_A produce central oxygen abundances that are too large for a crystallisation process similar to that found by Horowitz, Schneider & Berry (2010). Meanwhile, the rates An et al. (2016) agree not only with the oxygen mass fraction limit presented by Horowitz, Schneider & Berry (2010), but also their derived S-factor for an energy of 300 keV. Thus, we find that sequences dedicated to studying crystallisation using the method presented by Horowitz, Schneider & Berry (2010) should consider a lower reaction rate than that from NACRE for the  $^{12}\text{C}(\alpha, \gamma)^{16}\text{O}$  reaction to keep their analysis consistent with the input physics that they use.

The  $^{12}\text{C}(\alpha, \gamma)^{16}\text{O}$  reaction rates from Metcalfe (2003) that have been inferred from asteroseismology have adopted values similar to that of NACRE, with a reported

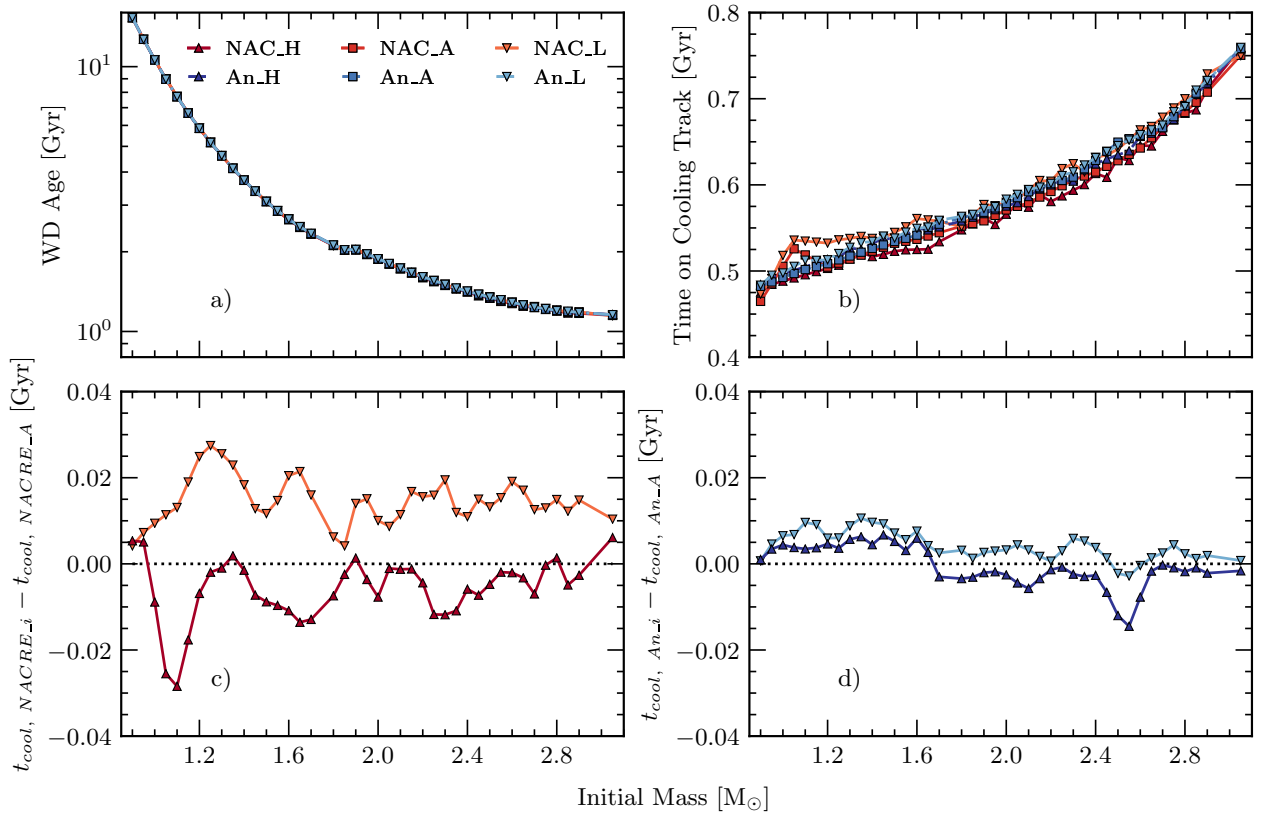


Figure 25 – Panel a) shows the final age (log scale) of the star on the final cooling track with an effective temperature  $T_{\text{eff}} = 10\,000\text{K}$ . Panel b) shows the time spent of the cooling track, defined as the time taken for a WD on the final cooling track to cool from its maximum effective temperature to an effective temperature of  $T_{\text{eff}} = 10\,000\text{K}$ . Panel c) and d) show the moving average for the difference of cooling times between the High/Low limits and the Adopted rate for the NACRE and An et al. (2016)  $^{12}\text{C}(\alpha, \gamma)^{16}\text{O}$  reaction rate, respectively. All panels are represented as functions of initial mass. The NACRE reaction rates are shown as different shades of red and those from An et al. (2016) are depicted by shades of blue. Furthermore, squares represent the respective adopted rates while darker-coloured triangles and lighter-coloured upside-down triangles represent the high and low limit uncertainties, respectively. In general, we find that the uncertainties of the  $^{12}\text{C}(\alpha, \gamma)^{16}\text{O}$  reaction rate have an negligible effect on the final ages of the stars at this point, whereas the cooling time can differ up to 8%.

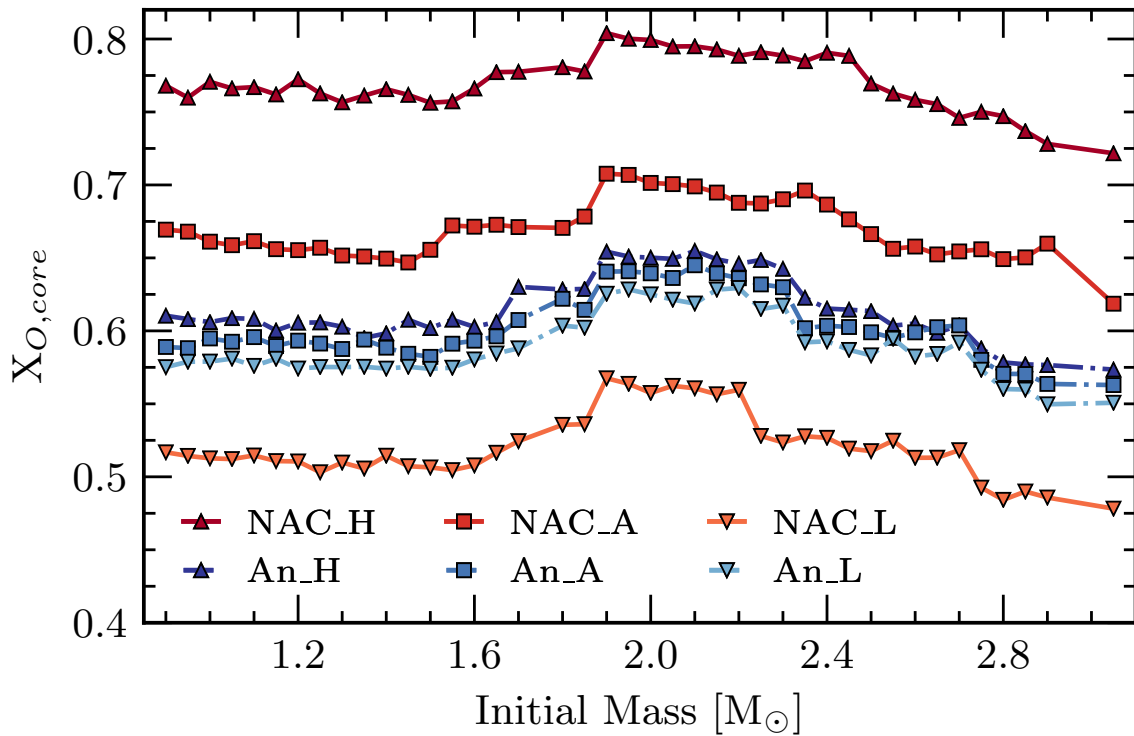


Figure 26 – Central oxygen mass fraction for the final WD as a function of initial mass. We show each calculated sequence. The trends for each considered reaction rate are similar to those found in Figure 16. There has been a slight increase in the central oxygen abundance since the CHB due to diffusion processes in the star. Additionally, squares represent the respective adopted rates while darker-coloured triangles and lighter-coloured upside-down triangles represent the high and low limit uncertainties, respectively.

reduced uncertainty. [Metcalf \(2003\)](#) report S-factors of  $S(300 \text{ keV})_{GD358} = 195 \pm 15$  and  $S(300 \text{ keV})_{CBS114} = 190 \pm 15$  for the DBVs GD 358 and CBS 114, respectively. Although the S-factors are larger than those derived by [Horowitz, Schneider & Berry \(2010\)](#), the  $^{12}\text{C}(\alpha, \gamma)^{16}\text{O}$  reaction rate from CBS 114 still produces oxygen mass fractions that agree with [Horowitz, Schneider & Berry \(2010\)](#) for their crystallisation process. This could perhaps be due to the different prescription for mixing length and overshooting used during the core helium burning phases.

### 3.3.4 Inner Chemical Profile

Figure 27 shows the abundance profiles of white dwarf models with a stellar mass of  $M_* = 0.548 M_{\odot}$ ,  $T_{\text{eff}} = 20000\text{K}$  and an initial mass of  $M_i = 1.30 M_{\odot}$ . Sequences that consider a reaction rate from NACRE are shown in the top panel and those from [An et al. \(2016\)](#) are represented in the bottom panel. All sequences finish with similar structure to those shown in Figure 27. The profiles depict a DA white dwarf configuration, with a hydrogen-rich envelope, a helium buffer and a C/O core. Where the abundance of carbon reaches it's maximum, we hereafter refer to this as the carbon peak.

We show that the interior of the star has a consistent trend where the carbon peak is higher for lower reaction rates - an outcome of a less efficient reaction rate which leaves behind a larger abundance of carbon. Furthermore, the position of the carbon peak changes with the reaction rates, moving away from the centre as the reaction rate increases. We find in general that differences between An\_A and the An\_H/An\_L reaction rates do not affect this region drastically (bottom panel), unlike that of the NACRE  $^{12}\text{C}(\alpha, \gamma)^{16}\text{O}$  reaction rate considerations (top panel).

The abundance profile and composition gradients in these central regions that lie within the range of  $1 < -\log_{10}(1 - M_r/M_*) < 2$  affect the peaks in the Brunt-Väisälä frequency, which disturbs the period spectrum structure (see [Córscico & Althaus \(2006\)](#), [Romero et al. \(2012a\)](#), for details. This is an outcome of the pulsation modes that are trapped in this region through the mode-trapping mechanism. We confirm that uncertainties of the  $^{12}\text{C}(\alpha, \gamma)^{16}\text{O}$  reaction rate may affect the pulsation period spectrum. Another region where the Brunt-Väisälä frequency is affected is in the He/H transition region. In particular, the position of the He/H transition will impact the period spectrum ([Romero et al., 2012b](#); [Romero et al., 2013](#)).

A further interesting result during the WD stage would be how a study of convection in 3D affects the sequences produced. [Tremblay et al. \(2013\)](#) found that the final mass reduces in their work as a result, up to  $0.1 M_{\odot}$ . Although it should not produce any differences to the position or width of the DAV instability strip. As well as this, 3D modelling of convection within WD interiors removes the problem in the surface gravity distribution of cool DA white dwarfs ([Eisenstein et al., 2006](#); [Gianninas; Bergeron; Ruiz, 2009](#); [Tremblay et al., 2011](#)).

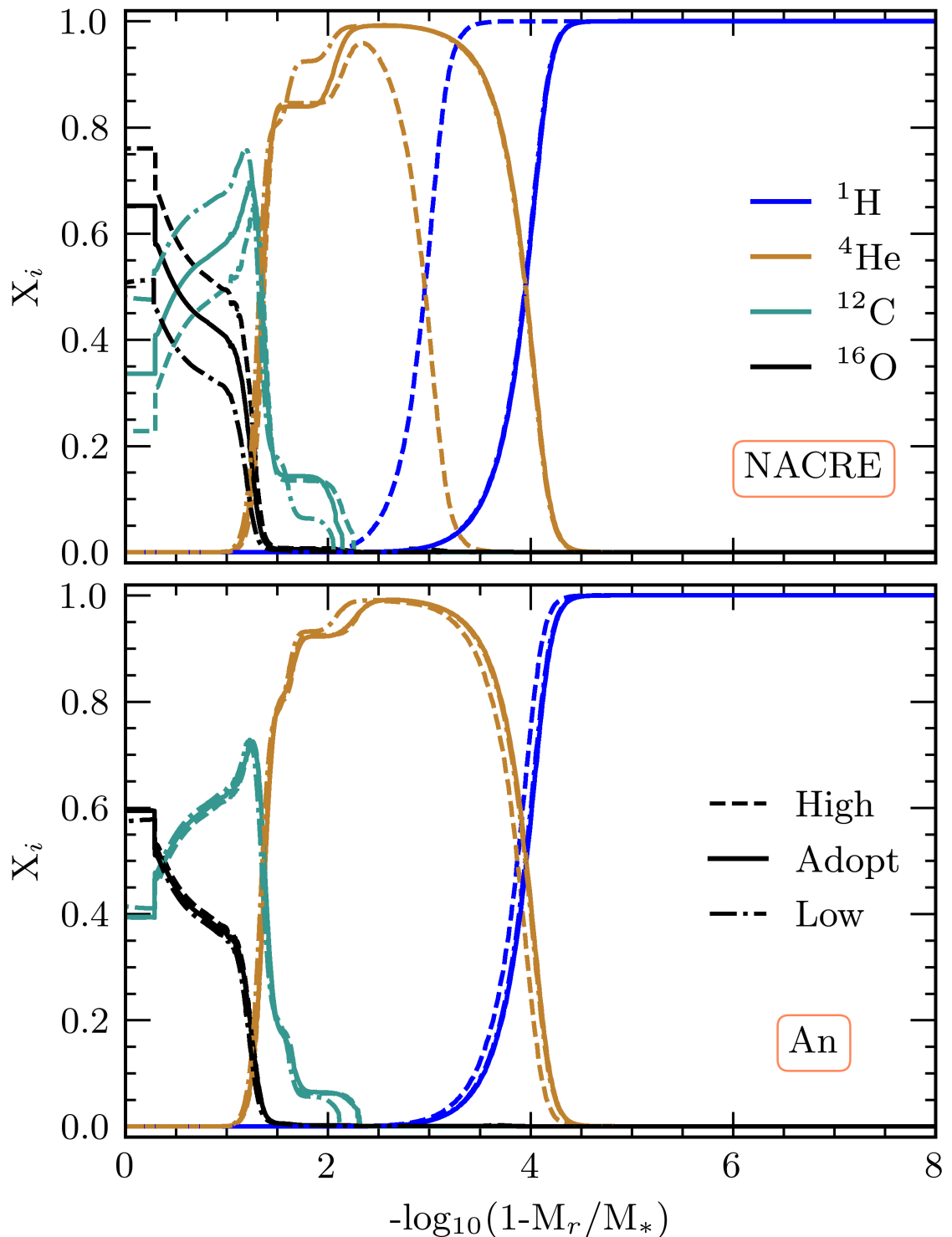


Figure 27 – In both panels we show the abundance profiles of sequences considering an initial mass of  $M_i = 1.30 M_\odot$ . The top panel represents the adopted rate and its uncertainties for the NACRE rate, and the same for the [An et al. \(2016\)](#) rates in the bottom panel. The line-styles for each rate are shown in the legend in the bottom panel and the colours for each element is shown in the legend in the top panel.





## 4 Conclusion

In this work we analyse the impact of the different estimates and their respective uncertainties for the  $^{12}\text{C}(\alpha, \gamma)^{16}\text{O}$  reaction rate on the inner structure and evolutionary properties of low and intermediate-mass stars. Considered values are adopted from the works of NACRE (Angulo et al., 1999) and those from An et al. (2016). We have computed stellar sequences from the ZAMS until a white dwarf with a luminosity of  $\log(L/L_{\odot}) = -3$  on final cooling track. Similar initial metallicities were considered ( $Z_i = 0.01$ ) as well as initial masses in the range of  $0.90 \leq M/M_{\odot} \leq 3.05$ . The different considerations for the  $^{12}\text{C}(\alpha, \gamma)^{16}\text{O}$  reaction rates are highlighted in Section 1.4.

Below is a summary of the main results, which are followed by a conclusion on which nuclear reaction rates produce a more realistic stellar computation.

1. As expected, all stages previous to the Core Helium Burning stage (CHB) do not find any differences as a result of the  $^{12}\text{C}(\alpha, \gamma)^{16}\text{O}$  reaction rate uncertainties. Whereas all other stages do have their evolutions altered.
2. The C/O ratio of the core in the final model of each sequence is affected by the  $^{12}\text{C}(\alpha, \gamma)^{16}\text{O}$  reaction rate as expected, with lower C/O ratios for larger reaction rates. We find that the decrease in the C/O ratio for initial masses greater than the transition mass increase again at larger masses. The mass at which this increase occurs is dependent on the considered  $^{12}\text{C}(\alpha, \gamma)^{16}\text{O}$  reaction rate, such that it occurs for higher masses if higher reaction rates are considered. This is due to an increased number of mixing episodes, a cause of larger energy outputs increasing convective efficiency which brings fresh helium to the core during the CHB. Note that significant differences between the adopted rate and high/low limits occur only for those rates taken from NACRE which has a much larger uncertainty than those from An et al. (2016).
3. The CHB lifetime is dependent on the considered reaction rate, a higher reaction rate produces a greater lifetime. We deem this to be a consequence in the number of mixing episodes extending the core helium burning lifetime, although further research would be beneficial to confirm this. Between the adopted rate and high/low limits, we find a difference up to 12 Myr for the NACRE rates and up to 4 Myr for those from An et al. (2016). Such differences are not insignificant, as was found by Straniero (2007).
4. Differences in the size of the convective mass during the CHB may influence the possible propagation modes in asteroseismological studies of sdB pulsators (Heber,

- 2009).
5. The helium core mass at the beginning of the first thermal pulse (TP) is independent of the considered  $^{12}\text{C}(\alpha, \gamma)^{16}\text{O}$  reaction rate up to and including the transition mass. Above this mass, we find a maximum difference of  $\approx 0.01M_{\odot}$  between NACRE\_H and NACRE\_L, with lower reaction rates producing a lower helium core mass. Additionally our minimum helium core mass at this point occurs at our transition mass, which is in agreement with Kalirai, Marigo & Tremblay (2014), Marigo et al. (2020).
  6. Growth of the helium core mass between the first TP and the final mass reaches a maximum of 19%, with growths greater than 10% occurring in the mass range  $1.70 \leq M_i/M_{\odot} \leq 2.60$  which is in agreement with Bird & Pinsonneault (2011) and Kalirai, Marigo & Tremblay (2014). The largest growths occur for the lower reaction rates due to more available hydrogen which remained after the CHB. There are no significant differences between the rates taken from An et al. (2016) due to the limits being smaller in relation to their adopted rate than those from NACRE.
  7. The number of TPs during the Thermally Pulsing-Asymptotic Giant Branch (TP-AGB) is dependent on the considered  $^{12}\text{C}(\alpha, \gamma)^{16}\text{O}$  reaction rate. We find that lower reaction rates increase the number of TPs due to a larger hydrogen fuel aiding the outward growth of the helium core mass by fuelling the unstable He-shell with a greater supply of fresh helium.
  8. Third Dredge-Up episodes (TDUs) occur for sequences in the initial mass range of  $2.40 \leq M_i/M_{\odot} \leq 3.05$  with dredge-up efficiency parameters  $\lambda_d = 0.033 - 0.124$ . This mass range is independent of the considered  $^{12}\text{C}(\alpha, \gamma)^{16}\text{O}$  reaction rate. Additionally, the values of  $\lambda_d$  between the considered  $^{12}\text{C}(\alpha, \gamma)^{16}\text{O}$  reaction rate uncertainties are not significant. Furthermore, the depth of each TDU is independent of the  $^{12}\text{C}(\alpha, \gamma)^{16}\text{O}$  reaction rate.
  9. We find that the final ages of the sequences are in general independent of the considered reaction rate. However, during the final cooling track, we find differences on the order of 0.01 Gyr between the adopted rates and high/low limits. This is true for both those rates taken from NACRE and An et al. (2016). This difference in the cooling time agrees with the works of Prada Moroni & Straniero (2002), Salaris et al. (2010), Isern, Artigas & García-Berro (2013). Such an uncertainty is much less than the ages deduced from observational data, which can be up to the order of a Gyr when ageing from galactic disk studies (Hansen et al., 2002).
  10. The final C/O ratio in the core shows a similar trend to that at the end of the CHB. The oxygen abundance increases slightly due to the diffusion processes. The final

oxygen mass fraction for NACRE\_A and NACRE\_H sequences are greater than the values derived by Horowitz, Schneider & Berry (2010) for crystallisation of a C/O core. The reaction rates from An et al. (2016) agree closely with the derived values of Horowitz, Schneider & Berry (2010). As such, future works should consider a lower reaction rate than that of the often used NACRE\_A when considering the crystallisation process of Horowitz, Schneider & Berry (2010).

11. The inner structure of the star is affected by the uncertainties within the considered reaction rates, particularly those from NACRE. The position and height of the carbon peak is significantly affected by the difference between the adopted rate and high/low limits of the reaction rate for the NACRE considerations, being larger and closer to the centre for the least efficient reaction rates, while as the efficiency increases the carbon peak becomes smaller and moves further away from the centre. This may affect the modes in which pulsations can occur during the ZZ Ceti instability strip (Córscico; Althaus, 2006; Romero et al., 2012b).

Although differences have been found in the chemical structure by considering different reaction rate estimates for the  $^{12}\text{C}(\alpha, \gamma)^{16}\text{O}$  reaction and its uncertainties, further analysis into this topic is required. For instance, extending the initial mass range to larger masses can give information on the impact of these reaction for stars where the central composition is made up of O/Ne/Mg during the WD cooling stage. In addition, since the final composition of the helium core mass does depend on the reaction rate values (D’Antona; Mazzitelli, 1990; Dominguez et al., 1999; Romero; Campos; Kepler, 2015), this may lead to an alternate crystallisation efficiency and cooling post-crystallisation. Other reactions not considered in this work could also affect the abundance of  $^{12}\text{C}$  and  $^{16}\text{O}$  (especially the reverse reactions of those considered in this work:  $^{16}\text{O}(\gamma, \alpha)^{12}\text{C}$ ). The effect of this is that it would change the overall abundances of  $^{12}\text{C}$  and  $^{16}\text{O}$  which is important in the reaction rate considered in this work, as shown in Equation 1.16. It is important to note, however, that this reaction does not dominate over those considered in this work and its analysis is included in many modern determinations of the  $^{12}\text{C}(\alpha, \gamma)^{16}\text{O}$  reaction rate (Aliotta et al., 2021).

It is difficult to assess which consideration for the  $^{12}\text{C}(\alpha, \gamma)^{16}\text{O}$  reaction rate is a more “realistic” evaluation. However, in my opinion, stellar evolutionary computations should start considering the lower reaction rates from An et al. (2016) and other similar reaction rates such as that from deBoer et al. (2017), more often. This is for a few reasons: if the crystallisation mechanism of Horowitz, Schneider & Berry (2010) is considered, the reaction rates from An et al. (2016) produce a composition much like that which was derived by Horowitz, Schneider & Berry (2010) for use in their crystallisation mechanism; in addition, a lower value than that of NACRE\_A for the  $^{12}\text{C}(\alpha, \gamma)^{16}\text{O}$  reaction rate is required for matching observed pulsation period spectra for DAVs, in terms of matching

the helium buffer and hydrogen envelope masses (Romero et al., 2012b; Clemens et al., 2017). The NACRE\_A rate is too large and uncertain and thus the oxygen mass fraction is larger than one would expect for the crystallisation of Horowitz, Schneider & Berry (2010) as well as constraining further the sizes of the helium buffer and hydrogen envelope of the sequences.

The uncertainties from the NACRE source reproduce vast uncertainties in all parameters throughout the evolution. This is particularly important for the structure of the WDs and the evolution of the convective core mass during the CHB. Both of which significantly may significantly affect the pulsation period of the possible DAVs or sdB variable stars (Heber, 2009; Romero; Campos; Kepler, 2015; Constantino et al., 2016; De Gerónimo et al., 2017). On the other hand, the uncertainties from An et al. (2016) (which were assumed to be arbitrary due to the in-depth discussion of deBoer et al. (2017)) did not show any significant changes to the same processes as the uncertainties from NACRE. This indicates that uncertainties up to  $\approx 5\%$  for the  $^{12}\text{C}(\alpha, \gamma)^{16}\text{O}$  reaction rate are acceptable in creating accurate models post-CHB. Previous hypothesis claim that 10% is an acceptable uncertainty to accurately model the C/O interior of stars, however no fully evolutionary sequences from the ZAMS have yet been produced to back up this claim. This work could be used as a base for such sequences, increasing the uncertainties from An et al. (2016) to 10% of the adopted rate. Additionally, it would be useful to see if the uncertainties from deBoer et al. (2017) would produce similar results for equal uncertainties as they claim their uncertainties would be similar to An et al. (2016) if they followed the same method for the determination of the uncertainties.

Finally, I conclude this work by stating that the work presented here has been published in MNRAS, entitled “The impact of the uncertainties in the  $^{12}\text{C}(\alpha, \gamma)^{16}\text{O}$  reaction rate on the evolution of low– to intermediate–mass stars” (Pepper et al., 2022). The work has been reviewed by an anonymous referee and their comments have been implement, producing a more compete work. I thank them for their input.

# Bibliography

- Abia, C. et al. s-Process Nucleosynthesis in Carbon Stars. , v. 579, n. 2, p. 817–831, nov. 2002.
- Aliotta, M. et al. The Status and Future of Direct Nuclear Reaction Measurements for Stellar Burning. *arXiv e-prints*, p. arXiv:2109.14418, set. 2021.
- An, Z.-D. et al. Astrophysical S factor of the  $^{12}\text{C}(\alpha, \gamma)^6\text{O}$  reaction calculated with reduced R -matrix theory. , v. 92, n. 4, p. 045802, out. 2015.
- An, Z.-D. et al. New Astrophysical Reaction Rate for the  $^{12}\text{C}(\alpha, \gamma)^{16}\text{O}$  Reaction. , v. 817, p. L5, jan. 2016.
- Angulo, C. et al. A compilation of charged-particle induced thermonuclear reaction rates. , v. 656, n. 1, p. 3–183, ago. 1999.
- Aoyama, S.; Suzuki, T. K. Effects of axions on nucleosynthesis in massive stars. , v. 92, n. 6, p. 063016, set. 2015.
- Augustine, C. N. et al. SN Ia Explosions from Hybrid CarbonOxygenNeon White Dwarf Progenitors that Have Mixed during Cooling. , v. 887, n. 2, p. 188, dez. 2019.
- Augustson, K. C. et al. Convection and Differential Rotation in F-type Stars. , v. 756, n. 2, p. 169, set. 2012.
- Battinelli, P.; Demers, S. Miras among C stars. , v. 568, p. A100, ago. 2014.
- Beck, P. G. *Asteroseismology of Red-Giant Stars: Mixed Modes, Differential Rotation, and Eccentric Binaries*. Tese (Doutorado) — Instituut voor Sterrenkunde, KU Leuven, Celestijnenlaan 200D, B-3001 Leuven, Belgium; paul.beck@ster.kuleuven.be, dez. 2013.
- Bertelli, G. et al. Evolutionary models for low and intermediate mass stars with convective overshooting. , v. 66, p. 191–234, nov. 1986.
- Bertelli, G.; Bressan, A. G.; Chiosi, C. Evolution of intermediate mass stars : the role of convective overshooting and stellar wind. , v. 150, p. 33–52, set. 1985.
- Bethe, H. A. Energy Production in Stars. *Physical Review*, v. 55, n. 5, p. 434–456, mar. 1939.
- Bird, J. C.; Pinsonneault, M. H. A Bound on the Light Emitted during the Thermally Pulsing Asymptotic Giant Branch Phase. , v. 733, n. 2, p. 81, jun. 2011.
- Bloecker, T. Stellar evolution of low and intermediate-mass stars. I. Mass loss on the AGB and its consequences for stellar evolution. , v. 297, p. 727, maio 1995.
- Boeltzig, A. et al. Shell and explosive hydrogen burning. Nuclear reaction rates for hydrogen burning in RGB, AGB and Novae. *European Physical Journal A*, v. 52, n. 4, p. 75, abr. 2016.

- Böhm-Vitense, E. Über die Wasserstoffkonvektionszone in Sternen verschiedener Effektivtemperaturen und Leuchtkräfte. Mit 5 Textabbildungen. , v. 46, p. 108, jan. 1958.
- Bono, G. et al. Intermediate-Mass Star Models with Different Helium and Metal Contents. , v. 543, n. 2, p. 955–971, nov. 2000.
- Boothroyd, A. I.; Sackmann, I. J. Low-Mass Stars. III. Low-Mass Stars with Steady Mass Loss: Up to the Asymptotic Giant Branch and through the Final Thermal Pulses. , v. 328, p. 653, maio 1988.
- Bradt, H. *Astrophysics Processes*. [S.l.: s.n.], 2008.
- Bressan, A. et al. Evolutionary Sequences of Stellar Models with New Radiative Opacities. II.  $Z = 0.02$ . , v. 100, p. 647, set. 1993.
- Bressan, A. et al. PARSEC: stellar tracks and isochrones with the PAdova and TRieste Stellar Evolution Code. , v. 427, n. 1, p. 127–145, nov. 2012.
- Brochard, F. et al. étude des désexcitations électromagnétiques du deuxième niveau  $j+$  du noyau  $^{16}\text{O}$  situé à 11,096 mev. *J. Phys. France*, v. 36, n. 2, p. 113–115, 1975. Disponível em: <<https://doi.org/10.1051/jphys:01975003602011300>>.
- Brown, G. E. et al. Formation of high mass X-ray black hole binaries. , v. 6, p. 457–470, out. 2001.
- Burbidge, E. M. et al. Synthesis of the Elements in Stars. *Reviews of Modern Physics*, v. 29, n. 4, p. 547–650, jan. 1957.
- Burgers, J. M. *Flow Equations for Composite Gases*. [S.l.: s.n.], 1969.
- Burrows, A.; Liebert, J. The science of brown dwarfs. *Reviews of Modern Physics*, v. 65, n. 2, p. 301–336, abr. 1993.
- Busso, M.; Gallino, R.; Wasserburg, G. J. Nucleosynthesis in Asymptotic Giant Branch Stars: Relevance for Galactic Enrichment and Solar System Formation. , v. 37, p. 239–309, Jan 1999.
- Campos, F. et al. A comparative analysis of the observed white dwarf cooling sequence from globular clusters. , v. 456, n. 4, p. 3729–3742, Mar 2016.
- Cassisi, S. et al. Updated Electron-Conduction Opacities: The Impact on Low-Mass Stellar Models. , v. 661, n. 2, p. 1094–1104, jun. 2007.
- Caughlan, G. R.; Fowler, W. A. Thermonuclear Reaction Rates V. *Atomic Data and Nuclear Data Tables*, v. 40, p. 283, 1988.
- Chamandy, L. et al. Common envelope evolution on the asymptotic giant branch: unbinding within a decade? , v. 495, n. 4, p. 4028–4039, maio 2020.
- Chamel, N. et al. On the Maximum Mass of Neutron Stars. *International Journal of Modern Physics E*, v. 22, n. 7, p. 1330018, jul. 2013.
- Chandrasekhar, S. The Maximum Mass of Ideal White Dwarfs. , v. 74, p. 81, jul. 1931.
- Clayton, D. D. *Principles of stellar evolution and nucleosynthesis*. [S.l.: s.n.], 1968.

- Clemens, J. C. et al. Seismology of an Ensemble of ZZ Ceti Stars. In: Tremblay, P. E.; Gaensicke, B.; Marsh, T. (Ed.). *20th European White Dwarf Workshop*. [S.l.: s.n.], 2017. (Astronomical Society of the Pacific Conference Series, v. 509), p. 255.
- Constantino, T. et al. The treatment of mixing in core helium burning models - I. Implications for asteroseismology. , v. 452, n. 1, p. 123–145, set. 2015.
- Constantino, T.; Campbell, S. W.; Lattanzio, J. C. The treatment of mixing in core helium-burning models - III. Suppressing core breathing pulses with a new constraint on overshoot. , v. 472, n. 4, p. 4900–4909, dez. 2017.
- Constantino, T. et al. The treatment of mixing in core helium burning models - II. Constraints from cluster star counts. , v. 456, n. 4, p. 3866–3885, mar. 2016.
- Cook, A. W.; Youngs, D. Rayleigh-Taylor instability and mixing. *Scholarpedia*, v. 4, n. 2, p. 6092, 2009. Revision #91699.
- Córsico, A. H.; Althaus, L. G. Asteroseismic inferences on GW Virginis variable stars in the frame of new PG 1159 evolutionary models. , v. 454, n. 3, p. 863–881, ago. 2006.
- Cristallo, S. et al. Evolution, Nucleosynthesis, and Yields of Low-Mass Asymptotic Giant Branch Stars at Different Metallicities. , v. 696, p. 797–820, maio 2009.
- Cristallo, S. et al. Evolution, Nucleosynthesis, and Yields of AGB Stars at Different Metallicities. III. Intermediate-mass Models, Revised Low-mass Models, and the ph-FRUITY Interface. , v. 219, n. 2, p. 40, ago. 2015.
- Cukanovaite, E. et al. Calibration of the mixing-length theory for structures of helium-dominated atmosphere white dwarfs. , v. 490, n. 1, p. 1010–1025, nov. 2019.
- Cyburt, R. H. et al. The JINA REACLIB Database: Its Recent Updates and Impact on Type-I X-ray Bursts. , v. 189, n. 1, p. 240–252, jul. 2010.
- D’Antona, F.; Mazzitelli, I. The fastest evolving white dwarfs. , v. 347, p. 934–949, dez. 1989.
- D’Antona, F.; Mazzitelli, I. The Fastest Evolving White Dwarfs. , v. 347, p. 934, Dec 1989.
- D’Antona, F.; Mazzitelli, I. Cooling of white dwarfs. , v. 28, p. 139–181, 1990.
- Daszynska-Daszkiewicz, J. et al. Testing stellar opacities using asteroseismology. *arXiv e-prints*, p. arXiv:1912.00409, Dec 2019.
- De Gerónimo, F. C. et al. Asteroseismology of ZZ Ceti stars with fully evolutionary white dwarf models. I. The impact of the uncertainties from prior evolution on the period spectrum. , v. 599, p. A21, mar. 2017.
- De Gerónimo, F. C. et al. The Impact of the Uncertainties in the  $^{12}\text{C}(\alpha,\gamma)^{16}\text{O}$  Reaction Rate on the Asteroseismology of ZZ Ceti Stars: First Results. In: \_\_\_\_\_. *19th European Workshop on White Dwarfs*. [S.l.: s.n.], 2015. (Astronomical Society of the Pacific Conference Series, v. 493), p. 225.

- Deboer, R.; Brune, C.; Wiescher, M. Extrapolating the  $^{12}\text{C}(\alpha,\gamma)^{16}\text{O}$  cross section to astrophysical energies using phenomenological R-matrix. In: *APS Division of Nuclear Physics Meeting Abstracts*. [S.l.: s.n.], 2019. (APS Meeting Abstracts, v. 2019), p. FG.003.
- deBoer, R. J. et al. The  $^{12}\text{C}(\alpha,\gamma)^{16}\text{O}$  reaction and its implications for stellar helium burning. *Reviews of Modern Physics*, v. 89, n. 3, p. 035007, jul. 2017.
- Doherty, C. L. et al. Nucleosynthesis in Super-AGB Stars. In: Kerschbaum, F.; Wing, R. F.; Hron, J. (Ed.). *Why Galaxies Care about AGB Stars III: A Closer Look in Space and Time*. [S.l.: s.n.], 2015. (Astronomical Society of the Pacific Conference Series, v. 497), p. 247.
- Doherty, C. L. et al. Super-AGB Stars and their Role as Electron Capture Supernova Progenitors. , v. 34, p. e056, nov. 2017.
- Dominguez, I. et al. Intermediate-Mass Stars: Updated Models. , v. 524, n. 1, p. 226–241, out. 1999.
- Domínguez, I.; Straniero, O.; Isern, J. Asymptotic giant branch stars as astroparticle laboratories. , v. 306, n. 1, p. L1–L7, jun. 1999.
- Doolittle, H. D. The Disintegration of  $\text{Li}^7$  Bombarded by Slow Protons. *Physical Review*, v. 49, n. 11, p. 779–782, jun. 1936.
- Eddington, A. S. *The Internal Constitution of the Stars*. [S.l.: s.n.], 1926.
- Eisenstein, D. J. et al. A Catalog of Spectroscopically Confirmed White Dwarfs from the Sloan Digital Sky Survey Data Release 4. , v. 167, n. 1, p. 40–58, nov. 2006.
- Farmer, R. et al. Constraints from Gravitational-wave Detections of Binary Black Hole Mergers on the  $^{12}\text{C}(\alpha,\gamma)^{16}\text{O}$  Rate. , v. 902, n. 2, p. L36, out. 2020.
- Ferguson, J. W. et al. Low-Temperature Opacities. , v. 623, n. 1, p. 585–596, abr. 2005.
- Forbes, D. A. et al. The SLUGGS survey: inferring the formation epochs of metal-poor and metal-rich globular clusters. , v. 452, n. 1, p. 1045–1051, set. 2015.
- Forestini, M.; Charbonnel, C. Nucleosynthesis of light elements inside thermally pulsing AGB stars: I. The case of intermediate-mass stars. , v. 123, p. 241–272, jun. 1997.
- Fowler, W. A.; Caughlan, G. R.; Zimmerman, B. A. Thermonuclear Reaction Rates. , v. 5, p. 525, jan. 1967.
- Frost, C. A.; Lattanzio, J. C. On the Numerical Treatment and Dependence of the Third Dredge-up Phenomenon. , v. 473, p. 383, dez. 1996.
- Fynbo, H. O. U. et al. Revised rates for the stellar triple- $\alpha$  process from measurement of  $^{12}\text{C}$  nuclear resonances. , v. 433, p. 136–139, jan. 2005.
- Fynbo, H. O. U.; Freer, M. Rotations of the Hoyle State in Carbon-12. *Physics Online Journal*, v. 4, p. 94, nov. 2011.
- Gai, M. Studies in Nuclear Astrophysics with an Optical Readout TPC (O-TPC) at HI $\gamma$ S. In: *Journal of Physics Conference Series*. [S.l.: s.n.], 2012. (Journal of Physics Conference Series, v. 337), p. 012054.



- Gai, M. et al. An optical readout TPC (o-TPC) for studies in nuclear astrophysics with gamma-ray beams at HIs1. *Journal of Instrumentation*, IOP Publishing, v. 5, n. 12, p. P12004–P12004, dec 2010. Disponível em: <<https://doi.org/10.1088/1748-0221/5/12/p12004>>.
- Gallino, R. et al. Evolution and Nucleosynthesis in Low-Mass Asymptotic Giant Branch Stars. II. Neutron Capture and the S-Process. , v. 497, n. 1, p. 388–403, Apr 1998.
- Gamow, G. Zur Quantentheorie des Atomkernes. *Zeitschrift fur Physik*, v. 51, n. 3-4, p. 204–212, mar. 1928.
- Gamow, G.; Teller, E. The Rate of Selective Thermonuclear Reactions. *Physical Review*, v. 53, n. 7, p. 608–609, abr. 1938.
- García-Berro, E.; Ritossa, C.; Iben ICKO, J. On the Evolution of Stars that Form Electron-Degenerate Cores Processed by Carbon Burning. III. The Inward Propagation of a Carbon-Burning Flame and Other Properties of a  $9 M_{\odot}$  Model Star. , v. 485, n. 2, p. 765–784, ago. 1997.
- Gautschy, A. Helium Ignition in the Cores of Low-Mass Stars. *arXiv e-prints*, p. arXiv:1208.3870, ago. 2012.
- Ghasemi, H. et al. The effects of near-core convective shells on the gravity modes of the subdwarf B pulsator KIC 10553698A. , v. 465, n. 2, p. 1518–1531, fev. 2017.
- Gianninas, A.; Bergeron, P.; Ruiz, M. T. Spectroscopic analysis of DA white dwarfs from the McCook & Sion catalog. In: *Journal of Physics Conference Series*. [S.l.: s.n.], 2009. (Journal of Physics Conference Series, v. 172), p. 012021.
- Glass, I. S.; Evans, T. L. A period-luminosity relation for Mira variables in the Large Magellanic Cloud. , v. 291, n. 5813, p. 303–304, jun. 1981.
- Goldman, S. R. et al. A dearth of OH/IR stars in the Small Magellanic Cloud. , v. 473, n. 3, p. 3835–3853, jan. 2018.
- Goldreich, P.; Scoville, N. OH-IR stars. I. Physical properties of circumstellar envelopes. , v. 205, p. 144–154, abr. 1976.
- Görres, J. et al. Low-energy resonances in  $^{14}\text{N}(\alpha,\gamma)^{18}\text{F}$  and their astrophysical implications. , v. 62, n. 5, p. 055801, nov. 2000.
- Guo, J.-J.; Li, Y. Influence of the He-flash convective overshoot on mode trapping efficiency in g-mode pulsating subdwarf B stars. , v. 478, n. 3, p. 3290–3297, ago. 2018.
- Guzik, J. A. et al. Investigating Opacity Modifications and Reaction Rate Uncertainties to Resolve the Cepheid Mass Discrepancy. *arXiv e-prints*, p. arXiv:2002.04073, fev. 2020.
- Guzik, J. A. et al. Sound speed and oscillation frequencies for solar models evolved with Los Alamos ATOMIC opacities. *IAU Focus Meeting*, v. 29B, p. 532–535, jan. 2016.
- Handler, G.; Metcalfe, T. S.; Wood, M. A. The asteroseismological potential of the pulsating DB white dwarf stars CBS 114 and PG 1456+103. , v. 335, n. 3, p. 698–706, set. 2002.

- Hansen, B. M. S. et al. The White Dwarf Cooling Sequence of the Globular Cluster Messier 4. , v. 574, n. 2, p. L155–L158, ago. 2002.
- Hansen, B. M. S. et al. An age difference of two billion years between a metal-rich and a metal-poor globular cluster. , v. 500, n. 7460, p. 51–53, ago. 2013.
- Hansen, C. J.; Kawaler, S. D. *Stellar Interiors. Physical Principles, Structure, and Evolution*. [S.l.: s.n.], 1994.
- Hebbard, D. F.; Vogl, J. L. Elastic scattering and radiative capture of protons by C <sup>13</sup>. *Nuclear Physics*, v. 21, p. 652–675, dez. 1960.
- Heber, U. Hot Subdwarf Stars. , v. 47, n. 1, p. 211–251, set. 2009.
- Heger, A. et al. Massive star evolution: nucleosynthesis and nuclear reaction rate uncertainties. , v. 46, n. 8-10, p. 463–468, jul. 2002.
- Heil, M. et al. The <sup>13</sup>C( $\alpha$ ,n) reaction and its role as a neutron source for the s process. , v. 78, n. 2, p. 025803, ago. 2008.
- Heisenberg, W. Über den anschaulichen Inhalt der quantentheoretischen Kinematik und Mechanik. *Zeitschrift für Physik*, v. 43, n. 3-4, p. 172–198, mar. 1927.
- Henyey, L.; Vardya, M. S.; Bodenheimer, P. Studies in Stellar Evolution. III. The Calculation of Model Envelopes. , v. 142, p. 841, out. 1965.
- Herwig, F. The evolution of AGB stars with convective overshoot. , v. 360, p. 952–968, ago. 2000.
- Herwig, F. Evolution of Asymptotic Giant Branch Stars. , v. 43, n. 1, p. 435–479, Sep 2005.
- Herwig, F. et al. On the formation of hydrogen-deficient post-AGB stars. , v. 349, p. L5–L8, set. 1999.
- Herwig, F. et al. Stellar evolution of low and intermediate-mass stars. IV. Hydrodynamically-based overshoot and nucleosynthesis in AGB stars. , v. 324, p. L81–L84, ago. 1997.
- Horowitz, C. J.; Schneider, A. S.; Berry, D. K. Crystallization of Carbon-Oxygen Mixtures in White Dwarf Stars. , v. 104, n. 23, p. 231101, jun. 2010.
- Hoyle, F. The synthesis of the elements from hydrogen. , v. 106, p. 343, jan. 1946.
- Hoyle, F. On Nuclear Reactions Occuring in Very Hot STARS.I. the Synthesis of Elements from Carbon to Nickel. , v. 1, p. 121, set. 1954.
- Hu, H. et al. Slowing down atomic diffusion in subdwarf B stars: mass loss or turbulence? , v. 418, n. 1, p. 195–205, nov. 2011.
- Hubbard, W. B.; Lampe, M. Thermal Conduction by Electrons in Stellar Matter. , v. 18, p. 297, jul. 1969.
- Hubble, E. A Relation between Distance and Radial Velocity among Extra-Galactic Nebulae. *Proceedings of the National Academy of Science*, v. 15, n. 3, p. 168–173, mar. 1929.

- Iben, I. J.; MacDonald, J. The effects of diffusion due to gravity and due to composition gradients on the rate of hydrogen burning in a cooling degenerate dwarf. I - The case of a thick helium buffer layer. , v. 296, p. 540–553, set. 1985.
- Iben I., J.; Tutukov, A. V. Supernovae of type I as end products of the evolution of binaries with components of moderate initial mass. , v. 54, p. 335–372, fev. 1984.
- Iglesias, C. A.; Rogers, F. J. Radiative Opacities for Carbon- and Oxygen-rich Mixtures. , v. 412, p. 752, ago. 1993.
- Iglesias, C. A.; Rogers, F. J. Updated Opal Opacities. , v. 464, p. 943, jun. 1996.
- Imbriani, G. et al. The bottleneck of CNO burning and the age of Globular Clusters. , v. 420, p. 625–629, jun. 2004.
- IRELAND, M. J. et al. Pulsation of m-type mira variables with moderately different mass: search for observable mass effects. *Monthly Notices of the Royal Astronomical Society*, Oxford University Press (OUP), v. 355, n. 2, p. 444–450, Dec 2004. ISSN 1365-2966. Disponível em: <<http://dx.doi.org/10.1111/j.1365-2966.2004.08336.x>>.
- Isern, J.; Artigas, A.; García-Berro, E. White dwarf cooling sequences and cosmochronology. In: *European Physical Journal Web of Conferences*. [S.l.: s.n.], 2013. (European Physical Journal Web of Conferences, v. 43), p. 05002.
- J Jeans, J. H. The Stability of a Spherical Nebula. *Philosophical Transactions of the Royal Society of London Series A*, v. 199, p. 1–53, jan. 1902.
- JPLPublic. *Stellar Evolution*. 2019. [Online; accessed June 1, 2020]. Disponível em: <<https://www.jpl.nasa.gov/infographics/infographic.view.php?id=10737>>.
- Kalirai, J. S.; Marigo, P.; Tremblay, P.-E. The Core Mass Growth and Stellar Lifetime of Thermally Pulsing Asymptotic Giant Branch Stars. , v. 782, n. 1, p. 17, fev. 2014.
- Karakas, A. I.; Lattanzio, J. C. Production of Aluminium and the Heavy Magnesium Isotopes in Asymptotic Giant Branch Stars. , v. 20, n. 3, p. 279–293, jan. 2003.
- Karakas, A. I.; Lattanzio, J. C. The Dawes Review 2: Nucleosynthesis and Stellar Yields of Low- and Intermediate-Mass Single Stars. , v. 31, p. e030, jul. 2014.
- Karakas, A. I.; Lattanzio, J. C.; Pols, O. R. Parameterising the Third Dredge-up in Asymptotic Giant Branch Stars. , v. 19, n. 4, p. 515–526, jan. 2002.
- Keller, G. R.; Bianchi, L.; Maciel, W. J. UV spectral analysis of very hot H-deficient [WCE]-type central stars of planetary nebulae: NGC 2867, NGC 5189, NGC 6905, Pb 6 and Sand 3. , v. 442, n. 2, p. 1379–1395, ago. 2014.
- Kippenhahn, R.; Ruschenplatt, G.; Thomas, H. C. The time scale of thermohaline mixing in stars. , v. 91, n. 1-2, p. 175–180, nov. 1980.
- Kippenhahn, R.; Weigert, A. *Stellar Structure and Evolution*. [S.l.: s.n.], 1990.
- Kippenhahn, R.; Weigert, A. *Stellar Structure and Evolution*. [S.l.: s.n.], 1994.
- Kobayashi, C.; Karakas, A. I.; Lugaro, M. The Origin of Elements from Carbon to Uranium. , v. 900, n. 2, p. 179, set. 2020.

- Kunitomo, M. et al. Orbital Evolution of Planets around Intermediate-Mass Giants. In: Schuh, S.; Drechsel, H.; Heber, U. (Ed.). *American Institute of Physics Conference Series*. [S.l.: s.n.], 2011. (American Institute of Physics Conference Series, v. 1331), p. 314–318.
- Kunz, R. et al. Astrophysical Reaction Rate of  $^{12}\text{C}(\alpha, \gamma)^{16}\text{O}$ . , v. 567, p. 643–650, mar. 2002.
- Kunz, R. et al.  $^{12}\text{C}(\alpha, \gamma)^{16}\text{O}$ : The Key Reaction in Stellar Nucleosynthesis. *Physical Review Letters*, v. 86, p. 3244–3247, abr. 2001.
- Ladenburg, R.; Kanner, M. H. On the Scattering Cross Section of Fast Neutrons by Hydrogen. *Physical Review*, v. 52, n. 12, p. 1255–1255, dez. 1937.
- Langer, N. Evolution of massive stars in the Large Magellanic Cloud : models with semiconvection. , v. 252, p. 669–688, dez. 1991.
- Lauffer, G. R.; Romero, A. D.; Kepler, S. O. New full evolutionary sequences of H- and He-atmosphere massive white dwarf stars using MESA. , v. 480, p. 1547–1562, out. 2018.
- Ledoux, P. Stellar Models with Convection and with Discontinuity of the Mean Molecular Weight. , v. 105, p. 305, mar. 1947.
- Lemaître, G. Expansion of the universe, A homogeneous universe of constant mass and increasing radius accounting for the radial velocity of extra-galactic nebulae. , v. 91, p. 483–490, mar. 1931.
- Lenz, P. Asteroseismology of stars on the upper main sequence. *arXiv e-prints*, p. arXiv:1206.2147, jun. 2012.
- Maciel, W. J.; Rodrigues, T. S.; Costa, R. D. D. Kinematic ages of the central stars of planetary nebulae. , v. 47, p. 401–407, out. 2011.
- Marigo, P. Asymptotic Giant Branch evolution at varying surface C/O ratio: effects of changes in molecular opacities. , v. 387, p. 507–519, maio 2002.
- Marigo, P. Can the third dredge-up extinguish hot-bottom burning in massive AGB stars? , v. 467, n. 3, p. 1139–1146, jun. 2007.
- Marigo, P. et al. Evolution of thermally pulsing asymptotic giant branch stars - I. The COLIBRI code. , v. 434, n. 1, p. 488–526, set. 2013.
- Marigo, P. et al. Carbon star formation as seen through the non-monotonic initial-final mass relation. *Nature Astronomy*, jul. 2020.
- Matteucci, F. *Chemical Evolution of Galaxies*. [S.l.: s.n.], 2012.
- Matteucci, F. Modelling the chemical evolution of the Milky Way. , v. 29, n. 1, p. 5, dez. 2021.
- Mazzitelli, I.; Dantona, F. Evolution from the main sequence to the white dwarf stage for a 3 solar mass star. , v. 308, p. 706–720, set. 1986.
- Metcalf, T. S. White Dwarf Seismology and the  $^{12}\text{C}(\alpha, \gamma)^{16}\text{O}$  Rate. In: *NATO ASIB Proc. 105: White Dwarfs*. [S.l.: s.n.], 2003. v. 105, p. 251.

- Metcalf, T. S.; Winget, D. E.; Charbonneau, P. Preliminary Constraints on  $^{12}\text{C}(\alpha, \gamma)^{16}\text{O}$  from White Dwarf Seismology. , v. 557, n. 2, p. 1021–1027, ago. 2001.
- Montalbán, J. et al. Testing Convective-core Overshooting Using Period Spacings of Dipole Modes in Red Giants. , v. 766, n. 2, p. 118, abr. 2013.
- Morinaga, H. Interpretation of Some of the Excited States of  $4n$  Self-Conjugate Nuclei. *Physical Review*, v. 101, n. 1, p. 254–258, jan. 1956.
- Ophel, T. R. et al. A remeasurement of the  $^{12}\text{C}(\alpha, \gamma_0)^{16}\text{O}$  excitation function in the vicinity of the 12.44 and 13.1 MeV levels of  $^{16}\text{O}$ . *Nuclear Physics A*, v. 273, p. 397–409, nov. 1976.
- Öpik, E. On the Upper Limit of Stellar Masses. *Publications of the Tartu Astrofizica Observatory*, v. 30, p. A42–A46, jan. 1938.
- Özel, F. et al. On the Mass Distribution and Birth Masses of Neutron Stars. , v. 757, n. 1, p. 55, set. 2012.
- Paxton, B. et al. Modules for Experiments in Stellar Astrophysics (MESA). , v. 192, p. 3, jan. 2011.
- Paxton, B. et al. Modules for Experiments in Stellar Astrophysics (MESA): Planets, Oscillations, Rotation, and Massive Stars. , v. 208, p. 4, set. 2013.
- Paxton, B. et al. Modules for Experiments in Stellar Astrophysics (MESA): Binaries, Pulsations, and Explosions. , v. 220, p. 15, set. 2015.
- Paxton, B. et al. Modules for Experiments in Stellar Astrophysics (MESA): Convective Boundaries, Element Diffusion, and Massive Star Explosions. , v. 234, p. 34, fev. 2018.
- Paxton, B. et al. Modules for Experiments in Stellar Astrophysics (MESA): Pulsating Variable Stars, Rotation, Convective Boundaries, and Energy Conservation. *arXiv e-prints*, mar. 2019.
- Pepper, B. T. et al. The impact of the uncertainties in the  $^{12}\text{C}(\alpha, \gamma)^{16}\text{O}$  reaction rate on the evolution of low- to intermediate-mass stars. , v. 513, n. 1, p. 1499–1512, jun. 2022.
- Perlmutter, S.; Turner, M. S.; White, M. Constraining Dark Energy with Type Ia Supernovae and Large-Scale Structure. , v. 83, n. 4, p. 670–673, jul. 1999.
- Poelarends, A. J. T. et al. The Supernova Channel of Super-AGB Stars. , v. 675, n. 1, p. 614–625, Mar 2008.
- Prada Moroni, P. G.; Straniero, O. Calibration of White Dwarf Cooling Sequences: Theoretical Uncertainty. , v. 581, n. 1, p. 585–597, dez. 2002.
- Preston, M. A.; Whaling, W. Physics of the Nucleus. *American Journal of Physics*, v. 31, n. 1, p. 65–66, jan. 1963.
- Prialnik, D. *An Introduction to the Theory of Stellar Structure and Evolution*. [S.l.: s.n.], 2009.
- Raffelt, G. G. Axion bremsstrahlung in red giants. , v. 41, n. 4, p. 1324–1326, fev. 1990.

- Raffelt, G. G. *Stars as laboratories for fundamental physics : the astrophysics of neutrinos, axions, and other weakly interacting particles*. [S.l.: s.n.], 1996.
- Rauscher, T.; Thielemann, F.-K. Tables of Nuclear Cross Sections and Reaction Rates: AN Addendum to the Paper “ASTROPHYSICAL Reaction Rates from Statistical Model Calculations” (). *Atomic Data and Nuclear Data Tables*, v. 79, n. 1, p. 47–64, Sep 2001.
- Rayleigh, L. Xxxiii. on maintained vibrations. *The London, Edinburgh, and Dublin Philosophical Magazine and Journal of Science*, Taylor Francis, v. 15, n. 94, p. 229–235, 1883. Disponível em: <<https://doi.org/10.1080/14786448308627342>>.
- Reimers, D. Circumstellar envelopes and mass loss of red giant stars. In: \_\_\_\_\_. *Problems in stellar atmospheres and envelopes*. [S.l.: s.n.], 1975. p. 229–256.
- Renedo, I. et al. New Cooling Sequences for Old White Dwarfs. , v. 717, n. 1, p. 183–195, Jul 2010.
- Rezzolla, L.; Most, E. R.; Weih, L. R. Using Gravitational-wave Observations and Quasi-universal Relations to Constrain the Maximum Mass of Neutron Stars. , v. 852, n. 2, p. L25, jan. 2018.
- Riess, A. G. et al. Observational Evidence from Supernovae for an Accelerating Universe and a Cosmological Constant. , v. 116, n. 3, p. 1009–1038, set. 1998.
- Ritossa, C.; García-Berro, E.; Iben ICKO, J. On the Evolution of Stars that Form Electron-degenerate Cores Processed by Carbon Burning. V. Shell Convection Sustained by Helium Burning, Transient Neon Burning, Dredge-out, Urca Cooling, and Other Properties of an 11  $M_{\text{solar}}$  Population I Model Star. , v. 515, n. 1, p. 381–397, abr. 1999.
- Rogers, F. J.; Nayfonov, A. Updated and Expanded OPAL Equation-of-State Tables: Implications for Helioseismology. , v. 576, n. 2, p. 1064–1074, set. 2002.
- Romero, A. D.; Campos, F.; Kepler, S. O. The age-metallicity dependence for white dwarf stars. , v. 450, n. 4, p. 3708–3723, jul. 2015.
- Romero, A. D. et al. Toward ensemble asteroseismology of ZZ Ceti stars with fully evolutionary models. , v. 420, n. 2, p. 1462–1480, fev. 2012.
- Romero, A. D. et al. A public database for white dwarf asteroseismology with fully evolutionary models: I. Chemical profiles and pulsation periods of ZZ Ceti (DAV) stars. *arXiv e-prints*, p. arXiv:1204.6101, Apr 2012.
- Romero, A. D. et al. Asteroseismological Study of Massive ZZ Ceti Stars with Fully Evolutionary Models. , v. 779, n. 1, p. 58, dez. 2013.
- Sahoo, S. K. et al. Mode identification in three pulsating hot subdwarfs observed with TESS satellite. , v. 495, n. 3, p. 2844–2857, maio 2020.
- Salaris, M.; Cassisi, S. *Evolution of Stars and Stellar Populations*. [S.l.: s.n.], 2005.
- Salaris, M. et al. A Large Stellar Evolution Database for Population Synthesis Studies. VI. White Dwarf Cooling Sequences. , v. 716, n. 2, p. 1241–1251, jun. 2010.
- Salaris, M. et al. The Cooling of CO White Dwarfs: Influence of the Internal Chemical Distribution. , v. 486, n. 1, p. 413–419, set. 1997.

- Salaris, M. et al. Semi-empirical White Dwarf Initial-Final Mass Relationships: A Thorough Analysis of Systematic Uncertainties Due to Stellar Evolution Models. , v. 692, n. 2, p. 1013–1032, fev. 2009.
- Salpeter, E. E. Nuclear Reactions in Stars Without Hydrogen. , v. 115, p. 326–328, mar. 1952.
- Salpeter, E. E. Nuclear Reactions in the Stars. I. Proton-Proton Chain. *Physical Review*, v. 88, n. 3, p. 547–553, Nov 1952.
- Saumon, D.; Chabrier, G.; van Horn, H. M. An Equation of State for Low-Mass Stars and Giant Planets. , v. 99, p. 713, ago. 1995.
- Schönberg, M.; Chandrasekhar, S. On the Evolution of the Main-Sequence Stars. , v. 96, p. 161, set. 1942.
- Schwarzschild, K. On the equilibrium of the Sun's atmosphere. *Nachrichten von der Königl. Gesellschaft der Wissenschaften zu Göttingen. Math.-phys. Klasse*, v. 195, p. 41–53, jan. 1906.
- Segretain, L. et al. Cooling Theory of Crystallized White Dwarfs. , v. 434, p. 641, out. 1994.
- Siess, L. Evolution of massive AGB stars. II. model properties at non-solar metallicity and the fate of Super-AGB stars. , v. 476, n. 2, p. 893–909, dez. 2007.
- Smartt, S. J. Progenitors of Core-Collapse Supernovae. , v. 47, n. 1, p. 63–106, set. 2009.
- Snedden, C. CNO Abundances of Stars Undergoing First Dredge up Mixing. In: Michaud, G.; Tutukov, A. V. (Ed.). *Evolution of Stars: the Photospheric Abundance Connection*. [S.l.: s.n.], 1991. v. 145, p. 235.
- Spruit, H. C. The growth of helium-burning cores. , v. 582, p. L2, out. 2015.
- Stancliffe, R. J. The effects of thermohaline mixing on low-metallicity asymptotic giant branch stars. , v. 403, n. 1, p. 505–515, mar. 2010.
- Stancliffe, R. J.; Glebbeek, E. Thermohaline mixing and gravitational settling in carbon-enhanced metal-poor stars. , v. 389, n. 4, p. 1828–1838, out. 2008.
- Stancliffe, R. J. et al. Carbon-enhanced metal-poor stars and thermohaline mixing. , v. 464, n. 3, p. L57–L60, mar. 2007.
- Straniero, O. Challenges for nuclear astrophysics: low mass stars. , v. 78, p. 492, jan. 2007.
- Straniero, O. et al. The Chemical Composition of White Dwarfs as a Test of Convective Efficiency during Core Helium Burning. , v. 583, p. 878–884, fev. 2003.
- Suda, T.; Hirschi, R.; Fujimoto, M. Y. Stellar Evolution Constraints on the Triple- $\alpha$  Reaction Rate. , v. 741, n. 1, p. 61, nov. 2011.
- Sukhbold, T.; Adams, S. Missing red supergiants and carbon burning. , v. 492, n. 2, p. 2578–2587, fev. 2020.

- Takayama, M.; Saio, H.; Ita, Y. On the pulsation modes of OGLE small amplitude red giant variables in the LMC. , v. 431, n. 4, p. 3189–3195, jun. 2013.
- Tayar, J. et al. The Correlation between Mixing Length and Metallicity on the Giant Branch: Implications for Ages in the Gaia Era. , v. 840, n. 1, p. 17, maio 2017.
- Taylor, G. I. The instability of liquid surfaces when accelerated in a direction perpendicular to their planes. I. *R. Soc. Lond*, v. 201, p. 192–196, mar. 1950.
- Thompson, I. J.; Nunes, F. M. *Nuclear Reactions for Astrophysics: Principles, Calculation and Applications of Low-Energy Reactions*. [S.l.: s.n.], 2009.
- Thoul, A. A.; Bahcall, J. N.; Loeb, A. Element Diffusion in the Solar Interior. , v. 421, p. 828, fev. 1994.
- Tilley, D. R.; Weller, H. R.; Cheves, C. M. Energy levels of light nuclei  $A = 16-17$ . *Nuclear Physics A*, v. 564, p. 1–183, nov. 1993.
- Timmes, F. X.; Swesty, F. D. The Accuracy, Consistency, and Speed of an Electron-Positron Equation of State Based on Table Interpolation of the Helmholtz Free Energy. , v. 126, p. 501–516, fev. 2000.
- Tremblay, P. E. et al. Granulation properties of giants, dwarfs, and white dwarfs from the CIFIST 3D model atmosphere grid. , v. 557, p. A7, set. 2013.
- Tremblay, P. E. et al. Solution to the problem of the surface gravity distribution of cool DA white dwarfs from improved 3D model atmospheres. , v. 531, p. L19, jul. 2011.
- Tremblay, P. E. et al. Spectroscopic analysis of DA white dwarfs with 3D model atmospheres. , v. 559, p. A104, nov. 2013.
- Tur, C.; Heger, A.; Austin, S. M. On the Sensitivity of Massive Star Nucleosynthesis and Evolution to Solar Abundances and to Uncertainties in Helium-Burning Reaction Rates. , v. 671, n. 1, p. 821–827, dez. 2007.
- Tur, C.; Heger, A.; Austin, S. M. Production of  $^{26}\text{Al}$ ,  $^{44}\text{Ti}$ , and  $^{60}\text{Fe}$  in Core-collapse Supernovae: Sensitivity to the Rates of the Triple Alpha and  $^{12}\text{C}(\alpha, \gamma)^{16}\text{O}$  Reactions. , v. 718, p. 357–367, jul. 2010.
- Ulrich, R. K. Thermohaline Convection in Stellar Interiors. , v. 172, p. 165, fev. 1972.
- Umeda, H. et al. Evolution of 3-9  $M_{\text{solar}}$  Stars for  $Z=0.001-0.03$  and Metallicity Effects on Type Ia Supernovae. , v. 513, n. 2, p. 861–868, mar. 1999.
- Unglaub, K.; Bues, I. The chemical evolution of hot white dwarfs in the presence of diffusion and mass loss. , v. 359, p. 1042–1058, jul. 2000.
- van Loon, J. T. et al. An empirical formula for the mass-loss rates of dust-enshrouded red supergiants and oxygen-rich Asymptotic Giant Branch stars. , v. 438, n. 1, p. 273–289, jul. 2005.
- Vassiliadis, E.; Wood, P. R. Evolution of Low- and Intermediate-Mass Stars to the End of the Asymptotic Giant Branch with Mass Loss. , v. 413, p. 641, ago. 1993.
- Ventura, P. et al. Gas and dust from metal-rich AGB stars. , v. 641, p. A103, set. 2020.



- Ventura, P.; Marigo, P. Evolution and chemical yields of AGB stars: effects of low-temperature opacities. , v. 399, n. 1, p. L54–L58, out. 2009.
- Wachter, A. et al. An improved mass-loss description for dust-driven superwinds and tip-AGB evolution models. , v. 384, p. 452–459, mar. 2002.
- Wagenhuber, J.; Groenewegen, M. A. T. New input data for synthetic AGB evolution. , v. 340, p. 183–195, dez. 1998.
- Wallerstein, G. et al. Synthesis of the elements in stars: forty years of progress. *Reviews of Modern Physics*, v. 69, n. 4, p. 995–1084, Oct 1997.
- Weaver, T.; Woosley, S. Nucleosynthesis in massive stars and the  $^{12}\text{C}(\alpha, \gamma)^{16}\text{O}$  reaction rate. *Physics Reports*, v. 227, n. 1, p. 65 – 96, 1993.
- Weidemann, V. Revision of the initial-to-final mass relation. , v. 363, p. 647–656, nov. 2000.
- Weiss, A.; Ferguson, J. W. New asymptotic giant branch models for a range of metallicities. , v. 508, n. 3, p. 1343–1358, dez. 2009.
- West, C.; Heger, A.; Austin, S. M. The Impact of Helium-burning Reaction Rates on Massive Star Evolution and Nucleosynthesis. , v. 769, n. 1, p. 2, maio 2013.
- Williams, J. H.; Haxby, R. O.; Shepherd, W. G. The Disintegration of Beryllium and the Masses of the Beryllium Isotopes. *Physical Review*, v. 52, n. 10, p. 1031–1034, nov. 1937.
- Williams, J. H.; Shepherd, W. G.; Haxby, R. O. The Disintegration of Lithium by Deuterons. *Physical Review*, v. 52, n. 5, p. 390–396, set. 1937.
- Williams, J. H. et al. A Resonance Process in the Disintegration of Boron by Protons. *Physical Review*, v. 51, n. 6, p. 434–438, mar. 1937.
- Winget, D. E. et al. The Physics of Crystallization From Globular Cluster White Dwarf Stars in NGC 6397. , v. 693, n. 1, p. L6–L10, mar. 2009.
- Winget, D. E. et al. Whole Earth Telescope Observations of the DBV White Dwarf GD 358. , v. 430, p. 839, ago. 1994.
- Woosley, S. E. et al. Nuclear data needs for the study of nucleosynthesis in massive stars. , v. 718, p. 3–12, maio 2003.
- Woosley, S. E.; Heger, A.; Weaver, T. A. The evolution and explosion of massive stars. *Reviews of Modern Physics*, v. 74, n. 4, p. 1015–1071, nov. 2002.
- Woosley, S. E.; Weaver, T. A. The Evolution and Explosion of Massive Stars. II. Explosive Hydrodynamics and Nucleosynthesis. , v. 101, p. 181, Nov 1995.
- Wu, C. et al. The formation of type Ia supernovae from carbon-oxygen-silicon white dwarfs. , v. 495, n. 1, p. 1445–1460, maio 2020.
- Xu, Y. et al. NACRE II: an update of the NACRE compilation of charged-particle-induced thermonuclear reaction rates for nuclei with mass number  $A \leq 16$ . *Nuclear Physics A*, v. 918, p. 61–169, nov. 2013.

Yakovlev, D. G.; Urpin, V. A. Thermal and Electrical Conductivity in White Dwarfs and Neutron Stars. , v. 24, p. 303, jun. 1980.

Yoon, S. C.; Langer, N.; Norman, C. Single star progenitors of long gamma-ray bursts. I. Model grids and redshift dependent GRB rate. , v. 460, n. 1, p. 199–208, dez. 2006.


Zimmerman, W. R. et al. Unambiguous Identification of the Second  $2^+$  State in C12 and the Structure of the Hoyle State. , v. 110, n. 15, p. 152502, abr. 2013.

# Appendix



# APPENDIX A – Published Works

# The impact of the uncertainties in the $^{12}\text{C}(\alpha, \gamma)^{16}\text{O}$ reaction rate on the evolution of low- to intermediate-mass stars

Ben T. Pepper,<sup>1</sup>  A. G. Istrate<sup>2</sup>, A. D. Romero<sup>1</sup> and S. O. Kepler<sup>1</sup>

<sup>1</sup>Physics Institute, Universidade Federal do Rio Grande do Sul, 91501-900 Porto-Alegre, RS, Brazil

<sup>2</sup>Department of Astrophysics/IMAPP, Radboud University, P O Box 9010, NL-6500 GL Nijmegen, The Netherlands

Accepted XXX. Received YYY; in original form ZZZ

## ABSTRACT

One of the largest uncertainties in stellar evolutionary computations is the accuracy of the considered reaction rates. The  $^{12}\text{C}(\alpha, \gamma)^{16}\text{O}$  reaction is particularly important for the study of low- and intermediate-mass stars as it determines the final C/O ratio in the core which influences the white dwarf cooling evolution. Thus, there is a need for a study of how the computations of white dwarfs and their progenitors that are made to date may be affected by the uncertainties of the  $^{12}\text{C}(\alpha, \gamma)^{16}\text{O}$  reaction rates. In this work we compute fully evolutionary sequences using the MESA code with initial masses in the range of  $0.90 \leq M_i/M_\odot \leq 3.05$ . We consider different adopted reaction rates, obtained from the literature, as well as the extreme limits within their uncertainties. As expected, we find that previous to the core helium burning stage, there are no changes to the evolution of the stars. However, the subsequent stages are all affected by the uncertainties of the considered reaction rate. In particular, we find differences to the convective core mass during the core helium burning stage which may affect pulsation properties of subdwarfs, the number of thermal pulses during the asymptotic giant branch and trends between final oxygen abundance in the core and the progenitor masses of the remnant white dwarfs.

**Key words:** nuclear reactions – stars: abundances – stars: evolution

## 1 INTRODUCTION

Single stellar evolution is fuelled by nuclear reactions that occur within the stellar interior (Bethe 1939; Hoyle 1946, 1954; Burbidge et al. 1957). These reactions not only release energy which allows the star to support itself against gravitational collapse and remain in hydrostatic equilibrium, but also change the composition of the star: this is known as nucleosynthesis (Eddington 1920; Hoyle 1954; Burbidge et al. 1957). The study of these nuclear reactions is where nuclear physics and astronomy come hand-in-hand; an understanding of what happens at the fundamental level provides a better knowledge of how stars evolve and influence their environment. Particularly, improved estimations of the often uncertain reaction rate data, including formula fitted to such data, will improve the accuracy of stellar evolution codes and the understanding of stellar evolution (Caughlan & Fowler 1988; Angulo et al. 1999; Katsuma 2012; Xu et al. 2013; An et al. 2016). Such estimations are hereafter referred to as ‘reaction rates’.

The  $^{12}\text{C}(\alpha, \gamma)^{16}\text{O}$  reaction during the central helium burning stage is considered to be the most important mechanism for defining the white dwarf (WD) core composition (Salaris & Cassisi 2005; D’Antona & Mazzitelli 1990; De Gerónimo et al. 2017; Deboer et al. 2019). However, the reaction rate for this reaction has an extremely large uncertainty (Fowler et al. 1967; Caughlan & Fowler 1988; Kunz

et al. 2002; An et al. 2016; Deboer et al. 2017, 2019). The main entrance channel for the  $^{12}\text{C}+\alpha$  mechanism ( $E_{\alpha_0} = 7.16$  MeV) does not have a resonance channel close to this threshold, the closest occurring at  $E_x = 9.59$  MeV. Instead, the low energy cross-section is largely influenced by the  $1^{-1}$  ( $E_x = 7.12$  MeV) and  $2^{+}$  ( $E_x = 6.92$  MeV) subthreshold states (see Figure 2 of Deboer et al. 2017, for details). The primary influence of these two nearby subthreshold states and the addition of possible resonant transitions in the wings of the broad channel at  $E_x = 9.59$  MeV makes the nuclear cross-section extremely difficult to estimate (see Fowler et al. 2002; An et al. 2016; Deboer et al. 2017, 2019; Aliotta et al. 2021).

During the core helium burning (CHB) stage, carbon is produced from the fusion of three helium nuclei via the triple- $\alpha$  process (Salpeter 1952; Kippenhahn & Weigert 1990; Salaris & Cassisi 2005; Prialnik 2009). As the abundance of helium in the core depletes, the probability of carbon interacting with helium to produce oxygen [via  $^{12}\text{C}(\alpha, \gamma)^{16}\text{O}$ ] is larger than that of the triple- $\alpha$  process at late times during the core helium burning stage (Salaris & Cassisi 2005). Thus, the  $^{12}\text{C}(\alpha, \gamma)^{16}\text{O}$  reaction is of great importance and is vital to model the carbon-oxygen (C/O) abundance in the inner chemical profiles for all stellar masses, but particularly low- and intermediate-mass stars (Woosley & Weaver 1995; Weaver & Woosley 1993; Wallerstein et al. 1997).

The C/O abundance, therefore the  $^{12}\text{C}(\alpha, \gamma)^{16}\text{O}$  reaction, is important in many areas of stellar evolution. Such as, influencing the pulsation properties of ZZ Ceti stars (De Gerónimo et al. 2015, 2017).

\* E-mail: ben.pepper2012@gmail.com

Differences between the considered  $^{12}\text{C}(\alpha, \gamma)^{16}\text{O}$  reaction rate will also affect the duration of the core helium burning stage (Deboer et al. 2017). In addition, the  $^{12}\text{C}(\alpha, \gamma)^{16}\text{O}$  reaction impacts supernova explosions as the outcome is related to the composition of the final WD (e.g. Iben & Tutukov 1984; Wu et al. 2020) and third dredge-up episodes (TDUs) during the asymptotic giant branch (AGB) stage (Frost & Lattanzio 1996; Karakas et al. 2002; Marigo 2002; Karakas & Lattanzio 2003; Marigo 2007; Cristallo et al. 2009; Weiss & Ferguson 2009; Ventura & Marigo 2009; Kalirai et al. 2014; Matteucci 2021). Furthermore, thermonuclear explosions of C/O WDs impacts the ignition of Type Ia supernovae, an important event in constraining cosmological parameters (Perlmutter et al. 1999; Riess et al. 1998). The enrichment of the outer layer of the AGB stars from dredge-up and the mass-loss affects the chemical evolution of galaxies (Matteucci 2012; Boothroyd & Sackmann 1988; Kobayashi et al. 2020; Ventura et al. 2020; Cristallo et al. 2015; Matteucci 2021). Additionally, the  $^{12}\text{C}(\alpha, \gamma)^{16}\text{O}$  reaction governs whether a star will form a neutron star or black hole (Brown et al. 2001; Heger et al. 2002; Tur et al. 2007; West et al. 2013; Sukhbold & Adams 2020). Gravitational wave detections from black hole mergers can also be used to constrain the  $^{12}\text{C}(\alpha, \gamma)^{16}\text{O}$  reaction rate by determining the mass of the black hole and the fraction of carbon and oxygen that remains (see Farmer et al. 2020, for details).

De Gerónimo et al. (2015) and De Gerónimo et al. (2017) consider 3 different reaction rates: an adopted rate from Angulo et al. (1999) and the high and low rates from Kunz et al. (2002). They consider these alternate rates for the CHB until the thermally pulsing asymptotic giant branch (TP-AGB) phase with a sole focus on how the pulsational properties are affected in ZZ Ceti stars, rather than all stages as we attempt in this work.

In this work, we use stellar evolutionary models as tools to study the impact of the  $^{12}\text{C}(\alpha, \gamma)^{16}\text{O}$  reaction rate uncertainties on the stellar structure and evolution of low- and intermediate-mass stars. The paper is organised as follows. Section 2 describes the input physics and numerical tool used to compute the evolutionary sequences, as well as a deeper discussion of the considered  $^{12}\text{C}(\alpha, \gamma)^{16}\text{O}$  reaction rates used in this work. In section 3 we present and discuss our results. We summarise our work in section 4, concluding our findings and indicating future areas where the impact of this work may affect.

## 2 NUMERICAL TOOLS

### 2.1 MESA Input Physics

In this work we employ the Modules for Experiments in Stellar Astrophysics (MESA) code version-r15140 (see Paxton et al. (2011, 2013, 2015, 2018), for details). We compute the full evolutionary sequence from the zero age main sequence (ZAMS) through both core hydrogen and helium burning stages, leading to the AGB and the white dwarf stage (WD). The computation stops when the stellar model reaches a luminosity of  $\log(L/L_{\odot}) = -3$  on the WD cooling track. This stopping condition is applied such that the sequences have experienced their evolution through the DAV instability strip (Fontaine & Brassard 2008; Winget & Kepler 2008; Althaus et al. 2010). This allows for asteroseismology of ZZ Ceti stars to be performed in the future. The final WD masses obtained in this work range from  $0.513M_{\odot} \leq M_f/M_{\odot} \leq 0.691M_{\odot}$ . The initial mass range considered in this work is selected such that all sequences evolve into a carbon–oxygen WD (examples of works which consider/include a similar mass range are Renedo et al. 2010; Romero et al. 2015; De Gerónimo et al. 2017; Marigo et al. 2020).

We compute a total of 246 sequences, with an initial metallicity of  $Z_i = 0.01$  and 41 initial masses in the range of  $0.90 \leq M_i/M_{\odot} \leq 3.05$ . For each initial mass, we compute the full evolution considering 6 different formulae for the  $^{12}\text{C}(\alpha, \gamma)^{16}\text{O}$  reaction rate. The 6 reaction rates are adapted from Angulo et al. (1999) and An et al. (2016). Each source comprises 3 reaction rates: the adopted rate, the low and high limiting values, given by the reported uncertainties of the respective rate (see Section 2.2). The rates taken from Angulo et al. (1999) are part of the NACRE compilation and have been used extensively in other computations (Renedo et al. 2010; Romero et al. 2015; De Gerónimo et al. 2017). The reaction rates from An et al. (2016) are less recognised, but boast a lower uncertainty on their reported adopted reaction rate. More detail on these rates and their significance can be found in Section 2.2.

We use the reaction network 'basic.net', which comprises 33 individual reactions including the full p-p chain, CNO cycle,  $3\alpha$  up until  $^{24}\text{Mg}$ , which contains the  $^{12}\text{C}(\alpha, \gamma)^{16}\text{O}$  reaction. This network also includes 8 individual isotopes:  $^1\text{H}$ ,  $^3\text{He}$ ,  $^4\text{He}$ ,  $^{12}\text{C}$ ,  $^{14}\text{N}$ ,  $^{16}\text{O}$ ,  $^{20}\text{Ne}$ ,  $^{24}\text{Mg}$  in addition to elementary and  $\alpha$  particles.

In our computations, we consider the default radiative opacity tables within MESA. These are from Ferguson et al. (2005) (for  $2.7 \leq \log T \leq 4.5$ ) and from the OPAL project (for  $3.75 \leq \log T \leq 8.7$ ) (Iglesias & Rogers 1993, 1996). Furthermore, we consider OPAL Type 2 tables as they allow for varying amounts of C and O, which are needed for helium burning and beyond (Iglesias & Rogers 1996; Paxton et al. 2011).

We adopt the standard mixing length free parameter as  $\alpha = 2.0118$ . This value is adopted from the work of Guzik et al. (2016) who found this value to be a good approximation for sequences that consider the solar metallicity when using the opacity tables from the OPAL project. To derive this value, Guzik et al. (2016) compared calculated non-adiabatic solar oscillation frequencies and solar interior sound speeds to observed frequencies and helioseismic inferences. However, it should be noted that Guzik et al. (2016) consider an initial metallicity of  $Z_i = 0.015$ , rather than the value we consider in this work ( $Z_i = 0.01$ ). Such a difference would alter the value of the  $\alpha$  parameter if a similar analysis was performed with this initial metallicity consideration. Convective mixing is treated as a time-dependent diffusion process, with the diffusion coefficient given as,

$$D_{EM} = D_0 \exp(-2z/fH_P) \quad (1)$$

where  $H_P$  is the pressure scale-height at the convective boundary,  $D_0$  is the diffusion coefficient of the unstable regions that are near the convective boundary, and  $z$  is the geometric distance from the convective boundary.  $f$  is an adjustable free parameter that controls the efficiency of mixing by setting the size of the overshooting region (Herwig et al. 1997; Herwig 2000). We take the value of  $f = 0.016$  for all regions of the model for this work, following the same consideration of overshooting as Herwig (2000); Weiss & Ferguson (2009); De Gerónimo et al. (2017). This treatment of the convective boundaries was also adopted by other authors for single stellar evolution computations (Weiss & Ferguson 2009; Romero et al. 2015; De Gerónimo et al. 2017).

The presence of dredge-up episodes during the core helium burning stage is relevant for the final composition of WDs (Prada Moroni & Straniero 2002; Straniero et al. 2003; Renedo et al. 2010). During the thermally pulsing AGB phase, although overshooting was considered at the boundary of the convective H-rich envelope during the TP-AGB, the third dredge-up episodes did not occur. Therefore, the evolution of the hydrogen–exhausted core (which is hereafter simply referred to as "the helium core mass") and the final mass of the

sequences for those which should experience some third dredge-up episodes will be affected (see Section 3.2). We define the "helium core mass" as the region from the centre until the local abundance of hydrogen is greater than  $10^{-6}$ . Additional models were computed to assess the impact of the third dredge-up on the core mass growth during the thermal pulses (see Section 3.2 and Appendix B for details).

For regions stable against convection according to the Ledoux criterion, but there is an inversion of mean molecular weight, we employ thermohaline mixing. In MESA this is treated as a diffusion process, as above, with a diffusion coefficient produced by the stability analysis of Ulrich (1972) and Kippenhahn et al. (1980). For the efficiency parameter of thermohaline mixing, we consider  $\alpha_{th} = 1.0$  (see Equation 14 of Paxton et al. 2013, for details)). Thermohaline mixing was considered in order to smooth a discontinuity in the carbon and oxygen chemical profiles at the edge of the C/O core, during the early-AGB.

Towards the end of the core helium burning stage, when the central He abundance is lower than  $\sim 10\%$ , breathing pulse-like instabilities may appear. However, these events are attributed to adopted algorithms rather than to the physics of convection (see Straniero et al. 2003; Romero et al. 2015; Constantino et al. 2016, 2017, for details). To suppress the breathing pulses, when the central abundance of He drops below 0.13, we neglect convection until the central abundance of helium decreases below  $10^{-6}$ , similar to the prescription used by Renedo et al. (2010) and Romero et al. (2015). Without this prescription, the final carbon-to-oxygen (C/O) ratios can vary rapidly (up to  $\pm 0.1$ ) with small increments of initial mass ( $0.05 M_{\odot}$ ).

During the main sequence (MS), red-giant branch (RGB) and core helium burning stages, the mass-loss due to stellar winds follows the rate based on the Reimers formula (see Reimers 1975). The asymptotic giant branch and subsequent evolution follow a rate based on the Bloeker formula instead (see Bloeker 1995). We set our scale factors to be  $\eta_R = 0.5$  and  $\eta_B = 0.2$  for the Reimers and Bloeker formulae, respectively. These values are chosen as they reproduce a WD with a similar final mass to that found by Renedo et al. (2010) for  $M_i = 1.00 M_{\odot}$  with  $Z_i = 0.01$ .

A grey atmosphere is employed for the entire evolution of all sequences, which utilises the grey Eddington  $\tau$  relation. We consider the equations of state ELM EOS and DT2 EOS, which are derived from the HELM EOS (Timmer & Swesty 2000) and the SCVH tables (Saumon et al. 1995), respectively.

Once the star leaves the AGB, we employ an element diffusion process from the work of Burgers (1969). We refer to element diffusion as the physical mechanism for mixing chemicals that includes gravitational settling, thermal diffusion and chemical diffusion. Gravitational settling leads to denser element diffusing towards the core, while lighter elements float towards the surface. Thermal diffusion acts in the same direction as gravitational settling, although to a lesser extent, bringing highly charged and more massive species to the central regions of the star. Chemical diffusion, however, works against this general direction (see Iben & MacDonald 1985; Thoul et al. 1994, for details). In addition to the aforementioned processes, MESA includes radiative accelerations (Hu et al. 2011) into their element diffusion prescription. These radiative forces are negligible in hot regions, as well as being computationally demanding. Hence, we do not consider the effects of radiative levitation. Our element diffusion process is applied to the following isotopes:  $^1\text{H}$ ,  $^3\text{He}$ ,  $^4\text{He}$ ,  $^{12}\text{C}$ ,  $^{14}\text{N}$ ,  $^{16}\text{O}$ ,  $^{20}\text{Ne}$ ,  $^{24}\text{Mg}$ .

## 2.2 The $^{12}\text{C}(\alpha, \gamma)^{16}\text{O}$ Reaction

Here we discuss a brief, yet relevant, history of  $^{12}\text{C}(\alpha, \gamma)^{16}\text{O}$  reaction rate evaluations. We lead this into further detail for the  $^{12}\text{C}(\alpha, \gamma)^{16}\text{O}$  reaction rate prescriptions from Angulo et al. (1999) and An et al. (2016), discussing their differences to the previous determinations from the literature.

Fowler et al. (1967) organised the first symposium of reaction rate cross-sections that included the  $^{12}\text{C}(\alpha, \gamma)^{16}\text{O}$  reaction. At the time, many resonant factors were neglected and were updated by Caughlan & Fowler (1988). However, it is believed that some resonances were still neglected and the treatment of the S-factor in this work produced values that are too small and require a scale factor of  $\sim 2$  to produce a realistic S-Factor (Angulo et al. 1999; Kunz et al. 2002; Heil et al. 2008; An et al. 2016; Deboer et al. 2017, 2019).

Built upon the works of Fowler et al. (1967); Caughlan & Fowler (1988) and those associated works in between, Angulo et al. (1999) provided a strong basis for the  $^{12}\text{C}(\alpha, \gamma)^{16}\text{O}$  reaction within the NACRE compilation. Angulo et al. (1999) provided the reaction rates for 86 different reactions, including  $^{12}\text{C}(\alpha, \gamma)^{16}\text{O}$ . For the S-factor calculations, Angulo et al. (1999) considered the values for non-resonant energies. For narrow resonances, however, they fit the resulting cross-section using a Briet-Wigner model. When the effects of different resonant energies overlap, they use a multi-resonance fit, shown in equation 29 of Angulo et al. (1999). Angulo et al. (1999) state that their analysis is numerical for the majority, although they do provide an analytical approach for each reaction, for completeness. They find that their numerical approach yields a higher accuracy for their calculated reaction rates. The quoted S-Factor value from Angulo et al. (1999) for a stellar energy of 300 keV is  $S(300 \text{ keV}) = 199 \pm 64 \text{ keV b}$ , resulting in a reaction rate ( $RR$ ) of  $RR(300 \text{ keV}) = (9.11_{-3.67}^{+3.69}) \cdot 10^{-15} \text{ cm}^3 \text{ mole}^{-1} \text{ s}^{-1}$ . A stellar energy of  $E = 300 \text{ keV}$  is often chosen as the energy at which to compare the S-factors across different works, as it is associated with the ignition of core helium burning. In this work, we consider the adopted rate of Angulo et al. (1999) (NACRE\_A) and the highest and lowest reaction rate within the uncertainties (NACRE\_H and NACRE\_L, respectively). Hereafter, we refer to the collective  $^{12}\text{C}(\alpha, \gamma)^{16}\text{O}$  reaction rates from Angulo et al. (1999) as 'NACRE'.

An et al. (2016) point out that the resonance parameters used by Kunz et al. (2002), which were taken from Tilley et al. (1993), neglect the ground state transitions from the works of Brochard, F. et al. (1975); Ophel et al. (1976). This results in a larger value for the expected reaction rate at helium burning temperatures. Instead, An et al. (2016) use the reduced R-matrix and S-factor derived by An et al. (2015) to estimate the reaction rate, which accounted for all transitions.

In their computations, An et al. (2015) and An et al. (2016) found a significant reduction to the uncertainty of their S-factors when compared to that of Angulo et al. (1999),  $S(300 \text{ keV}) = 162.7 \pm 7.3 \text{ keV b}$ . The reaction rate for the same energy resulted  $RR(300 \text{ keV}) = (7.83 \pm 0.35) \times 10^{-15} \text{ cm}^3 \text{ mole}^{-1} \text{ s}^{-1}$ . We consider the adopted rate from An et al. (2016) (An\_A) and the highest and lowest reaction rate within the uncertainties (An\_H and An\_L, respectively). However, the S-factor calculation of An et al. (2015), seems to neglect external contributions for ground state energy levels, making this approximation not valid for high precision analysis (Deboer et al. 2017). Therefore, we treat the uncertainties of the  $^{12}\text{C}(\alpha, \gamma)^{16}\text{O}$  reaction rate from An et al. (2016) as arbitrary differences to determine the effect of the urgent need for more precise  $^{12}\text{C}(\alpha, \gamma)^{16}\text{O}$  reaction rate uncertainties, as claimed by Kunz et al. (2002); Tur et al. (2010). Some works further claim that the uncer-



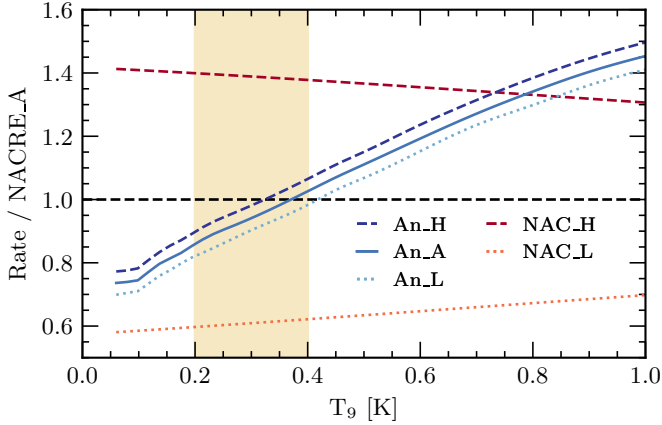


**Figure 1.** Ratios of each reaction rate considered when compared to the adopted NACRE rate for the  $^{12}\text{C}(\alpha, \gamma)^{16}\text{O}$  reaction, as a function of temperature, where  $T_9 = T/10^9$ . The beige shaded region defines the temperatures where helium burning occurs. During the core helium burning stage is also where the  $^{12}\text{C}(\alpha, \gamma)^{16}\text{O}$  reaction is most prominent. The light-orange dotted and red dashed lines represent the NACRE\_L and NACRE\_H considerations, respectively. The solid blue line defines the adopted rate from [An et al. \(2016\)](#) with the An\_L and An\_H rates being depicted as light-blue dotted and dark-blue dashed lines, respectively.

tainty must be less than 10% to be on par with non-nuclear physical uncertainties (see [Woodsley et al. 2003](#); [Deboer et al. 2017](#), for details).

Figure 1 shows a comparison between the adopted reaction rates from [An et al. \(2016\)](#), NACRE and all of their associated uncertainties. In this figure, we depict for each rate, the ratio between the rate and the value for NACRE\_A, as a function of temperature. For an analysis including other works, see Figure 4 of [An et al. \(2016\)](#). As can be seen from Figure 1, for energies characteristic of stellar energies, the An\_A, An\_H and An\_L reaction rates are lower than for NACRE\_A for most temperatures within the beige shaded region, characteristic of core helium burning temperatures. We therefore expect to have a larger C/O ratio in the core after the central helium burning stage for the sequences which consider the rate from [An et al. \(2016\)](#) when compared to those sequences which consider NACRE\_A. It can also be seen in Figure 1 that the range between NACRE\_H and NACRE\_L includes all the other prescriptions within the region of helium burning temperatures, which will lead to the largest differences in the C/O ratio after the core helium burning stage. At higher temperatures (greater than those considered to be helium burning temperatures) the reaction rate from [An et al. \(2016\)](#) is larger than that from NACRE. These temperatures are not reached in the sequences computed within this work.

### 3 RESULTS AND DISCUSSIONS

In this section we describe in detail the effects that the uncertainties of the  $^{12}\text{C}(\alpha, \gamma)^{16}\text{O}$  reaction rate have on the inner structure and evolution for low- and intermediate-mass single stars. As expected, during the pre-main sequence, main sequence (MS) and red-giant branch (RGB), we find no differences to the evolution since the  $^{12}\text{C}(\alpha, \gamma)^{16}\text{O}$  reaction only becomes important, and increasingly more dominant, during the CHB as the central helium abundance decreases ([Salaris & Cassisi 2005](#); [Spruit 2015](#); [Deboer et al. 2019](#)). Thus, we report no difference between the different  $^{12}\text{C}(\alpha, \gamma)^{16}\text{O}$  reaction rates at the time of, or shortly after, the helium-flash or a non-degenerate helium ignition. We only show the results from

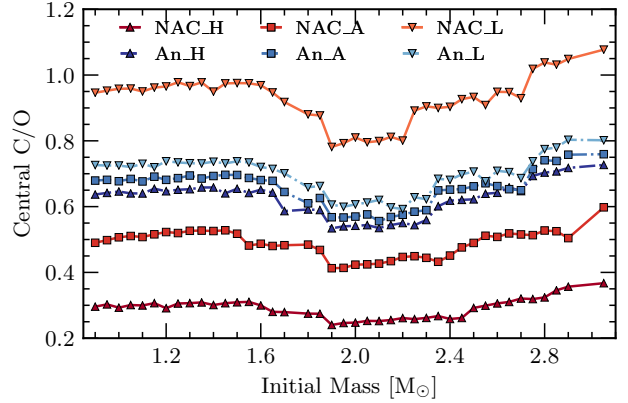


**Figure 2.** Central C/O ratio at the end of the CHB as a function of initial mass. The red points represent the reaction rates considered by NACRE and the blue points are those considered by [An et al. \(2016\)](#). Additionally, squares represent the respective adopted rates while darker-coloured triangles and lighter-coloured upside-down triangles represent the high and low limit uncertainties, respectively.

the CHB, AGB and WD stages where we expect some differences to occur due to the uncertainties and separate literature sources of the  $^{12}\text{C}(\alpha, \gamma)^{16}\text{O}$  reaction rate. We consider each evolutionary stage separately in chronological order.

#### 3.1 The Core Helium Burning Phase

Figure 2 shows the carbon-to-oxygen (C/O) ratio for each star at the end of CHB, as a function of initial mass. As expected due to the large uncertainties of the reaction rate from NACRE, the smallest and largest C/O ratios come from the NACRE\_H and NACRE\_L rates, respectively. Note that when all reaction rates from [An et al. \(2016\)](#) are considered, the values for the C/O ratios are between the values corresponding to NACRE\_A and NACRE\_L.

We find that the C/O ratio at the end of the CHB decreases for all considered reaction rates around an initial mass of  $M_i = 1.90 M_\odot$ . This mass corresponds to the minimum mass for which helium burning starts in non-degenerate conditions, and will be referred to as the transition mass. The C/O ratio increases again for higher initial masses (between  $2.20 \leq M_i/M_\odot \leq 2.45$ ). We find that the initial mass where the increase of the C/O ratio occurs is dependent on the considered  $^{12}\text{C}(\alpha, \gamma)^{16}\text{O}$  reaction rate, such that higher reaction rates have a wider initial mass range for the decreased C/O ratio and lower reaction rates have a narrower initial mass range. For example, the NACRE\_H has the widest range ( $1.90 \leq M_i/M_\odot \leq 2.45$ ) whereas the NACRE\_L has the narrowest range ( $1.90 \leq M_i/M_\odot \leq 2.20$ ). Furthermore, we find no difference to the initial mass range between the adopted rate from [An et al. \(2016\)](#) and the An\_H and An\_L rates. We also add that the decrease in the C/O ratio is more pronounced for less efficient reaction rates, see Figure 2, for details.

Figure 3 shows the time spent in the CHB as a function of initial mass for the High and Low reaction rate formulas for NACRE (left panel) and [An et al. \(2016\)](#) (right panel). We consider the difference in the CHB age from the values obtained using the respective adopted reaction rate for each panel. Considering the NACRE rates (left panel of Figure 3), we find that the CHB lifetime can be up to 12 Myr shorter (longer) from the adopted rate if we consider NACRE\_L (NACRE\_H) reaction rate, which is roughly a 7% difference. On the other hand the differences between the [An et al. \(2016\)](#) rates are much lower (right panel of Figure 3), up to 4 Myr translating to a

difference of 4%. Such changes to the CHB lifetimes due to limits of the uncertainties on the  $^{12}\text{C}(\alpha, \gamma)^{16}\text{O}$  reaction rate are not negligible, particularly for the rate taken from NACRE. Constantino et al. (2016) found that the difference in the ratio of HB-to-AGB stars in a sample of 48 globular clusters could be explained by the differences in the CHB duration due to the uncertainties in the  $^{12}\text{C}(\alpha, \gamma)^{16}\text{O}$  reaction rate.

The top panel of Figure 4 shows the CHB history of the convective mass. The convective mass is defined as the mass-coordinate of the core convective boundary, such that convection occurs between this mass-coordinate and the centre. Additionally, the bottom panel of Figure 4 shows the luminosities of the  $3\alpha$  process and the  $^{12}\text{C}(\alpha, \gamma)^{16}\text{O}$  reaction (the latter will be referred to as  $C\alpha$  luminosity), for the NACRE reaction rates. As expected, the  $C\alpha$  luminosity increases when the more efficient reaction rates are considered. Furthermore, the contribution from the  $3\alpha$  process decreases for higher reaction rates due to the helium reservoir being depleted faster by the more efficient  $^{12}\text{C}(\alpha, \gamma)^{16}\text{O}$  reaction.

Mixing episodes due to the convective core during the CHB extends from the C/O core to the He-rich layers above, so we define the convective mass as the mass of the convective core. Figure 4 also shows that higher reaction rates produce more mixing episodes which are characterised by sudden increases of the convective mass. These enhanced convective episodes bring fresh helium from the helium region above the C/O core which not only increases the duration of the CHB but also increases the abundance of oxygen in the core (Ghasemi et al. 2017; Guo & Li 2018).

Convective mixing episodes induce a chemical discontinuity between the fully mixed core and the radiative layer, increasing the opacity beyond the convective boundary. In a class of CHB pulsating stars, sdB stars (see Heber 2009, for an in depth discussion), g-modes propagate from the surface all the way until the boundary of the convective core (Ghasemi et al. 2017). Since we find significant differences to the size of the convective core and number of mixing episodes between the NACRE adopted reaction rate and its uncertainties for the  $^{12}\text{C}(\alpha, \gamma)^{16}\text{O}$  reaction rate, the precision of asteroseismology for these objects is limited and must be considered in the calculations of the pulsation period spectrum. However for the adopted rate taken from An et al. (2016), the high and low limits (An\_H and An\_L, respectively) do not produce a significant change to the convective core mass and the total number of mixing episodes and would therefore produce a more precise study of the g-mode pulsations (see Figure A1 in Appendix A, for an example of the same case that considers the reaction rates from An et al. (2016)). The implications for asteroseismology from the treatment to mixing during the CHB has been studied by Constantino et al. (2015) who found that changes to the composition and He-burning reaction rates do not significantly change the period spacing of pulsations for pulsators during the CHB stage. However, the period values could be more sensitive to the changes in the chemical profile.

The total energy produced by the  $^{12}\text{C}(\alpha, \gamma)^{16}\text{O}$  reaction during the CHB is presented in Figure 5. The values shown in Figure 5 are moving averages. We compute the total energy by integrating the  $C\alpha$  luminosity with respect to time for the CHB duration. Figure 5 shows the ratio between the different reaction rates and the NACRE\_A (top panel) and An\_A (bottom panel) reaction rates, as a function of initial mass. If we consider the reaction rates from An et al. (2016), the differences are generally smaller than 10%, the largest difference occurs for the sequence with an initial mass of  $2.85 M_{\odot}$  that considers An\_H. In most cases, the differences are no larger than 5% (70.7% of the sequences for An\_H and 82.9% of the sequences for An\_L).

We find larger differences between the limits of  $^{12}\text{C}(\alpha, \gamma)^{16}\text{O}$

NACRE rates when compared to the NACRE\_A formula, as shown in the top panel of Figure 5. In this case we also compare the adopted reaction rate from An et al. (2016). If we consider how NACRE\_H differs from NACRE\_A, we find that the energy production for the majority of the sequences are greater than 10% than that of the NACRE\_A case, with a few exceeding a difference of 20%. For NACRE\_L, the carbon energy produced differs more than 30% from the NACRE\_A rate. The extra energy produced from the high rates when compared to the adopted rates increases the temperature gradient further allowing convection to continue, causing the extra mixing episodes shown in Figure 4 (Kippenhahn & Weigert 1990; Prialnik 2009).

Considering the adopted rate from An et al. (2016), the absolute value of the differences in carbon energy produced due to An\_H and An\_L appears to be independent of either selection. This is not the case for the NACRE rates. A limiting factor for the amount of energy produced is the abundance of available helium. This is more of a limit for the NACRE\_H case due to lack of available helium inhibiting further reactions to occur. The NACRE\_L will always produce less carbon energy and so is not limited by the helium abundance or lack thereof. The smaller uncertainties of the rates taken from An et al. (2016) are not large enough to produce such an effect.

The CHB stage is where the  $^{12}\text{C}(\alpha, \gamma)^{16}\text{O}$  reaction is the most active. In particular, we find that the largest differences due to the considered  $^{12}\text{C}(\alpha, \gamma)^{16}\text{O}$  reaction rate appear in the final C/O ratio, CHB duration, energy generation rate and the number of experienced mixing episodes. The primary reason that we find such changes to these properties is due to the changes in energy generation that affects the convection efficiency in this phase. Furthermore, we find that the differences between the An\_H and An\_L rates from the An\_A rate are generally insignificant, unlike those of the NACRE uncertainties which are intrinsically larger. A final point to add is that, in future works, the use of overshooting parameters specifically designed for the CHB would be interesting. Works such as Spruit (2015) claim to keep the convective boundaries stable inhibiting the need for manual breathing pulse suppression, as performed in this work, whilst keeping "stable" convection active throughout the evolution (Spruit 2015; Constantino et al. 2017).

### 3.2 The Asymptotic Giant Branch Phase

During the AGB the energy production is given by two shell sources, the hydrogen-shell at the base of the hydrogen-rich envelope and the He-shell on top of the C/O core. Hydrogen burning occurs through the CNO cycle, while He-burning is through the  $3\alpha$  process. Towards the end of the AGB, the He-burning shell will become thin enough to trigger unstable burning, and the thermal pulses (TPs) begin (e.g. Kippenhahn & Weigert 1990; Iben 1991). During the interpulse period between the TPs, the outer convection zone may be deep enough to bring the products of He-shell burning to the surface, this is known as the third dredge-up (TDU) (Wallerstein et al. 1997; Busso et al. 1999; Herwig 2005; Karakas & Lattanzio 2014).

Well known consequences of TDUs are a reduction of the helium core mass and changes to the surface composition, leading to the formation of C-stars (Frost & Lattanzio 1996; Busso et al. 1999; Karakas et al. 2002; Weiss & Ferguson 2009; Romero et al. 2015; Marigo et al. 2020). The extent of the reduction of the helium core mass from TDU episodes is parameterised by the dredge-up efficiency parameter,  $\lambda_d^1$  (see Karakas et al. 2002; Marigo et al. 2013,

<sup>1</sup> The dredge-up efficiency parameter is defined as the fraction of helium

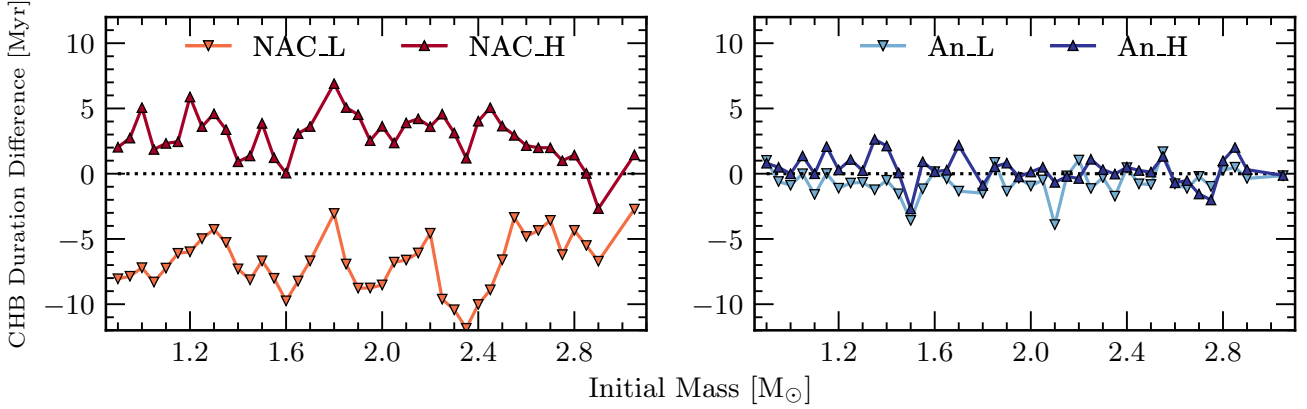


**Figure 3.** Differences to the duration of the CHB stage due to associated reaction rate uncertainties as a function of initial mass. The differences are calculated between each limit of the reaction rate due to their uncertainties and the adopted rate of each case. The left panel shows the differences of the uncertainties of the rate calculated by NACRE and the right panel shows the same from the rate of An et al. (2016). Darker-coloured triangles and lighter-coloured upside-down triangles represent the high and low limit uncertainties, respectively.

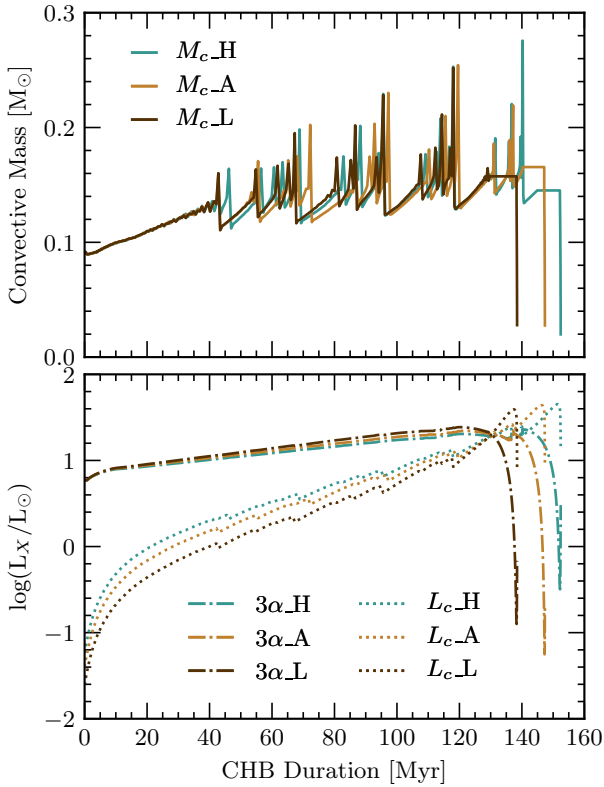


**Figure 4.** History of the convective mass (top panel),  $3\alpha$  luminosity and the luminosity of the  $^{12}\text{C}(\alpha, \gamma)^{16}\text{O}$  reaction during the CHB (bottom panel). The history is given in terms of the CHB duration. This plot in particular considers all NACRE prescriptions for the  $^{12}\text{C}(\alpha, \gamma)^{16}\text{O}$  reaction rate for an initial mass of  $M_i = 2.45 M_{\odot}$ . Blue lines represent NACRE\_H, orange-brown depicts NACRE\_A and dark-brown shows NACRE\_L. Furthermore, the solid line represents the convective mass, dotted lines show the luminosity of the  $^{12}\text{C}(\alpha, \gamma)^{16}\text{O}$  reaction and dot-dash lines portray the  $3\alpha$  luminosity.

for details). The  $^{12}\text{C}(\alpha, \gamma)^{16}\text{O}$  reaction during this stage is essentially

core mass lost during the TDU episode over the helium core mass growth since the last TDU

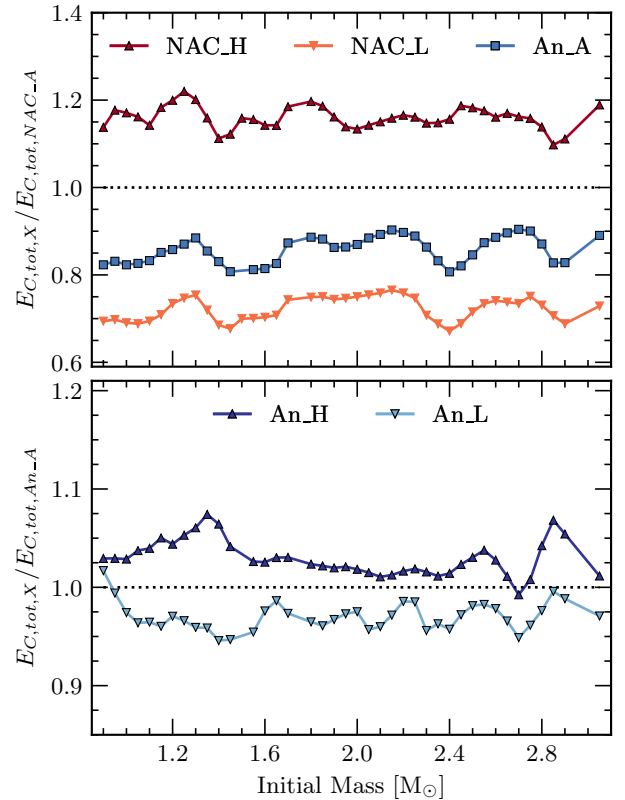


**Figure 5.** Ratios of the total energy produced by the  $^{12}\text{C}(\alpha, \gamma)^{16}\text{O}$  reaction as a function of initial mass. Values are presented in the form of moving averages. The energy produced is calculated by integrating the  $\text{C}\alpha$  luminosity shown in Figure 4 and is integrated with respect to time. The ratios in the top panel are in terms of the NACRE\_A rate and the ratios in the bottom panel are made in terms of An\_A. The red points represent the reaction rates considered by NACRE and the blue points are those considered by An et al. (2016). Additionally, squares represent the respective adopted rates while darker-coloured triangles and lighter-coloured upside-down triangles represent the high and low limit uncertainties, respectively.

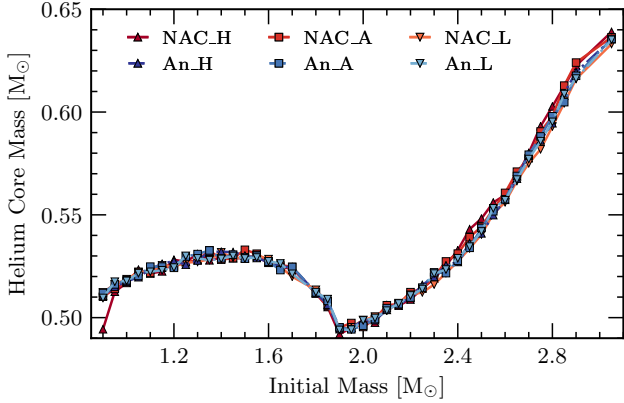


**Figure 6.** Helium core mass at the start of the first TP as a function of initial mass. All of the considered reaction rates and their uncertainties are shown within this figure. We find a minimum to the helium core mass for the same initial mass which corresponds to the transition mass where core helium burning begins on a non-degenerate core rather an electron degenerate core ( $M_i = 1.90 M_\odot$ ). Within the uncertainties, we find differences up to  $0.01 M_\odot$  for masses larger than  $M_i = 1.90 M_\odot$ . The red points represent the reaction rates considered by NACRE and the blue points are those from An et al. (2016). Additionally, squares represent the respective adopted rates while darker-coloured triangles and lighter-coloured upside-down triangles represent the high and low limit uncertainties, respectively.

inactive. There may be some fusion reactions between  $^{12}\text{C}$  and alpha particles at the edge of the C/O core but they are, however, insignificant. Thus, any difference between the sequences during the AGB is due to the effect that the  $^{12}\text{C}(\alpha, \gamma)^{16}\text{O}$  reaction rate has during the CHB.

Figure 6 shows the helium core mass at the first TP of each sequence as a function of initial mass. A minimum value occurs for an initial mass  $M_i = 1.90 M_\odot$ , which is the transition point as described in Section 3.1. The same result was found in the work of Kalirai et al. (2014), whose initial models come from those produced in Bressan et al. (2012). However, their transition point occurs for  $M_i = 2.00 M_\odot$  due the larger initial metallicity affecting the mass for which core helium burning ignites in degenerate conditions (Bertelli et al. 1986; Romero et al. 2015). We find that there is no significant difference to the helium core mass at the first TP as a result of different  $^{12}\text{C}(\alpha, \gamma)^{16}\text{O}$  reaction rates for masses lower than the transition point. Above this mass, the maximum difference between the NACRE rates is  $\sim 0.01 M_\odot$ , with NACRE\_L producing lower helium core masses and NACRE\_H producing larger helium core masses. This is due to the difference in energy outputs between the adopted rate, NACRE\_A, and the NACRE\_H/NACRE\_L rates. Higher reaction rates during the CHB increase the temperature throughout the star which favours the CNO-cycle (Boeltzig et al. 2016), allowing the helium core mass to develop further than sequences which consider lower reaction rates. There are no significant differences in the helium core mass at the first TP between the adopted rate from An et al. (2016) and An\_H/An\_L for any of the considered initial masses.

Figure 7 shows the growth of the helium core mass during the TP-AGB as a function of initial mass for each considered reaction rate. We find that the dramatic increase of core growth (for helium core mass growth  $\geq 10\%$  (Kalirai et al. 2014)) occurs in the range  $1.70 \leq M_i/M_\odot \leq 2.60$ , with a maximum increase of 19% occurring at  $M_i \approx 2.00 M_\odot$ . This result is in agreement with that of Bird & Pinsonneault (2011) and is similar to that of Kalirai et al. (2014), who find a helium core growth up to 30%. This discrepancy between their work and ours is due to not only a different initial metallicity, but

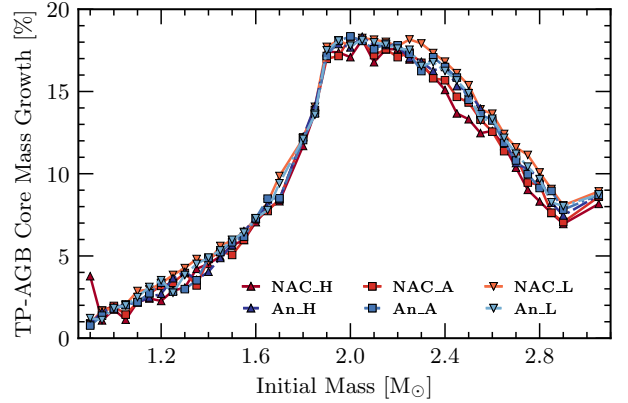


**Figure 7.** Percentage growth of the helium core mass during the AGB as a function of initial mass. Growth is calculated as the difference between the final mass of the core and the helium core mass described in Figure 6. We find that the largest growth occurs for initial masses  $\approx 2.00 M_\odot$ , peaking at 19%. Above initial masses of  $M_i = 2.90 M_\odot$ , it appears that the growth begins to plateau around 8-9%. The red points represent the reaction rates considered by NACRE and the blue points are those from An et al. (2016). Additionally, squares represent the respective adopted rates while darker-coloured triangles and lighter-coloured upside-down triangles represent the high and low limit uncertainties, respectively.

also their consideration of a less efficient mass-loss scheme for stages previous to the AGB (Reimers law with  $\eta_R = 0.2$  (Bressan et al. 2012)). Thus, the models used by Kalirai et al. (2014) have a larger mass of hydrogen fuel to produce a larger final mass (see Table 1 for our values of this variable and Bird & Pinsonneault (2011) for an in-depth discussion of the hydrogen fuel variable). Furthermore, possible differences to the energy produced in the H-rich envelope during the TP-AGB may affect the rate of the helium core growth (see Forestini & Charbonnel 1997; Marigo et al. 2013; Kalirai et al. 2014, for details).

Considering only the difference in helium core mass growth for NACRE\_A rate and it's NACRE\_H/NACRE\_L limits, we find that NACRE\_L has a larger core growth and NACRE\_H has smaller core growth. The increased core growth during the AGB for the NACRE\_L sequences is due to the smaller helium core mass at the first TP (see Figure 6) and as such more fuel to keep He-shell burning sustained, particularly for initial masses above the transition point where the core growth differences are greater (see Table 1). Additionally, during the TP-AGB, we find differences in the energy generation from the CNO cycle between the NACRE\_H/NACRE\_L limits in comparison with the NACRE\_A. The energy generation can be up to 25% lower (higher) when the NACRE\_H (NACRE\_L) reaction rate is considered.

Figure 8 shows the number of thermal pulses as a function of initial mass for each considered reaction rate. Moreover, it shows that lower reaction rates experience more TPs than higher reaction rates. This is related to the larger amount of available hydrogen to aid the outward growth of the helium core through a greater number of unstable He-shell burning episodes - TPs. We do not find any M-star to C-star transitions (see Marigo et al. 2020, for example) as convective overshooting about the boundary between the helium core and the He-exhausted core was disregarded during the TP-AGB, inhibiting the TDU (Herwig 2000; Romero et al. 2015). However, overshooting still occurred at the boundary of the H-rich core. We define the "He-exhausted core" as the region from the centre until the local abundance of helium is greater than  $10^{-6}$ .

Thermal pulses are strongly dependent on the mass-loss rate, he-

lium core mass and initial metallicity (Karakas et al. 2002; Cristallo et al. 2009; Weiss & Ferguson 2009; Renedo et al. 2010; Romero et al. 2015; De Gerónimo et al. 2017). We find that the number of thermal pulses in our computations is lower than that from the works of Weiss & Ferguson (2009); Renedo et al. (2010) and Romero et al. (2015) for a given initial mass, a similar treatment of convection and a similar helium core mass at the beginning of the TP-AGB phase. Difference in the number of TPs could be related to the different mass-loss schemes during the RGB stage. In this work we consider the mass-loss prescription from Bloeker (1995) while the works of Weiss & Ferguson (2009); Renedo et al. (2010) and Romero et al. (2015) consider a mass-loss scheme that produces a "super wind" stage towards the last TPs, making it more efficient in these last TPs but less so in the early TP-AGB (see Vassiliadis & Wood 1993; van Loon et al. 2005, for details). However, the trend in the number of experienced TPs as a function of initial mass obtained in our work agrees with other works (see Weiss & Ferguson 2009; Renedo et al. 2010; Romero et al. 2015).

To assess the effect of the TDU during the TP-AGB, we computed additional sequences, allowing convective overshooting to occur at all fully- or semi-convective boundaries, with  $f = 0.016$  (see Appendix B, for details on its effect). For sequences that consider the NACRE\_A prescription, TDU episodes occur for initial masses larger than  $M_i \geq 2.40 M_\odot$ , with the dredge-up efficiency parameter ( $\lambda_d$ ) showing values of  $\lambda_d = 0.033 - 0.124$  that increases with increasing initial mass. The abundance of carbon and oxygen at the surface does increase during each TDU in these additional models, but the C/O is still lower than 1 meaning that our models show an oxygen dominated surface. A higher value of the overshooting parameter may be necessary to produce C-stars (see Herwig et al. 1997; Karakas et al. 2002; Weiss & Ferguson 2009; Romero et al. 2015; Marigo et al. 2020, for examples of C-star transitions). For sequences where convective overshooting was considered across all boundaries during the AGB we find a decrease in the final helium core mass up to 0.63%. This value is much lower than the 15% decrease found by Karakas et al. (2002); Romero et al. (2015).

The sequences that have initial masses  $M_i < 2.40 M_\odot$  do not show any third dredge-up episodes, as such we do not expect any difference to the growth of the helium core or the final mass. For those sequences with initial masses  $M_i \geq 2.40 M_\odot$ , a more detailed study of the convective boundaries during the TP-AGB is required for more thorough analysis of why we find such weak dredge-up efficiency parameters.

In the case of NACRE\_H and NACRE\_L, we find that TDU episodes occur for the same initial mass range as that of the NACRE\_A sequences ( $2.40 \leq M_i/M_\odot \leq 3.05$ ). Additionally, the dredge-up efficiency parameters are also similar to those of the NACRE\_A sequences, with  $\lambda_d = 0.040 - 0.123$ . From the results gathered in this work, we find that the uncertainties of current  $^{12}\text{C}(\alpha, \gamma)^{16}\text{O}$  reaction rates are not significant in modelling the TDU.

The  $^{12}\text{C}(\alpha, \gamma)^{16}\text{O}$  reaction during the AGB is negligible during the TP-AGB. Instead, the main energy source occurs through the  $3\alpha$  reaction series and the CNO-cycle within the H-rich envelope (Herwig 2005; Karakas & Lattanzio 2014). Thus, we do not find any significant change to the peak TP luminosity nor the depth of each TDU, since the changes in core mass at the beginning of the TP-AGB are negligible as a result of the uncertainties of the  $^{12}\text{C}(\alpha, \gamma)^{16}\text{O}$  reaction rate, as shown in Figure 6 (see Wallerstein et al. 1997; Wagenhuber & Groenewegen 1998; Busso et al. 1999; Herwig 2005; Karakas & Lattanzio 2014, for details). However, the uncertainties of the overshooting efficiency raises a greater uncertainty in the surface composition during the AGB, as such we leave a detailed discussion

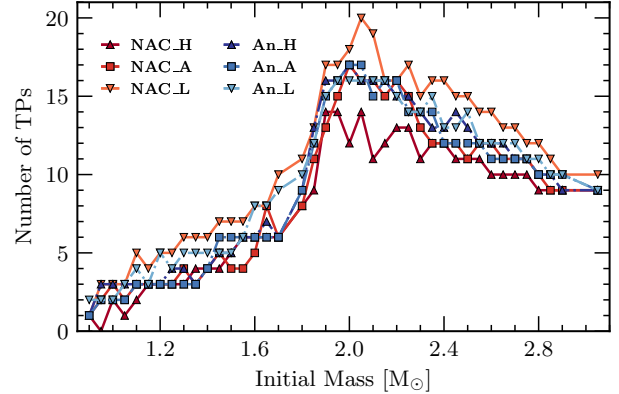


**Figure 8.** Number of TPs experienced as a function of initial mass. Each reaction rate consideration and their uncertainties are shown. We find that the number of TPs peaks at initial masses  $\approx 2.00 M_\odot$ , in-line with the largest core growth, as in Figure 7. We also show that lower reaction rates for the  $^{12}\text{C}(\alpha, \gamma)^{16}\text{O}$  reaction produce more TPs. The red points represent the reaction rates considered by NACRE and the blue points are those from An et al. (2016). Additionally, squares represent the respective adopted rates while darker-coloured triangles and lighter-coloured upside-down triangles represent the high and low limit uncertainties, respectively.

for a future work that considers the overshooting efficiency in more detail (Abia et al. 2002; Herwig 2005; Cristallo et al. 2009; Ventura & Marigo 2009; Karakas & Lattanzio 2014).

### 3.3 The White Dwarf Final Cooling Track

Figure 9 shows the initial-to-final mass relation (IFMR) for all sequences produced in this work. We find that there is no significant difference in the final mass of any given initial mass due to the  $^{12}\text{C}(\alpha, \gamma)^{16}\text{O}$  reaction rate. Considering the largest difference in the reaction rates, between NACRE\_H and NACRE\_L, the largest difference in the final mass for a given initial mass is less than  $0.01 M_\odot$  ( $< 2\%$ ).

In the interest of the pursuit for a global IFMR, we compare our IFMR to those of other works of a similar metallicity. We consider the IFMRs from the works of Weidemann (2000); Salaris et al. (2009) and Renedo et al. (2010). We find a similar trend with the work of Weidemann (2000), both of which consider the same mass-loss scheme from Bloeker (1995) for the AGB phase. The IFMRs from the works of Salaris et al. (2009) and Renedo et al. (2010) consider the mass-loss scheme from Vassiliadis & Wood (1993) for the AGB and show a much steeper gradient in their IFMRs. However, the core masses between this work and the works of Weidemann (2000); Salaris et al. (2009) and Renedo et al. (2010) are similar at the first TP. Thus, it is reasonable to assume that the difference is due to their considered mass-loss scheme for the IFMR determination.

By considering the third-order polynomial nature of the IFMR computed in this work, we fit a function to the NACRE\_A final masses to produce a general relation from the results of this work. This allows for a comparison to other IFMRs as well as other masses to be easily estimated, if desired. The following IFMR reproduces the IFMR of NACRE\_A well, such that the R-square value is  $R^2 = 0.9995$ :

$$M_f = 0.02047M_i^3 - 0.1051M_i^2 + 0.2323M_i + 0.3783M_\odot \quad (2)$$

where  $M_f$  is the final mass and  $M_i$  is the initial mass. The non-linear relationship described by Equation 2 is caused by the mass-loss rate

$M_i/M_\odot$	$\Delta M_{\text{growth}}/M_\odot$				$M_{\text{fuel}}/M_\odot$			
	NACRE_H	NACRE_A	NACRE_L	An_A	NACRE_H	NACRE_A	NACRE_L	An_A
1.00	0.009	0.010	0.009	0.009	0.007	0.008	0.007	0.008
1.50	0.030	0.027	0.031	0.031	0.024	0.022	0.026	0.025
1.60	0.037	0.038	0.039	0.038	0.030	0.031	0.031	0.031
2.00	0.085	0.091	0.089	0.091	0.069	0.073	0.072	0.073
2.90	0.043	0.044	0.050	0.048	0.035	0.035	0.040	0.039

**Table 1.** Values showing the TP-AGB helium core mass growth and fuel mass. We report the values from the following reaction rate considerations: NACRE\_H, NACRE\_A, NACRE\_L and An\_A. We do not report the values from the uncertainties of the rate taken from An et al. (2016) since they are negligible when compared to their adopted rate.

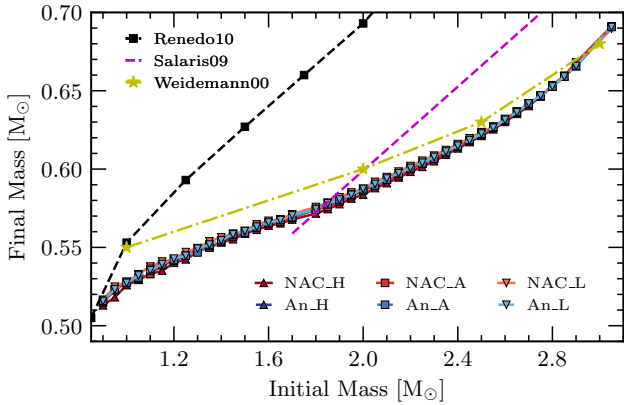


**Figure 9.** Initial-to-final mass relation of all sequences calculated as part of this work. Also shown are other IFMRs from the works of Weidemann (2000); Salaris et al. (2009); Renedo et al. (2010) (yellow stars, purple dashed line and black squares, respectively) for a comparison of their trends. The red points represent the reaction rates considered by NACRE, and the blue points are those from An et al. (2016). Additionally, squares represent the respective adopted rates while darker-coloured triangles and lighter-coloured upside-down triangles represent the high and low limit uncertainties, respectively. We find that the slope of the IFMR has a strong dependency on the considered mass-loss scheme considered during the AGB, with the scheme from Vassiliadis & Wood (1993) producing a steeper gradient and that from Bloeker (1995) showing a shallower gradient.

adopted on the AGB. The Bloeker (1995) scheme in particular has a large dependency on luminosity. It would be interesting to see how our IFMR holds for observational data as well as its dependency on metallicity - an important dependence as discussed in Romero et al. (2015).

In Figure 10 we show, in panel a), the final ages of a WD that has cooled to an effective temperature of  $T_{\text{eff}} = 10\,000\text{K}$  (log scale) as a function of initial mass for all the sequences computed in this work. The differences in the final ages due to the High/Low limits of each considered  $^{12}\text{C}(\alpha, \gamma)^{16}\text{O}$  reaction rate are in general negligible, with variations of the order  $\sim 0.01$  Gyr for both the NACRE and An et al. (2016)  $^{12}\text{C}(\alpha, \gamma)^{16}\text{O}$  reaction rate. The variations in the reported final ages due to the uncertainties of the  $^{12}\text{C}(\alpha, \gamma)^{16}\text{O}$  reaction rate are a magnitude lower than the populations studied in the works of Hansen et al. (2013); Forbes et al. (2015); Campos et al. (2016). As such, the impact that the  $^{12}\text{C}(\alpha, \gamma)^{16}\text{O}$  reaction rate has on final ages of WD models is currently negligible as compared to the greater uncertainty of ageing stellar populations.

Panels c) and d) of Figure 10 show the moving average for the

time spent on the cooling track for the NACRE and An et al. (2016)  $^{12}\text{C}(\alpha, \gamma)^{16}\text{O}$  reaction rates, respectively. We define this quantity as the time taken for a star on the final cooling track to cool from its maximum effective temperature until an effective temperature of  $T_{\text{eff}} = 10\,000\text{K}$ . During the final cooling track, the differences in the duration due to the reaction rates between the Adopted and High/Low limits generally differ up to 0.030 Gyr for those of NACRE and up to 0.015 Gyr for An et al. (2016). The general trend is in agreement with past discussions of the effect of the  $^{12}\text{C}(\alpha, \gamma)^{16}\text{O}$  reaction rate and cooling time during this stage of evolution, such that more oxygen-rich cores will produce a lower cooling time. This is due to the gravitational energy release during stratification occurring at earlier times for more oxygen-rich cores. As a consequence, the WD is left with a lower thermal content to feed the surface luminosity at later times. The larger the luminosity at which the stratification occurs, the shorter the resulting cooling times will be (D’Antona & Mazzitelli 1990; Prada Moroni & Straniero 2002; Salaris et al. 2010). Furthermore, for the High/Low limits of the NACRE rate, we find that NACRE\_L produces a greater absolute difference than that of NACRE\_H. This is due to the availability of helium during the CHB as discussed in Section 3.1.

After the settling and diffusion processes described in Section 2, the final oxygen abundances within the core of the sequences are presented in Figure 11, as a function of initial mass. We find similar trends to the oxygen mass fraction in this stage to those found at the end of the CHB. Although there are slight increases to the oxygen mass fraction due to the aforementioned diffusion processes (Unglaub & Bues 2000). Additionally, diffusion affects the C/O ratio throughout the star up to the surface and not just in the core (see Herwig 2000; Straniero et al. 2003, for details).

The onset of crystallisation begins when the core cools to a certain temperature,  $T_c$  (Segretain et al. 1994; Horowitz et al. 2010). This temperature is dependent on the internal composition of the star. Through observations of the globular cluster NGC 6397, Winget et al. (2009) report that the crystallisation of the WD core is similar to that of a pure carbon core. According to the phase diagram produced in Horowitz et al. (2010) and their limits for the maximum crystallisation temperature, this would require a limit to the oxygen mass fraction of  $X_{\text{O}} \leq 0.64$ . This requires that the maximum S-factor at 300 keV has an upper limit of  $S(300\text{keV}) \leq 170\text{keV b}$ . Considering the relationship between oxygen mass fraction and initial mass presented in Figure 11, we find that NACRE\_H and NACRE\_A produce central oxygen abundances that are too large for a crystallisation process similar to that found by Horowitz et al. (2010). Meanwhile, the rates An et al. (2016) agree not only with the oxygen mass fraction limit presented by Horowitz et al. (2010), but also their derived

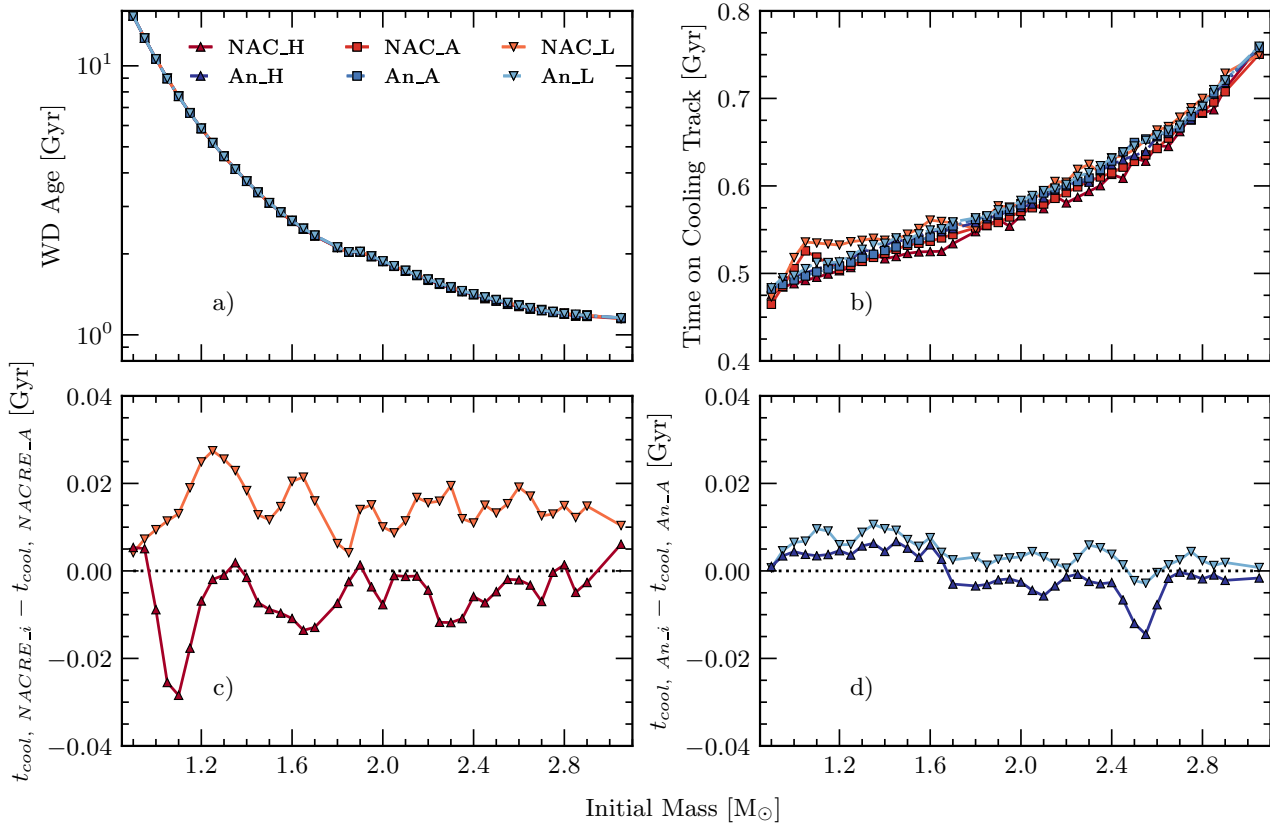


**Figure 10.** Panel a) shows the final age (log scale) of the star on the final cooling track with an effective temperature  $T_{\text{eff}} = 10000\text{K}$ . Panel b) shows the time spent of the cooling track, defined as the time taken for a WD on the final cooling track to cool from its maximum effective temperature to an effective temperature of  $T_{\text{eff}} = 10000\text{K}$ . Panel c) and d) show the moving average for the difference of cooling times between the High/Low limits and the Adopted rate for the NACRE and *An et al. (2016)*  $^{12}\text{C}(\alpha, \gamma)^{16}\text{O}$  reaction rate, respectively. All panels are represented as functions of initial mass. The NACRE reaction rates are shown as different shades of red and those from *An et al. (2016)* are depicted by shades of blue. Furthermore, squares represent the respective adopted rates while darker-coloured triangles and lighter-coloured upside-down triangles represent the high and low limit uncertainties, respectively. In general, we find that the uncertainties of the  $^{12}\text{C}(\alpha, \gamma)^{16}\text{O}$  reaction rate have a negligible effect on the final ages of the stars at this point, whereas the cooling time can differ up to 8%.

S-factor for an energy of 300 keV. Thus, we find that sequences dedicated to studying crystallisation using the method presented by *Horowitz et al. (2010)* should consider a lower reaction rate than that from NACRE for the  $^{12}\text{C}(\alpha, \gamma)^{16}\text{O}$  reaction to keep their analysis consistent with the input physics that they use.

Figure 12 shows the abundance profiles of white dwarf models with a stellar mass of  $M_* = 0.548M_{\odot}$ ,  $T_{\text{eff}} = 20000\text{K}$  and an initial mass of  $M_i = 1.30M_{\odot}$ . Sequences that consider a reaction rate from NACRE are shown in the top panel and those from *An et al. (2016)* are represented in the bottom panel. All sequences finish with similar structure to those shown in Figure 12. The profiles depict a DA white dwarf configuration, with a hydrogen-rich envelope, a helium buffer and a C/O core. Where the abundance of carbon reaches its maximum, we hereafter refer to this as the carbon peak.

We show that the interior of the star has a consistent trend where the carbon peak is higher for lower reaction rates - an outcome of a less efficient reaction rate which leaves behind a larger abundance of carbon. Furthermore, the position of the carbon peak changes with the reaction rates, moving away from the centre as the reaction rate increases. We find in general that differences between *An\_A* and the *An\_H*/*An\_L* reaction rates do not affect this region drastically (bottom panel), unlike that of the NACRE  $^{12}\text{C}(\alpha, \gamma)^{16}\text{O}$  reaction rate considerations (top panel).

The abundance profile and composition gradients in these central regions that lie within the range of  $1 < -\log_{10}(1 - M_r/M_*) < 2$  affect the peaks in the Brunt-Väisälä frequency, which disturbs the period spectrum structure (see *Córsico & Althaus 2006*; *Romero et al. 2012b*, for more details). This is an outcome of the pulsation modes that are trapped in this region through the mode-trapping mechanism. We confirm that uncertainties of the  $^{12}\text{C}(\alpha, \gamma)^{16}\text{O}$  reaction rate may affect the pulsation period spectrum. Another region where the Brunt-Väisälä frequency is affected is in the He/H transition region. In particular, the position of the He/H transition will impact the period spectrum (*Romero et al. 2012a, 2013*).

#### 4 CONCLUSIONS

In this work we analyse the impact that the limits of the  $^{12}\text{C}(\alpha, \gamma)^{16}\text{O}$  reaction rate has on the inner structure and evolutionary properties of low- and intermediate-mass stars. We consider the  $^{12}\text{C}(\alpha, \gamma)^{16}\text{O}$  reaction rates from NACRE (*Angulo et al. 1999*) and *An et al. (2016)*. We have computed stellar sequences from the ZAMS until the remnant white dwarf reaches a luminosity of  $\log(L/L_{\odot}) = -3$ . We applied similar starting parameters for different ensembles of reaction rates where we consider the adopted rate along with the

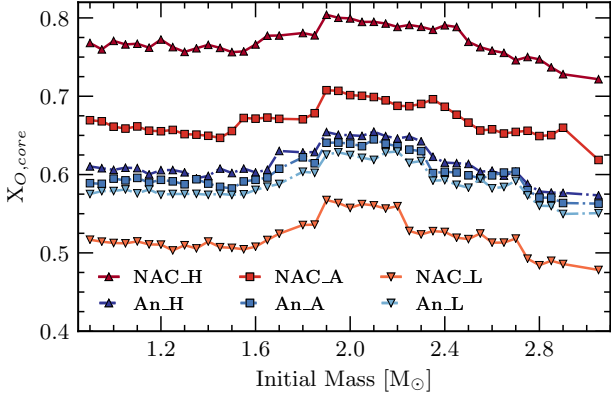


**Figure 11.** Central oxygen mass fraction for the final WD as a function of initial mass. We show each calculated sequence. The trends for each considered reaction rate are similar to those found in Figure 2. There has been a slight increase in the central oxygen abundance since the CHB due to diffusion processes in the star. Additionally, squares represent the respective adopted rates while darker-coloured triangles and lighter-coloured upside-down triangles represent the high and low limit uncertainties, respectively.

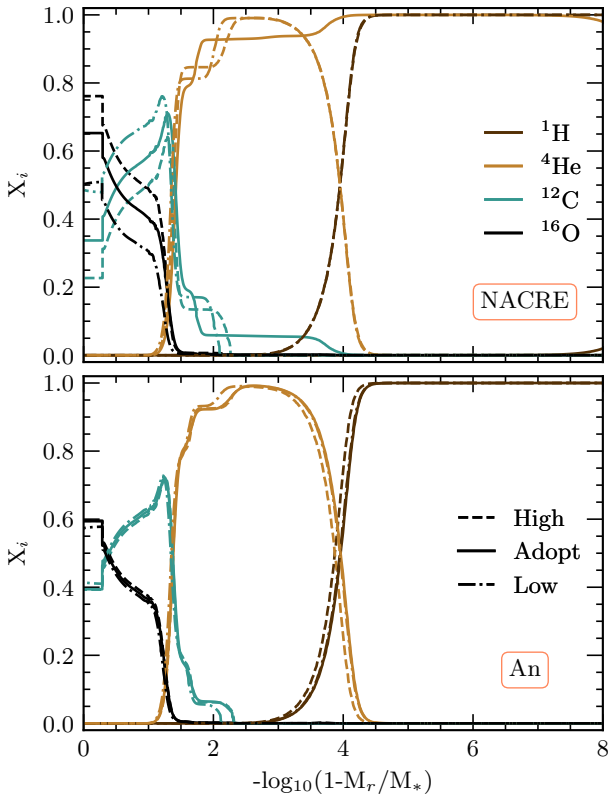


**Figure 12.** In both panels we show the abundance profiles of sequences considering an initial mass of  $M_i = 1.30 M_{\odot}$ . The top panel represents the adopted rate and its uncertainties for the NACRE rate, and the same for the An et al. (2016) rates in the bottom panel. The line-styles for each rate are shown in the legend in the bottom panel and the colours for each element is shown in the legend in the top panel. Colour version is available online.

upper and lower limits within the uncertainties of each source. We summarise our main results below.

- (i) The C/O ratio of the core in the final model of each sequence is affected by the  $^{12}\text{C}(\alpha, \gamma)^{16}\text{O}$  reaction rate as expected, with lower C/O ratios for larger reaction rates. We find that the decreased C/O ratio for initial masses greater than the transition mass increase again at higher masses. The mass at which this increase occurs is dependent on the considered  $^{12}\text{C}(\alpha, \gamma)^{16}\text{O}$  reaction rate, such that it occurs for higher masses if higher reaction rates are considered. This is due to an increased number of mixing episodes, a cause of larger energy outputs increasing convective efficiency which brings fresh helium to the core during the CHB. Note that significant differences between the adopted rate and high/low limits occur only for those rates taken from NACRE which has a much larger uncertainty than those from An et al. (2016).
- (ii) CHB lifetime is dependent on the considered reaction rate, a higher reaction rate produces a greater lifetime. We deem this to be a consequence in the number of mixing episodes extending the core helium burning lifetime, although further research would be beneficial to confirm this. Between the adopted rate and high/low limits, we find a difference up to 12 Myr for the NACRE rates and up to 4 Myr for those from An et al. (2016).
- (iii) The helium core mass at the beginning of the first TP is independent of the considered  $^{12}\text{C}(\alpha, \gamma)^{16}\text{O}$  reaction rate up to and including the transition mass. Above this mass, we find a maximum difference of  $\approx 0.01 M_{\odot}$  between NACRE\_H and NACRE\_L, with lower reaction rates producing a lower helium core mass. Additionally, our minimum helium core mass at this point occurs at our transition mass.
- (iv) Growth of the helium core mass between the first TP and the final mass reaches a maximum of 19%, with growths greater than 10% occurring in the mass range  $1.70 \leq M_i/M_{\odot} \leq 2.60$  which is in agreement with Bird & Pinsonneault (2011) and Kalirai et al. (2014). The largest growths occur for the lower reaction rates due to more available hydrogen which remained after the CHB. There are no significant differences between the rates taken from An et al. (2016) due to the limits being smaller in relation to their adopted rate than those from NACRE.
- (v) The number of TPs during the TP-AGB is dependent on the considered  $^{12}\text{C}(\alpha, \gamma)^{16}\text{O}$  reaction rate. We find that lower reaction rates increase the number of TPs due to a larger hydrogen fuel aiding the outward growth of the helium core mass by fuelling the unstable He-shell with a greater supply of fresh helium.
- (vi) TDU episodes occur for sequences in the initial mass range of  $2.40 \leq M_i/M_{\odot} \leq 3.05$  with dredge-up efficiency parameters  $\lambda_d = 0.033 - 0.124$ . This mass range is independent of the considered  $^{12}\text{C}(\alpha, \gamma)^{16}\text{O}$  reaction rate. Additionally, the values of  $\lambda_d$  between the considered  $^{12}\text{C}(\alpha, \gamma)^{16}\text{O}$  reaction rate uncertainties are not significant. Furthermore, the depth of each TDU is independent of the  $^{12}\text{C}(\alpha, \gamma)^{16}\text{O}$  reaction rate.
- (vii) The IFMR produced in this work has a similar trend to that of Weidemann (2000), who also consider a similar mass-loss prescription during the AGB. The IFMRs of Renedo et al. (2010) and Salaris et al. (2009) show a much steeper gradient and they consider the Vassiliadis & Wood (1993) mass-loss prescription during the AGB.
- (viii) We find that the final ages of the sequences are in general independent of the considered reaction rate. However, during the final cooling track, we find differences up to 10% between the adopted rates and high/low limits. This is true for both those rates taken from NACRE and An et al. (2016). This difference in the cooling time agrees with the works of Prada Moroni & Straniero (2002); Salaris et al. (2010); Isern et al. (2013).



- (ix) The final C/O ratio in the core shows a similar trend to that at the end of the CHB. The oxygen abundance increases slightly due to the diffusion processes. The final oxygen mass fraction for NACRE\_A and NACRE\_H sequences are greater than the values derived by Horowitz et al. (2010) for crystallisation of a C/O core. The reaction rates from An et al. (2016) agree closely with the derived values of Horowitz et al. (2010). As such, future works should consider a lower reaction rate than that of NACRE when considering the crystallisation process of Horowitz et al. (2010).
- (x) The inner structure of the star is affected by the uncertainties within the considered reaction rates, particularly those from NACRE. The position and height of the carbon peak is significantly affected by the difference between the adopted rate and high/low limits of the reaction rate for the NACRE considerations. This may affect the modes in which pulsations can occur during the ZZ Ceti instability strip (Córscico & Althaus 2006; Romero et al. 2012a).

Although we analyse the possible evolutionary stages where more accurate  $^{12}\text{C}(\alpha, \gamma)^{16}\text{O}$  reaction rates are needed, a deeper analysis of some effects are still required. For instance, a quantification of how the pulsation modes of sdB's and ZZ Ceti stars are affected, for example. Furthermore, we conclude that a lower reaction than that of NACRE\_A is favourable for the Horowitz et al. (2010) considerations of crystallisation, however, this must be further analysed as well. By limiting the uncertainties of  $^{12}\text{C}(\alpha, \gamma)^{16}\text{O}$  reaction rates to 10% of the adopted rate, as in An et al. (2016), reports a much better consistency of stellar parameters.

## ACKNOWLEDGEMENTS

BTP, ADR and SOK acknowledge support by CNPq and PRONEX-FAPERGS/CNPq. This study was financed in part by the Coordenação de Aperfeiçoamento de Pessoal de Nível Superior - Brasil (CAPES) - Finance Code 001. This research has made use of NASA's Astrophysics Data System. AGI acknowledges support from the Netherlands Organisation for Scientific Research (NWO). We also thank developers of the MESA software, which was used extensively in this work. Finally, we thank the anonymous referee for their input to make it a more complete work.

## DATA AVAILABILITY

The data is available upon request to the corresponding author.

## REFERENCES

- Abia C., et al., 2002, *ApJ*, **579**, 817
- Aliotta M., et al., 2021, arXiv e-prints, p. [arXiv:2109.14418](https://arxiv.org/abs/2109.14418)
- Althaus L. G., Córscico A. H., Isern J., García-Berro E., 2010, *A&ARv*, **18**, 471
- An Z.-D., et al., 2015, *Phys. Rev. C*, **92**, 045802
- An Z.-D., Ma Y.-G., Fan G.-T., Li Y.-J., Chen Z.-P., Sun Y.-Y., 2016, *ApJ*, **817**, L5
- Angulo C., et al., 1999, *Nuclear Phys. A*, **656**, 3
- Bertelli G., Bressan A., Chiosi C., Angerer K., 1986, *A&AS*, **66**, 191
- Bethe H. A., 1939, *Physical Review*, **55**, 434
- Bird J. C., Pinsonneault M. H., 2011, *ApJ*, **733**, 81
- Bloecker T., 1995, *A&A*, **297**, 727
- Boeltzig A., et al., 2016, *European Physical Journal A*, **52**, 75
- Boothroyd A. I., Sackmann I. J., 1988, *ApJ*, **328**, 653
- Bressan A., Marigo P., Girardi L., Salasnich B., Dal Cero C., Rubele S., Nanni A., 2012, *MNRAS*, **427**, 127
- Brochard, F. Chevallier, P. Disdier, D. Rauch, V. Scheibling, F. 1975, *J. Phys. France*, **36**, 113
- Brown G. E., Heger A., Langer N., Lee C.-H., Wellstein S., Bethe H. A., 2001, *New Astron.*, **6**, 457
- Burbidge E. M., Burbidge G. R., Fowler W. A., Hoyle F., 1957, *Reviews of Modern Physics*, **29**, 547
- Burgers J. M., 1969, *Flow Equations for Composite Gases*
- Busso M., Gallino R., Wasserburg G. J., 1999, *ARA&A*, **37**, 239
- Campos F., et al., 2016, *MNRAS*, **456**, 3729
- Caughlan G. R., Fowler W. A., 1988, *Atomic Data and Nuclear Data Tables*, **40**, 283
- Constantino T., Campbell S. W., Christensen-Dalsgaard J., Lattanzio J. C., Stello D., 2015, *MNRAS*, **452**, 123
- Constantino T., Campbell S. W., Lattanzio J. C., van Duijneveldt A., 2016, *MNRAS*, **456**, 3866
- Constantino T., Campbell S. W., Lattanzio J. C., 2017, *MNRAS*, **472**, 4900
- Córscico A. H., Althaus L. G., 2006, *A&A*, **454**, 863
- Cristallo S., Straniero O., Gallino R., Piersanti L., Domínguez I., Lederer M. T., 2009, *ApJ*, **696**, 797
- Cristallo S., Straniero O., Piersanti L., Gobrecht D., 2015, *ApJS*, **219**, 40
- D'Antona F., Mazzitelli I., 1990, *ARA&A*, **28**, 139
- De Gerónimo F. C., Córscico A. H., Althaus L. G., Romero A. D., 2015, *The Impact of the Uncertainties in the  $^{12}\text{C}(\alpha, \gamma)^{16}\text{O}$  Reaction Rate on the Asteroseismology of ZZ Ceti Stars: First Results*. p. 225
- De Gerónimo F. C., Althaus L. G., Córscico A. H., Romero A. D., Kepler S. O., 2017, *A&A*, **599**, A21
- Deboer R. J., et al., 2017, in *APS Division of Nuclear Physics Meeting Abstracts*. p. CC.006
- Deboer R., Brune C., Wiescher M., 2019, in *APS Division of Nuclear Physics Meeting Abstracts*. p. FG.003
- Eddington A. S., 1920, *The Observatory*, **43**, 341
- Farmer R., Renzo M., de Mink S. E., Fishbach M., Justham S., 2020, *ApJ*, **902**, L36
- Ferguson J. W., Alexander D. R., Allard F., Barman T., Bodnarik J. G., Hauschildt P. H., Heffner-Wong A., Tamanai A., 2005, *ApJ*, **623**, 585
- Fontaine G., Brassard P., 2008, *PASP*, **120**, 1043
- Forbes D. A., Pastorello N., Romanowsky A. J., Usher C., Brodie J. P., Strader J., 2015, *MNRAS*, **452**, 1045
- Forestini M., Charbonnel C., 1997, *A&AS*, **123**, 241
- Fowler W. A., Caughlan G. R., Zimmerman B. A., 1967, *ARA&A*, **5**, 525
- Frost C. A., Lattanzio J. C., 1996, *ApJ*, **473**, 383
- Ghasemi H., Moravveji E., Aerts C., Safari H., Vučković M., 2017, *MNRAS*, **465**, 1518
- Guo J.-J., Li Y., 2018, *MNRAS*, **478**, 3290
- Guzik J. A., Fontes C. J., Walczak P., Wood S. R., Mussack K., Farag E., 2016, *IAU Focus Meeting*, **29B**, 532
- Hansen B. M. S., et al., 2013, *Nature*, **500**, 51
- Heber U., 2009, *ARA&A*, **47**, 211
- Heger A., Woosley S. E., Rauscher T., Hoffman R. D., Boyes M. M., 2002, *New Astron. Rev.*, **46**, 463
- Heil M., et al., 2008, *Phys. Rev. C*, **78**, 025803
- Herwig F., 2000, *A&A*, **360**, 952
- Herwig F., 2005, *ARA&A*, **43**, 435
- Herwig F., Bloeker T., Schoenberner D., El Eid M., 1997, *A&A*, **324**, L81
- Herwig F., Bloeker T., Langer N., Driebe T., 1999, *A&A*, **349**, L5
- Horowitz C. J., Schneider A. S., Berry D. K., 2010, *Phys. Rev. Lett.*, **104**, 231101
- Hoyle F., 1946, *MNRAS*, **106**, 343
- Hoyle F., 1954, *ApJS*, **1**, 121
- Hu H., Tout C. A., Glebbeek E., Dupret M. A., 2011, *MNRAS*, **418**, 195
- Iben I. J., 1991, in *Michaud G., Tutukov A. V., eds. Vol. 145, Evolution of the Stars: the Photospheric Abundance Connection*. p. 257
- Iben I. J., MacDonald J., 1985, *ApJ*, **296**, 540
- Iben I. J., Tutukov A. V., 1984, *ApJS*, **54**, 335
- Iglesias C. A., Rogers F. J., 1993, *ApJ*, **412**, 752
- Iglesias C. A., Rogers F. J., 1996, *ApJ*, **464**, 943

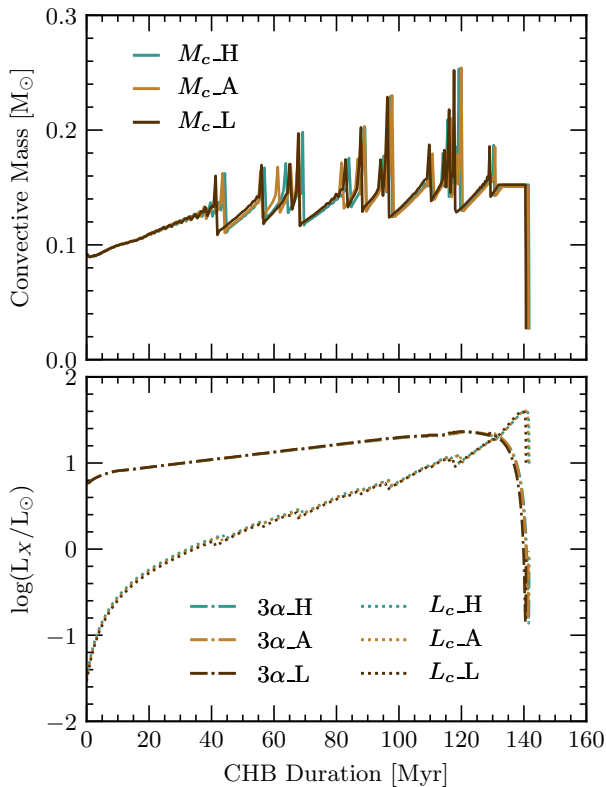
- Isern J., Artigas A., García-Berro E., 2013, in *European Physical Journal Web of Conferences*. p. 05002 ([arXiv:1212.0806](https://arxiv.org/abs/1212.0806)), doi:10.1051/epjconf/20134305002
- Kalirai J. S., Marigo P., Tremblay P.-E., 2014, *ApJ*, **782**, 17
- Karakas A. I., Lattanzio J. C., 2003, *Publ. Astron. Soc. Australia*, **20**, 279
- Karakas A. I., Lattanzio J. C., 2014, *Publ. Astron. Soc. Australia*, **31**, e030
- Karakas A. I., Lattanzio J. C., Pols O. R., 2002, *Publ. Astron. Soc. Australia*, **19**, 515
- Katsuma M., 2012, *ApJ*, **745**, 192
- Kippenhahn R., Weigert A., 1990, *Stellar Structure and Evolution*
- Kippenhahn R., Ruschenplatt G., Thomas H. C., 1980, *A&A*, **91**, 175
- Kobayashi C., Karakas A. I., Lugaro M., 2020, *ApJ*, **900**, 179
- Kunz R., Fey M., Jaeger M., Mayer A., Hammer J. W., Staudt G., Harissopolous S., Paradellis T., 2002, *ApJ*, **567**, 643
- Marigo P., 2002, *A&A*, **387**, 507
- Marigo P., 2007, *A&A*, **467**, 1139
- Marigo P., Bressan A., Nanni A., Girardi L., Pumo M. L., 2013, *MNRAS*, **434**, 488
- Marigo P., et al., 2020, *Nature Astronomy*,
- Matteucci F., 2012, *Chemical Evolution of Galaxies*, doi:10.1007/978-3-642-22491-1.
- Matteucci F., 2021, *A&ARv*, **29**, 5
- Ophel T. R., Frawley A. D., Treacy P. B., Bray K. H., 1976, *Nuclear Physics A*, **273**, 397
- Paxton B., Bildsten L., Dotter A., Herwig F., Lesaffre P., Timmes F., 2011, *ApJS*, **192**, 3
- Paxton B., et al., 2013, *ApJS*, **208**, 4
- Paxton B., et al., 2015, *ApJS*, **220**, 15
- Paxton B., et al., 2018, *ApJS*, **234**, 34
- Perlmutter S., Turner M. S., White M., 1999, *Phys. Rev. Lett.*, **83**, 670
- Prada Moroni P. G., Straniero O., 2002, *ApJ*, **581**, 585
- Prialnik D., 2009, *An Introduction to the Theory of Stellar Structure and Evolution*
- Reimers D., 1975, *Circumstellar envelopes and mass loss of red giant stars*. pp 229–256
- Renedo I., Althaus L. G., Miller Bertolami M. M., Romero A. D., Córscico A. H., Rohrmann R. D., García-Berro E., 2010, *ApJ*, **717**, 183
- Riess A. G., et al., 1998, *AJ*, **116**, 1009
- Romero A. D., Córscico A. H., Althaus L. r. G., Miller Bertolami M. M., 2012a, *arXiv e-prints*, p. [arXiv:1204.6101](https://arxiv.org/abs/1204.6101)
- Romero A. D., Córscico A. H., Althaus L. G., Kepler S. O., Castanheira B. G., Miller Bertolami M. M., 2012b, *MNRAS*, **420**, 1462
- Romero A. D., Kepler S. O., Córscico A. H., Althaus L. G., Fraga L., 2013, *ApJ*, **779**, 58
- Romero A. D., Campos F., Kepler S. O., 2015, *MNRAS*, **450**, 3708
- Salaris M., Cassisi S., 2005, *Evolution of Stars and Stellar Populations*
- Salaris M., Serenelli A., Weiss A., Miller Bertolami M., 2009, *ApJ*, **692**, 1013
- Salaris M., Cassisi S., Pietrinferni A., Kowalski P. M., Isern J., 2010, *ApJ*, **716**, 1241
- Salpeter E. E., 1952, *ApJ*, **115**, 326
- Saumon D., Chabrier G., van Horn H. M., 1995, *ApJS*, **99**, 713
- Segretain L., Chabrier G., Hernanz M., García-Berro E., Isern J., Mochkovitch R., 1994, *ApJ*, **434**, 641
- Spruit H. C., 2015, *A&A*, **582**, L2
- Straniero O., Domínguez I., Imbriani G., Piersanti L., 2003, *ApJ*, **583**, 878
- Sukhbold T., Adams S., 2020, *MNRAS*, **492**, 2578
- Thoul A. A., Bahcall J. N., Loeb A., 1994, *ApJ*, **421**, 828
- Tilley D. R., Weller H. R., Cheves C. M., 1993, *Nuclear Physics A*, **564**, 1
- Timmes F. X., Swesty F. D., 2000, *ApJS*, **126**, 501
- Tur C., Heger A., Austin S. M., 2007, *ApJ*, **671**, 821
- Tur C., Heger A., Austin S. M., 2010, *ApJ*, **718**, 357
- Ulrich R. K., 1972, *ApJ*, **172**, 165
- Unglaub K., Bues I., 2000, *A&A*, **359**, 1042
- Vassiliadis E., Wood P. R., 1993, *ApJ*, **413**, 641
- Ventura P., Marigo P., 2009, *MNRAS*, **399**, L54
- Ventura P., Dell’Aglì F., Lugaro M., Romano D., Tailo M., Yagüe A., 2020, *A&A*, **641**, A103
- Wagenhuber J., Groenewegen M. A. T., 1998, *A&A*, **340**, 183
- Wallerstein G., et al., 1997, *Reviews of Modern Physics*, **69**, 995
- Weaver T., Woosley S., 1993, *Physics Reports*, **227**, 65
- Weidemann V., 2000, *A&A*, **363**, 647
- Weiss A., Ferguson J. W., 2009, *A&A*, **508**, 1343
- West C., Heger A., Austin S. M., 2013, *ApJ*, **769**, 2
- Winget D. E., Kepler S. O., 2008, *ARA&A*, **46**, 157
- Winget D. E., Kepler S. O., Campos F., Montgomery M. H., Girardi L., Bergeron P., Williams K., 2009, *ApJ*, **693**, L6
- Woosley S. E., Weaver T. A., 1995, *ApJS*, **101**, 181
- Woosley S. E., Heger A., Rauscher T., Hoffman R. D., 2003, *Nuclear Phys. A*, **718**, 3
- Wu C., Wang B., Wang X., Maeda K., Mazzali P., 2020, *MNRAS*, **495**, 1445
- Xu Y., Takahashi K., Goriely S., Arnould M., Ohta M., Utsunomiya H., 2013, *Nuclear Physics A*, **918**, 61
- van Loon J. T., Cioni M. R. L., Zijlstra A. A., Loup C., 2005, *A&A*, **438**, 273

## APPENDIX A: CONVECTION DURING CHB FOR AN RATES

Figure A1 shows the CHB history of the convective mass and the luminosities of the  $3\alpha$  process and the  $^{12}\text{C}(\alpha, \gamma)^{16}\text{O}$  reaction, for the reaction rates taken from An et al. (2016). This figure is analogous to that of Figure 4 which shows the same for the NACRE rates. We provide this figure to prove that we do not find any significant difference between the number of mixing episodes, luminosity from the  $3\alpha$  process and the  $^{12}\text{C}(\alpha, \gamma)^{16}\text{O}$  reaction. Thus, the high/low limits for the  $^{12}\text{C}(\alpha, \gamma)^{16}\text{O}$  reaction rate from An et al. (2016) does not affect the CHB in terms of energy production, mixing episodes or CHB duration. This was not found for the NACRE case, which is discussed in Section 3.1.

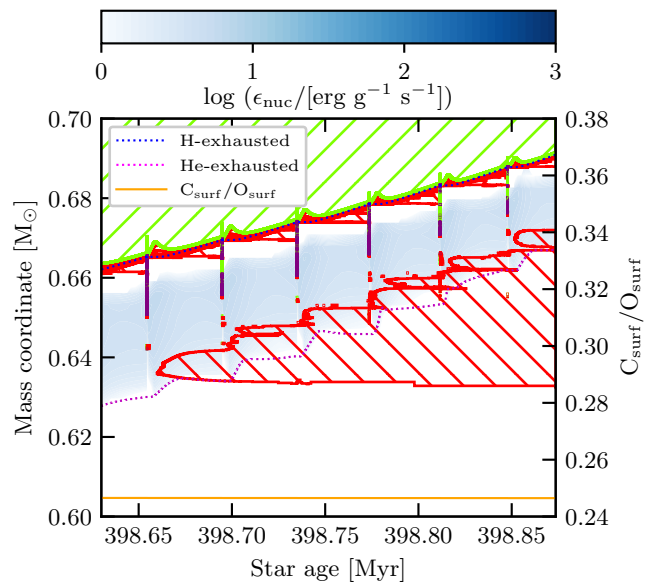
## APPENDIX B: ADDITIONAL AGB MODELS

Figure B1 shows the Kippenhahn diagram for the case of  $M_i = 3.05 M_\odot$  during the TP-AGB in the original NACRE\_A models. We represent the mass co-ordinate on the first y-axis and the surface C/O ratio on the second y-axis. Both values are plotted against the age of the sequence. These models did not consider convective overshooting around the border of the He-exhausted core. Green slashed areas show convective regions, red back slashed areas represent semi-convective regions and the purple regions are where overshooting occurs. The purple dotted line shows the history of the He-exhausted core mass and the blue dotted line represents the history of the helium core mass. The colour bar measures the energy generation rate from nuclear reactions. The solid orange line represents the C/O ratio at the surface. It can be seen that the overshooting occurs close to the envelope boundary and there is no overshooting about the semi-convective region of the He-exhausted core. As a result of this, we do not observe TDU episodes in the original models. We can be sure that there are no TDU episodes because of the lack of change in helium core mass and that the surface C/O ratio remains constant, which would change if TDUs were experienced (Frost & Lattanzio 1996; Herwig et al. 1999; Karakas et al. 2002; Weiss & Ferguson 2009; Romero et al. 2015; De Gerónimo et al. 2017; Marigo et al. 2020).



**Figure A1.** History of the convective mass (top panel),  $3\alpha$  luminosity and the luminosity of the  $^{12}\text{C}(\alpha, \gamma)^{16}\text{O}$  reaction during the CHB (bottom panel). The history is given in terms of the CHB duration. This plot in particular considers all An et al. (2016) prescriptions for the  $^{12}\text{C}(\alpha, \gamma)^{16}\text{O}$  reaction rate for an initial mass of  $M_i = 2.45 M_\odot$ . Blue lines represent An\_H, orange-brown depicts An\_A and dark-brown shows An\_L. Furthermore, the solid line represents the convective mass, dotted lines show the luminosity of the  $^{12}\text{C}(\alpha, \gamma)^{16}\text{O}$  reaction and dot-dash lines portray the  $3\alpha$  luminosity.

Figure B2 shows the same as Figure B1 but allows for convective overshooting at each boundary. We find that, with the new prescription, convection and overshooting extends throughout the helium buffer. For this reason material can be "dredged-up" from the core to the surface. This results in the helium core mass and He-exhausted core masses changing with each convective episode - an outcome of TDU episodes (Frost & Lattanzio 1996; Herwig et al. 1999; Karakas et al. 2002; Weiss & Ferguson 2009; Romero et al. 2015; De Gerónimo et al. 2017; Marigo et al. 2020). Furthermore, we find an increase in the surface C/O ratio with each TDU as material travels from the stellar interior to the surface. The surface C/O ratio, however, remains less than 1. This indicates a larger overshooting parameter is required for M-star to C-star transitions.



**Figure B1.** Kippenhahn diagram for during the TP-AGB for the case of  $M_i = 3.05 M_\odot$  of the original models. We represent the mass co-ordinate on the first y-axis and the surface C/O ratio on the second y-axis. Both values are plotted against the age of the sequence. This model did not consider convective overshooting at boundary of the He-exhausted core which inhibited the TDU. The colour bar measures the energy generation rate from nuclear reactions. The blue dotted line represents the helium core mass while the purple dotted line represents the He-exhausted core. Green slashed regions show convection and the red back slashed regions represent where regions of the star are semi-convective. Finally, purple areas are where overshooting occurs.

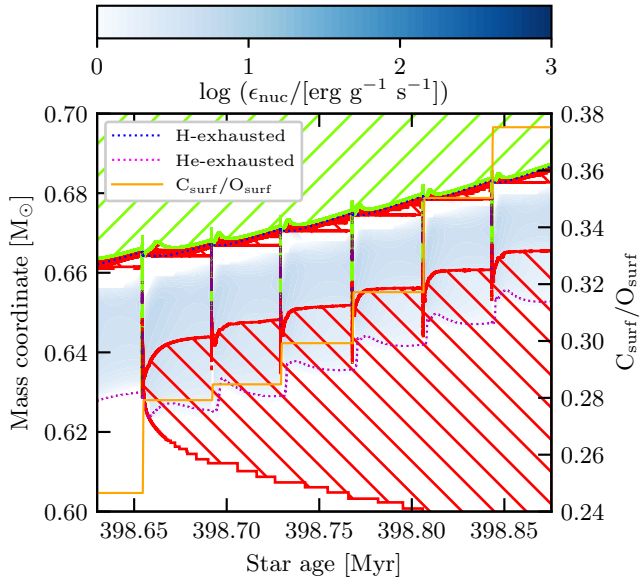


**Figure B2.** Kippenhahn diagram for during the TP-AGB for the case of  $M_i = 3.05 M_\odot$  of the new models. We represent the mass co-ordinate on the first y-axis and the surface C/O ratio on the second y-axis. Both values are plotted against the age of the sequence. The colour bar measures the energy generation rate from nuclear reactions. This model considered convective overshooting at all convective boundaries, allowing for TDUs to occur. The blue dotted line represents the helium core mass while the purple dotted line represents the He-exhausted core. Green slashed regions show convection and the red back slashed regions represent where regions of the star are semi-convective. Finally, purple areas are where overshooting occurs.

## APPENDIX B – Inlists Used in this Work

An example of an inlist for the MESA code used to run the evolutionary sequences is displayed below. The shown code has the initial conditions of  $M_i = 1.00 M_\odot$  and  $Z_i = 0.01$ . The pgstar section of the inlist is not required for sequences as it only displays the running values in plots. Instead of including it within the main inlist, I used a second inlist to control these plots.

```
&star_job

show_log_description_at_start = .true.
create_pre_main_sequence_model = .false.

load_saved_model = .false.
saved_model_name = 'start.mod'

save_model_when_terminate = .true.
save_model_filename = 'my_final_model.mod'

change_D_omega_flag = .true.
new_D_omega_flag = .true.

! this seems not to be working in most of the evolution, so I would keep it off
! RTIs

!change_RTI_flag = .true.
!change_initial_RTI_flag = .true.
!new_RTI_flag = .true.

! Reaction Networks — if we don't need anything specific, I would suggest
! to go only with the basic net

set_rates_preference = .true.
new_rates_preference = 1 ! Use NACRE Rates

! num_special_rate_factors = 1
! reaction_for_special_factor(1) = 'r_c12_ag_o16'
! special_rate_factor(1) = 1 ! Scale factor for c12 -> o16 reaction

! Own Rates

rate_tables_dir = 'rates'
! net_reaction_filename = 'reactions.list'

pgstar_flag = .true.

! instead of doing from pre-main sequence, I set the metallicity as such here

relax_initial_Z = .true.
new_Z = 0.01
relax_initial_Y = .true.
new_Y = 0.26
```

```

/ ! end of star_job namelist

&eos

/ ! end of eos namelist

&kap

    Zbase = 0.01d0
    kap_file_prefix = 'gs98'
    use_Type2_opacities = .true.

/ ! end of kap namelist

&controls
    read_extra_controls_inlist1 = .true.
    extra_controls_inlist1_name = "inlist_extra" ! contains initial mass

    he_core_boundary_h1_fraction = 1d-6
    c_core_boundary_he4_fraction = 1d-6
    o_core_boundary_c12_fraction = 1d-6

    num_trace_history_values = 2
    trace_history_value_name(1) = 'rel_E_err'
    trace_history_value_name(2) = 'log_rel_run_E_err'

! stellar wind

    cool_wind_full_on_T = 9.99d9
    hot_wind_full_on_T = 1d10
    cool_wind_RGB_scheme = 'Reimers'
    cool_wind_AGB_scheme = 'Blocker'
    RGB_to_AGB_wind_switch = 1d-4
    Reimers_scaling_factor = 0.5d0
    Blocker_scaling_factor = 0.2d0 ! 0.8d0

!Convection related

    use_Ledoux_criterion = .true.
    mixing_length_alpha = 2.0118
    alpha_semiconvection = 0.1
    thermohaline_coeff = 1.0
    do_conv_premix = .false.
    conv_premix_avoid_increase = .false.

! this seems to me to have quite an impact —maybe worth having a look — core overshooting
! vs shell overshooting

! Overshooting

    overshoot_scheme(1) = 'exponential'
    overshoot_zone_type(1) = 'any'
    overshoot_zone_loc(1) = 'any'
    overshoot_bdy_loc(1) = 'any'
    overshoot_f(1) = 0.020
    overshoot_f0(1) = 0.004

!### mesh adjustment

```

---

```

max_allowed_nz = 8000
mesh_delta_coeff = 1.0
max_dq = 1d-3
min_dq_for_xa = 1d-5
mesh_delta_coeff = 1.0

xa_function_species(1) = 'he4'
xa_function_weight(1) = 10
xa_function_param(1) = 1d-1

mesh_dlog_pp_dlogP_extra = 0.2d0
mesh_dlog_cno_dlogP_extra = 0.2d0
mesh_dlog_3alf_dlogP_extra = 0.1d0
mesh_dlog_burn_c_dlogP_extra = 0.1d0
mesh_dlog_burn_n_dlogP_extra = 0.2d0
mesh_dlog_burn_o_dlogP_extra = 0.1d0
mesh_dlog_cc_dlogP_extra = 0.1d0
mesh_dlog_co_dlogP_extra = 0.1d0
mesh_dlog_oo_dlogP_extra = 0.1d0

!### timestep controls

report_why_dt_limits = .true.
delta_HR_limit = 0.004d0
delta_HR_hard_limit = 0.1d0

delta_lg_XH_cntr_limit = 0.01d0
delta_lg_XH_cntr_hard_limit = 0.1

delta_dX_div_X_cntr_limit = 0.01d0
delta_dX_div_X_cntr_hard_limit = 0.02
delta_lg_XH_cntr_max = 0
delta_lg_XH_cntr_min = -6.0d0

delta_lg_XHe_cntr_limit = 0.01d0
delta_lg_XHe_cntr_hard_limit = 0.02

delta_lgL_H_limit = 0.005
delta_lgL_H_hard_limit = 0.01
delta_lgL_He_limit = 0.005d0
delta_lgL_He_hard_limit = 0.1
delta_lgL_nuc_limit = 0.004
delta_lgL_nuc_hard_limit = 0.1
delta_lgTeff_limit = 0.01d0
delta_lgTeff_hard_limit = 0.1

!dH_decreases_only = .true.
!dH_div_H_limit_min_H =10
!dH_div_H_limit = 10
!dH_div_H_hard_limit =1.0
dHe_limit_min_He = 1d-1!!!1d-1
dHe_limit = 1d-1
dHe_hard_limit =0.5

```

```

dHe_decreases_only = .true.

dH_div_H_limit_min_H = 1e-3
dH_div_H_limit = 0.9d0

dH_div_H_hard_limit = 1d99
dX_limit_min_X = 1d-2
dX_limit = 1d-3
dX_hard_limit = 1d-2

!## solver controls

varcontrol_target =5d-4
solver_iters_timestep_limit =15
solver_itermin = 2

report_why_dt_limits = .true.
timestep_factor_for_retries = 0.8 ! 0.8
min_timestep_factor = 0.9 !0.9
max_timestep_factor = 1.05 ! 1.05d0
retry_hold = 1 ! default 1

redo_limit = -1 !100 ! -1

!ignore_species_in_max_correction = .true.
!scale_max_correction = 0.1d0

use_gold_tolerances = .true.
use_gold2_tolerances = .true.

! debugging

report_why_dt_limits =.true.
report_solver_progress = .true.
!report_all_dt_limits = .true.
!report_solver_dt_info = .true.
!report_dX_nuc_drop_dt_limits = .true.

! output

photo_interval = 50
profile_interval = 100
max_num_profile_models = 300
history_interval = 1
terminal_interval =2
write_header_frequency = 20

dH_div_H_limit_min_H = 1e-3
dH_div_H_limit = 0.9d0
dH_div_H_hard_limit = 2.0d0
!Teff_lower_limit = 3000
log_L_lower_limit = -3.0
max_model_number =150000

num_cells_for_smooth_gradL_composition_term = 0

```



```

delta_lgT_max_limit = 1d-2
delta_lgT_max_hard_limit = 0.1
delta_lgT_max_limit_lgT_min = 8.2d0

delta_lgT_max_at_high_T_limit = 1d-3
delta_lgT_max_at_high_T_hard_limit = 1d-2
delta_lgT_max_at_high_T_limit_lgT_min = 8.3

mesh_logX_species(1) = 'c12'
mesh_logX_min_for_extra(1) = -6
mesh_dlogX_dlogP_extra(1) = 0.2
mesh_dlogX_dlogP_full_on(1) = 2
mesh_dlogX_dlogP_full_off(1) = 1

mesh_logX_species(2) = 'o16'
mesh_logX_min_for_extra(2) = -3
mesh_dlogX_dlogP_extra(2) = 1.0
mesh_dlogX_dlogP_full_on(2) = 2
mesh_dlogX_dlogP_full_off(2) = 1

mesh_logX_species(3) = 'he4'
mesh_logX_min_for_extra(3) = -2
mesh_dlogX_dlogP_extra(3) = 0.5
mesh_dlogX_dlogP_full_on(3) = 2
mesh_dlogX_dlogP_full_off(3) = 1

max_delta_x_for_merge = 0.01
max_abs_rel_run_E_err = 0.5d0

!use_superad_reduction = .true.
max_resid_jump_limit = 1d10

max_resid_jump_limit = 1d12
max_corr_jump_limit = 1d12

max_model_number = 150000
/ ! end of controls namelist

&pgstar

read_extra_pgstar_inlist1 = .true.

extra_pgstar_inlist1_name = 'inlist_pgstar1'

/ ! end of pgstar namelist

```

The following code is a copy of the `run_star_extras.f90` file, which contains all of the additional subroutines used to complete this work. These subroutines include: increasing the resolution of helium burning during the core helium burning phase, turning on element diffusion as the star leaves the AGB, forcing rehomogenisation of the core following a similar prescription as [Renedo et al. \(2010\)](#), [Romero, Campos & Kepler \(2015\)](#) and suppression of the breathing pulses at the end of the CHB as described in Section 2.2.1, which also follows a similar treatment as performed in [Renedo et al. \(2010\)](#), [Romero, Campos & Kepler \(2015\)](#).

```

! *****
!
! Copyright (C) 2010 Bill Paxton
!
! this file is part of mesa.
!
! mesa is free software; you can redistribute it and/or modify
! it under the terms of the gnu general library public license as published
! by the free software foundation; either version 2 of the license, or
! (at your option) any later version.
!
! mesa is distributed in the hope that it will be useful,
! but without any warranty; without even the implied warranty of
! merchantability or fitness for a particular purpose. see the
! gnu library general public license for more details.
!
! you should have received a copy of the gnu library general public license
! along with this software; if not, write to the free software
! foundation, inc., 59 temple place, suite 330, boston, ma 02111-1307 usa
!
! *****

module run_star_extras

use star_lib
use star_def
use const_def
use math_lib
use eos_def

implicit none

include "test_suite_extras_def.inc"

! declarations for xtra_coef_os
real(dp) :: &
  xtra_coef_os_full_on, &
  xtra_coef_os_full_off, &
  xtra_coef_os_above_nonburn, &
  xtra_coef_os_below_nonburn, &
  xtra_coef_os_above_burn_h, &
  xtra_coef_os_below_burn_h, &
  xtra_coef_os_above_burn_he, &
  xtra_coef_os_below_burn_he, &
  xtra_coef_os_above_burn_z, &
  xtra_coef_os_below_burn_z, &
  xtra_dist_os_above_nonburn, &
  xtra_dist_os_below_nonburn, &
  xtra_dist_os_above_burn_h, &
  xtra_dist_os_below_burn_h, &
  xtra_dist_os_above_burn_he, &
  xtra_dist_os_below_burn_he, &
  xtra_dist_os_above_burn_z, &
  xtra_dist_os_below_burn_z
namelist /xtra_coef_os/ &
  xtra_coef_os_full_on, &
  xtra_coef_os_full_off, &
  xtra_coef_os_above_nonburn, &
  xtra_coef_os_below_nonburn, &

```

---

```

xtra_coef_os_above_burn_h, &
xtra_coef_os_below_burn_h, &
xtra_coef_os_above_burn_he, &
xtra_coef_os_below_burn_he, &
xtra_coef_os_above_burn_z, &
xtra_coef_os_below_burn_z, &
xtra_dist_os_above_nonburn, &
xtra_dist_os_below_nonburn, &
xtra_dist_os_above_burn_h, &
xtra_dist_os_below_burn_h, &
xtra_dist_os_above_burn_he, &
xtra_dist_os_below_burn_he, &
xtra_dist_os_above_burn_z, &
xtra_dist_os_below_burn_z
! end of declarations for xtra_coeff_os

! these routines are called by the standard run_star_check_model
contains

include "test_suite_extras.inc"

subroutine extras_controls(id, ierr)
  integer, intent(in) :: id
  integer, intent(out) :: ierr
  type (star_info), pointer :: s
  ierr = 0
  call star_ptr(id, s, ierr)
  if (ierr /= 0) return

  if (s% use_other_mesh_delta_coeff_factor) then ! setup for xtra_coeff_os
    call read_inlist_xtra_coeff_os(ierr)
    if (ierr /= 0) return
    s% other_mesh_delta_coeff_factor => other_mesh_delta_coeff_factor
  end if

  s% extras_startup => extras_startup
  s% extras_check_model => extras_check_model
  s% extras_finish_step => extras_finish_step
  s% extras_after_evolve => extras_after_evolve
  s% how_many_extra_history_columns => how_many_extra_history_columns
  s% data_for_extra_history_columns => data_for_extra_history_columns
  s% how_many_extra_profile_columns => how_many_extra_profile_columns
  s% data_for_extra_profile_columns => data_for_extra_profile_columns
end subroutine extras_controls

!****      code for xtra_coeff_os

subroutine read_inlist_xtra_coeff_os(ierr)
  use utils_lib
  integer, intent(out) :: ierr
  character (len=256) :: filename, message
  integer :: unit

  filename = 'inlist_xtra_coeff_os'

  write(*,*) 'read_inlist_xtra_coeff_os'

  ! set defaults

```

```

xtra_coef_os_full_on = 1d-4
xtra_coef_os_full_off = 0.1d0
xtra_coef_os_above_nonburn = 1d0
xtra_coef_os_below_nonburn = 1d0
xtra_coef_os_above_burn_h = 1d0
xtra_coef_os_below_burn_h = 1d0
xtra_coef_os_above_burn_he = 1d0
xtra_coef_os_below_burn_he = 1d0
xtra_coef_os_above_burn_z = 1d0
xtra_coef_os_below_burn_z = 1d0
xtra_dist_os_above_nonburn = 0.2d0
xtra_dist_os_below_nonburn = 0.2d0
xtra_dist_os_above_burn_h = 0.2d0
xtra_dist_os_below_burn_h = 0.2d0
xtra_dist_os_above_burn_he = 0.2d0
xtra_dist_os_below_burn_he = 0.2d0
xtra_dist_os_above_burn_z = 0.2d0
xtra_dist_os_below_burn_z = 0.2d0

open(newunit=unit, file=trim(filename), action='read', delim='quote', iostat=ierr)
if (ierr /= 0) then
  write(*, *) 'Failed to open control namelist file', trim(filename)
else
  read(unit, nml=xtra_coef_os, iostat=ierr)
  close(unit)
  if (ierr /= 0) then
    write(*, *) 'Failed while trying to read control namelist file', trim(filename)
    write(*, '(a)') &
      'The following runtime error message might help you find the problem'
    write(*, *)
    open(newunit=unit, file=trim(filename), action='read', delim='quote', &
      status='old', iostat=ierr)
    read(unit, nml=xtra_coef_os)
    close(unit)
  end if
end if

end subroutine read_inlist_xtra_coef_os

subroutine other_mesh_delta_coeff_factor(id, eps_h, eps_he, eps_z, ierr)
  use const_def
  use math_lib
  use chem_def
  integer, intent(in) :: id
  real(dp), intent(in), dimension(:) :: eps_h, eps_he, eps_z
  integer, intent(out) :: ierr
  type (star_info), pointer :: s
  real(dp) :: he_cntr, full_off, full_on, alfa_os
  integer :: k, kk, nz, max_eps_loc
  real(dp) :: xtra_coef, xtra_dist, coef, Hp, r_extra, max_eps, eps
  logical :: in_convective_region
  logical, parameter :: dbg = .false.

  include 'formats'

  !write(*,*) 'enter other_mesh_delta_coeff_factor'
  ierr = 0
  if (xtra_coef_os_above_nonburn == 1d0 .and. &
    xtra_coef_os_below_nonburn == 1d0 .and. &

```

```

xtra_coef_os_above_burn_h == 1d0 .and. &
xtra_coef_os_below_burn_h == 1d0 .and. &
xtra_coef_os_above_burn_he == 1d0 .and. &
xtra_coef_os_below_burn_he == 1d0 .and. &
xtra_coef_os_above_burn_z == 1d0 .and. &
xtra_coef_os_below_burn_z == 1d0) return

call star_ptr(id, s, ierr)
if (ierr /= 0) return

nz = s% nz
he_cntr = s% xa(s% net_iso(ihe4),nz)
full_off = xtra_coef_os_full_off
full_on = xtra_coef_os_full_on
if (he_cntr >= full_off) then
  alfa_os = 0
else if (he_cntr <= full_on) then
  alfa_os = 1
else
  alfa_os = (full_off - he_cntr)/(full_off - full_on)
end if
!write(*,1) 'alfa_os', alfa_os
if (alfa_os == 0) return

! first go from surface to center doing below convective boundaries
in_convective_region = (s% mixing_type(1) == convective_mixing)
k = 2
max_eps = -1d99
max_eps_loc = -1
do while (k <= nz)
  eps = eps_h(k) + eps_he(k) + eps_z(k)
  if (in_convective_region) then
    if (s% mixing_type(k) == convective_mixing) then
      if (eps > max_eps) then
        max_eps = eps
        max_eps_loc = k
      end if
    else
      in_convective_region = .false.
      if (max_eps < 1d0) then
        xtra_coef = xtra_coef_os_below_nonburn
        xtra_dist = xtra_dist_os_below_nonburn
      else if (eps_h(max_eps_loc) > 0.5d0*max_eps) then
        xtra_coef = xtra_coef_os_below_burn_h
        xtra_dist = xtra_dist_os_below_burn_h
      else if (eps_he(max_eps_loc) > 0.5d0*max_eps) then
        xtra_coef = xtra_coef_os_below_burn_he
        xtra_dist = xtra_dist_os_below_burn_he
      else
        xtra_coef = xtra_coef_os_below_burn_z
        xtra_dist = xtra_dist_os_below_burn_z
      end if
      xtra_coef = xtra_coef*alfa_os + (1-alfa_os)
      if (xtra_coef > 0 .and. xtra_coef /= 1) then
        coef = xtra_coef
        do
          if (s% mixing_type(k) /= overshoot_mixing) exit
          if (coef < s% mesh_delta_coeff_factor(k)) then
            s% mesh_delta_coeff_factor(k) = coef
            !write(*,2) 'below mesh_delta_coeff_factor(k)', &

```

```

        ! k, s% mesh_delta_coeff_factor(k)
    end if
    if (k == nz) exit
    k = k+1
end do
if (xtra_dist > 0) then
    Hp = s% P(k)/(s% rho(k)*s% grav(k))
    r_extra = max(0d0, s% r(k) - xtra_dist*Hp)
    if (dbg) write(*,2) 'extra_below_overshoot_region', &
        k, s% r(k)/Rsun, Hp/Rsun, r_extra/Rsun
    do
        if (s% r(k) < r_extra) exit
        if (coef < s% mesh_delta_coeff_factor(k)) then
            s% mesh_delta_coeff_factor(k) = coef
            !write(*,2) 'extra below mesh_delta_coeff_factor(k)', &
                ! k, s% mesh_delta_coeff_factor(k)
        end if
        if (k == nz) exit
        k = k+1
    end do
end if
end if
if (dbg) write(*,2) 'done_with_extra_below_overshoot_region', k
if (dbg) write(*,*)
end if
else if (s% mixing_type(k) == convective_mixing) then
    in_convective_region = .true.
    max_eps = eps
    max_eps_loc = k
end if
k = k+1
end do

! now go from center to surface doing above convective boundaries
in_convective_region = (s% mixing_type(nz) == convective_mixing)
k = nz-1
max_eps = -1d99
max_eps_loc = -1
do while (k >= 1)
    eps = eps_h(k) + eps_he(k) + eps_z(k)
    if (in_convective_region) then
        if (s% mixing_type(k) == convective_mixing) then
            if (eps > max_eps) then
                max_eps = eps
                max_eps_loc = k
            end if
        else
            in_convective_region = .false.
            if (max_eps < 1d0) then
                xtra_coef = xtra_coef_os_above_nonburn
                xtra_dist = xtra_dist_os_above_nonburn
            else if (eps_h(max_eps_loc) > 0.5d0*max_eps) then
                xtra_coef = xtra_coef_os_above_burn_h
                xtra_dist = xtra_dist_os_above_burn_h
            else if (eps_he(max_eps_loc) > 0.5d0*max_eps) then
                xtra_coef = xtra_coef_os_above_burn_he
                xtra_dist = xtra_dist_os_above_burn_he
            else
                xtra_coef = xtra_coef_os_above_burn_z
                xtra_dist = xtra_dist_os_above_burn_z
            end if
        end if
    end if
end do

```

```

end if
xtra_coef = xtra_coef*alfa_os + (1-alfa_os)
if (dbg) write(*,2) 'xtra_coef_to_surf', s% model_number, xtra_coef

if (xtra_coef > 0 .and. xtra_coef /= 1) then
  coef = xtra_coef
  do
    if (s% mixing_type(k) /= overshoot_mixing) exit
    if (coef < s% mesh_delta_coeff_factor(k)) then
      s% mesh_delta_coeff_factor(k) = coef
      !write(*,2) 'above_mesh_delta_coeff_factor(k)', &
      ! k, s% mesh_delta_coeff_factor(k)
    end if
    if (k == 1) exit
    k = k-1
  end do
  if (xtra_dist > 0) then
    Hp = s% P(k)/(s% rho(k)*s% grav(k))
    r_extra = min(s% r(1), s% r(k) + xtra_dist*Hp)
    if (dbg) write(*,2) 'extra_above_overshoot_region', &
    k, s% r(k)/Rsun, Hp/Rsun, r_extra/Rsun
    do
      if (s% r(k) > r_extra) exit
      if (coef < s% mesh_delta_coeff_factor(k)) then
        s% mesh_delta_coeff_factor(k) = coef
        !write(*,2) 'extra_above_mesh_delta_coeff_factor(k)', &
        ! k, s% mesh_delta_coeff_factor(k)
      end if
      if (k == 1) exit
      k = k-1
    end do
  end if
end if
if (dbg) write(*,2) 'done_with_extra_above_overshoot_region', k
if (dbg) write(*,*)
end if
else if (s% mixing_type(k) == convective_mixing) then
  in_convective_region = .true.
  max_eps = eps
  max_eps_loc = k
end if
k = k-1
end do

end subroutine other_mesh_delta_coeff_factor

!**** end of code for xtra_coeff_os

subroutine extras_startup(id, restart, ierr)
  integer, intent(in) :: id
  logical, intent(in) :: restart
  integer, intent(out) :: ierr
  type (star_info), pointer :: s
  ierr = 0
  call star_ptr(id, s, ierr)
  if (ierr /= 0) return
  call test_suite_startup(s, restart, ierr)
end subroutine extras_startup

```

```

subroutine extras_after_evolve(id, ierr)
  integer, intent(in) :: id
  integer, intent(out) :: ierr
  type (star_info), pointer :: s
  real(dp) :: dt
  ierr = 0
  call star_ptr(id, s, ierr)
  if (ierr /= 0) return
  call test_suite_after_evolve(s, ierr)
end subroutine extras_after_evolve

! returns either keep_going, retry, or terminate.
integer function extras_check_model(id)
  use eos_def
  integer, intent(in) :: id
  integer :: ierr, handle
  real(dp) :: numfrac_c12, numfrac_o16, Z53
  type (star_info), pointer :: s
  ierr = 0
  call star_ptr(id, s, ierr)
  if (ierr /= 0) return
  extras_check_model = keep_going

! if ( (s% center_he4 < 0.98) .AND. (s% center_he4 > 1d-4) ) then
!   s% history_interval = 2
!   s% profile_interval = 10
!   if (s% center_he4 < 0.3) then
!     s% dt = 1.d4 * 3.14*365*24*60*60

!   end if
!end if

if ( (s% star_mass - s% he_core_mass) < 1d-3 ) then
  numfrac_c12 = (s% center_c12 / 12) / ( (s% center_c12 / 12) &
    + (s% center_o16 / 15.9949146) )
  numfrac_o16 = (s% center_o16 / 15.9949146) / ( (s% center_c12 / 12) &
    + (s% center_o16 / 15.9949146) )
  Z53 = (numfrac_c12 * 6**(5.d0/3.d0)) + (numfrac_o16 * 8**(5.d0/3.d0))
  s% eos_rq% PC_Gamma_start_crystal = ( 178.4 / 6**(5.d0/3.d0) ) * Z53 / s% x_ctrl(1)
  s% eos_rq% PC_Gamma_full_crystal = (( 178.4 / 6**(5.d0/3.d0) ) * Z53 / s% x_ctrl(1)) + 20
endif
end function extras_check_model

integer function how_many_extra_history_columns(id)
  integer, intent(in) :: id
  integer :: ierr
  type (star_info), pointer :: s
  ierr = 0
  call star_ptr(id, s, ierr)
  if (ierr /= 0) return
  how_many_extra_history_columns = 0
end function how_many_extra_history_columns

subroutine data_for_extra_history_columns(id, n, names, vals, ierr)
  integer, intent(in) :: id, n
  character (len=maxlen_history_column_name) :: names(n)

```



```

    real(dp) :: vals(n)
    integer, intent(out) :: ierr
    type (star_info), pointer :: s
    ierr = 0
    call star_ptr(id, s, ierr)
    if (ierr /= 0) return
end subroutine data_for_extra_history_columns

integer function how_many_extra_profile_columns(id)
    use star_def, only: star_info
    integer, intent(in) :: id
    integer :: ierr
    type (star_info), pointer :: s
    ierr = 0
    call star_ptr(id, s, ierr)
    if (ierr /= 0) return
    how_many_extra_profile_columns = 1
end function how_many_extra_profile_columns

subroutine data_for_extra_profile_columns(id, n, nz, names, vals, ierr)
    use star_def, only: star_info, maxlen_profile_column_name
    use const_def, only: dp
    integer, intent(in) :: id, n, nz
    character (len=maxlen_profile_column_name) :: names(n)
    real(dp) :: vals(nz,n), numfrac_c12, numfrac_o16, Z53
    integer, intent(out) :: ierr
    type (star_info), pointer :: s
    integer :: k
    ierr = 0
    call star_ptr(id, s, ierr)
    if (ierr /= 0) return
    names(1) = 'Horowitz_Gamma_Limit'
    numfrac_c12 = (s% center_c12 / 12) / ( (s% center_c12 / 12) + (s% center_o16 / 15.9949146) )
    numfrac_o16 = (s% center_o16 / 15.9949146) / ( (s% center_c12 / 12) &
        + (s% center_o16 / 15.9949146) )
    Z53 = (numfrac_c12 * 6**(5.d0/3.d0)) + (numfrac_o16 * 8**(5.d0/3.d0))
    do k = 1, nz
        vals(k, 1) = ( 178.4 / 6**(5.d0/3.d0) ) * Z53 / s% x_ctrl(1)
    end do
end subroutine data_for_extra_profile_columns

! returns either keep_going, retry, or terminate.
integer function extras_finish_step(id)
    use chem_def
    integer, intent(in) :: id
    integer :: ierr, nz, k, core_lim, core_zones
    real(dp) :: c_cntr, o_cntr, avg_o16_core, avg_c12_core, M
    real(dp) :: avg_h1_core, avg_he3_core, avg_he4_core, avg_ne20_core, avg_n14_core
    real(dp) :: avg_mg24_core
    type (star_info), pointer :: s
    ierr = 0
    call star_ptr(id, s, ierr)

! Increase resolution during the CHB

    if ((log10(s% power_h_burn) > 1.7) .or. (log10(s% power_he_burn) > 1.7)) then

```

```

s% use_gold_tolerances = .false.
s% use_gold2_tolerances = .false.

s% tol_correction_norm = 3d-4
s% tol_max_correction = 3d-2
write(*,*) "relax_tolerance_"
s% gold2_tol_residual_norm1 = 1d-10
s% gold2_tol_max_residual1 = 1d-8

else
s% tol_correction_norm = 3d-5
s% tol_max_correction = 3d-3
write(*,*) "normal_tolerance_"
end if

! Element diffusion at the end of the AGB

if (((s% star_mass_h1) < 1d-2) .and. ((s% log_L_surf) < 3.5)) then
s% do_element_diffusion = .true.
write(*,*) "element_diffusion_is_on"
end if

! Brute Force Rehomogenisation

if ( (s% photosphere_r < 0.1 ) .and. (s% Teff < 20000) .and. (s% Teff > 19950 ) ) then
write(*,*) "Rehomogenise_Start"
nz = s% nz
c_cntr = s% xa(s% net_iso(ic12),nz)
o_cntr = s% xa(s% net_iso(io16),nz)
do k = 1, nz
if (s% xa(s% net_iso(io16), k) .gt. o_cntr) then
core_lim = k
exit
end if
end do
core_zones = nz - core_lim
avg_o16_core = 0
avg_c12_core = 0
avg_h1_core = 0
avg_he3_core = 0
avg_he4_core = 0
avg_ne20_core = 0
avg_n14_core = 0
avg_mg24_core = 0
M = 0
do k = core_lim, nz
M = s% dm(k) + M
end do
do k = core_lim, nz
avg_o16_core = avg_o16_core + (s% xa(s% net_iso(io16), k)) * (s% dm(k)) / M
avg_c12_core = avg_c12_core + (s% xa(s% net_iso(ic12), k)) * (s% dm(k)) / M
avg_h1_core = avg_h1_core + (s% xa(s% net_iso(ih1), k)) * (s% dm(k)) / M
avg_he3_core = avg_he3_core + (s% xa(s% net_iso(ihe3), k)) * (s% dm(k)) / M
avg_he4_core = avg_he4_core + (s% xa(s% net_iso(ihe4), k)) * (s% dm(k)) / M
avg_ne20_core = avg_ne20_core + (s% xa(s% net_iso(ine20), k)) * (s% dm(k)) / M
avg_n14_core = avg_n14_core + (s% xa(s% net_iso(in14), k)) * (s% dm(k)) / M
avg_mg24_core = avg_mg24_core + (s% xa(s% net_iso(img24), k)) * (s% dm(k)) / M
end do

```

---

```

do k = core_lim, nz
  s% xa(s% net_iso(io16), k) = avg_o16_core
  s% xa(s% net_iso(ic12), k) = avg_c12_core
  s% xa(s% net_iso(ih1), k) = avg_h1_core
  s% xa(s% net_iso(ihe3), k) = avg_he3_core
  s% xa(s% net_iso(ihe4), k) = avg_he4_core
  s% xa(s% net_iso(ine20), k) = avg_ne20_core
  s% xa(s% net_iso(in14), k) = avg_n14_core
  s% xa(s% net_iso(img24), k) = avg_mg24_core
end do

write(*,*) "Rehomogenise_End"
write(*,*) "Core_Mass=", M
write(*,*) "c_cnr=", s% xa(s% net_iso(ic12),nz)
write(*,*) "o_cnr=", s% xa(s% net_iso(io16),nz)

end if

! Breathing Pulse Suppression

if ( (s% center_he4 <= 0.1 ) .and. (s% center_he4 >= 1d-6) ) then
  s% overshoot_f(1) = 1d-99
  s% overshoot_f0(1) = 1d-99
else
  s% overshoot_f(1) = 0.020
  s% overshoot_f0(1) = 0.004
endif
nz = s% nz
write(*,*) s% overshoot_f(1)

if (ierr /= 0) return
  extras_finish_step = keep_going
end function extras_finish_step

end module run_star_extras

```



## APPENDIX C – Tables of Key Results

Below I present a table of values for select initial masses. The values reported are the final mass, final central oxygen mass fraction, the number of TPs experienced, the final age, CHB lifetime and the mass of the helium core mass at the start of the first TP. Not all of the sequences produced in this work are represented. The initial masses selected are  $M_i/M_\odot = 0.90, 1.30, 1.50, 1.90, 2.20, 2.45, 2.70$  and  $3.05$ . This includes: the mass limits in this work, the initial mass which the contribution from the p-p chain and CNO cycle is equal during the MS, our transition point, masses in which the core C/O ratio reduces (see Section 3.1), in addition to some intermediate masses to bridge large jumps in the table of initial masses. For the above initial masses, the NACRE\_L, NACRE\_A, NACRE\_H and An\_A considerations to the  $^{12}\text{C}(\alpha, \gamma)^{16}\text{O}$  reaction rate are reported in Table 2. I choose not to show the An\_L and An\_H values in the table below as they do not vary from An\_A as significantly as the uncertainties from NACRE.

	0.90 $M_{\odot}$				1.30 $M_{\odot}$			
	NAC_L	NAC_A	NAC_H	An_A	NAC_L	NAC_A	NAC_H	An_A
Final Mass / $M_{\odot}$	0.517	0.515	0.513	0.516	0.550	0.549	0.547	0.547
Helium Core Mass @ 1st TP / $M_{\odot}$	0.512	0.510	0.494	0.512	0.527	0.528	0.531	0.531
Number of TPs	1	1	1	1	6	4	3	3
Final Central C/O ratio	0.517	0.669	0.768	0.589	0.510	0.652	0.757	0.588
CHB Lifetime / Myr	98.5	106.6	108.6	101.1	95.2	99.5	104.1	97.7
Final Age / Gyr	15.301	15.299	15.313	15.313	4.623	4.603	4.608	4.605
	1.50 $M_{\odot}$				1.90 $M_{\odot}$			
	NAC_L	NAC_A	NAC_H	An_A	NAC_L	NAC_A	NAC_H	An_A
Final Mass / $M_{\odot}$	0.560	0.560	0.559	5.60	0.582	0.579	0.578	0.580
Helium Core Mass @ 1st TP / $M_{\odot}$	0.529	0.533	0.529	0.529	0.494	0.495	0.492	0.495
Number of TPs	7	4	5	6	17	13	14	15
Final Central C/O ratio	0.506	0.656	0.756	0.582	0.568	0.708	0.804	0.641
CHB Lifetime / Myr	95.8	102.5	106.4	101.7	252.4	261.2	265.7	255.1
Final Age / Gyr	3.103	3.096	3.090	3.096	2.043	2.031	2.039	2.037
	2.20 $M_{\odot}$				2.45 $M_{\odot}$			
	NAC_L	NAC_A	NAC_H	An_A	NAC_L	NAC_A	NAC_H	An_A
Final Mass / $M_{\odot}$	0.602	0.600	0.598	0.600	0.620	0.618	0.617	0.619
Helium Core Mass @ 1st TP / $M_{\odot}$	0.511	0.512	0.509	0.510	0.534	0.539	0.543	0.534
Number of TPs	16	16	13	16	15	12	11	12
Final Central $^{16}\text{O}$ Abundance	0.560	0.688	0.788	0.636	0.519	0.676	0.788	0.603
CHB Lifetime / Myr	198.9	203.5	207.1	201.7	138.5	147.4	152.4	141.4
Final Age / Gyr	1.609	1.602	1.595	1.609	1.377	1.370	1.363	1.384
	2.70 $M_{\odot}$				3.05 $M_{\odot}$			
	NAC_L	NAC_A	NAC_H	An_A	NAC_L	NAC_A	NAC_H	An_A
Final Mass / $M_{\odot}$	0.642	0.642	0.640	0.642	0.690	0.691	0.691	0.691
Helium Core Mass @ 1st TP / $M_{\odot}$	0.575	0.578	0.580	0.579	0.633	0.636	0.639	0.636
Number of TPs	12	11	10	11	10	9	9	9
Final Central $^{16}\text{O}$ Abundance	0.518	0.654	0.746	0.604	0.478	0.619	0.722	0.563
CHB Lifetime / Myr	99.1	102.7	104.6	101.7	58.7	61.4	62.8	60.5
Final Age / Gyr	1.242	1.233	1.231	1.233	1.146	1.149	1.159	1.156

Table 2 – Final Mass, helium core mass at the start of the first TP, number of TPs experienced, final central oxygen mass fraction, lifetime of the CHB and the final age of the sequences are shown. Values are given for the initial masses of  $M_i/M_{\odot} = 0.90, 1.30, 1.50, 1.90, 2.20, 2.45, 2.70$  and  $3.05$ . We show the NACRE adopted rate (NAC\_A) and its high/low uncertainties (NAC\_H/NAC\_L), as well as the adopted rate from [An et al. \(2016\)](#) (An\_A).

# APPENDIX D – Perspectives for Future Work

This section discusses additional physics that will be added to the sequences produced thus far in the course, as well as other considerations for some of the physics already applied. I plan to include different wind schemes (specifically for the AGB stages) in addition to axion emission due to Bremsstrahlung and Compton Scattering. These sequences will be utilised in future works which are described. I give a brief introduction to each topic that I plan on researching as an extension of the results reported in this work, then it is described how they are related to the work that has already been produced. Finally I give a motivation and an aim of the future work.

## D.1 Emission of particles during stellar evolution: Axions

Axions are theoretical particles which can conserve the CP symmetry in strong interactions, but they have so far eluded detection. The production of axions within stellar interiors is derived mainly from three different mechanisms: Atomic recombination and de-excitation, Bremsstrahlung, and Compton interactions. Our future work will focus on the latter two interactions as they are deemed to be the dominant processes for low to intermediate-mass stars (Raffelt, 1990; Raffelt, 1996; Domínguez; Straniero; Isern, 1999)

The emission of axions due to Compton scattering is related to the electron degeneracy for fixed temperatures and densities (Raffelt, 1990; Raffelt, 1996). With a larger degeneracy, electrons occupy states of higher momentum which increases the scattering cross-section of the interaction. The increased cross-section can overcome the blocking from Pauli effects. As presented, we find negligible differences to the overall degeneracy of the cores as a result of different  $^{12}\text{C}(\alpha,\gamma)^{16}\text{O}$  reaction rates. However, since Compton scattering is an important mechanism in axion emission, I find it important to study if there are any differences into the axion emission rate due to different considerations for the  $^{12}\text{C}(\alpha,\gamma)^{16}\text{O}$  reaction rate.

Considerations to the emission of axions due to Bremsstrahlung is also important during the RGB and WD stages where the cores are degenerate. Bremsstrahlung emission occurs due to the interaction between an electron and an atomic nucleus (Kippenhahn; Weigert, 1990; Prialnik, 2009). As in degenerate cores the electron density is higher than the photon density, Bremsstrahlung emission within degenerate cores is of particular importance.

I believe that it is worth investigating how the differences in electron degeneracy that we found in this study could lead to differing emission rates of axions. These differing emission rates may affect some key stellar features, such as the WD cooling rate, which are used to constrain the properties of axions. I aim to produce computations which include subroutines that add the contribution of energy loss due to axions to quantify the differences to the axion emission rates for the different ensembles of reaction rate formulas.

## D.2 Differing Wind Schemes during the AGB

A general relation for the mass-loss due to wind scheme has not yet been formed. There are many relations that have been derived which relate the mass-loss rate to the following: mass, radius, luminosity, composition and rotation period of a star (Reimers, 1975; Bloeker, 1995; Vassiliadis; Wood, 1993; Wachter et al., 2002). The use of different mass-loss rates produces sequences, that consider similar initial conditions, to be very distinct later in the evolution (see Figure 24, for an example of the IFMR).

The use of other mass-loss due to wind schemes on the sequences produced in this course, particularly during the AGB phase, would be a useful work. It would provide further insight into the growth of the helium core, which is dependent on the mass-loss rate during the TP-AGB (Weiss; Ferguson, 2009; Renedo et al., 2010; Romero; Campos; Kepler, 2015; De Gerónimo et al., 2017; Marigo et al., 2020). The mass-loss rate of Vassiliadis & Wood (1993) has already been implemented during this course (see Section 2.3.3, for details). However, it has not been used so far in the models presented in this work. By applying such a rate to these sequences, we can analyse how properties such as the helium core growth may be affected.

I believe this is an important future task as a result of this work to allow better comparisons between other sequences which consider other mass-loss rates. In addition, it may provide new information on how the  $^{12}\text{C}(\alpha,\gamma)^{16}\text{O}$  reaction rate effects the selected mass-loss rate, if at all, and the subsequent evolution as a result.